CHARLES J. CLEARY

AWARDS

for

Papers on Material Sciences

Edited by LYNN E. CATOE
SCIENCE AND TECHNOLOGY DIVISION
LIBRARY OF CONGRESS

PUBLISHED IN 1962 FOR
DIRECTORATE OF MATERIALS AND PROCESSES
AERONAUTICAL SYSTEMS DIVISION
WRIGHT-PATTERSON AIR FORCE BASE, OHIO

Foreword

This book is one of three prepared by the staff of the Science and Technology Division of the Library of Congress, at the request and with the financial support of the Directorate of Materials and Processes (Materials Central), Wright-Patterson Air Force Base, Ohio. These three books have been compiled and published as part of the activities of the Materials Central in connection with the celebration of its forty-fifth year as the center of materials research and development for the United States Air Force. Three activities of Materials Central are highlighted in these publications. One is a compilation of award-winning technical papers prepared by Materials Central personnel, the second is a collection of abstracts of scientific and technical papers and reports prepared by Materials Central and its scientific and industrial contractors during the past decade and a half, and the third is a chronology of significant materials events beginning forty-five years ago and ending in the present. It is believed these three books will provide a valuable permanent set of references to anyone interested in the materials sciences.

Introduction

The Charles J. Cleary Award of the Materials Central was established in 1951.

The purpose of this award is to stimulate internal technical activity within the Materials Central by recognizing the outstanding reports and papers published by the personnel of the Central, and in so doing, provide a means to honor the memory of Charles J. Cleary, who made so many significant contributions to the materials sciences.

From the candidate papers nominated by the respective laboratory chiefs, a final selection is made by a committee representing all of the laboratories of the Central. In addition to the winning paper, three candidate papers receive honorable mention.

It is fitting that this award, established to promote progress in the materials sciences, should honor Charles J. Cleary, who contributed so greatly to the solution of monumental materials problems. Born on October 12, 1891, in Boston, Massachusetts, he graduated from the Lowell Textile Institute with a degree in textile engineering (ca. 1915). Upon leaving the Institute, he was employed with the Textile Division of the National Bureau of Standards.

When the United States became actively engaged in World War I, Mr. Cleary resigned his position at the Bureau of Standards and enlisted in what was then the Aviation Section of the Signal Corps. He was accepted for pilot training and, after receiving his wings, was an instructor for several months. He was later transferred to Langley Field where he was assigned to camouflage development. He was the pilot on the first airplane flights to demonstrate the effectiveness of aircraft camouflage over land and water.

In 1920, he was transferred to McCook Field, Dayton, Ohio, where he became Chief of the Textiles Branch of the Materials Laboratory, which had come into being about a year previously. Here he was actively engaged in both the fabric and finishes for fabric covered aircraft.

Under his direction, a cotton cloth, which with modification is being used today, was developed to replace imported linen and the finish was changed from an expensive and temperamental cellulose acetate to the cellulose nitrate doping system. The Air Force still uses cellulose nitrate dope for fabric covered airfoil surfaces.

1st Lt. Cleary reverted to reserve status in the late 1920's, but remained active in the Reserve Corps and maintained his pilot proficiency for another ten years. He held the rank of major at the time he became inactive in the Reserve Corps.

Along with his activity in textiles, he held the responsibility for the development of rubber products, including aircraft tires. At the outbreak of World War II, two critical problems were placed in his hands.

One of these problems was the development of a textile material for parachutes. Although work had continued for years on the development of a substitute for Japanese silk for parachutes, it was not until the discovery of nylon that a promising material came into light. Mr. Cleary was one of the first to receive samples of the newly discovered fiber, and, after initial tests, went all out to stimulate development and production of nylon parachutes. Without his untiring effort, the air war might have been waged without parachutes, or at best, with an ersatz item. The nylon parachute is a lasting memorial to his contribution to aviation history.

The second problem was the almost overnight requirement to change aircraft tire production from what approached pilot plant scale to a production line item. After getting tire production lines well under way in the United States, Mr. Cleary was selected as one of a group to establish production facilities for B–17 tires in England.

Like silk, the supply of natural rubber was cut off by Japan. Faced with the problem of rapidly dwindling supplies of natural rubber, Mr. Cleary

immediately pressed the wartime-developed synthetic rubbers into use for Air Force equipment.

In addition to his technical capabilities, Mr. Cleary had a personality that is rarely found. He had few equals in his ability to influence people and make friends. His ability to meet any situation with an appropriate anecdote was known throughout the Air Force.

Mr. Cleary's health began to fail during the last two years of the war. He suffered a fatal heart attack on returning from a local high school football game on the evening of September 29, 1945. He was 53 years old. At the time of his death, Mr. Cleary held the dual position of Assistant Chief of the Materials Laboratory and Chief of the Textiles and Rubber Branch.

Contents

ALBRECHT HERZOG

Elevated Temperature Fatigue Testing of
Turbine Buckets

1952

ALBRECHT HERZOG

Albrecht Herzog was born January 2, 1901, in Frankfurt-am-Main, Germany. He attended the German High School in Constantinople, Turkey, until 1918, and then returned to Germany where he attended the Institute of Technology in Darmstadt. He received the M.S. degree in mechanical engineering in 1925 and the Ph. D. degree in 1936.

In 1925, he was employed by the Darmstadt Institute of Technology as a laboratory engineer, and at the time of his departure in 1935 was head of the Laboratory for Engineering Construction. From 1938 to 1946, he was assigned as scientist and branch chief of the Department for Strength Research of the Institute for Aeronautical Research, Brunswick, Germany.

Mr. Herzog came to the United States in 1946 under contract to Wright-Patterson Air Force Base, Ohio. He was assigned to what was then the Materials Laboratory and has remained with this organization since that time. He is currently in the Advanced Metallurgical Studies Branch, Metals and Ceramics Laboratory, Directorate of Materials and Processes.

Mr. Herzog was a member of the Ernst Ludwig Society of the Institute of Technology, Darmstadt, Germany, and of the Lilienthal Society, Berlin, Germany. He is currently a member of the Scientific Society for Aviation (WGL), Germany, and is listed in the tenth edition of *American Men of Science*.

BIBLIOGRAPHY

Research report on determination of strains and stresses in construction materials by the stress coat method. Brunswick (Berlin), 1936.

With Kayser and Steinhardt. Dehnungsmessungen und Spannungsuntersuchungen an geschweissten Vollwandträgern. Der Stahlbau (Berlin), 10 (5/6): 33-37, February 26, 1937.

Research report on strains and stresses of bent beams. Der Stahlbau (Berlin), 1938.

With Kayser. Versuche zur Klärung des Spannungsverständes in Rahmenrücken. Der Stahlbau (Berlin), 12 (2): 9-15, January 20, 1939.

Research report on strains and stresses in piston groups. Published as "UM" report by Zentrale für Wissenschaftliches Berichtswesen (Berlin), 1944.

Research report on rotating bending fatigue tests of hard chromium-plated and nitrided bars. Published as "UM" report by Zentrale für Wissenschaftliches Berichtswesen (Berlin), 1944.

Elevated Temperature Fatigue Testing of Turbine Buckets. I. Calculations of Natural Frequencies and Stresses and Proposed Testing Methods. Wright Air Development Center, Materials Laboratory, Wright-Patterson Air Force Base, Ohio. AF Technical Report no. 5928, May 1950.

3

Elevated Temperature Fatigue Testing of Turbine Buckets. II. Fatigue Tests of Turbine Buckets under Static Axial and Superimposed Vibrational Bending Loads. Wright Air Development Center. Materials Laboratory, Wright-Patterson Air Force Base, Ohio. AF Technical Report no. 5936, March 1953.

Fatigue Testing of Turbine Buckets. Presented at the Spring Meeting of the Society for Experimental Stress Analysis in Los Angeles, Calif., April 1955. In: Proceedings of the Society for Experimental Stress Analysis, XV(1):21-34, 1957.

The Notch Sensitivity of Structural and Gas Turbine Materials under Creep Rupture Load. Paper presented at the Institutes of Technology in Munich, Darmstadt and Karlsruhe, Germany, July 1960.

Strength Investigations on Unidimensionally Grown, Crystalline Iron Whiskers. Paper presented at the Institutes of Technology in Munich, Darmstadt and Karlsruhe, Germany, July 1961.

A Contribution to the Morphology of Unidimensionally Grown, Crystalline Iron Whiskers. Paper presented at the University of Saarbruecken, Germany, July 1961.

Morphology and Strength of Iron Whiskers. Paper presented at the University of Michigan, Ann Arbor, Michigan, March 1962.

Elevated Temperature Fatigue Testing of Turbine Buckets

A. HERZOG

Part 1. Calculations of Natural Frequencies and Stresses and Proposed Testing Methods

INTRODUCTION

Present developments in aircraft design necessitate precise knowledge about the behavior of materials under elevated temperatures and combined stresses. An essential component in modern aircraft is the jet engine. The materials exposed to the most severe conditions in such an engine are those used in the design of combustion chambers, vanes and buckets. These components have to operate without failure for about 1,000 hours. The most unfavorable conditions prevail in buckets due to the combination of centrifugal stresses, vibrations and temperatures imposed. In the investigation of turbine buckets the stress in the material under observation is affected by such variables as shape, load, temperature, modulus of elasticity, damping due to fastening, and internal friction in the material. Because one or more of these variables affect each bucket, many types of bucket failures have been observed. The investigation described in this paper was undertaken to determine the influences of stress on bucket failure.

For many years the NACA conducted engine tests on the stand to investigate buckets by measuring stresses and strains at operating speeds and temperatures. Very valuable information was obtained. However, the actual operation of the engine for such tests imposed considerable restrictions on the type of measurement and the locations from which most reliable data could be obtained. In addition the instrumentation of such a test engine became very complex and expensive. Despite this effort only certain ratios of centrifugal to vibrational loads could be realized, while other load ratios apparently occurred in engines during flight. These considerations and consequently the desire to devise a simpler method

to simulate service conditions led to the development of the test method to be presented. A satisfactory laboratory test will assure sufficient flexibility provided that the ratio of axial to the vibrational bending load can be adjusted to all pertinent values and if the amplitudes are large enough to obtain fatigue failures within short time periods. The latter condition is essential for establishing s-n diagrams in the lifetime range of the specimens.

In the engine test it is difficult to accurately determine the number of cycles to failure. The engine has to be stopped in order to check the buckets for the start of fatigue failures, and the cooling and thermal effects impose unknown stresses on the buckets. Successive engine starts will involve similar stresses in the opposite direction, thereby clouding the final results. Any approach attempted should try to eliminate such difficulties. However, disadvantages also have to be tolerated for the benefit of obtaining a simple test arrangement. Once such a test procedure is developed it may be used for testing not only turbine buckets but also similarly loaded parts in the engine like compressor blades, compressor vanes in various shapes and fastenings at any temperature desired and with the application of various ratios of tension to bending stresses.

It is emphasized that the tests presented approximate service conditions in such a way that they simulate the main forces acting and that they can be checked by other considerations. During actual service operation other smaller and less influential forces may be superimposed over the fundamental stress distribution which may change failure locations. However, the main distribution of forces is maintained. The tests were conducted

at the fundamental frequency of the bucket including the additional masses of the test equipment. If under these circumstances the experimental results coincide with the results obtained from service, provided the latter pertain to the same vibrational mode, it can be assumed that the point where the failure occurs is located at the critical fibre in both test and service. This leads to the concept that despite a substitution of the static load for the centrifugal load the relative stress distribution closely approaches that obtained in service.

In the specific case of operating a bucket in an engine additional stresses such as thermal and aerodynamic stresses may be superimposed over the fundamental stress system. Thermal stresses occur only when the engine is starting or is cooling therefore occurring during a relatively short portion of the operational time. Aerodynamic stresses are continuously present; however, their magnitude is not very large. The refinement of the test procedure including such additional influences may be exercised in future.

Basically the approach selected permits a calculation of the main stresses to be expected in operating a bucket which has been designed for aerodynamic efficiency. After completion of such a calculation the necessary information is obtained for prediction of maximum stresses pertaining to the assumed speed and unit amplitude of the vibration.

The comparison between the maximum stress for the bucket material and the multiple of the unit stress previously calculated indicates the maximum possible amplitude which can be permitted without failing the bucket. If the maximum permissible amplitude stays below amplitudes usually obtained for buckets considering the damping factors resulting from the root fastening and the internal damping of the material at temperature, the part will be designed safely to resist fatigue failures.

TEST METHOD

The factors just mentioned and particularly the action of external forces as they act on buckets during engine operation were considered in the development of the test device shown schematically in Fig. 1. The turbine wheel is suspended in a fork by a center bolt which can be tightened to keep the wheel from rotating. The fork can be rotated around the
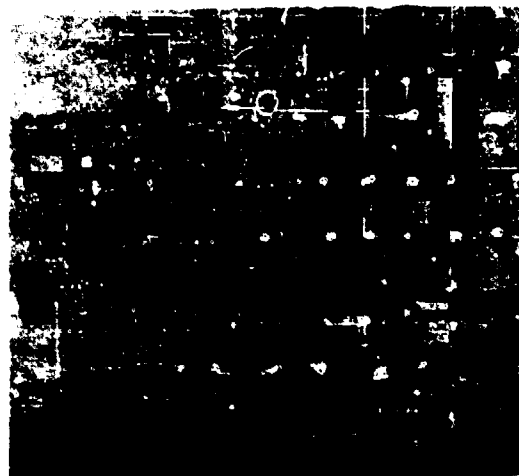
Figure 1. Test stand for service simulated bucket investigation.

center axis of the frame structure and is fastened with a nut in the proper position to the upper part of the frame. The centrifugal force can then be simulated by a static axial load applied to the bucket by means of wedging jaws. Fig. 2 shows the gripping arrangement on the bucket. The jaws wedge into a centerpiece which has seatings for knife edges aligned lateral to the bucket axis. The knife edge axis was directed through the centroid of the cross section area of the bucket at the fastening location. A ring with supports for the knife edges as shown in Fig. 2 transmits the axial force to a pull bar which in turn is fastened to a nut with a washer, both with spherical contact faces in order to allow for alignment. In tightening this nut any desired tensile force may be applied to the bucket.

Figure 2. Bucket grip and attachment with freedom for lateral vibration.

6

However, some freedom of movement is still possible for laterally applied vibrational forces due to the knife edge arrangement. The lateral forces are introduced into the system at the ring mentioned above and the ring is vibrated at 150 cycles per second, the natural frequency of the bucket system. The cross section of the bucket is curved and in order to prevent undesired stress from being introduced by the grips, the wedging jaws have to fit this curvature accurately.

The application of an axial load to the bucket instead of a centrifugal force produces a difference in the stresses applied. However, for investigative purposes the stress in the critical area may be adjusted to the proper value. Since smaller moments occur nearer the bucket tip than at the critical cross section and since the temperature is lower in this region, the significant combined axial and bending stress is still to be expected at the critical cross section.

Parallel to the axis of the knife edges the armature of the vibration generating magnet is fastened. The magnet is located in front of the armature leaving an airgap of 0.064 inch. For maximum efficiency at a given amplitude the proper size of this gap is critical. However, the 0.064-inch gap size was satisfactory and was kept constant throughout the investigation. The magnet coil is activated by a 3,000 watt amplifier manufactured by Oakton Engineering Company of Chicago. The amplifier was designed to furnish the fundamental and second harmonic frequencies of the buckets with large amplitudes. This is necessary because short time fatigue tests which can be carried out only with large stresses consequently require large amplitudes.

The bucket airfoil sections between the root and the grip were heated inductively. The induction heating coil was shaped and the distance from the specimen was maintained such that the same temperature distribution over the included length was obtained as that measured during engine operation in test stands. So far not many actual temperature measurements over the airfoil length of the bucket have been made in operating engines and no information is available from actual flight conditions. However, when these data are obtained actual conditions can be reproduced. The frequency used for induction heating was 30 mc. The heater had a capacity of 3.5 kw and full output energy was seldom necessary. In continuous operation for

fatigue tests the temperature could be kept fairly constant without additional refinements provided drafts in the testing room were prevented.

INSTRUMENTATION

(a) Axial Load Measurements

As indicated before, several variables had to be maintained constant in order to interpret the results clearly. Fig. 3 shows a general view of the test arrangement with test stand, amplifier, induction heater and temperature recorder.
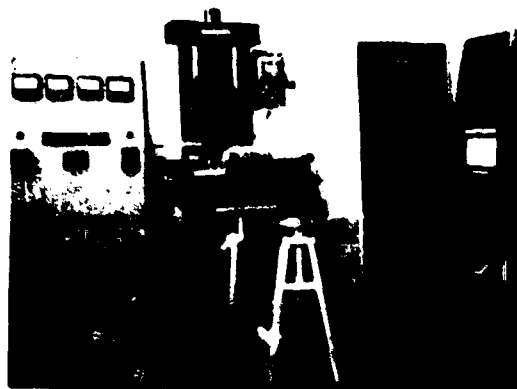
FIGURE 3. General arrangement of the test equipment.

The axial load was checked and adjusted by strain gages on the axial pull bar. For precise results the modulus of elasticity of the bar material is essential. It was determined separately by a careful investigation. During the tests the load originally applied was checked frequently.

The creep of the bucket material at high temperature levels could have been a factor. Thus tests were made to determine the influence to be expected by imposing a constant tensile load. This investigation showed that for the axial loads, materials, and temperatures used, no significant influence could be measured over extended time periods. Therefore the control of this variable was neglected.

The actual stresses on the bucket in the critical area were measured with strain gages at room temperature. For this purpose ten electrical strain gages were placed around the perimeter of the critical cross section. These gages were used for static and dynamic measurements. One compensating gage was utilized in connection with a suitable switch and an SR-4 strain indicator. For static measurements the switch permitted the sub

stitution of individual active gages on the bucket in the measuring circuit.

(b) Dynamic Measurements

For dynamic measurements the active gage was used as one arm in a bridge operated with a 3-volt battery as shown schematically in Fig. 4. The
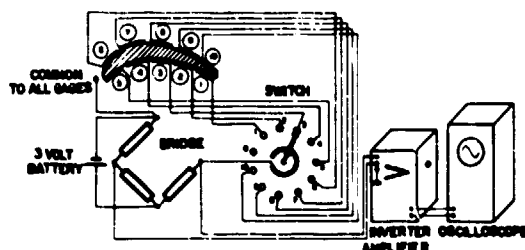

FIGURE 4. Strain gage circuit for dynamic measurements.

potential across the bridge was fed into an inverter amplifier, the output of which was connected to the Y-axis of a Dumont dual beam oscilloscope. Starting from the point where the axial load was applied to the bucket the plain vibrational stresses could be measured.

For elevated temperatures the strains could not be measured because of space limitations and influences by the induction coil. In this case deflection readings were taken and the corresponding stresses on the bucket at the desired location were calculated from the deflection using the stress and deflection measurements at room temperature as a calibration. The deflection during vibration at temperature was determined by applying a mirror to the jaw holder and utilizing a Strobotac and scale as shown in Fig. 5. Adjusting the Strobotac to approximately the operating frequency of the bucket, deflection angle could be read in radians
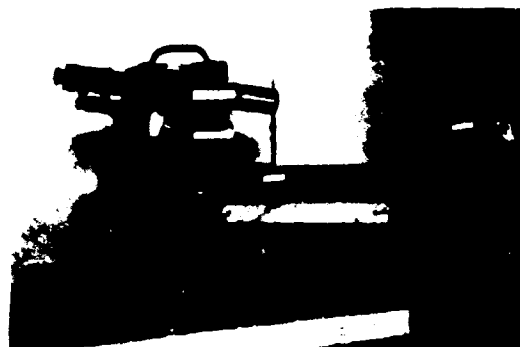

FIGURE 5. Optical system for measuring dynamic deflection.

by means of a telescope which was aimed at the mirror so that the scale in front of the Strobotac could be read. The mirror holder was rigid in order to have no natural vibration of its own in the vicinity of the test frequencies and consequently no difference in reading was obtained between a mirror on the bucket and one at the jaw holder. Therefore it could be assumed that the readings with the mirror on the jaw holder reflected the true deflection of the bucket at the gripping location.

For fatigue measurements the number of cycles to failure have to be determined. This was accomplished by checking the vibration frequency of the bucket as closely as possible and by measuring the elapsed time to failure. The amplifier was equipped with a timer which was activated at the instant the plate voltage was applied which corresponds to the instant when vibrations were generated.

The bucket system was vibrated at the fundamental frequency which was fairly low due to the additional masses necessary for applying the static and the vibrational bending forces.

The overall system inside the frame has several resonance points. Beside the actual bucket frequency the most noticeable other resonant frequencies were those of the frame, the frame on its supports and the cantilever support plate for the magnetic driver. However, all of these were fairly well displaced from the bucket frequency thus imposing no special problems. Nevertheless, one other frequency caused difficulties in some cases. This frequency was the natural torsional frequency of the bucket. It is well known that the fundamental torsional and bending frequencies are often close in parts which have low natural frequencies. In this investigation the separation of these two frequencies was complicated due to the screw type neutral axis which produced a small amount of torsional movement under bending loads However, this difficulty was overcome by the addition of small masses on the ring thus displacing the bending from the torsional resonance point. A sidelight which might be noted here is that the influence of frequency on fatigue limits is being investigated separately and may be reported at a later time as a theoretical evaluation.

(c) Temperature Measurements

The measurement of temperatures at the heated section of the bucket presented some

8

problems. These tests were conducted using a Radiamatic pyrometer with a Honeywell recorder set for a temperature range of 800° F to 1900° F. The optical system in the Radiamatic was designed for a distance of 6 inches from the heated surface and a target area of ¼ inch. Thus it was possible to aim the device between two turns of the heating coil. The airfoil area was then checked for temperature distribution in the axial and in the lateral direction. The same indicating location at the trailing edge was used for recording the nominal temperature during successive fatigue tests.

The calibration of the Radiamatic is critical because it is a total radiation pyrometer which was adjusted to black body temperature. Thus the emissivity of the bucket material under operational conditions has to be the base for the measurements. In order to calibrate the device a small disc of the material to be measured was placed inside a crucible which was located in a metal tube. The disc was heated by a resistance wire coil inside the tube. For comparison of temperatures a thermocouple was welded to the disc and the Radiamatic was aimed at the location controlled by the thermocouple. Calibration readings were taken after the disc was oxidized on the surface over an extended time period. In this way the Radiamatic was set to coincide with the thermocouple readings and this temperature was assumed for setting the bucket temperature at the hottest area of the trailing edge.
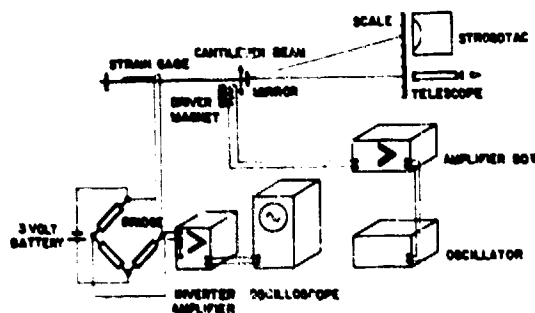

FIGURE 6. Schematic diagram of dynamic calibration instrumentation.

EVALUATION OF STRESS MEASUREMENTS

The axial strains measured at the previously mentioned 10 locations around the perimeter of the critical cross section of the bucket were used
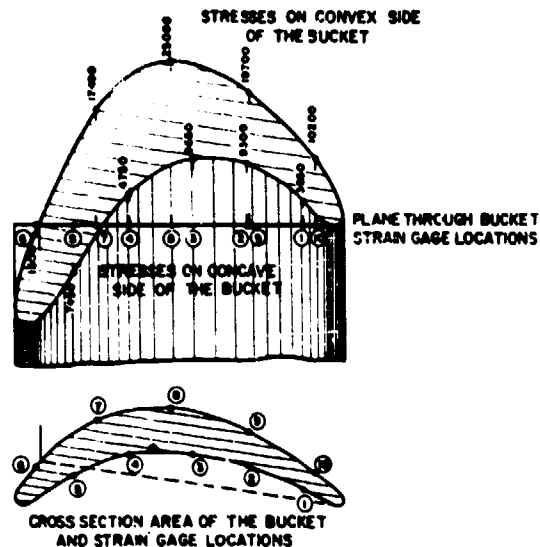
FIGURE 7. Distribution of axial stresses on the concave and convex sides of the cross section.

to calculate the stresses. For this calculation the modulus of elasticity of the bucket material at the applicable temperature was utilized. Four series of readings were taken and averaged.

The stresses were plotted together with a presentation of the cross section area of the bucket at the critical location in the direction in which they act as shown in Fig. 7. Then the equilibrium between the external and the internal forces at this section was checked. The deviation between the applied and the calculated forces was 0.65 percent. However every case investigated showed some bending in addition to the axial force, as shown in Fig. 7. This bending was due both to the bucket shape with its screw type neutral axis and the tilt of the bucket away from the radial direction.

In operating engines these bending stresses will also be superimposed on the plain centrifugal stress for the same reasons although their magnitude will probably be different. The only essential difference between stresses on the bucket in this test and the actual operation of a bucket in an engine is the distribution of stresses over the length. In the test stand the constant axial load produces increasing stresses toward the bucket tip because of the decreasing cross sectional area whereas in the operating engine stresses increase toward the root because of the mass increase with increasing distance from the tip. The tilt of the bucket is

9

used in some designs to compensate for the gas forces though this compensation is exactly true only for one fixed speed of the wheel and for a certain temperature and will not hold for different conditions. It is therefore questionable whether such a design will be beneficial.

One purpose of this investigation was the comparison of fatigue stresses in critical fibres under combined loads with the results obtained in the conventional axial loading fatigue tests. The critical fibres in fatigue in this test are those on the leading edge. The static axial stress on these fibres is frequently close to zero so that only completely reversed dynamic stresses have to be considered. Therefore if the test results obtained from the test stand for the buckets and from reversed bending load fatigue test machines agree for the same maximum stress then the design stresses for various bucket designs can be determined theoretically by using reversed bending load fatigue test data.

The dynamic stresses due to vibrational bending were investigated separately as mentioned. In preparation for this measurement calibration of the instruments was necessary showing the relationship between dynamic stress on the beam and amplitude on the oscilloscope screen. Fig. 6 shows schematically the arrangement for the calibration in which a cantilever beam of uniform cross section over the length was used. Using
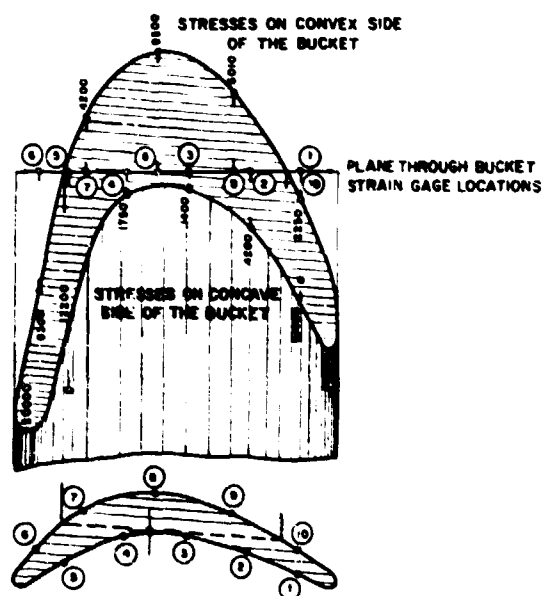

FIGURE 8. Distribution of dynamic stresses on the concave and convex sides of the cross section.

the standard static relationship the stress at the location of the strain gage was calculated from the deflection and plotted against the amplitude on the oscilloscope screen. Since both the inverter amplifier and the oscilloscope had linear characteristics a linear relationship between the two variables resulted.

For the dynamic measurements on the bucket a bridge circuit was used as previously described. Thus the stresses around the perimeter of the bucket at the critical cross section could be measured at room temperature. The result was plotted as shown in Fig. 8. It can be seen that the stress distribution does not represent plain bending because the compression and tension forces are not equivalent. The areas on each side of the plane through the centroid parallel to the main bending plane are different in size. The reason for this result is the arrangement of the vibrating system. When this system is moved perpendicular to the system axis at the point where the axial force is applied to the bucket this axial force increased with increasing lateral amplitudes. For high axial forces and rigidity in respect to length these forces may increase considerably. Consequently the measurements include the increase in axial force. Fig. 9 can not be interpreted as a simple superposition of Fig. 7 and Fig. 8, because the dynamic stress shown in Fig. 8 was increased proportionally to such an extent that the maximum combined stress would be equal to the stress at the endurance limit of the material. Fig. 9 therefore shows the maximum permissible stress at the edge of the bucket and the distribution of related stresses around the cross section.

In order to check the variation of axial force with lateral amplitude, measurements of the change of axial force were made by connecting the calibration system for dynamic stress measurements to the strain gages on the pull bar. Considerable non-linear increase of axial stress was obtained as the lateral amplitude was increased.

Measurements were conducted for one amplitude with all ten readings taken around the perimeter of the cross section. An additional investigation determined the relationship of the axial stress to amplitude. These basic calibration data were suitable for application to the theoretical evaluation of the actual stresses on the bucket.

For the evaluation of the dynamic measurements the diagram of the stress distribution had to be corrected because it increases the superimposed axial forces resulting from the

deflection of the system as previously mentioned. Then compensation of compression and tension forces on either side of the neutral axis in plain bending can be checked. The external vibrating force can be determined from the spring constant, the mass of the system and the frequency of the vibration, for unit deflection provided the damping w s small as it was maintained in the test by means of a special fastening arrangement at the root of the bucket. The distance from the fastening point of the cantilever beam is 3 inches. The comparison of the external and the internal moment at the cross section calculated from the stress distribution has not been completed as yet, but preliminary measurements indicate a deviation of about 1 or 2 percent.

It may be noted that the maximum stresses occur at the edges and on the convex side near the center of the cross section. The edges are under nearly complete reversals of stress while in the center of the bucket zero to maximum type dynamic stress is present.

Finally the static axial stress pattern was added to the vibrational distribution and Fig. 9 shows the result of the combined forces proportionally increased such that the stress reached the endurance limit at the leading edge. The general distribution indicates a major influence by bending. Consequently the more severe fatigue stresses prevail at the edges. Since the
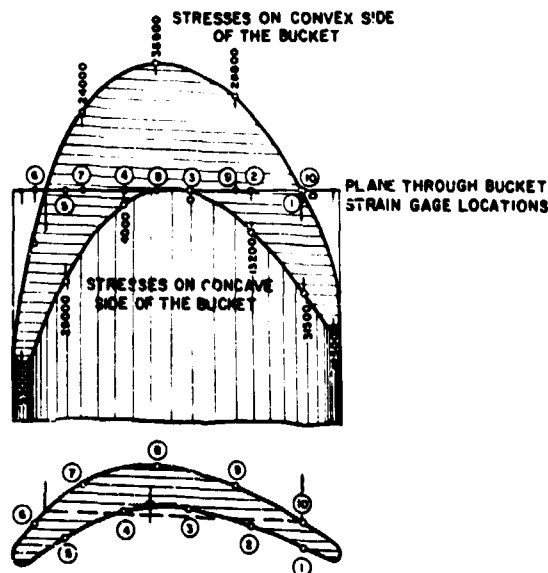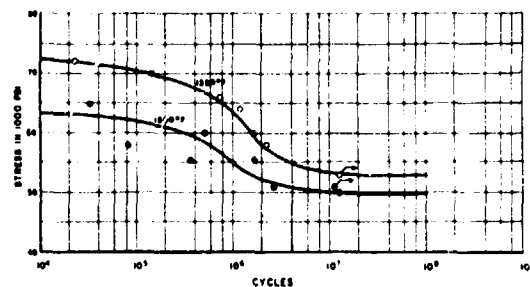

FIGURE 10 Fatigue strength of S-816 turbine buckets at 1350° F and 1500° F. Maximum stress at the leading edge.

leading edge shows the absolute maximum stress, failure is obtained at this location.

At elevated temperatures the stresses at the critical cross section were calculated from the deflection measurements at those temperatures. As deflection includes the influences of uneven temperature distribution over the length, changes in the modulus of elasticity at various locations is important. Consequently, these changes are included in the ratio of the deflection at elevated temperature to that at room temperature. This approach to the determination of the stress from the measured deflection under elevated temperatures is discussed in WADC Technical Report 5936 Part 2.

Fig. 10 shows the fatigue diagrams for buckets made of S-816. The fatigue limit for S-816 was 50,000 psi for 1500° F nominal temperature and 53,000 psi for 1350° F. This is close to or at the axial load fatigue limit for tests on the same material and for the same test temperature. Comparison with axial load fatigue data should also be valid for higher engine speeds. A comparison with Haynes Stellite 21 is presented in Fig. 11 which shows the superiority of the S-816 material. Presently check tests are being conducted to see how much change will be obtained when the temperature is raised to 1700° F for S-816 and to see how this material will behave for short time fatigue tests.

The failure locations and appearances obtained from this test apparatus agreed well with the locations and appearances observed in many service failures as shown in Figs. 12, 13 and 14. Although exact temperatures and stresses occurring in flight are not known, good agreement was obtained between calculated and experimentally determined stresses and frequencies for the test temperatures used.
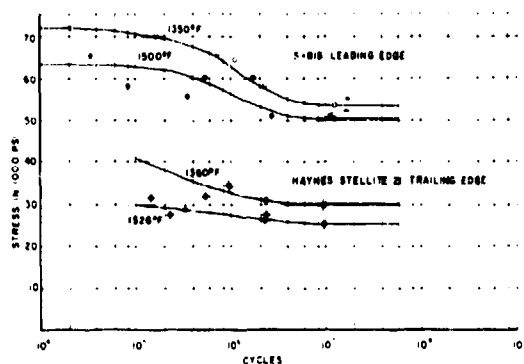
FIGURE 9. Distribution of combined stresses on the concave and convex sides of the cross section.

APPLICATION OF TEST RESULTS FOR BUCKET DESIGN

It may be helpful to consider the application of this stress analysis to bucket design. Under combined axial and bending loads the edges of buckets will always be the most highly stressed locations. It depends on the shape and on the location of the centroids in various cross sections in respect to the center of the root whether the leading or the trailing edge will have the maximum dynamic stress.

A fairly complete theoretical stress analysis covering the main forces acting on a bucket is possible when areas, moments of inertia at various stations over the length and centroids are known and when the load and the temperature distributions are established. The load and temperature data has to be based on flight conditions and presently an attack on this problem is being made.

From the tests it appears that the most highly stressed fibre in the critical cross section of a bucket under operational conditions fails at about the fatigue limit for conventional axial loading tests conducted with the same nominal temperature. Knowing this fact the designer is in a position to calculate the approximate stresses and to obtain an impression about the behavior of this engine part under anticipated loads. Starting with the centrifugal forces existing it will also be possible for the designer to calculate the maximum possible safe amplitude of vibration. Damping will be provided partly by the material at temperature due to internal friction and to a larger extent by the provision for friction in the root fastening. The amount of damping may
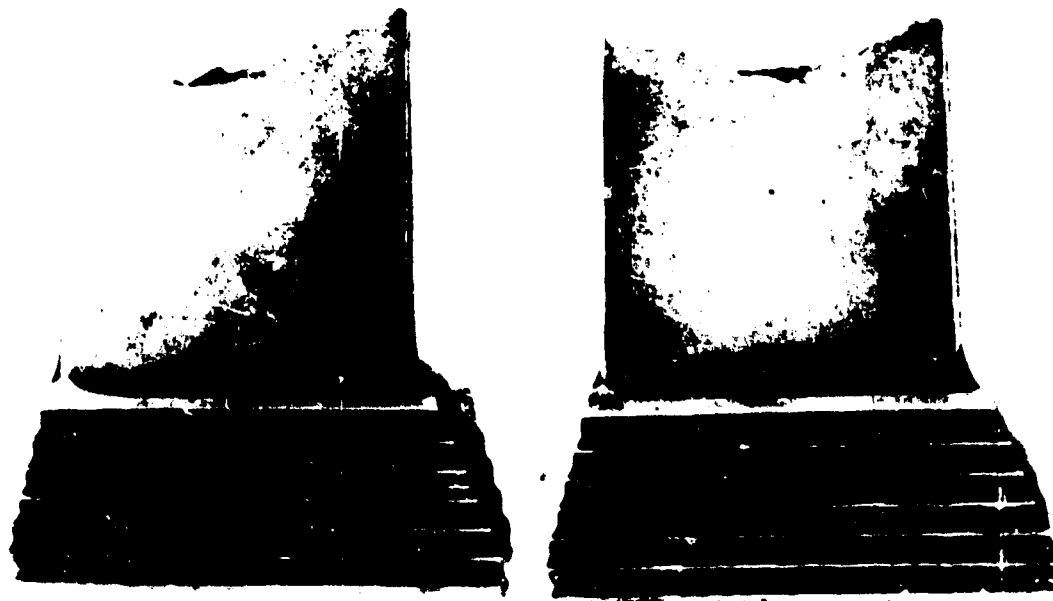
FIGURE 12. Service failures of buckets. The arrow indicates the area of the fatigue failure. Material: Haynes Stellite 21.
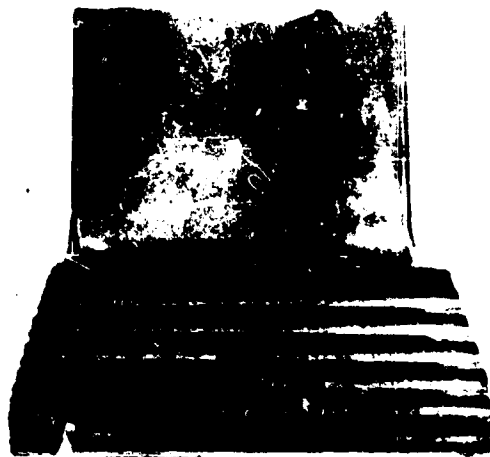
FIGURE 13. Failure of a test bucket. Material: Haynes Stellite 21.

also be considered in design for limiting the amplitude. However, increasing the damping by a loose bucket fit in a nonrotating wheel will not be sufficient because under centrifugal forces the buckets become tight again. To obtain the intended bucket service life it appears to be necessary to keep a tight fit in the lower serrations of the Christmas tree root in order to take the axial force and to allow some clearance for those serrations located close to the airfoil to provide damping.

It also seems to be essential to allow for some flexibility in the airfoil of the bucket and to avoid cross sections which are too large. If the airfoil is too stiff, the buckets will act as rigid levers at the wheel serrations and will originate failures in the rim of the wheel. The best design would be a balanced stress distribution such that every part of an assembly would take an even share of the load under all operating conditions.

CONCLUSIONS

It has been shown that by special arrangements it may be possible to investigate jet engine turbine buckets under simulated service conditions and to obtain measurements which permit a good concept of the general stress condition under which the part has to operate in service. The measurements could be checked by calculations based on equilibrium considerations between internal and external forces. The two forces have to be equal and of opposite direction. This information may also support new bucket design and eventually the design of compressor blades.

The method is applicable to the investigation of overheating problems of buckets encountered in flight and to the investigation of repeated

FIGURE 14. Test failure of a bucket. Material: Haynes Stellite 21.

thermal stresses and their influence in creating local residual stresses. It may also be used to investigate both the effects of damping on vibrations and the influences of changes in root design.

A further aspect in the improvement of the method is the investigation of the influence of higher harmonies on the stress distribution. However, this problem involves considerable difficulty in transferring the necessary energy from the driver unit to the small test specimen at the frequencies involved and with the amplitudes necessary to obtain short time failures. An attempt to test the second harmonic frequency may be made in the future.

Part 2. Fatigue Tests of Turbine Buckets under Static Axial and Super-imposed Vibrational Bending Loads

ABSTRACT   *The fatigue investigation of turbine blades in a special device, permitting the application of static axial and superimposed vibrational bending loads by means of an electromagnet, is discussed. The excitation of the vibration of the axially loaded bucket was adjusted to the fundamental frequency of this system.   The most important factors causing damping effects and energy losses during vibration are considered.   Special attention is given to the measuring methods for obtaining stress and deflection values of the vibrating bucket under dynamic load.   The tests were conducted at room and at elevated temperatures.   The results are discussed and compared with fatigue tests under similar conditions using simple specimens and standard testing devices.*

INTRODUCTION

In the investigation of turbine buckets, the behavior of the material under observation as affected by variables such as shape, load (static and dynamic), the resulting stress gradients, elevated temperatures, and damping due to fastenings is of great importance. Because of this variety of conditions, it was desirable to build a testing device suitable for investigating all or at least the most important of these factors. All such factors are present during operation of the buckets in service. Laboratory tests should approach service conditions as closely as possible.

Previous tests have been conducted under service conditions by operating the turbine wheels in the engine and by measuring speed, strains, and stresses at some locations, as well as temperatures. These tests have been very valuable as statistical material for the detection of dangerous frequencies, the kinds of vibration, the prevailing temperatures at critical spots in the turbine buckets, and similar observations. However, it was desirable that the investigation of bucket materials be sufficiently flexible to permit the adjustment of each variable for every desired value as well as the ratios one

to another and to continue the fatigue tests to failure. The failure point should be precisely determined, including the number of cycles required for failure. If the buckets are enclosed in the housing of an engine such observations are very difficult to make as the test has to be stopped at short intervals in order to detect the failures. Such a procedure is undesirable because of the discontinuity in stressing and heating the blade. In such a test, the ratios between axial and dynamic bending stresses also cannot be varied, and the dynamic stresses depend on the speed of the wheel, which determines the axial load, while vibration peaks occur only at some few speeds.

These reflections led to the development of a testing device for buckets which permits fairly well the application of all ratios under simulated service conditions, although the centrifugal force had to be replaced by a static axial load. Although this necessitated a much lower frequency due to the mass of the ... required for applying the axial load, it was possible to place the desired stress in the range of the probable failure. For the extrapolation of such tests to the higher frequency range in service, the frequency influence on the material is of importance. It is

believed that the frequency change up to several thousand cycles per second will not produce a considerable variation in regard to the fatigue strength, although some authors claim to have observed influences in this direction

Because of the input power limitation at present available for vibrating the bucket, only the fundamental frequency of the axial loaded bucket has been investigated. Most of the service failures occur at the second harmonic. This fact is not too important at present; for, if theoretical analysis corresponds well with test data obtained for the fundamental frequency, the investigation can be extended to the second harmonic frequency. In future test work, it is anticipated that a larger input power source will enable the tabulation of test results for the second harmonic also. Although the test method employed is satisfactory for use in the evaluation of any cantilever buckets, present test data are limited to buckets for the Allison J 35 engine.

TEST METHODS

The device used in conducting bucket vibration fatigue tests was previously described in AF Technical Report No. 5836, Part I. Generally, it corresponds to the setup for the tests reported herein. However, additional testing experience showed that several modifications were needed both in the testing device and in the testing procedure. Figure 1. As formerly described, the turbine wheel was suspended in a rigid frame. The jaws were clamped at a cross section close to the tip of the bucket and the axial force was applied through the loading ring and the weighing bar (Figure 2).

In this general arrangement, some very important precautions must be taken in order to get the maximum vibrational amplitude of the blade. When only a small vibration amplitude is obtained in such a test, the reason is always traceable to losses by damping. If these losses are avoided as nearly as possible, a larger amount of energy is then available for the excitation of the specimen. The accomplishment of this fundamental objective, however, may be obtained to a limited extent only. Some minimum losses will still remain. The two most important conditions for an optimum amplitude are the rigid mounting of the suspension fork and the tight clamping of the wheel in the fork. Another point is the clamping of the Christmas tree root of the bucket,

which should be as tight as possible in the wheel. This condition was obtained by inserting specially built root parts of blades in the slots neighboring the test bucket. The outside edges of these neighboring root parts close to the buckets tested were built up with a welded bead and machined to an angle of 30° to the radial centerline of the bucket across the width of the root. The edges above the root serration closest to the bucket were machined to an angle of 60° (Figure 3). Thus, the test bucket was forced radially outward and held tightly during test.

It was observed during preliminary tests that the deflection of the tip of the bucket decreased when loose fits were used at the root and most of the input energy was lost through friction. The connections at the threads in the loading ring and at the lower end of the weighing bar, which were tightened by the axial force, were much less critical.

Special care was given to the assembly of the loading device, as the seating for the knife edge suspension may be the origin of disturbances. These seatings were built as grooves in machined cylinders having a wide angle of 120° as shown in Figure 47 of Part I of this report. The seatings were inserted in the main jaw holder in corresponding holes and had a loose fit. Undoubtedly this method will also give losses when the buckets are vibrated perpendicular to the axis. However, for the present tests the amplitude was sufficient. Care was necessary in aligning the seatings with the axis of the device as they sometimes turned in the round holes, preventing the desired movement due to the transverse vibration forces.

For easy mounting of the jaws and their holder, it was advantageous to drill two holes close to the bucket tip and insert a dowel in each. These dowels supported the jaws until they could grip the tapered bucket. The axial tensile force then caused the jaws, having outside wedge-like faces, to grip the bucket very tightly. The jaws had been equipped for good gripping action with small, inserted, rectangular pieces taken from a file and ground at the inserted surfaces. The gripping pieces had to fit the curvature very accurately in order to distribute the axial forces evenly across the width of the bucket.

As formerly explained, the vibrating force was introduced at the suspension ring, using an electromagnet. The electrical data of this magnet may be determined for a given steady frequency with a maximum efficiency. However, operating it .:
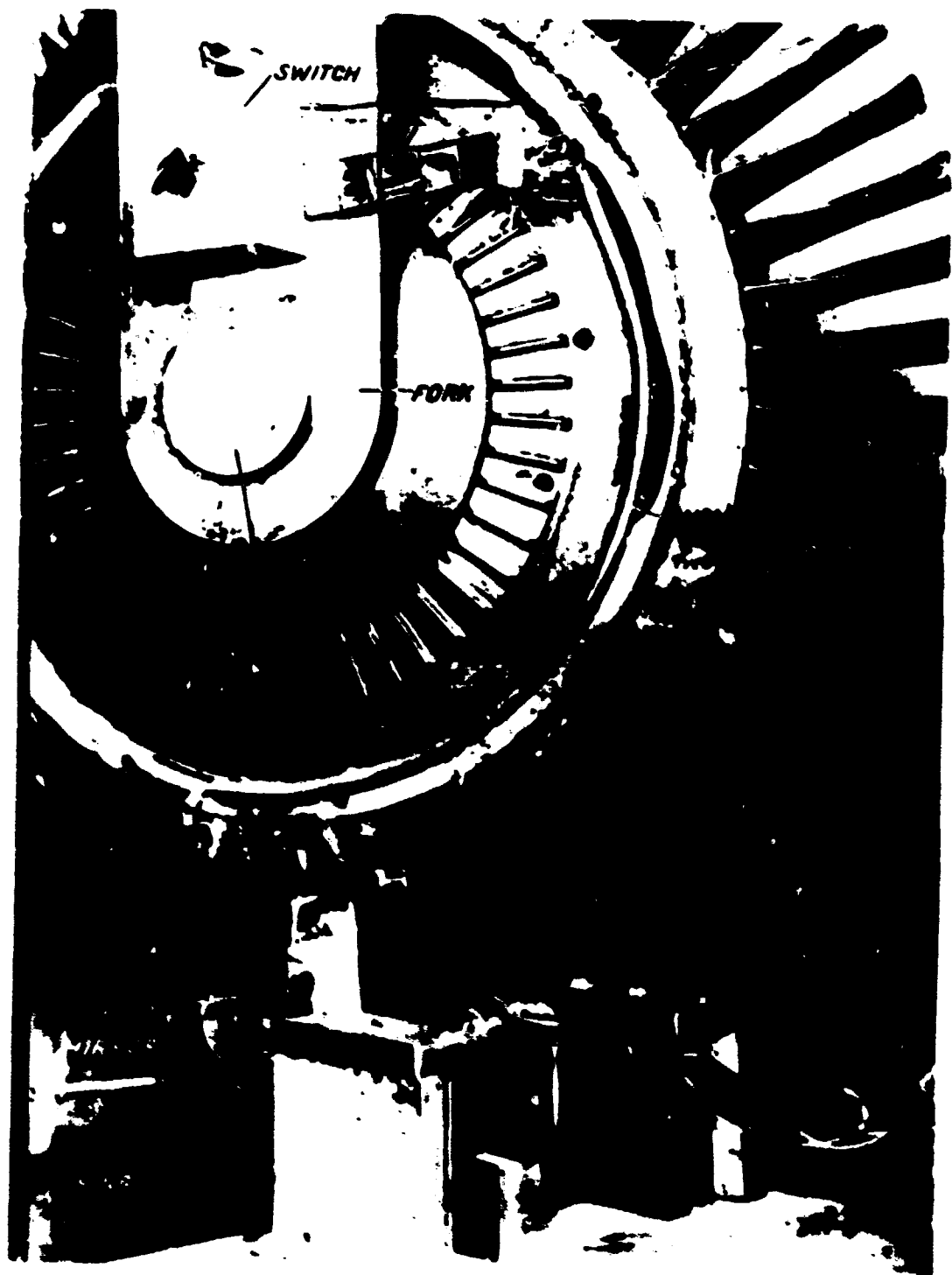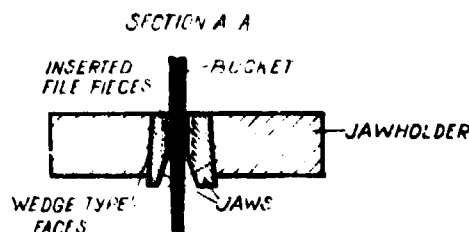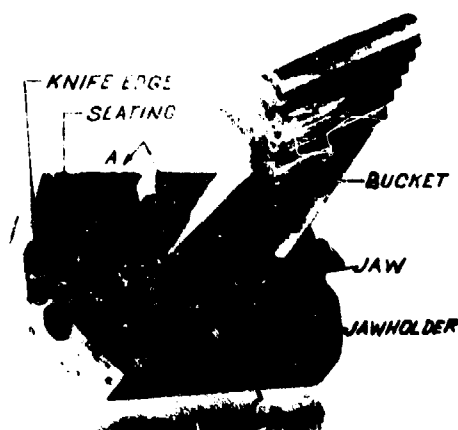
SWITCH

FORK

FIGURE 2. Bucket gripping.

different frequencies far separated from each other, (for example, at fundamental and second harmonic), caused the output power to be low for the frequency for which it was not designed. The reason for this behavior was that the output transformer of the amplifier could not be matched with the magnet. However, it was possible to adjust it to the fundamental frequency at around 150 cps. In this case, an optimum of output energy could be obtained. During testing, an oscilloscope was connected to the leads of the exciting magnet, which indicated the proper function of the device. The wave on the screen showed the slipping of the
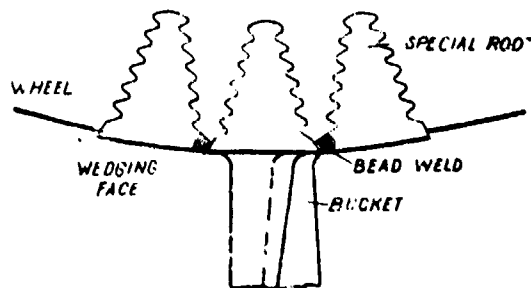
FIGURE 3. Bucket fastening in the wheel.

knife edges in their seatings at the points of reversed motion as deviation from the proper curves at the peaks and valleys. They may be avoided in future tests by using crossed flexure plates in addition to the knife edges for maintaining an exact moving center without any shift.

For tests at higher frequencies, it will be desirable to decrease the weight or mass of the parts needed for applying the axial load. Particularly, the loading ring may be lightened by holes, which will probably give a larger deflection of the bucket tip under vibrating load.

AXIAL LOAD MEASUREMENTS

For setting the desired ratio between the static axial and the dynamic stress, it was necessary to measure both. The weighing bar acted as a dynamometer for axial load. Strain gages of the wire resistance type were glued to this specimen and connected so as to compensate for bending. The readings were taken with a strain gage indicator which indicated a load drop at the start of a fatigue failure. No automatic, load-maintaining device for axial loads has been available for such small elongations. During the tests, the load could be kept constant without difficulty, as the fatigue test shows microscopic elongation only in the last stage when specimens are very close to failure. The load was reset from time to time by hand, as required, by noting any load drop shown on the strain gage instrument; however, this did not affect the test results, as the test time was measured to the beginning of the specimen failure.

At elevated temperatures this procedure is not entirely satisfactory as it requires a very close observation of the instrument during tests. This was experienced especially in the beginning of a test due to the expansion by heating slowly all parts of the device. An extended preheating period was needed to heat all parts near the test bucket to stable temperatures. The elongation of these parts then caused a decrease in the static axial load. The load was reset by hand during elevated temperature tests as described for the room temperature tests, but in this case the resetting period was included in the test time. In future tests a loading gear motor may be used for automatic control. It will be connected to an elongation indicating and controlling device not yet designed and developed because of the extremely small elongation values which need special consideration to give satisfactory results.

DYNAMIC STRESS MEASUREMENTS

The second very important measurement was the determination of the bucket strains and stresses under the dynamic deflection. There are different possibilities for obtaining these data as previously mentioned in Part I of this report. For the final test a deflection measuring method was chosen which had to be calibrated in stresses. The deflection measurement was conducted by the method described in the previous report with strobotac, scale, telescope and mirror, the latter being the only part necessary on the bucket. It could be kept sufficiently small in size and mass so that it did not disturb any frequencies of the vibrating parts.

In a special calibration test described in detail later in this report the relation between mirror amplitude and strain at different points of the bucket had to be investigated. For the measurements of the strains, wire strain gages were applied to the bucket at one cross section. The difficulty of this method is the measurement of the amplification of the strain values and the recording of the vibration strain curve at 130 cps and eventually at higher frequencies due to the presence of superimposed stray frequencies caused by the operation of the testing device.

VIBRATION EXCITATION

In general, the procedure for generation of the vibrations was described in the former report. A very critical point is the setting of the magnetic gap between the electromagnet and the bucket, as the efficiency decreases with the square of the distance. Unfortunately, the movement of the bucket is not plain bending, due to the screw type neutral axis. Plain bending would give a parallel displacement. In the case of the bucket, a torsional motion is superimposed over the bending, changing the gap in an inefficient way. Additionally, the constant field of the magnet system imposed a constant tensile force on the armature. Consequently, the gap t . to be kept approximately ¼ inch wide to avoid contact which resulted in sticking because the vibrating system, even though axially loaded, was relatively weak in the perpendicular direction.

The magnet system was excited by an a frequency oscillator whose output was fed into an amplifier of 1,400 watts output. The output wave at the terminals of the magnet was a sine wave up to very high frequencies. The distortion, if

present at all, was not visible on the screen of the oscilloscope.

The amplifier kept the vibration amplitude constant as long as no change in the spring constant of the vibrating system occurred. A small failure, even when not visible at the bucket or at the threaded ends of the weighing bar, displaced the natural frequency and thus decreased the amplitude. From this time on, an almost continuous control of the frequency by hand was necessary. For the final rupture, an increase in the introduced energy was required to maintain the original amplitude. Fatigue failure in the threaded ends of the weighing bar occurred only twice throughout the many tests completed.

STRESS PROBLEMS

The predominant aim of conducting tests on buckets by applying axial loads and superimposed bending forces is to indicate the limit to which the material may be loaded as a bucket. Unfortunately, it cannot be assumed that the distribution of stresses in such a complex part as a bucket is uniform over the cross section area. The bucket has a tapered, shell type shape with a screw type neutral axis; and, the theoretical determination of the stress distribution over the width in any cross section is doubtful without an exact knowledge of the location of the axial static and the dynamic bending loads introduced. The latter is an undetermined load, as the vibrating system consists of the bucket, the ring, and the jaws for the application of the axial forces and the weighing bar. It is not known precisely which part of the weight or mass of these parts is acting on the bucket and which is acting on the weighing bar.

Because of its screw type shape under the axial and bending forces, the bucket reacts not only in the related directions, but also in a torsional moment around the longitudinal axis. For this reason, it was decided to experimentally measure the desired static and dynamic stresses on the bucket in order to obtain a true picture of the stresses imposed. A knowledge of the true stress distribution permits a more accurate means for the determination of the stresses at the fatigue limit.

TEST DEVELOPMENT

The measurement of the strains on parts as small as buckets included some difficulties because

19

of the lack of accurate measuring devices. However, it could be accomplished at room temperature. For use at elevated temperatures, only a few strain gages are available, none of which are really accurate.

For the dynamic tes.s, wire strain gages were used because of the convenient recording possibilities. The g..ge has a length of ⅛ inch and a width of ¼ inch with a resistance of 120 ohms, from which sufficient accuracy could be expected. In applying the gage at a section having very large strain gradients, gage size is important.

The investigation started basically from measurements using the wire strain gage in static bending with a definite external loading moment. By measuring the strain at the center of each strain gage and plotting the related stresses at their proper locations on the cross section of the bucket and then by calculating the internal moment, an excellent comparison for accuracy is possible between the external and the internal moment which are necessarily equal.

Proceeding from this basic comparison, the buckets could be loaded in axial tension and the stresses determined. The mean stress (overall average) could be computed and multiplied by the cross sectional area at the location of the wire strain gages to obtain the load which had to be equal to the introduced external axial load. The external axial load was measured as strain on the weighing bar.

An essential part of the procedure described is a knowledge of the moduli of elasticity for both tension and compression of the material investigated, Haynes Stellite 21 (Vitallium). The axial and the bending stresses can then be calculated from the strains. As no data for the compression modulus were available in the literature, tests at room temperature were conducted.

After the completion of the static tests, a method was developed for measuring the dynamic strains at frequencies up to 150 cps. The dynamic measurements were made to evaluate the stresses actually induced in a vibrating bucket The dynamic strains had to be recorded at the same instant as the bucket deflection measurements in order to correlate the deflections and the strains.

The calibration of the test set u,   accomplished with a steel cantilever beam of uniform cross section area on which the dynamic strains were measured simultaneously by the wire strain gage and by an optical method. The stress at the

location of the strain gage could be calculated using the latter method.

Using the same set up for the vibrating bucket under axial load, the bending stresses could be recorded by starting the test after the application of the axial load. The measured stresses were plotted at the corresponding locations superimposing axial and bending stresses. The result was used for determination of the stress at the fatigue limit of the specimen, correlating the deflection to the stress, since during fatigue tests only deflections were measured.

MODULI MEASUREMENTS

Since no compression data for modulus of elasticity of Haynes Stellite 21 (Vitallium) were available and since for the evaluation of the strain measurements the moduli for compression and tension were necessary this value was measured at room temperature. The moduli of elasticity are not necessarily equal for tension and compression for all materials and some precaution seemed to be desirable for cast materials. the properties of which are not thoroughly known.
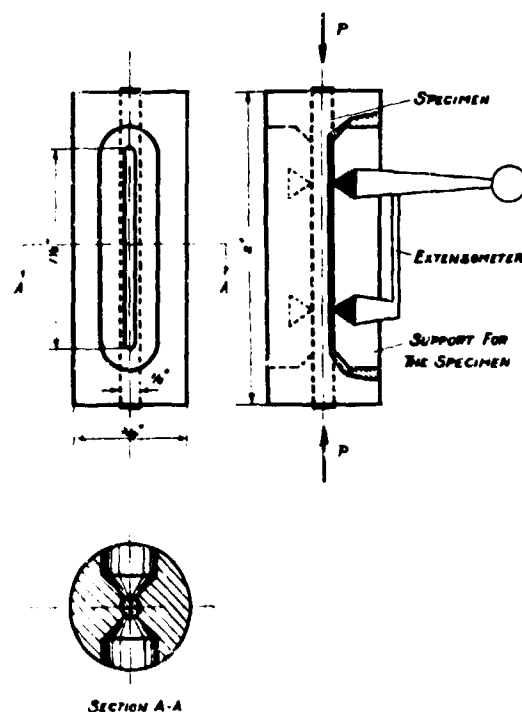

FIGURE 4. Device for the measurement of the elasticity modulus in compression.

Some cylindrical specimens with uniform cross section were machined from the center part of a bucket, starting at the root section. The specimens had a diameter of 0.125 inches and a length of 2 inches. The axial orientation of the specimen was parallel to the axis of the bucket

These specimens were inserted in a brass cylinder (Figure 4) which had two openings in the cylinder wall opposite each other to allow the fastening of two extensometers on the specimen. The brass cylinder enclosed the specimen very closely to avoid buckling under axial compression load.

Tests were conducted in the standard manner for determination of the moduli of elasticity and the readings, the evaluation and the results including the overall average value are given in Table I. The diagram presenting these results is shown in Figure 5. The measurements follow a straight line showing linearity for the modulus of elasticity for compression up to 25,000 psi. The value obtained was E Compression 36.4 × 10⁶

psi, which is approximately the same as the modulus for tension.

Load, lbs	Stress, psi	Gage reading		E Modulus psi × 10⁻⁶
		Average units	in in × 10⁻⁶	
0	0	0	0	0
50	4,090	2.85	117	34.2
100	8,180	5.48	225	36.5
150	12,270	8.28	340	36.0
200	16,360	10.85	445	37.4
250	20,450	13.35	545	37.4
300	24,540	16.23	663	36.8

Modulus of Elasticity in compression, average 36.4 × 10⁶ psi.

BUCKET CROSS SECTIONAL AREA MEASUREMENTS

Usually under axial load and superimposed vibrating bending, the failure occurred at 2.37 inches from the bucket tip. The cross section at this point was used for the measurement of the stresses, for, they are probably highest at this position according to the calculations in Part I of this report. The stress distribution which was calculated is substantiated by the location of both laboratory and service fatigue failures of buckets. The cross section area of a bucket was determined by making a paraffine mold of the blade and slicing the desired cross section (2.37 inches from the tip). Then, the ordinates at various stations along the cross section area were measured by means of a shop microscope. A straight line connecting the trailing and leading edges was selected as the x-axis with the y-axis perpendicular and touching the outside of the area measured, as shown in Figure 3.

After plotting the measured values to a 5:1 scale, the enclosed area was measured with a planimeter. The measurements are given in Table II, from which the area of 0.37 sq. inches was determined.

ACCURACY OF BENDING STRESS MEASUREMENTS

A bucket was inserted with its Christmas tree root into a block cut from a turbine wheel. The block was fastened to a heavy cast iron stand and a pair of jaws fitting the bucket shape were tightened around the blade in the vicinity of the

σ IN PSI
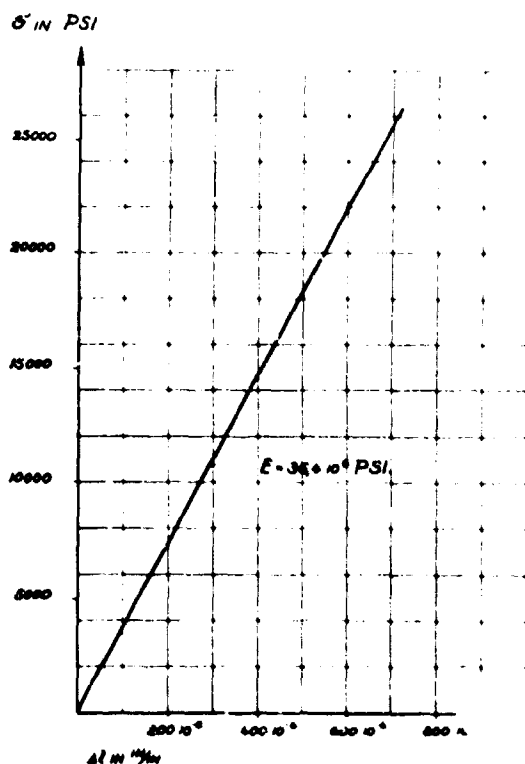
E = 36.4 × 10⁶ PSI

Δl IN in/in

FIGURE 5. Stress-strain curve for compression for the determination of the compression modulus of elasticity of Vitallium (Haynes Stellite 21).

Area = 0.77 in².
Scale 5 : 1.
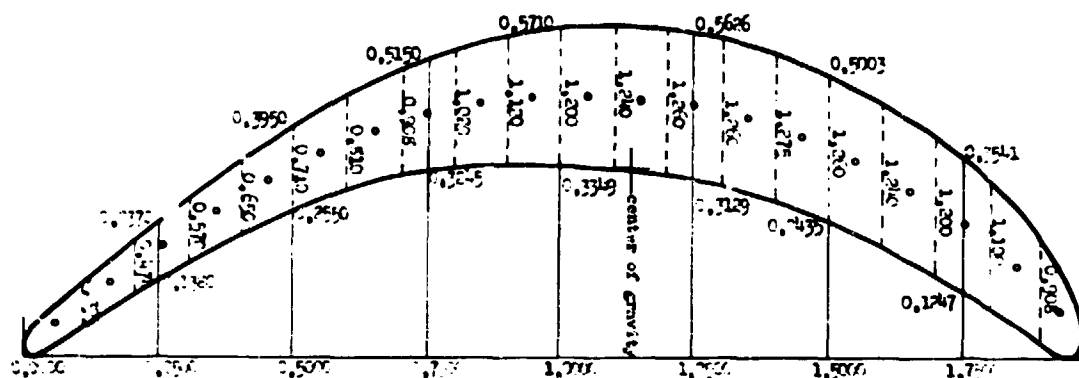
FIGURE 6.   Determination of the area at the measured cross section of the bucket.
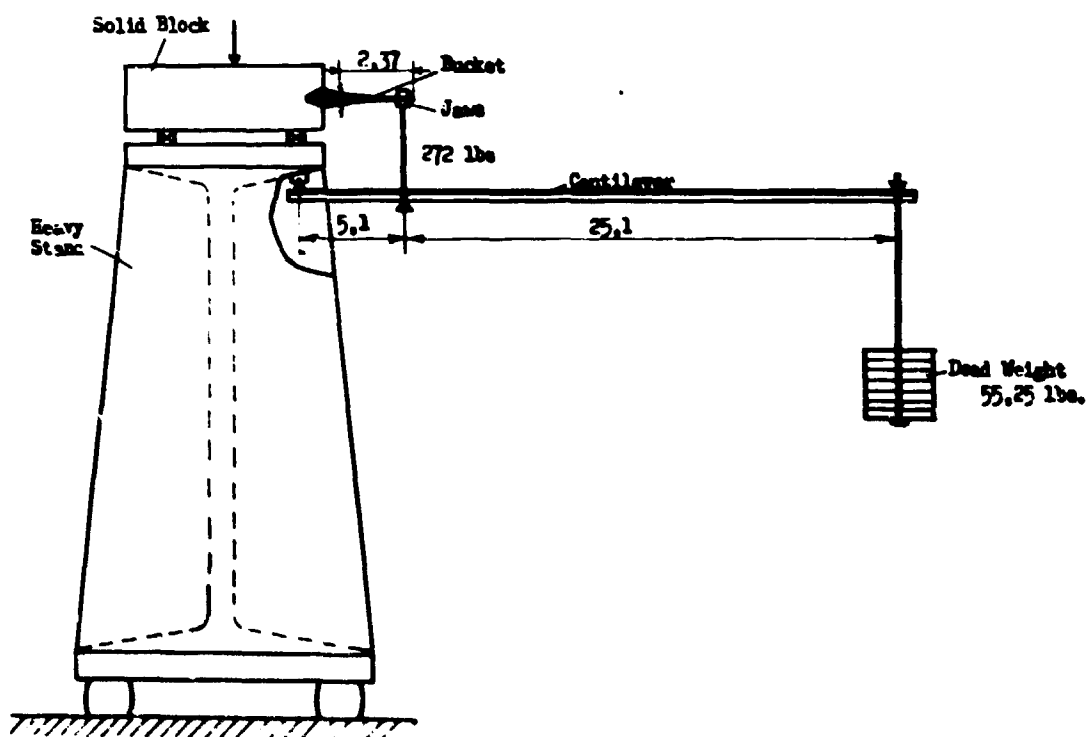
FIGURE 7.   Schematic presentation of the test arrangement for static bending tests with buckets.

Bucket chord	Thickness				
	Gage	Reading	Corrected to zero base line		
x	y_1	y_2	y_1	y_2	y
0.0000	1.2000	......	0.0000	.....	0.0000
0.2500	1.3380	1.4370	0.1380	0.2370	0.0990
0.5000	1.1550	1.5950	0.2550	0.3950	0.1400
0.7500	1.5245	1.7150	0.3245	0.5150	0.1905
1.0000	1.5349	1.7710	0.3349	0.5710	0.2361
1.2500	1.5129	1.7626	0.3129	0.5626	0.2499
1.5000	1.4435	1.7003	0.2435	0.5003	0.2568
1.7500	1.3247	1.5541	0.1247	0.3541	0.2294
1.9863	1.2000	.....	0.0000	.....	0.0000

All values in inches

$$y = y_2 - y_1$$

Cross section area = 0.37 in.²
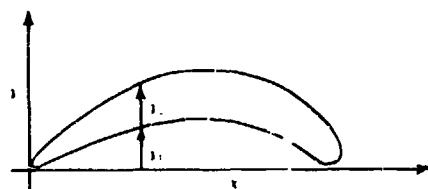
tip permitting the application of a bending moment. The latter was obtained by a lever system parallel to the bucket suspended at the tip and suspended at the short end underneath the fastening block (Figure 7). The outside end of the lever beam was loaded by dead weights thus applying to the bucket an external moment determined by the lever ratio and the weight. The internal moment was measured with wire strain gages on the concave and the convex side of the blade.

The test readings are given in Table III. The strains read between the unloaded and the loaded condition were converted into stresses using the elasticity modulus of $E = 36.4 \times 10^5$ psi for the material. Figure 8 shows in a 5:1 scale the measured cross sectional area of the bucket for which the strain measurements were taken. The above mentioned stresses were plotted at the corresponding surface locations around the section. The stresses, though acting in a direction perpendicular to the cross section plane, were plotted in that plane, perpendicular to a line connecting the two edges, and with the edge of the cross sectional area as the zero point.

To obtain the internal moment the cross sectional area was divided into a number of smaller areas each one 0.1 inch wide. Each small area and its center of gravity was determined. Each

Table III. *Static units and stresses for a turbine bucket in static bending using Baldwin Southwark SR-4 gages (A-8) 580 in-lbs bending moment*

Locations No.	Specimen bucket			Differences at cycle end $\times 10^{-6}$	Total difference $\times 10^{-6}$	Stress, psi
	Loaded $\times 10^{-6}$	Unloaded $\times 10^{-6}$	Loaded $\times 10^{-6}$			
1	372	1,298	420	+48	−878	−32,000
2	1,330	1,468	1,330	0	−138	− 5,000
3	732	981	736	+ 4	−245	(− 8,900)
4	466	700	472	+ 6	−288	− 8,300
5	1,058	1,587	1,076	+18	−511	−18,600
6	996	1,258	1,002	+ 6	−256	− 9,350
7	958	703	953	0	+255	+ 9,300
8	1,052	468	1,062	+10	+594	+21,500
9	932	588	944	+12	+256	+ 9,350
10	1,168	1,670	1,181	+13	−489	−17,800

Modulus of Elasticity for Vitallium = 36.4×10^9 psi

Gage locations.

23
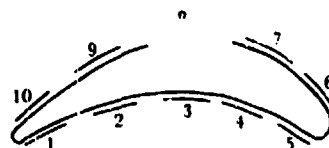
increment area times the average stress acting on that area gives the total force acting on each area. The forces acting on one side of a line approximately parallel to the line connecting the edges of the bucket represent tensile stresses, while those on the opposite of this line represent compressive stresses. The resultant of all of these calculated forces is a force acting at the center of gravity of the cross section of the bucket. By using a graphical method of plotting the force acting on each area and drawing the funicular diagram related to the locations of the centers of gravity of the small areas the position of the resultant force could be obtained. By exercising the same procedure in the perpendicular direction the intersection of the two resultant forces indicated the accurate center of gravity for all forces covering the whole cross sectional area. This method, which is well known from basic mechanics, although not very often used, permitted a very accurate determination of the needed rotation centers and of the forces representing the internal moment. The graphical evaluation of the measurements as described above is shown in Figure 8. The external moment was calculated by considering the lever distances and the dead weight on the end of the lever arm. The weight was 55.25 lbs. and as shown in Figure 6:

$$M = 0 = -5.1 L + 55.25 \times 25.1$$

The load introduced into the bucket is then.

$$L = 272 \text{ lbs.}$$

The moment at the considered cross sectional area, located 2.12 inches from the point of the load introduction was:

$$M_z = 2.12 \times 272 = 580 \text{ in. lbs.}$$

With the moment known, the stress in the outermost fibres of the bucket cross sectional area could be calculated. If the measurements are accurate the calculated values will be located at the stress curve obtained from the measurements. The stress curve intersects the convex bucket edge at two points and the connecting line of these points represents the neutral plane going through the center of gravity of the area. The distances at the three outermost fibres from the neutral plane are:

$$C_u^l = 0.340 \text{ inches}$$

$$C_u^r = 0.340 \text{ inches}$$

$$C_o = 0.252 \text{ inches}$$

If the moment of inertia is determined the corre-

sponding moments of resistance become:

$$W_u^l = \frac{I}{C} = \frac{0.51 \times 10^{-2}}{0.340} = 1.50 \times 10^{-2} \text{ in}^3$$

$$W_u^r = \frac{0.51 \times 10^{-2}}{0.340} = 1.50 \times 10^{-2} \text{ in}^3$$

$$W_0 = \frac{0.51 \times 10^{-2}}{0.252} = 2.02 \times 10^{-2} \text{ in}^3$$

The moment of inertia was obtained for the unsymmetrical area of the bucket as 0.51×10^{2} in^4 by the graphical method of Mohr. The resulting stresses are:

$$\sigma_u^l = \frac{M}{W} = \frac{580}{1.50 \times 10^{-2}} = 38,500 \text{ psi}$$

$$\sigma_u^r = \frac{580}{1.50 \times 10^{-2}} = 38,500 \text{ psi}$$

$$\sigma_o = \frac{580}{1.50 \times 10^{-2}} = 28,500 \text{ psi}$$

The curve in Figure 7 shows that the measured stress in the center of the convex side deviates considerably from the given calculated stress $\delta_o = 28,500$ psi. This fact is probably due to the size of the wire strain gages which are too wide for the large stress gradients present at the center locations. The evaluation of the stress distribution was conducted as outlined above and the centers of gravity were determined for each part—tension and compression side—separately. Table IV shows the average stress for each small area and its represented force. The centers where those forces act are obtained graphically. In Figure 8 the distance of those centers for the tensile as well as for the compressive forces from each other is

0.314 inches

This distance being determined the internal moment becomes

$$M = 0.314 \frac{1,889 + 1,813}{2} = 0.314 \times 1,851 = 581 \text{ lbs.}$$

compared to the external moment of 580 in. lbs. The deviation is

$$\pm \frac{1}{580} \cdot 100 = +0.17\%$$

Considering the partial moments for each side it is obvious that they differ. To a certain extent biaxial stress conditions, especially in the center of the area far away from the free edges are responsible for this error. This possibility is indicated by the values of the tensile and compressive moments (1,889 and 1,813 in. lbs.) which should be equal.

TABLE IV. *Calculation of the internal forces for the graphical determination of the centers of gravity of a bucket under a bending load*

Small area No.	Thickness		Width w inches	Size [1] of the small areas, in²	Average [2] stress in the small area, psi	Force on small area, lbs
	δ₁ inches	δ₂ inches				
(1) Concave side of the bucket (compression)						
1	0.197	0.375	....	0.00752	29,800	171
2	0.375	0.472	....	0.00847	25,100	213
3	0.472	0.550	....	0.01022	20,000	205
4	0.550	0.656	....	0.01200	13,700	164
5	0.650	0.395	....	0.01045	8,500	89
6	0.395	0.216	....	0.00611	6,300	39
7	0.216	0.098	......	0.00314	2,500	8
8				....	....	....
9				....	....	....
10			0.5000	....	....	....
11				....	....	....
12				....	....	....
13	0.078	0.178		0.00256	900	2
14	0.178	0.315		0.00493	1,800	9
15	0.315	0.492		0.00807	3,000	24
16	0.492	0.710		0.01202	4,200	51
17	0.710	0.945		0.01655	6,100	101
18	0.945	1.100		0.02045	8,400	171
19	1.100	0.905		0.02005	15,600	312
20	0.905	0.275		0.01180	28,000	330
						ΣF – 1,889
(2) Convex side of the bucket (tension)						
1	0.000	0.315		0.00315	2,300	7
2	0.315	0.570		0.00885	1,100	36
3	0.570	0.810		0.01380	7,300	100
4	0.810	0.985		0.01795	8,700	156
5	0.985	1.120		0.02105	9,600	206
6	1.120	1.180		0.02300	10,600	240
7	1.180	1.180	0.5000	0.02360	10,900	256
8	1.180	1.160		0.02340	10,500	245
9	1.160	1.080		0.02310	9,400	220
10	1.080	0.945		0.02025	8,000	162
11	0.945	0.745		0.01690	6,300	106
12	0.745	0.530		0.01275	4,700	60
13	0.530	0.235		0.00765	2,500	19
						ΣF – 1,813

[1] Small area $w\frac{1}{5} \cdot \frac{\delta_1 + \delta_2}{2} \cdot \frac{1}{5}$ considering the scale 5:1 in each direction.

[2] Graphically determined stress acting in the center of gravity in each small area.

The fit of the root near the center was better than toward the outside edges. Practically it will not be possible to avoid such conditions for the tool used in machining the serrations always has a tendency to produce a greater tolerance on the edges than in the center. A stress co

investigation for the bucket under a static load showed a slight concentration of the principal stress lines toward the center of the bucket root which also indicates that biaxial stress conditions are responsible to some extent for the deviation encountered.
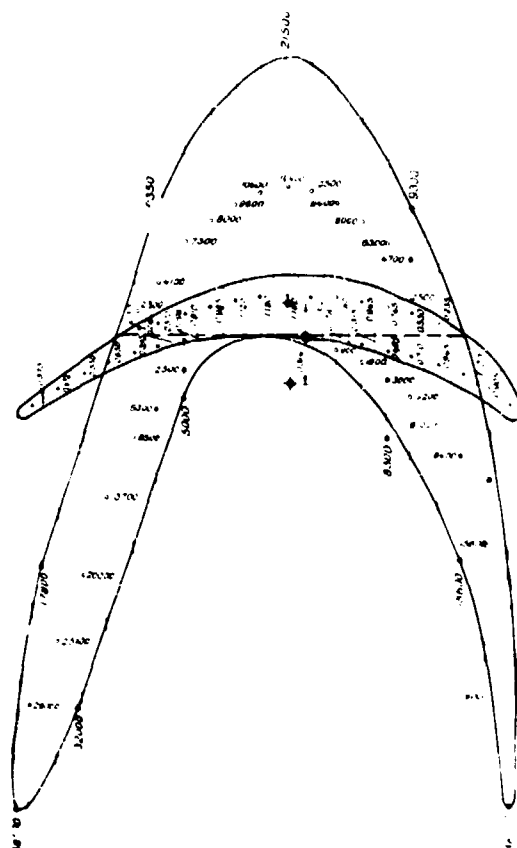
AXIAL STRESS MEASUREMENTS

The same bucket used for flexure calibration, with the wire strain gages in place, was also used for measuring the stress distribution under the axial static load. It was placed in the bucket testing device and axially loaded through the weighing bar, the strain of which was measured by means of wire strain gages and an SR 4 strain indicator. The latter measurements showed the external load of the bucket specimen. This could be compared to the internal reaction by the same procedure as was used for the bending test. The measured strains coordinated to the locations around the cross section area are shown Table V. The corresponding stresses were by using the modulus of elasticity for vitak a of E 36.4 · 10⁶ psi. These stresses are plotted in Figure 9 which is an isometric view of the cross

section area and with stresses shown above the area. The evaluation in Table VI gave only a very small deviation of the center of gravity for the tensile resultant from the actual center of gravity for the area (0.024 inches). The force obtained was 2,453 lbs. and the average stress with an area of 0.37 in² is:

$$\frac{2,453}{0.37} = 6,700 \text{ psi}$$

As shown in Table V the weighing bar carried a tensile load of 2,600 lbs. This gives an accuracy of:

$$\frac{147}{2,600} \cdot 100 = -5.6\%$$

This accuracy is satisfactory considering the difficulty of such measurements.

BENDING STRESS MEASUREMENTS

The measurements of the vibrating bending stresses on the small buckets up to 200 cps represented a special problem as no measuring device was available for recording rapidly changing strains up to a strain changing velocity of 200 cps. Measurements were made with wire strain gages at the same locations as for the axial static tests. The SR 4 strain indicator was used as the source of the carrier frequency in the bridge circuit and as an amplifier for the signal. For recording the results an oscillograph was connected to the output amplifier of the indicator. The assembly was calibrated with a vibrating cantilever beam of uniform cross sectional area on which wire strain gages close to the fastening point indicated the strain. On the free end of the cantilever beam a mirror was attached for the measurement of the end deflections. The system was excited to resonance by means of a Hewlett-Packard audiofrequency oscillator connected to an amplifier and a magnet system placed underneath the beam close to the free end. The mirror at the free end of the vibrating beam was lighted with a strobotac operated at approximately the same frequency as the vibrating beam. Thus a transparent scale placed in front of the strobotac could be viewed and read with a telescope containing a cross mark. The distance between the mirror and the scale considering the double angle shown by the mirror represented the magnification. The accuracy of this comparison method was very good. A schematic drawing of the test

The strain in the dynamometer specimen was 290×10^{-6} in/in.
The cross section area of the weighing bar was 0.305 in².
Then the load is: $290 \times 10^{-6} \times 29.4 \times 10^6 \times 0.305 = 2,600$ lbs.
The cross section area of the bucket at the measured station is 0.37 in² (2.37 inches from the tip).
The average stress at this location is then:

$$\frac{2,600}{0.37} = 7,000 \text{ psi}$$

Location No.	Strain in in/in $\times 10^6$				Strain average $\times 10^{-6}$ in/in	Stress, psi
	Run 1	Run 2	Run 3	Run 4		
1	+70	+45	+150	+90	+91	+3,300
2	+110	+105	+110	+130	+113	+4,100
3	+105	+160	+155	+170	+160	+5,800
4	+135	+115	+100	+110	+115	+4,200
5	0	+20	−50	−40	−27	(−900)*
6						
7	+195	+200	+190	+200	+196	+7,100
8	+330	+340	+340	+310	+330	+12,000
9	+365	+360	+340	+320	+348	+12,600
10	+190	+170	+165	+170	+174	+6,300

The modulus of elasticity of the bucket was $36.4 \cdot 10^6$ psi.
*Not included in Figure 14.

TABLE VI.—*Calculation of the internal forces under an axial load*

Small area No.	Thickness		Width w inches	Volume [1] of the small areas in²	Average stress [2] in the small area psi	Force on small area, lbs
	δ_1 inches	δ_2 inches				
1	0.197	0.395		0.00752	2,575	19.4
2	0.395	0.474		0.00869	4,800	41.6
3	0.474	0.570		0.01044	6,150	64.4
4	0.570	0.650		0.01220	7,100	86
5	0.650	0.710		0.01360	7,900	108
6	0.710	0.810		0.01520	8,600	130
7	0.810	0.908		0.01718	8,650	148
8	0.908	1.020		0.01928	8,700	168
9	1.020	1.120		0.02140	8,600	184
10	1.120	1.300	0.500	0.02320	8,250	192
11	1.200	1.240		0.02440	7,730	189
12	1.240	1.260		0.02500	7,200	180
13	1.260	1.260		0.02520	6,800	172
14	1.260	1.275		0.02535	6,400	162
15	1.275	1.260		0.02535	6,050	153
16	1.230	1.240		0.02500	5,600	140
17	1.240	1.200		0.02440	5,150	126
18	1.200	1.100		0.02300	4,450	107
19	1.100	0.908		0.02008	3,000	60
20	0.908	0.275		0.01183	2,000	24

$$\Sigma F = 2,453.4$$

[1] Small area $w \cdot \frac{\delta_1 + \delta_2}{2} \cdot \frac{1}{5}$ considering the scale 5:1 in direction.

[2] Graphically determined stress acting in the center of gravity in each small area.

The external force was 2,600 lbs. consequently the error is

$$\frac{146.6}{2,600} \cdot 100 = -5.6\%.$$
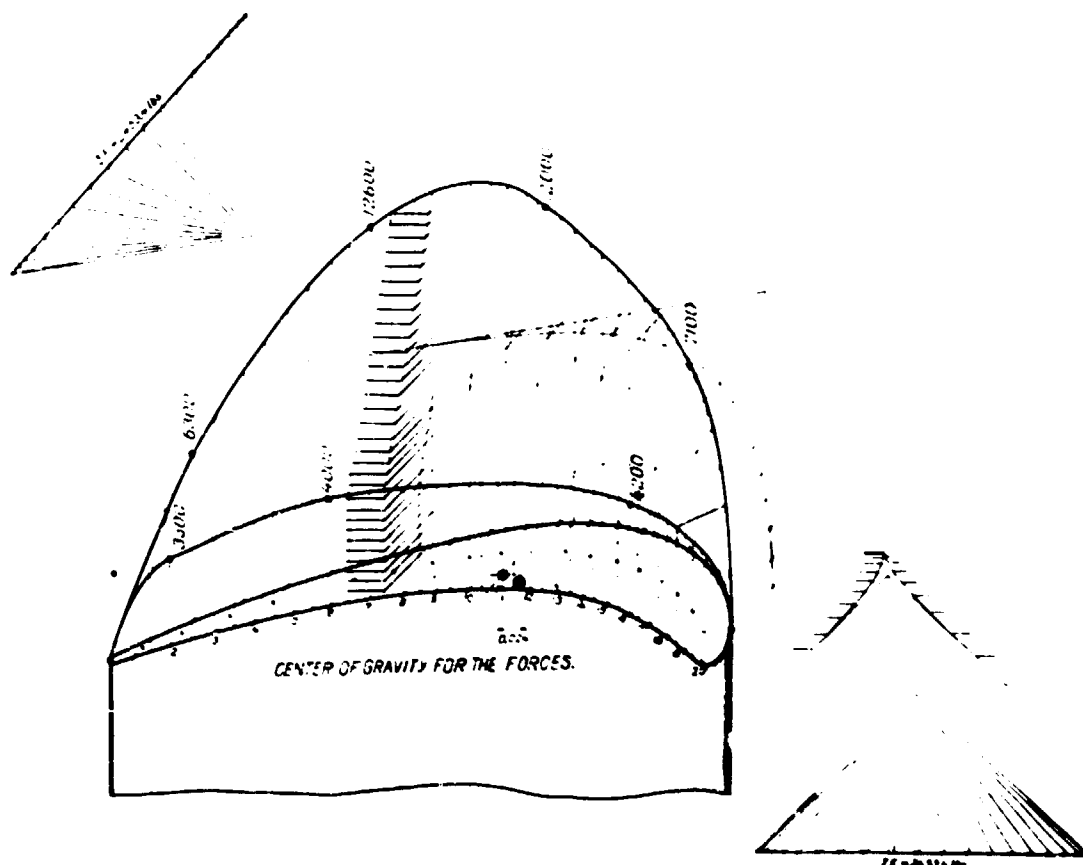
FIGURE 9. Stress distribution over a cross section area of the bucket for axial tension and the determination of the center of gravity for the axial forces.
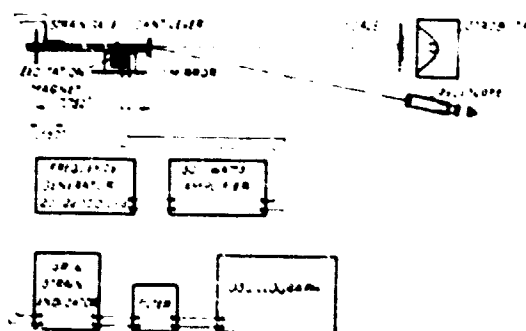
FIGURE 10. Scheme of the test arrangement for calibration.

assembly is shown in Figure 10. The amplitude of the vibrating beam was increased in steps and for each step the output signal of the motor was recorded on the chart of the oscillograph. Finally, the stresses at the location of the gages were calculated from the deflection angle (based on the distance of the mirror from the scale), and the stresses were plotted against the recorded amplitude on the oscillograph chart.

The resulting curve is shown in Figure 11 and some recorded calibration steps are presented in Figure 12. The recorded strain curve gives the frequency to 130 cps. Beyond the natural frequency of the cantilever beam a lower frequency is superimposed resulting from the loading procedure as the beam was vibrated at its natural frequency or close to it where it is difficult to maintain a stable excitation. For each step the average of the amplitudes over a period of 1/10 sec. was evaluated for the determination of an average amplitude.

Since the calibration was known for the uniform beam, the measuring equipment could be connected directly to the strain gages on the bucket by inserting a switch between the strain indicator
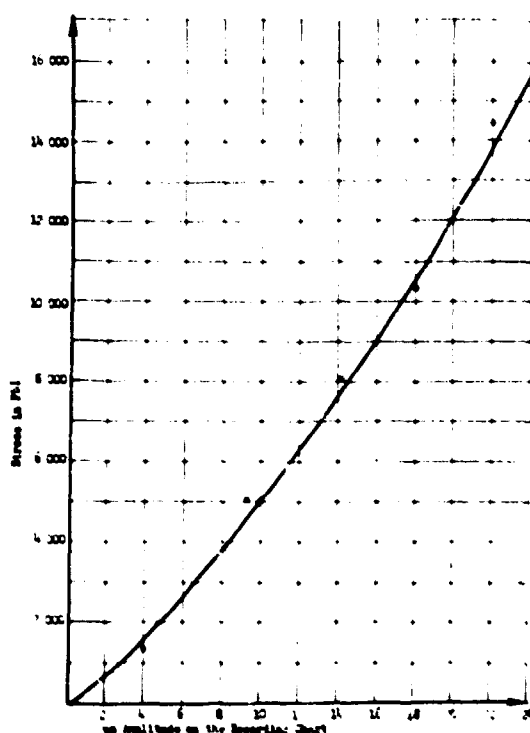
Figure 11. Stress amplitude calibration diagram for steel materials for evaluation of dynamic stress measurements at 130 cps.

130 CPS

AMPLITUDE = 18,15 mm

DEFL._MIRROR = 13,7

and the gages. This switch was needed to connect the strain indicator alternately to the different strain gages around the bucket. The recording equipment described above represented one channel. For more channels several strain indicators, including all the additional test equipment, would have been necessary. In measuring several locations during a continuous vibration of the bucket a simultaneous recording of all strain gages was not essential and one channel was satisfactory as long as the switch did not disturb the resistance in the circuit. This was checked for the switch selected and the resistance was found to be sufficiently low to avoid difficulties.

For the dynamic bending measurements a mirror was attached to the bucket. The static axial load was applied and then the bending vibration was introduced and the deflection was measured optically. In order to correlate the deflection with the stress, ten strain gages were placed on the bucket at the same locations as for the static axial tests. Readings were taken successively for all on the gages. To insure that all of the gage readings were taken while the bucket was being vibrated with a constant amplitude, mirror measurements

Figure 12. Typical oscillograph record and related mirror deflections for calibration.

of the deflection were taken before the strain as each gage was recorded. Figure 13 shows a typical record of this test. Thus the correlation between deflection and stress at each measured location could be investigated.

In the case of two points of special interest are the trailing edge of the bucket and the center point on the convex side. Both locations show maximum stress values either in completely reversed or in zero to maximum bending. The

LOCATION 9.
AMPLITUDE :
AVERAGE = 15.05mm
σ_9 = 8350 PSI.
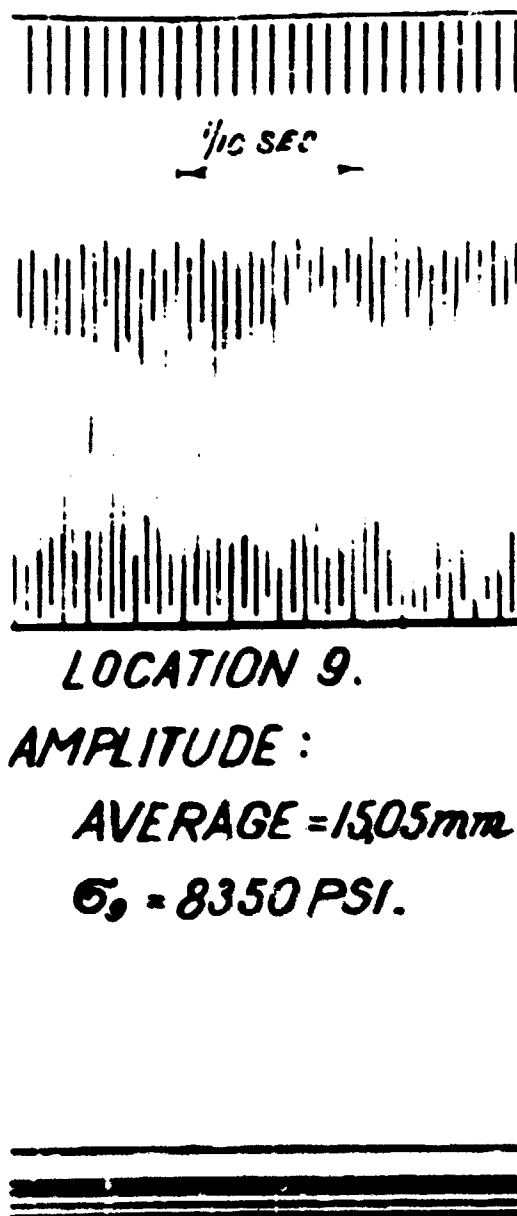
Fig. 13. Typical oscillograph record and evaluation in stress for dynamic loading both on the bucket

evaluation following is given for both runs. Depending on the fatigue characteristics for the material the failure may start at either location. Generally failures will begin at the trailing edge.

for with a completely reversed stress a larger amount of energy is consumed than for a zero to maximum stress. However, the failure may originate in the center, especially for higher loads, if the vibratory stress exceeds the highest allowable load for a given number of cycles for zero to maximum stress.

The records for the ten locations around the cross section of the bucket are evaluated by use of the diagram in Figure 11. Table VII shows the values obtained by this measurement. In the evaluation it should be noted that the diagram in Figure 11 is plotted for stresses on steel beams. In order to get true stresses for vitallium the above stresses are multiplied by the ratio of the moduli of elasticity for the two materials:

$$r = \frac{E_{vitallium}}{E_{steel}} = 1.238$$

In Figure 14 the stress values of Table VII are plotted at their respective locations perpendicular to the actual cross section with the edge as the zero line. The full line represents the stresses for the deflection of the bucket in one direction and the dashed line for the deflection in the opposite direction.

The curve for the actual stresses under combined loading is determined by superimposing the bending stresses on the axial static stresses as measured above. The stresses for this case are shown in Table VIII and in Figure 15. The presentation is given in the same manner as was explained for Figure 8. The stress curve shown in Figure 15 intersects for the two deflection directions with the edge of the cross section at different points. By drawing lines through the corresponding points, these lines include an angle which indicates a torsional moment of the bucket during operation as was observed in the optical deflection measurement during vibration.

During the fatigue tests the deflection was measured. This measurement was evaluated in stress at the two locations on the bucket: the trailing edge and the center on the convex side. In the elastic range the stress increases proportionally to the deflection. The stress was measured for a selected deflection of 30 mm on the scale. The ratio of the stress acting in the fatigue test corresponding to different deflections obtained and the stress measured by the calibration had to be equal to the ratio of the deflections.

Location No.	Measured double amplitude, mm	Bending stress range,[1] psi	Bending stress range,[2] psi	True bending stress,[3] psi	Remarks
1					Gage broken
2	33.5	9,600	11,850	5,925	
3	30.1	5,100	6,300	3,150	
4	27.3	9,500	11,750	5,875	
5	8	14,850	18,400	9,200	
6					Gage broken
7	40.5	12,300	15,200	7,600	
8	45.6	14,600	18,000	9,000	
9	40.1	8,350	10,350	5,175	
10	47.1	15,200	18,900	9,400	

[1] Stress as given by calibration chart Fig. 9.
[2] True stress for vitallium is obtained by multiplying the values from the chart with the factor $E_v E_s = 1.238$.
[3] See text.

TABLE VIII. Total stresses as measured on buckets under axial static tension and vibrational bending

Location No.	Vibrational bending stress, psi	Static axial tension stress, psi	Total stresses	
			Psi	Psi
1				
2	±5,925	−4,100	−10,025	1,825
3	±3,150	−5,800	−8,950	2,650
4	±5,875	−4,200	−10,075	1,675
5	±9,200	*900	−9,200	9,200
6				
7	±7,600	−7,100	300	−11,700
8	±9,000	−12,000	−3,000	−21,000
9	±5,175	−12,600	−7,425	17,730
10	±9,400	−6,300	−15,700	3,100

*Not included in Fig. 11

then the stress for each fatigue test could be calculated from the deflection by:

$$\frac{y}{30} \, 18,000 = \sigma \text{ in psi (for the trailing edge)}$$

y = deflection measured in the fatigue test
30 mm = deflection measured in the calibration test
18,000 = stress measured in psi in the calibration test for 30 mm deflection

The stresses at the two locations are calculated in this manner and presented in Table IX.

The procedures as stated apply for room temperature tests. For elevated temperature tests service temperatures were simulated. The elevated temperature over the length of the bucket caused an increase in the deflection of the cantilever beam compared to that at room temperature using the same load.

The temperature distribution over the bucket length was measured by the NACA and the Materials Laboratory. Based on these measurements which are plotted in Figure 16, the ratio of
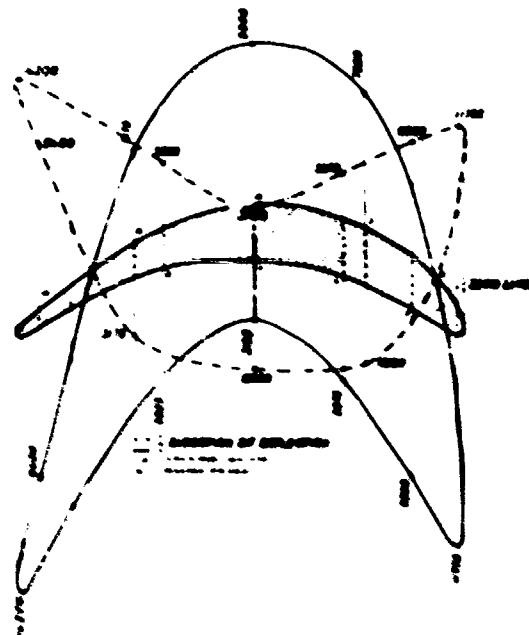
Figure 11. Stress distribution for vibrational bending load

the modulus of elasticity $\frac{E_s}{E}$ could be obtained where

E_s equals the constant modulus at the root section and E the changing modulus over the length if the relation of the modulus of elasticity versus temperature is known. This relation was obtained by an interpretation of the tests of other authors and was plotted in Figure 17. As shown, the different authors give widely varying values from one another. The present consideration was based on the Allison curve with which the above mentioned ratio was calculated.

Table IX. *Measurement of deflections for an SN-diagram and calculation of stresses for the trailing edge and for the center at the convex side of the bucket under axial static tensile and vibrational bending forces at room and elevated temperatures*

Bucket No.	Axial load, lbs	Mirror reading, mm	Stress at		Number of cycles $\times 10^6$	Remarks*
			Trailing edge, psi	Center convex side, psi		
Room temperature						
1		80	29, 000	33, 500	2. 45	Failure
2		148	53, 500	62, 000	0. 5	Failure
3	2, 600	95	34, 400	40, 000	0. 35	Failure
4		76	27, 500	32, 000	1. 86	Failure
5		69	25, 000	29, 000	5. 5	Failure
6		65	23, 500	27, 200	14. 0	No failure
Temperature 1360° F.						
1		72	29, 500	34, 500	9. 1	No failure
2	2, 600	77	31, 500	36, 900	0. 55	Failure
3		84	34, 100	40, 000	0. 94	Failure
4		75	30, 500	36, 000	2. 16	Failure
Temperature 1526° F.						
1		68	27, 500	32, 100	1. 25	Failure
2		66	27, 000	32, 100	0. 235	Failure
3	2, 600	62	25, 000	29, 200	9. 8	No failure
4		77	31, 200	35, 400	0. 156	Failure
5		72	27, 900	34, 000	0. 335	Failure
6		64	26, 000	30, 200	1. 15	Failure

*See text for discussion of failures.
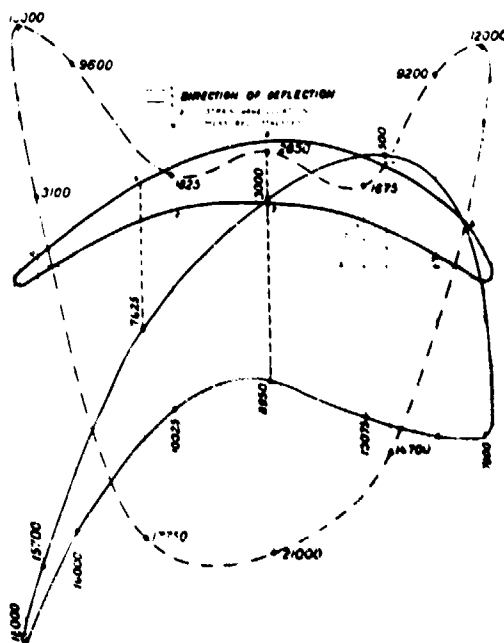
Figure 15. Stress distribution for total axial tension and vibrational bending load.

Figure 16. Actual temperature distribution over the bucket length, ratio of moduli of elasticity by non-uniform temperature
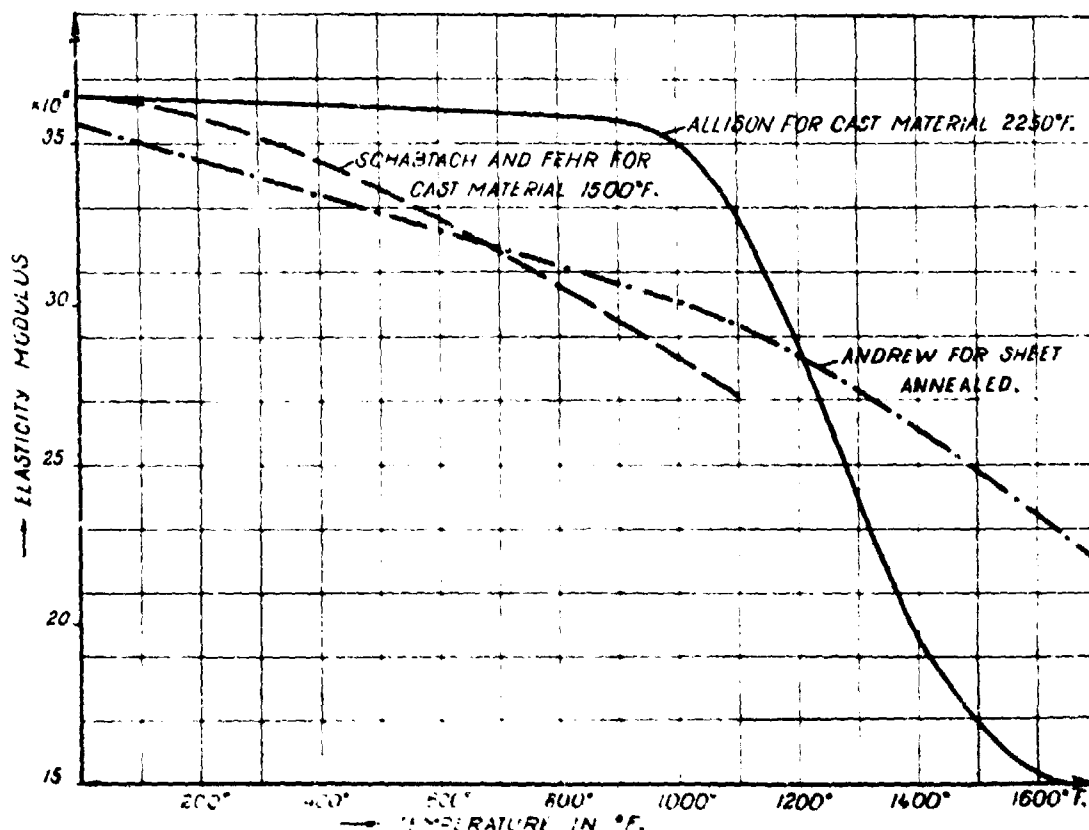
FIGURE 17. Modulus of elasticity of Vitallium (Haynes Stellite 21) versus temperature.

For elevated temperatures basically the same considerations may be used as for room temperature to obtain the true stresses but the resulting stress has to be corrected by a factor which accounts for the increased deflection of the bucket. This factor will not change very much for different loads on the beam. For the presented investigation this factor was assumed to be constant. The true bending forces on the bucket are not known because of the complex system of forces involved. It is assumed that a considerable part of the bending load acts as a single load by the kind of load introduction used. Therefore, the factor was determined for a cantilever beam with a length corresponding to the distance between the root and the introduction point of the lateral vibration force into the bucket. For such a cantilever beam the deflection for a single load on the free end at room temperature as well as at elevated temperature was determined. The comparison is shown in Figure 18. The ratio y'_R / y'_T of the two deflection values at the measured

station of the length was determined for the two temperatures 1,360° F. and 1,526° F. y'_R is the deflection at room temperature and y_T the one at elevated temperature at this location of the beam. Thus:

$$\frac{\sigma_R}{\sigma_T} = \frac{y'_R}{y'_T} \quad \text{or} \quad \sigma_T = \sigma_R \frac{y'_T}{y'_R}$$

Therefore we obtain for the true stress at elevated temperature in respect to the considerations above:

$$\sigma = 13,000 \frac{y_T \cdot y'_T}{30 \cdot y'_R}$$

where y'_R and y'_R are defined as above and y_T is the measured deflection under vibration at elevated temperature.

With this relation the stress values for the two SN curves at elevated temperatures were obtained Table IX. The resulting SN diagrams are presented in Figure 19 and Figure 20, which are plotted for the two important peak stress locations:

33

Figure 18. Change in deflection for nonuniform temperature distribution over the bucket length and ratio at the measured cross section.

the trailing edge and the outer fibre at the convex side of the bucket.

At room temperature the endurance lir   r the bucket was 22,000 psi for the trailing   + and 26,400 psi for the center. If the endur   .e

limit for flat specimens in completely reversed bending for cast vitallium is 33,000 psi, as other authors have found, the bucket tested in simulated service conditions shows 67% of the stress from the standard test for the trailing edge and 80%

FIGURE 19. Fatigue tests with Vitallium (Haynes Stellite 21). Buckets under axial tension and superimposed vibrational bending load at room and elevated temperatures. Stresses at the trailing edge.

● 75° F   Δ 1360° F   x 1520° F

for the center. Probably the apparent loss is due to the following conditions. The stress is not quite uniaxial in the tapered shell and residual stress conditions exist from the casting procedure.

The distribution of the stresses over the length of the bucket is presented in Figure 21. As the bucket is a tapered cantilever beam the stresses resulting from the static load increase toward the free end. Under centrifugal load the tendency toward increased stresses is directed to the root section. Over these stresses vibrational bending stresses are superimposed correspondent to their distribution over the length. The variation is caused by the cross sectional changes of the bucket. The maximum stress may not exceed the fatigue stress of 22,000 psi measured above. Thus the point of maximum stress over the length was determined to be at a distance of 1.80 inches from the root. In the tests fractures occurred at that location with a slight deviation in each direction for individual buckets. The location range corre-

sponds also to the calculations in Part I of this report and to the location of failures in service insofar as they occurred from the vibration at the fundamental frequency.

Considering the start of a failure in the fractured section two cases have to be observed. In most cases the fatigue failure started at the trailing edge similar to the behavior of the bucket in service. However, in a few cases at elevated temperatures the fatigue failure nucleus was observed in the center of the convex side. The consumed energy at this point is close to or above the one at the other critical location at the trailing edge and would therefore be expected to be the origin of some of the failures.

CONCLUSIONS

The fatigue properties of cast vitallium buckets or the J-33 gas turbine engine were investigated under simulated service conditions. It was neces-
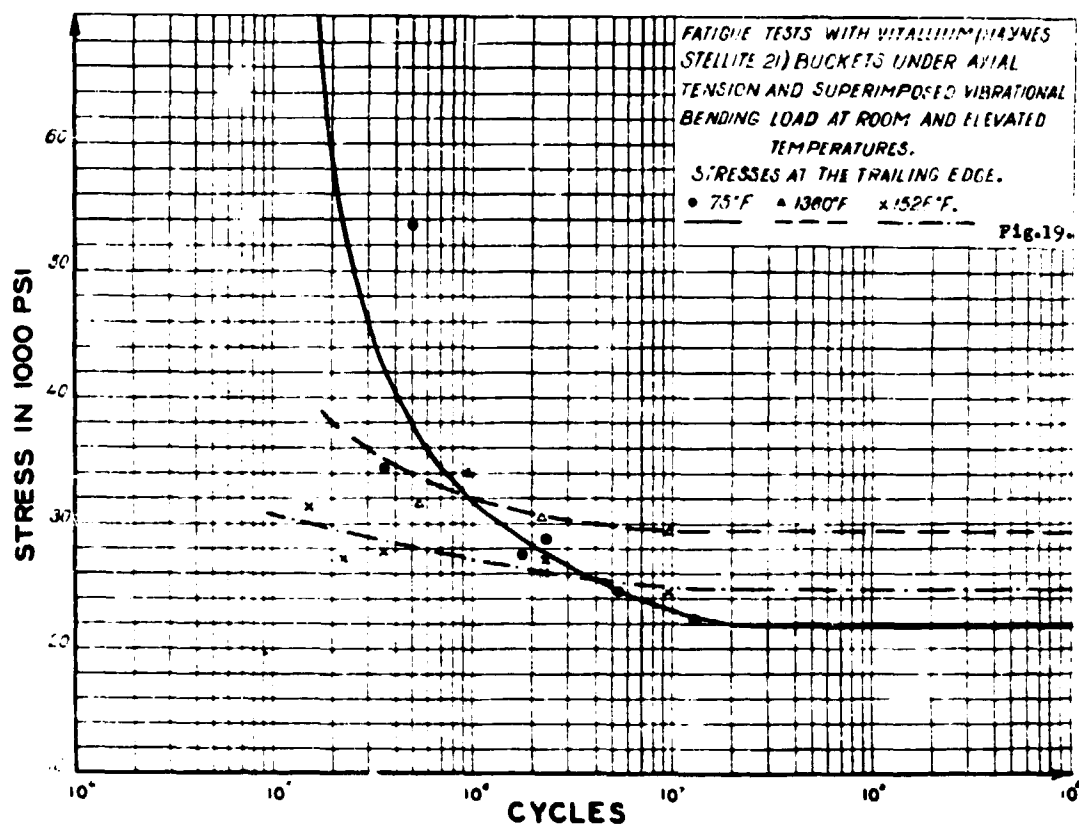
35
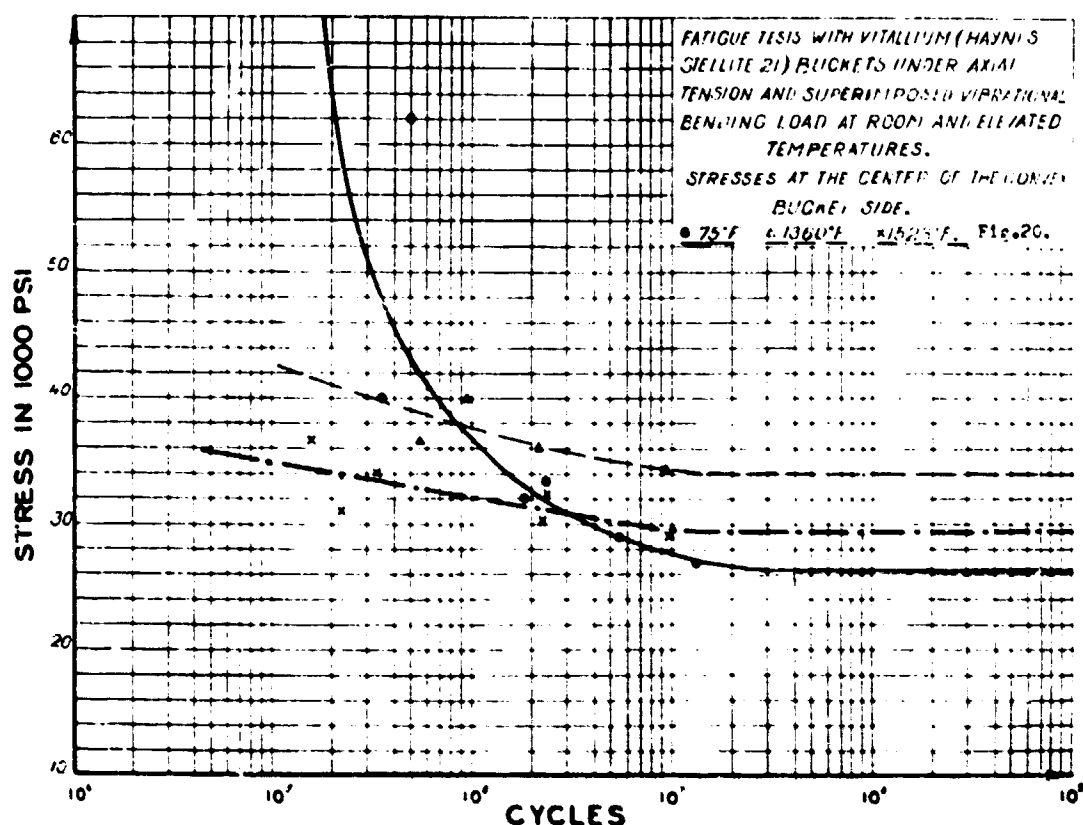
Fig. æ 20. Fatigue tests with Vitallium (Haynes-Stellite 21). Buckets under axial tension and superimposed vibrational bending load at room and elevated temperatures. Stresses at the center of the convex bucket side.
● 75° F   ▲ 1,360° F   x 1,526° F

sary to develop the method and equipment to do this. The centrifugal force on the bucket is simulated by an axial load. The bending vibrational loads are superimposed on the axial load and at the same time the temperature gradients are approximated. A method was developed to carry out such tests and the evaluation thereof is presented. The stresses present in the bucket during the tests were measured and an SN diagram plotted to indicate the fatigue strength of the buckets under the simulated service conditions. The results seem to justify the following conclusions:

(a) The test method developed permits the investigation of various ratios of axial to bending loads for desired temperatures and temperature gradients and for various sizes and shapes of buckets.

(b) A method of predicting the location of fractures is presented and confirmed by the results.

(c) The fatigue strength increases at elevated temperatures (over room temperature) for cast vitallium bucket in the same manner as for standard plate bending specimens.

(d) The fatigue strength of the buckets was slightly less than for plate bending specimens probably due to influence of biaxial stresses and residual stresses in the buckets.

(e) It is possible to make reasonably accurate stress measurements even on such small parts as buckets and to check this accuracy by means of equilibrium considerations between the external and internal forces resulting from static calibration tests.

(f) Different stress conditions exist simultaneously at various locations in the bucket. For example, for a given static axial preload and bending amplitude, the center of the bucket varies from zero to a maximum tensile stress and the

36
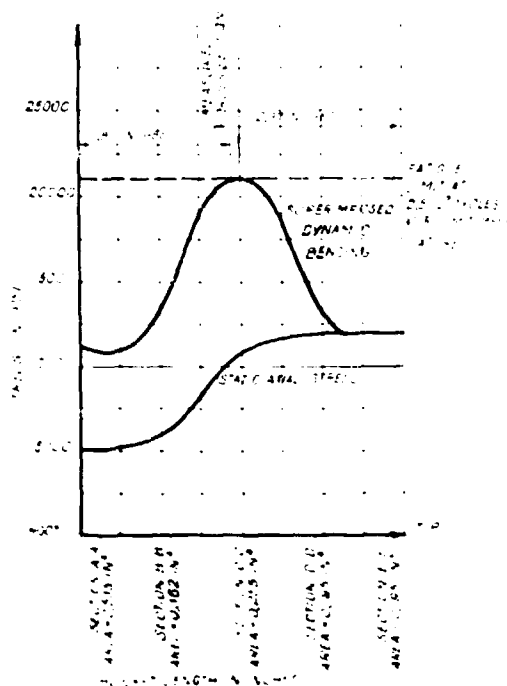
Figure 21. Actual distribution of stresses over the bucket length at the fatigue limit.

trailing edge is stressed in completely reversed loading.

(g) The motion of the bucket is a combination of plane bending and superimposed torsion due to the screw type neutral axis.

(h) The vibration amplitude of, and hence the stresses in, the bucket is a very sensitive function of the root damping.

RECOMMENDATIONS

It is recommended that the following additional work be accomplished:

(a) Investigate additional materials in the form of buckets to establish a definite relationship, if possible, between the bucket fatigue test at the fundamental frequency, and a standard materials fatigue test. If a consistent relationship is found, further investigations of materials proposed for buckets can be evaluated by a simple standard test.

(b) Extend the bucket fatigue test of applicable materials to higher harmonics.

(c) Extend the preliminary work on damping at the root section by investigating the energy consumption of fits having various controlled toler-

ances (under simulated centrifugal loads). These tolerances should be controlled in such a manner that the designer of new buckets can utilize this information in an effort to determine the type of fit with the greatest possible damping and consequently the lowest vibrational stresses in the buckets.

REFERENCES

(1) J. E. Farmer, F. N. Darmara, and F. D. Poulson. Cyclic Engine Tests of Cast Vitallium Turbine Buckets—I. NACA Research Memorandum, RM E7J23, 1948. Restricted.

(2) J. E. Farmer, G. C. Deutsch, and P. F. Sikora. Cyclic Engine Tests of Cast Vitallium Turbine Buckets—II. NACA Research Memorandum, RM E7J24, 1948.

(3) W. C. Morgan, R. H. Kemp, and S. S. Manson. Vibration of Turbine Blades in a Turbojet Engine During Operation. NACA Research Memorandum, RM E7L18, 1948. Restricted.

(4) W. C. Morgan, R. K. Kemp, and S. S. Manson. Vibration of Loosely Mounted Turbine Blades During Service Operation of a Turbojet Engine with Centrifugal Compressor and Straight Flow Combustion Chambers. NACA Research Memorandum, RM E9J07, 1949.

(5) H. Kemp, and W. Morgan. Analytical Investigation of Distribution of Centrifugal Stresses and their Relation to Limiting Operating Temperatures in Gas Turbine Blades. NACA Research Memorandum, RM E7L05, 1948.

(6) J. E. Farmer. Relation of Nozzle Blade and Turbine Bucket Temperatures to Gas Temperatures in a Turbojet Engine. NACA Research Memorandum, RM E7L12, 1948.

(7) C. Yaker, C. F. Robards, and F. B. Garrett. Investigation of Mechanisms of Blade Failure of Forged Hastelloy 3 and Cast Stellite 21 Turbine Blades in Turbojet Engines. NACA Research Memorandum, RM E51D16, 1951.

(8) G. T. Harris and M. T. Watkins. Variation of Elastic Moduli with Temperature for Various Steels and Pure Metals. IRON AND STEEL INSTITUTE, Symposium 1951, p. 175–181.

(9) P. H. Frith. Fatigue Tests at Elevated Temperatures. IRON AND STEEL INSTITUTE, Symposium 1951, p. 175–181.

(10) H. Woodhouse. Turbine Blade Fastenings, a Review of Early and Modern Designs. MACHINE DESIGN, 1951.

(11) J. R. Driver. A Simple and Exact Method of Calculating Turbine Bucket and Axial Compressor Blade Torsional and Flexural Frequencies. Turbine Development Group Report No. TD—18, Allison Division, GMC, Indianapolis, 14 May 1946.

C. W. Andrews. Effect of Temperature on the Modulus of Elasticity. METAL PROGRESS, July 1950

(13) Schabtach and Fehr. Measurement of Damping of Engineering Materials during Flexural Vibration at Elevated Temperatures. Annual Meeting of the ASME, New York, 1943.

(14) R. R. Ferguson. Effects of Magnitude of Vibratory Load Superimposed on Mean Tensile Load on Mechanism of the Time to Fracture of Specimens and Correlation to Engine Blades. NACA Research Memorandum, RME52F17, October 1952. Restricted.

(15) F. B. Garrett, C. A. Gyorgak and F.W. Weeton. Behavior of Forged S-876 Turbine Blades in Steady State Operation of T-33-9 Turbojet Engine with Stress Rupture and Metallographic Evaluations. NACA Research Memorandum, RME52L17. Restricted.

WILLIAM H. RECTOR

Elevated-Temperature Testing Procedures

Continuous Recording of Time-Deformation Readings During Creep-Rupture
Testing at Temperatures Up to 1200° F

1953

WILLIAM H. RECTOR

William H. Rector was born in Portsmouth, Ohio, July 6, 1921. He attended the University of Dayton and joined the Metals Branch of the Materials Central in 1941. He remained with the Materials Central until December 1956, serving in a military capacity from December 1942 to December 1945.

Upon leaving the Materials Central in 1956, he joined the Arcweld Manufacturing Company, Grove City, Pennsylvania, where he is currently general sales manager for creep-rupture machines and related elevated temperature testing equipment.

Mr. Rector is a member of the American Society for Metals, the American Society for Testing and Materials, and the American Instrument Society.

TEST SPECIMEN

THERMOCOUPLES

SET SCREWS FOR
CLAMPING OF GAGE
TO SPECIMEN

STRAIN COUNTER

CONTROL
PANEL FOR
GAGE OPERATION

DRIVE CABLE

CLAMP BAR
GAGE TO PULL ROD

TIME METERS
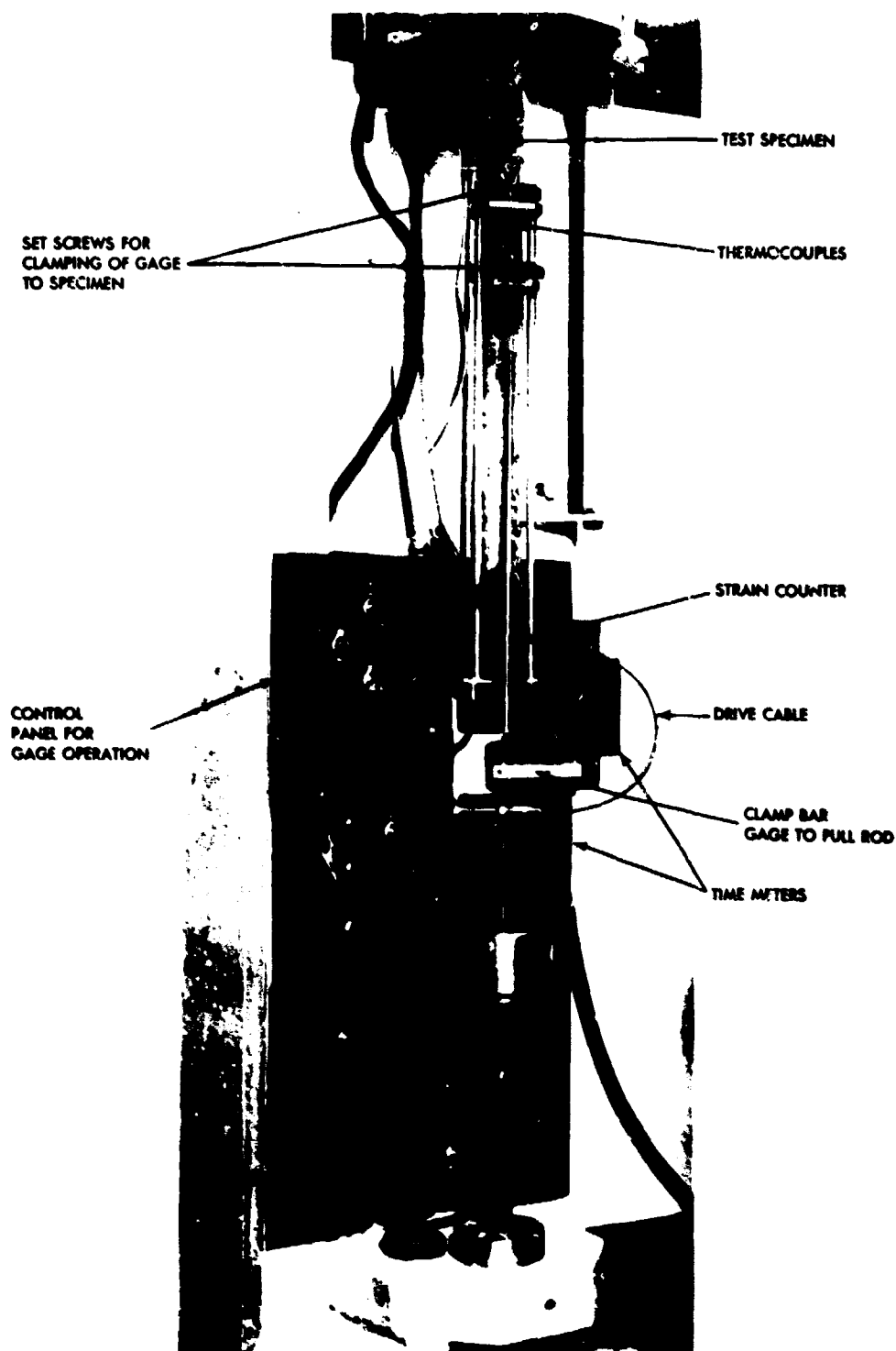
Figure 1   Strain gage assembly.

12

Elevated Temperature Testing Procedures

Continuous Recording of Time-Deformation Readings During Creep-Rupture Testing at Temperatures Up to 1200° F

W. H. RECTOR

ABSTRACT—*A new method of recording deformation during creep-rupture testing at temperatures up to 1200° F is presented. This method has the advantages of: (1) obtaining a continuous time-deformation record up to failure, compared to the intermittent readings obtained using the former manual method and (2) being completely automatic and saving the technician's time required to make manual measurements. This method employs cameras to record the data. A description of the equipment is given.*

I. INTRODUCTION

This report was written to describe the equipment and test procedures used in obtaining a continuous record of time-deformation readings during creep-rupture tests on various alloy sheet materials and metal-to-metal adhesive bonded specimens for time periods from a few hours up to thousands of hours of test time. Several types of materials have been tested using this equipment but no description of this particular procedure has been previously presented.

II. STRAIN GAGE

The test specimen normally used for sheet material is approximately twenty inches in length by one and one quarter inches in width with a two inch gage length which is one half inch in width. The extensometer is attached to the specimen gage length by means of pointed stainless steel or high temperature alloy set screws.

The elevated temperature strain apparatus employed in this procedure is of standard design, manufactured by the Baldwin-Lima-Hamilton Corp., Model PsH-8. The strain reading is indicated on a motor driven counter, which reads deformation in 0.000025 inch increments.

A test specimen mounted in a standard lever-type creep-rupture frame is shown in Figure 1 (Furnace removed) with strain gage, control and recording thermocouples attached. On the front of the test frame is shown the panel containing the electronic system for the strain gage operation, deformation counter, and timing devices.

Two time counters are used for accurately recording test time; one is a revolution counter calibrated to read to the nearest ¼₀ hour while a standard clock with a sweep second hand is used to indicate the time in seconds and minutes during the initial loading of the test specimen and early stages of creep.

III. RECORDING EQUIPMENT

Since the strain measuring equipment described above required laboratory personnel to take readings at various times throughout the it was noted that a considerable amount of able test information was being lost during the nights and over weekends when personnel were off duty. Considerable thought was given

to devising a more suitable means of recording these test data not only during off-duty hours but also automatically, thereby relieving laboratory personnel for other duties. Several methods of automatic recording were investigated.

A decision was reached to automatically photograph the strain counter and time meters at predetermined periods throughout the day. Several methods of photographing the different meters were studied and the final solution was obtained by revamping motion picture cameras for single-frame exposure operation. A Standard Aircraft Bomb Spotting Camera, which is a 35 mm. motion picture camera with a shutter speed of ½ of a second was modified for this particular task. The motion picture drive assembly was removed and replaced by a specially designed tandem solenoid mechanism.

The solenoid mechanism serves a twofold purpose: first, it actuates the camera shutter and second, as the shutter closes, a second solenoid drives a clutch which in turn advances the film to the next frame. The camera holds 100 feet of film, with 16 exposures to the foot, which in most instances will record an entire creep-rupture test.

An f: 2.3 25 m. lens is used with the camera which covers a relatively wide area and has a focal length of approximately one foot. This allows the camera to be placed close to the test frame, thereby not taking up aisle space in front of the test frame. The camera is mounted on top of a 1¼ inch pipe which in turn is mounted rigidly to the floor to prevent the camera from moving while in operation. Originally a bracket was mounted on the test frame for holding the camera but this proved unsatisfactory, since energizing the camera vibrated the test frame which in turn transmitted the vibration to the strain gage causing false motion to be recorded on the strain counter.

A camera unit is shown in Figure 2 illustrating its location on the pipe stand and its location with respect to the testing frame.

In order to illuminate and reduce shadows on the strain counter and time meters, two 100 candle power, 24 volt DC, aircraft landing lights are mounted on the camera. One light is mounted three inches above and the other three inches below the center line of the camera lens. The location of these lights is shown in Figure 2.

IV. ELECTRONIC CONTROL

As was mentioned in previous paragraphs, the cameras and lighting were of aircraft type which were originally designed for airborne use for operation on a 24 volt DC power supply. Therefore, it was necessary to obtain a 24 volt DC supply for this operation. Since it was found that each camera and its lighting required 7 to 9 amperes for one quarter second time interval, it was concluded that the most satisfactory voltage supply could be obtained by using a 24 volt storage battery. The use of an AC-DC voltage rectifier was contemplated, but due to high amperage requirements per unit, the capacity and size of the rectifier required were prohibitively large.

A control panel for the cameras' operation was designed and fabricated for control of fifteen camera stations. It was designed using two timing units, one for short time periods and the other for long time periods. These timing units are of the tandem recycling type; that is, each unit is made up of two timers so designed as to enable two operations to be completed in each cycle. One timer of each unit controls the interval between photographic exposures while the second timer of each unit controls the time of the photographic exposures.

The two timing units installed in the control panel enable a variety of time intervals to be selected depending upon the particular test being conducted. One timer is for 0–3 minutes operation and other is for 0–60 minutes. The second or operational timer in each unit is a 0 to 5 seconds timer and is set for ¼ of a second operation. Each of the timers controls the holding coils of 60 ampere auxiliary relays which in turn control the direct current source for the cameras and lamps. A double pole, double throw, center position "off", toggle switch is located in the panel for each camera unit. This type switch enables the operator to connect the camera to either of the two tandem recycling timers or place it in the "off" position when not in use. Pilot lights at the top and bottom of each switch indicate which timer is being used by that unit.

Installed in the lower half of the control panel are a battery charger, two 24 volt storage batteries and auxiliary switches. This section is wired to

STRAIN COUNTER

CAMERA

TIME METERS

ILLUMINATION
LAMPS
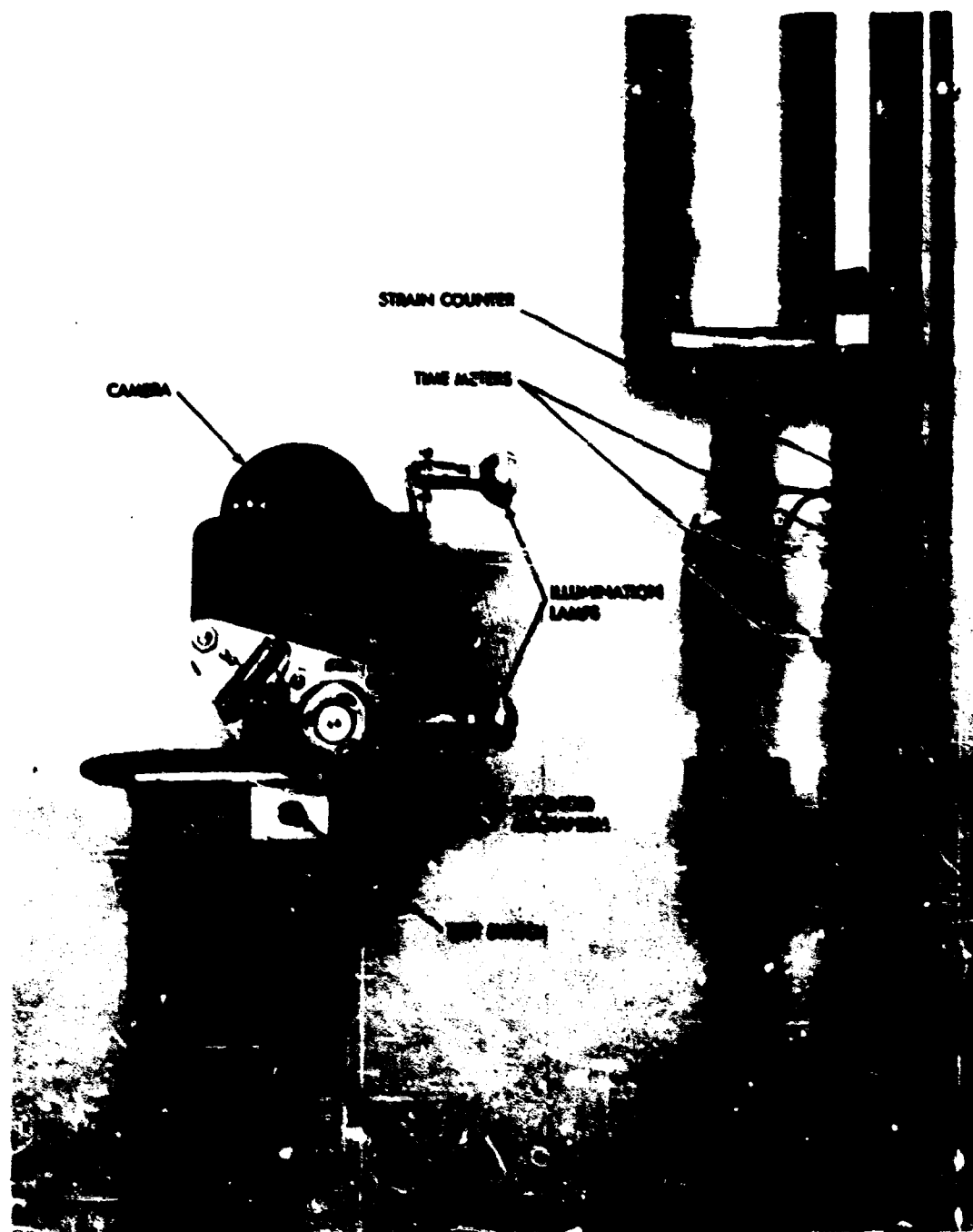
FIGURE 2. Photographic recording system.

45

CAMERA SWITCH
(FOR EACH UNIT)

PILOT LAMPS

SHORT-TIME TANDEM
RECYCLING TIMER

LONG-TIME TANDEM
RECYCLING TIMER

MAIN PANEL
SWITCH

BATTERY CHARGER
SWITCH

BATTERY CHARGING
AMPERES

NO. 1 BATTERY
SWITCH

NO. 2 BATTERY
SWITCH

BATTERY CHARGER
CONTROL
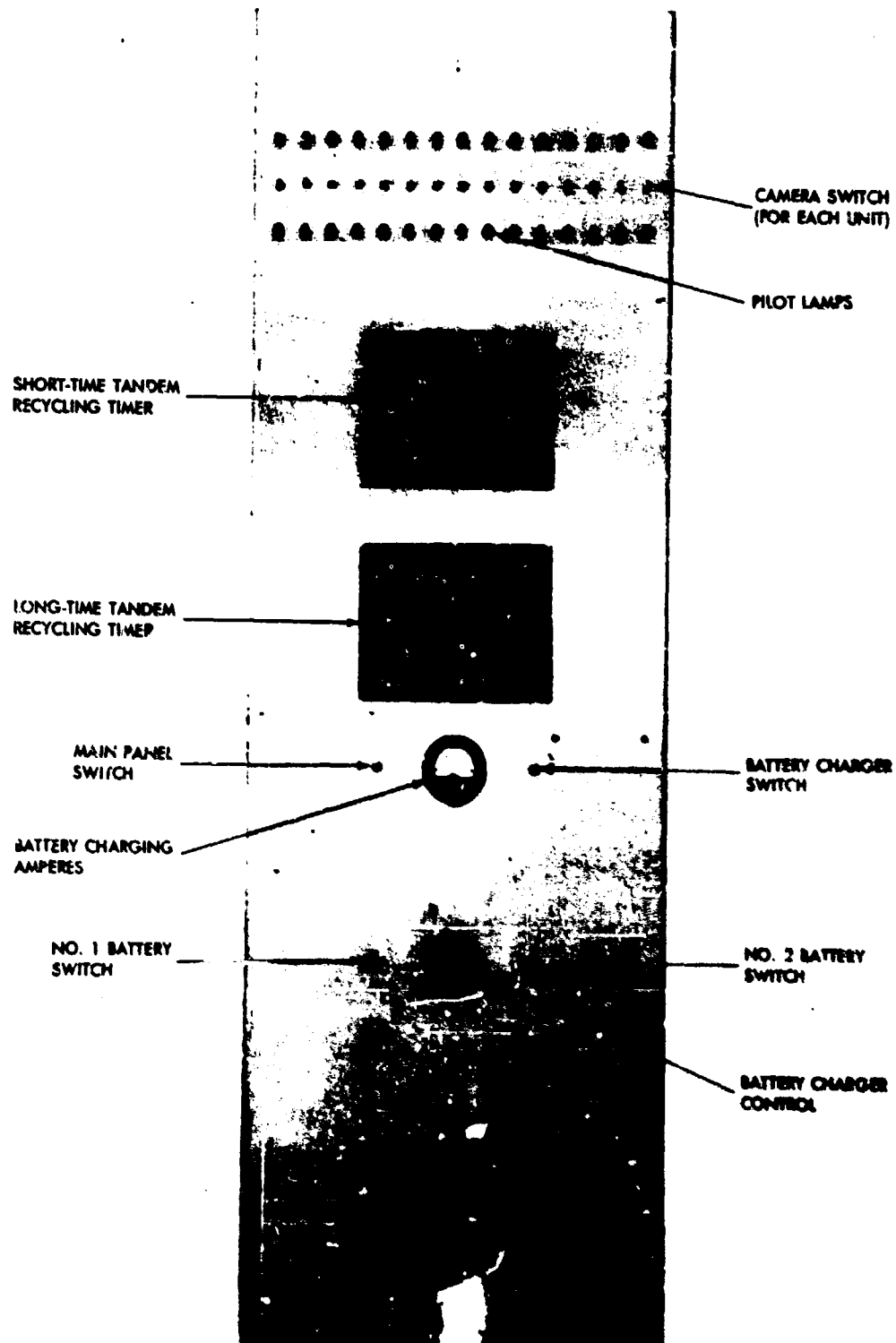
FIGURE 3. Control panel.

46

permit the use of either battery as a voltage supply while the other is being re-charged or both batteries may be used at once thereby permitting little drain on either battery.

Located at the base of each camera is an auxiliary switch which permits manual operation of the camera and Lighting. This enables the operator to check the function of the unit and aids in loading the film.

Figure 3 shows a photograph of the control panel with various sections indicated.

V. TEST DATA AND CURVES

All test data are recorded on Eastman Negative Super XX film and process developed. Processed film is read by means of a microfilm reader and the data recorded for each frame. The data obtained from these readings are used for the plotting of time-deformation curves. Shown in Figure 4 is a photograph enlargement of a single frame of 35 mm. test film showing the strain counter and timers.

SUMMARY

Two time-deformation curves are shown in Figure 5, one of which was produced from readings taken by personnel during the normal eight hour work period while the second was produced from data obtained from a regular test film. This clearly shows that a continuous type of recording is necessary to obtain a reliable time-deformation curve. As shown by the curve plotted by manual readings it is difficult to determine where the final stage of creep really started while the second curve clearly defines all the deformation occurring in the test specimen. The difference is more pronounced in tests of shorter duration where creep is accelerated due to the application of higher stresses thus requiring manual readings to be taken almost continuously. The loss of data during off duty hours would also be more significant in the shorter tests.

The photographic method of recording test data is highly beneficial in many ways. It (1) provides a permanent test record, (2) allows skilled personnel who were formerly taking manual readings to be free to accomplish other tasks, and (3) provides for reading of completed test films by clerical help. Formerly the manual readings were taken by qualified engineering personnel due to the accuracy and other requirements which were essential in obtaining the readings. It has been found that since this method of recording has been employed a saving of approximately 75 percent in man hours has been attained.
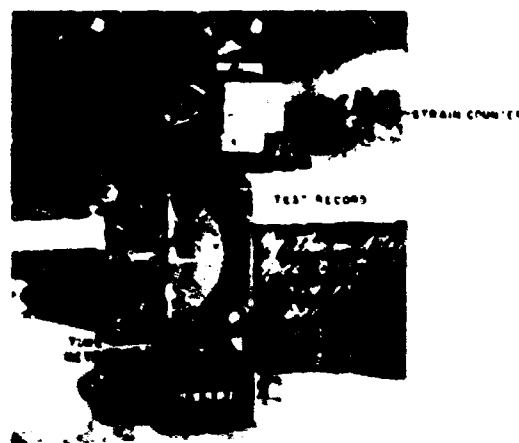
Figure 4.   Single frame photograph of test film.

TIME-DEFORMATION CURVES OF CLAD 24S-T3 ALUMINUM ALLOY
SPECIMEN AT 500°F. AND 10000 PSI

FIGURE 5

MANUAL READINGS

FILM READINGS

Figure 5. Comparison of manual and film readings.

FREEMAN F. BENTLEY
GEORGE RAPPAPORT

Quantitative Analysis of Elastomers Through the Infrared Spectra of Their Pyrolyzates

1954

50
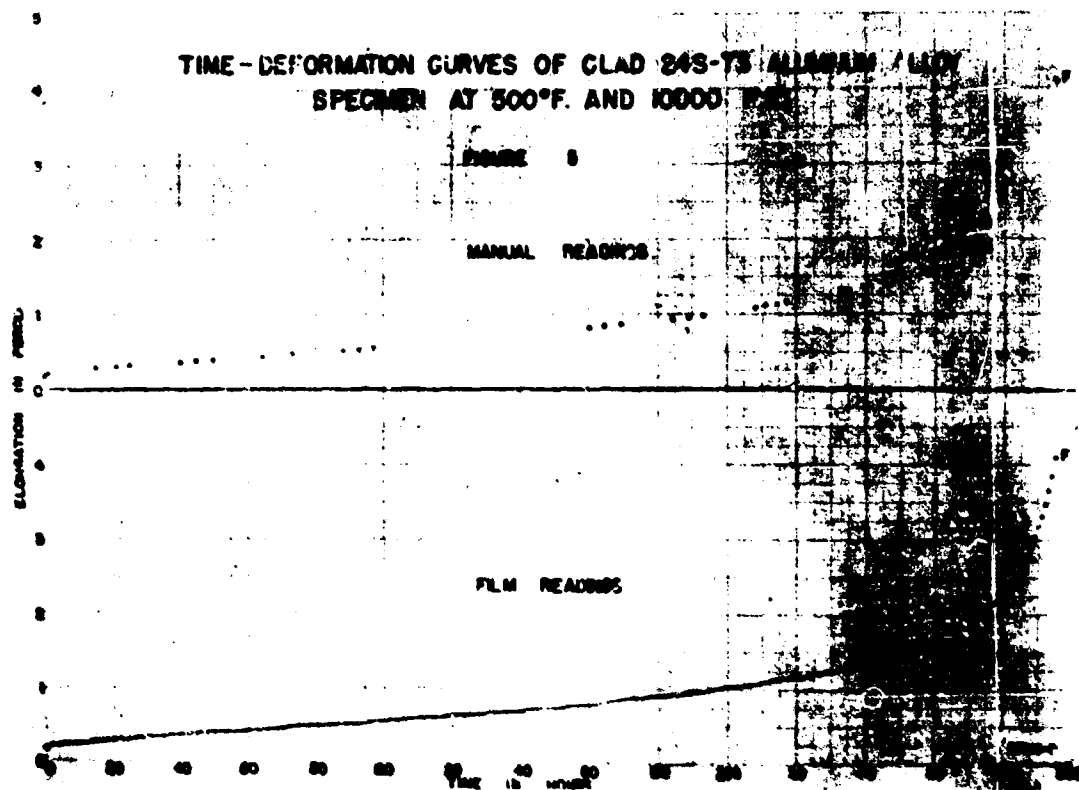
FREEMAN F. BENTLEY

Freeman F. Bentley was born August 15, 1920, in Cedartown, Georgia. He attended the West Georgia College, Carrollton, Georgia, from 1939 to 1941, and the American University, Washington, D.C., from 1941 to 1943 on a Congressional Scholarship. In 1943, he joined the military service and served with the U.S. Army in the European theatre of operations during World War II.

Upon the completion of his military service in January 1946, he joined the Nopco Chemical Company, Cedartown, Georgia, as an analytical chemist. The following September. he resumed his education at the University of Georgia. He received the B.S. degree in chemistry in 1947, and the M.S. degree in chemistry in 1949. In 1950, he received a National Research Foundation Scholarship at the Applied Science Research Laboratory, University of Cincinnati. In 1951, he came to the Physics Laboratory, Materials Central, where he is now chief of the Analytical Branch of the Physics Laboratory.

Mr. Bentley is a member of Phi Kappa Phi, Phi Lambda Upsilon, Gamma Sigma Epsilon, the American Chemical Society, the Society of Applied Spectroscopy, and the Coblentz Society on Infrared.

BIBLIOGRAPHY

Analytical Applications of Far Infrared Spectra. Paper presented at the Pittsburg Conference on Analytical Chemistry and Applied Spectroscopy, March 3, 1955.

With G. D. Oshesky. Infrared Spectra of Cyclopentamethylenedialkylsilanes in the 2-35 Micron Region. Journal of the American Chemical Society, 79 (9): 2057-2062, May 5, 1957.

Analytical Applications of Far Infrared Spectra. I. Historical Review, Apparatus and Technique. Paper presented at the General Motors Conference on Absorption Spectroscopy, May 25, 1957.

With J. A. Parker, E. A. Peterson, and D. Hale. Effects of Gamma Irradiation on Acrylonitrile-Butadiene Copolymers. Paper presented at the Meeting of the American Chemical Society, New York, N.Y., September 1957.

Analytical Applications of Far Infrared Spectra. II. Spectra-Structure Correlations in the Cesium Bromide Region. Paper presented at the Annual Meeting of the Optical Society of America, Columbus, Ohio, October 17, 1957.

With G. D. Oshesky Infrared Spectra of Cyclopentamethylenedialkylsilane in the 2-35 Micron Region. Paper presented at the Meeting of the American Chemical Society, Miami, Florida, April 19, 1958.

Analytical Applications of Far Infrared Spectra General Paper. Paper presented at the May Meeting of the American Association of Spectrographers, Chicago, Illinois, May 13, 1958.

Analytical Applications of Far Infrared Spectra General Paper. Paper presented at the Meeting of the National Society for Applied Spectroscopy, Cleveland, Ohio, November 19, 1958.

With E. F. Wolfarth, N. E. Srp, and W. R. Powell. Analytical Applications of Far Infrared Spectra. I. Historical Review, Apparatus and Techniques. Spectrochimica Acta, 13 (½): 1-30, November 1958.

Analytical Applications of Far Infrared Spectra. Paper presented at the Seminar, Eastman Kodak Company. Rochester, N.Y., December 1958.

With E. F. Wolfarth. Analytical Applications of Far Infrared Spectra. II. Spectra-Structure Correlation of Aliphatic and Aromatic Hydrocarbons in the Cesium Bromide Region. Spectrochimica Acta, 15 (¾): 165-205, May 1959.

With N. T. McDevitt. Analytical Applications of Far Infrared Spectra. III. Spectra-Structure Correlations of Bromo and Iodo Alkanes. Paper presented at the Tenth Annual Symposium on Spectroscopy, Chicago, Illinois, June 1, 1959.

With R. Isaac. The Infrared Spectra of Mono-Substituted Pyridines from 15-35 Microns. Paper presented at the Tenth Annual Symposium on Spectroscopy, Chicago, Illinois, June 1, 1959.

With M. T. Ryan. Analytical Applications of Far Infrared Spectra. IV. Spectra-Structure Correlations of Fatty Acids. Paper presented at the First Eastern Analytical Symposium, New York, N.Y., November 4, 1959.

With F. A. Miller, G. L. Carlson, and W. H. Jones. Infrared Spectra of Inorganic Ions in the Cesium Bromide Region. Paper presented in Pittsburgh, Pennsylvania, March 3, 1960.

With F. A. Miller, C. R. Carlson, and W. H. Jones. Infrared Spectra of Inorganic Ions in the Cesium Bromide Region. Spectrochimica Acta, 1960.

Analytical Applications of Far Infrared Spectroscopy. Lecture given at the Fifth Annual Infrared Spectroscopy Institute, Canisius College, Buffalo, N.Y., August 1961.

Far Infrared Spectrometry. Paper presented at the General Motors Spectrographic Conference, Research Laboratories, General Motors Corporation, Detroit, Michigan.

Handbook on Far Infrared Spectrometry. In preparation by the McGraw-Hill Book Company.

With E. F. Wolfarth and C. Tamborski. Analytical Applications of Far Infrared Spectra. III. The Infrared Spectra of Fatty Acids in the 15-35 Micron Region. Manuscript in preparation.

54
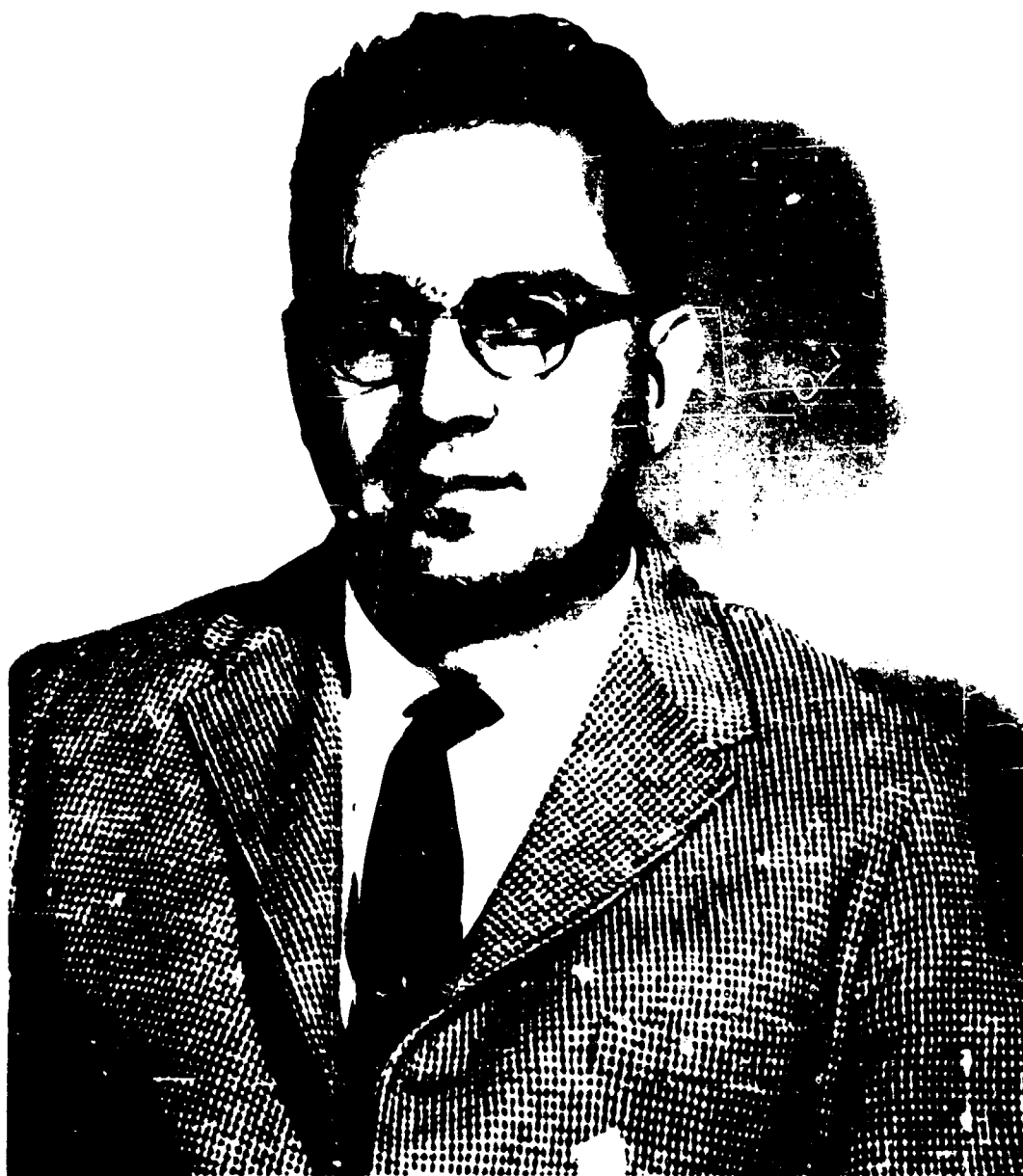
GEORGE RAPPAPORT

George Rappaport was born May 27, 1923, in Jaszbereny, Hungary, and received his elementary education in Europe. He completed his undergraduate work in this country and received his B.S. in chemistry from the University of Miami in 1944. From 1944 to 1946, he was with the United States Armed Forces and was assigned to the Physical Measurements Section of the Physics Laboratory, Materials Central. After separation from the service in 1946, he remained with the Materials Central where he engaged in infrared spectroscopic analysis until May 1953. He obtained his M.S. in chemistry through Ohio State University Graduate Extension at Wright-Patterson Air Force Base in 1950. In 1953, he joined the Inland Manufacturing Division, General Motors Corporation, where he is now employed. He completed the scholastic requirements for the Ph. D. in physical chemistry at Ohio State University during an educational leave of absence from this company during 1960–1961. Currently, he is engaged in research to complete the thesis for his doctorate degree.

Mr. Rappaport serves as chairman for a number of technical committees which include the Nominating Committee of the Society for Applied Spectroscopy, the Local Section (Dayton) of the Society for Applied Spectroscopy, the Absorption Subcommittee of the General Motors Spectrographic Committee, and the X-ray Subcommittee of the General Motors Spectrographic Committee. He is a member of the Phi Lambda Upsilon Honorary Chemical Society.

BIBLIOGRAPHY

Identification of Aircraft Materials by Infrared Spectroscopy.
Technical Data Digest, 14(14), July 15, 1949.

Application of Infrared Spectroscopy to Lubrication Engineering
Lubrication Engineering, 8(3):129–134, June 1952.

With M. Hauptschein, J. O'Brien, and R. Filler   Fluorinated Esthers
IV The Effect of Neighboring Fluorine Atoms on the Ester Carbonyl Frequency.
Journal of the American Chemical Society, 75(11): 2695–2697, June 2, 1953.

Quantitative Analysis of Elastomers Through the Infrared Spectra of Their Pyrolyzates

F. F. BENTLEY

G. RAPPAPORT

ABSTRACT—*A semiquantitative method is described for determining polymer blends and co-polymer ratios from the infrared spectra of their pyrolyzates (distillates). The method was established through the analysis of phenolic resin blends in Buna-N rubber, and by determining the percentage acrylonitrile in butadiene acrylonitrile co-polymers.*

The method described here permits the semiquantitative analysis of Buna N phenolic resin blends, which because of their physical state, cannot be analyzed by conventional methods. It also makes it possible to estimate the amounts of noncombustible materials in these polymers. The method is based on the pyrolyzate technique combined with standard infrared quantitative procedures.

INTRODUCTION

Infrared methods have been worked-out for the quantitative analysis of polymer blends and co-polymer ratios by other investigators (3). These methods are based on the fact that the polymers will dissolve in organic solvents and can be prepared free of compounding ingredients for spectroscopic investigations.

Buna-N phenolic resin blends cannot be analyzed by conventional methods because of their physical make-up. Buna-N phenolic resin blends were found to contain phenolic resin and all of the polymer blend did not dissolve in o-dichlorobenzene, the solvent commonly employed to dissolved vulcanized rubbers. The use of standard procedures for the quantitative analysis of the polymer blend is thus prevented.

The use of the infrared spectra of pyrolyzates (distillates) for the qualitative analysis of complex organic materials was demonstrated by Harms (1), Kruse and Wallace (2). They showed that unique and reproducible, although undoubtedly complex,

pyrolysis products were obtainable. These products gave distinct and reproducible infrared spectra. This fact led to the development of a semiquantitative method for the analysis of Buna-N phenolic resin blends through the infrared spectra of their pyrolyzates. The method is based on the pyrolysis technique combined with standard infrared quantitative procedures.

Pyrolysis products of several known blends of Buna-N phenolic resin were prepared and a working curve for the estimation of unknown blends was established. The validity of the semiquantitative pyrolysis technique was further established by determining the percentage acrylonitrile in Buna-N elastomers. The acrylonitrile content of Buna-N elastomers can be determined by conventional methods and was only included to demonstrate the general applicability of the semiquantitative pyrolysis method.

It is particularly noteworthy that the elastomers can be separated from carbon black and inorganic materials in the rubber, leaving a clean residue. The residue from the pyrolysis of several Buna-

N phenolic resin blends, containing known amounts of noncombustible materials, was collected and weighed to determine if the noncombustible ingredients could be analyzed along with the elastomer.

Although the results were somewhat high in each sample, due to a slight charring of the elastomer, the differences between the calculated and measured values were fairly constant. The pyrolysis technique, therefore, provides a semiquantitative method of determining the amount of material together with the elastomer. Furthermore, the technique isolates the inorganic materials from rubber in a form particularly suitable for spectrographic and X-ray analysis.

Apart from the longer time required to prepare the pyrolyzates the method discussed here appears to have several advantages from a qualitative aspect. These advantages are described in Appendix I.

Section 1.

SEMIQUANTITATIVE ANALYSIS OF BUNA-N PHENOLIC RESIN BLENDS AND CO-POLYMER RATIOS

APPARATUS:

Baird infrared Recording Spectrophotometer, Model B. Sargent Micro Furnace, Combustion Assembly, Zimmerli Gage, and a Duo-Seal Vacuum Pump. The pyrolysis was performed in a combustion assembly especially constructed for this investigation. The dimensions of the combustion assembly are probably not critical. It was designed to allow reproducible conditions of pyrolysis that is, obviously, more important for quantitative studies than for qualitative analysis. No detailed investigations were made on the effect of varied pyrolysis conditions on the composition of the pyrolyzates. An attempt was made to duplicate the initial pressure, time, and temperature conditions for the preparation of each pyrolyzate. The assembly and apparatus used to prepare the pyrolyzates are shown in Figures 1, 2 and 3.
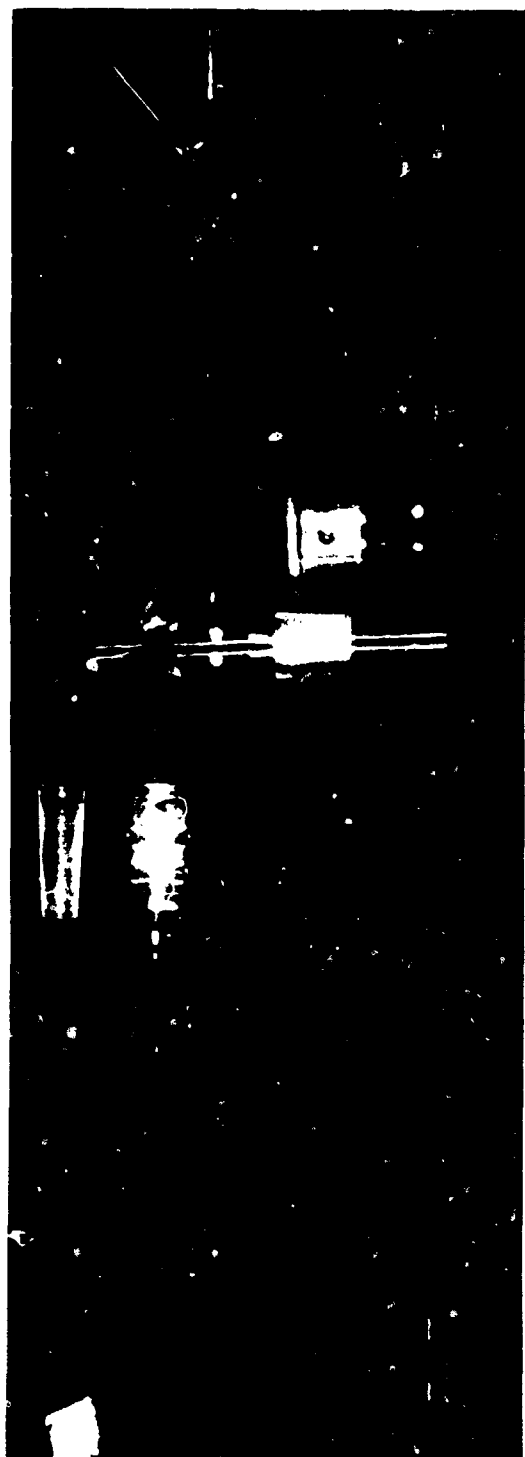
Figure 1. Combustion Apparatus—dismantled.
A. Combustion tube
B. Combustion assembly
C. Receiving flask

Figure 2. Assembled combustion apparatus.

CHEMICALS:

Chloroform, Octagon Process, Inc. USP Grade. Acetone, Eastman Kodak Product "white label" quality. Both chemicals were used directly from the bottle without further purification. Dry ice was used in a cold trap in the preparation of the pyrolyzates.

PROCEDURE:

A two gram sample of rubber was placed in the combustion tube (Fig. 1a), and the combustion apparatus assembled as shown in Figure 2. The combustion tube was placed in the furnace, the receiving flask (Fig. 1c) covered with dry ice, and the open end of the combustion assembly connected to the vacuum pump. The other tube of the assembly was connected to a Zimmerli Gage to record the pressure during the pyrolysis. The completely assembled apparatus is shown in Figure 3.

The pressure in the system was reduced to 2 mm of Hg., the furnace turned on, and the sample heated to a temperature of 540 to 580° C. This required about 15 minutes when the furnace was operated at 110 volts.

The pyrolysis products which formed were present in the dry ice trap and in the receiving tube leading to it. They were washed out with a 30-70 percent blend of acetone and chloroform. All the washings were combined and the solvent evaporated under identical conditions for each sample. The resulting tar-like pyrolyzate was placed between rocksalt plates using a 0.05 mm. spacer and the infrared spectra recorded on a Baird Model B Spectrophotometer. The spectra of the Buna-N polymers blended with 0–33 percent phenolic resins are shown in Figures 4 and 5. Absorption bands characteristic of a CN linkage in cured Buna-N elastomers with known amounts of acrylonitrile, are shown in Figure 6.

COMPUTATION OF DATA AND RESULTS

The method used for preparing the working curves for determining the phenolic resin content of Buna-N phenolic resin blend was that employed by Dinsmore and Smith (3). It was slightly modified by using base-line absorbance ratios. This was d   o minimize errors due to the inability of r   ducing sample thicknesses using demountab!   lls. The base line technique was used to circumvent possible errors due to the

FIGURE 3. Combustion apparatus used to prepare pyrolyzates.
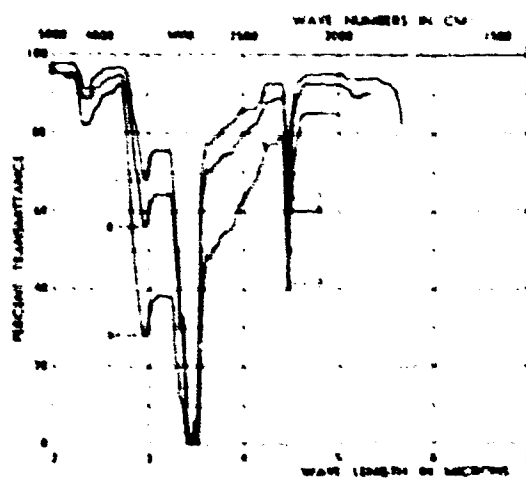
FIGURE 4a. Infrared spectra of pyrolyzates of Buna-N blended with 5%, 9%, and 16.7% phenolic resin.
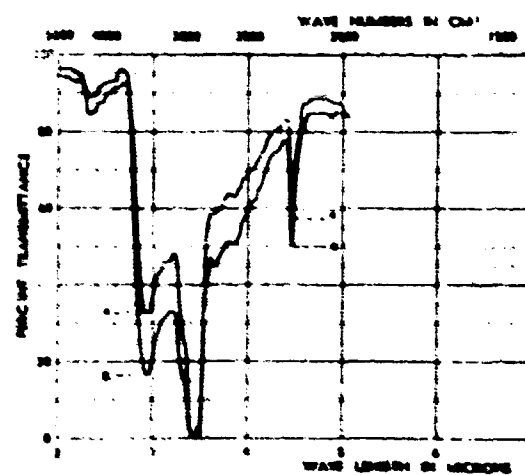
FIGURE 4b. Infrared spectra of pyrolyzates of Buna-N blended with 5% and 33.3% phenolic resin.
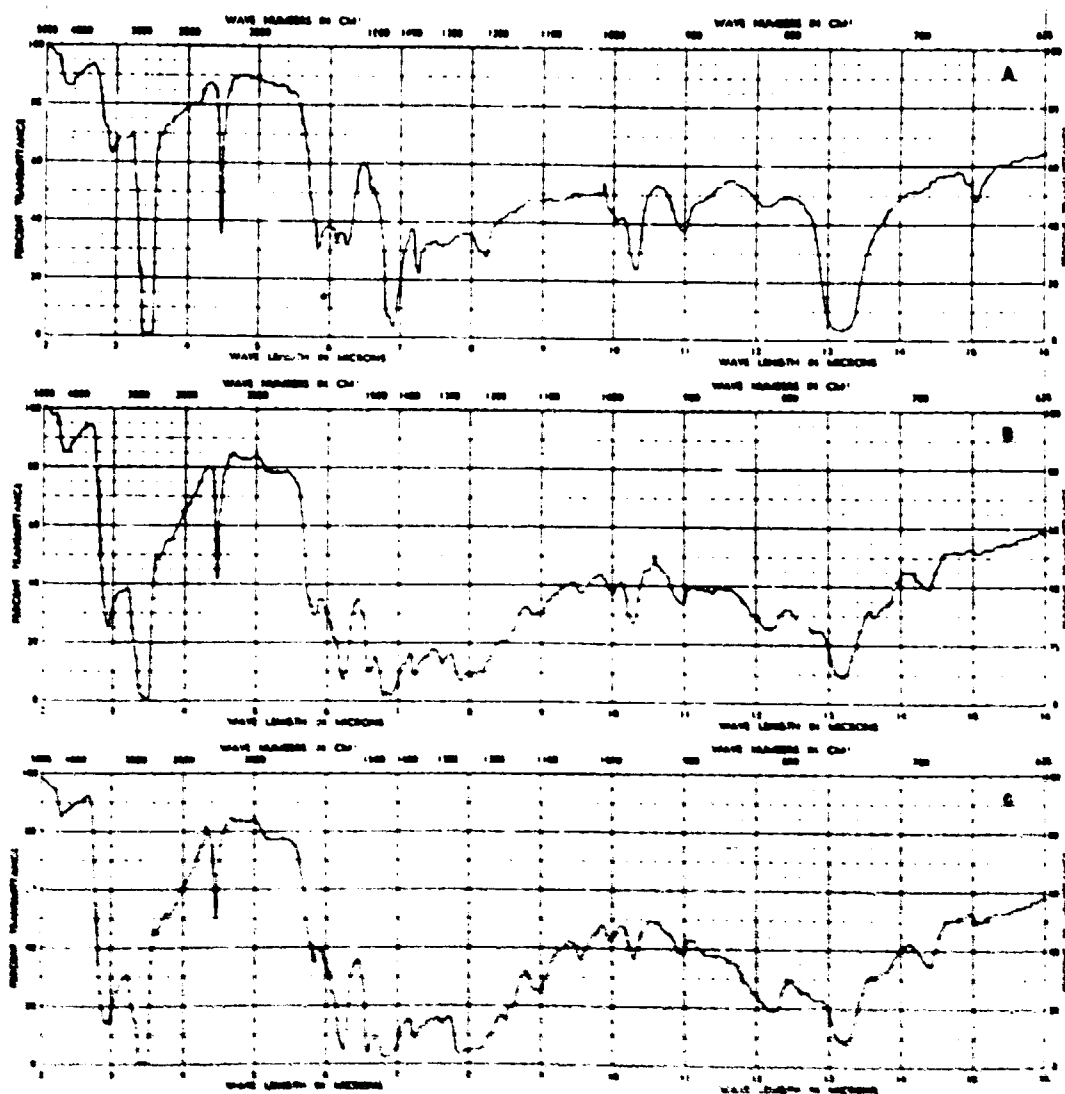
Figure 5   Buna-N phenolic resin blends

A. Pyrolyzate of Buna-N rubber

B. Pyrolyzate of Buna-N rubber blended with 16.7% phenolic resins

C. Pyrolyzate of Buna-N rubber blended with 33.3% phenolic resins

overall absorption of compounding ingredients other than those originating from the Buna-N rubber and phenolic resin.

A plot was made of the percent phenolic resin versus the ratio of the baseline absorbance measured at 2.95 and 4.45 microns. The absorption band at 2.95 microns is characteristic of the hydroxyl group in the phenolic resin, while the absorption band at 4.45 microns is characteristic

of the nitrile linkage in the Buna-N elastomer. Since the nitrile group constitutes a rather small portion of the Buna-N elastomer a gradual decrease in the intensity of the 4.45 micron band was observed when increasing amounts of phenolic resins were blended with the rubber. Conversely the 2.95 micron band increased rapidly when greater amounts of the phenolic resin were added to the rubber. This was desirable in establishing

61
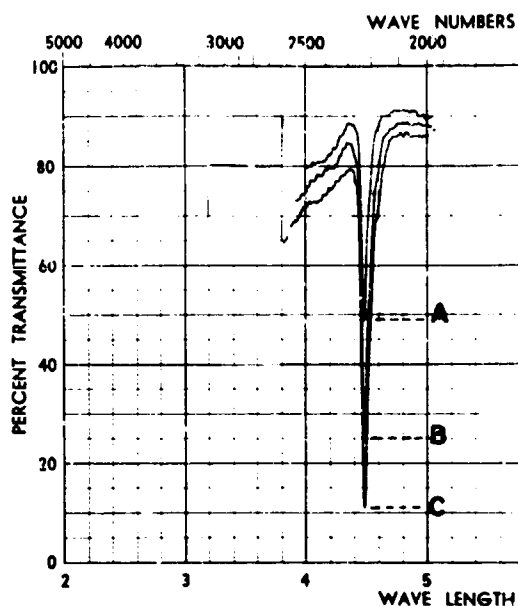
FIGURE 6. Pyrolyzate of Buna-N rubber containing A—19%; B—27.5%; C—35% acrylonitrile.

TABLE I.—Absorbance ratios and percentages of phenolic resin blends in Buna-N rubber

Sample No.	Percent phenolic resin	Absorbance of 2.95 band	Absorbance of 4.48 band	Absorbance ratio	Calibration curve
1	0	0.134	0.564	0.228	Fig. 8
2	0	0.179	0.556	0.322	Fig. 8
3	0	0.324	1.006	0.322	Fig. 8
4	5.5	0.198	0.301	0 658	Fig. 8
5	9.1	0.238	0.260	0.915	Fig. 8
6	16.7	0.359	0.250	1.440	Fig. 8
7	0	0.127	0.263	0.465	Fig. 9
8	0	0.105	0.249	0.422	Fig. 9
9	5.5	0.228	0.396	0.580	Fig. 9
10	5.5	0.232	0.377	0.615	Fig. 9
11	9.1	0.163	0.230	0.710	Fig. 9
12	9.1	0.158	0.224	0.703	Fig. 9
13	16.7	0.373	0 344	1.05	Fig. 9
14	16.7	0.380	0.350	1.08	Fig. 9
15	33.3	0.532	0.240	2.22	Fig. 9
16	33.3	0.544	0.232	2.34	Fig. 9
X		0.308	0.168	1.84	Fig. 9
X		0.321	0.176	1.83	Fig. 9

ratios of the two bands used in plotting the calibration curves.

The absorbance of the bands at 2.95 and 4.48 microns was computed according to the formula

$$A = Log_{10} \frac{I}{I}$$

The absorbance values and the percent phenolic resin blends for the samples analyzed are shown in Table I. The plot of the absorbance ratios of these bands, computed by the formula

$$P = \frac{\text{Absorbance of the 2.95 micron band}}{\text{Absorbance of the 4.48 micron band}}$$

against the percent phenolic resin blends are presented graphically in Figures 7 and 8.

The plot in Figure 7 constitutes the calibration curve for Buna-N polymers blended with 0 to 16 percent phenolic resins. A fairly straight line relationship was obtained for this set of data in the range shown. With higher percentages of phenolic resins in Buna-N rubber a straight line relationship is no longer observed. The working curve prepared from the spectra of Buna-N polymers blended with 0 to 33 percent phenolic resins is shown in Figure 8. A similar curve was obtained from the spectra of the same pyrolyzates recorded on a Model 21, Perkin-Elmer Spectrophotometer.

None of the calibration curves prepared for the Buna-N phenolic resin blends terminated at the origin of the coordinates, but rather at an absorbance reading of 0.3 to 0.5. The intercept indicated the presence of absorption in the 2.9 micron region in the Buna-N elastomers not blended with phenolic resins, which is, indeed, observed in the spectra of Buna-N rubber presented in Figure 5 A.

An absorption band at 4.48 microns, characteristic of a nitrile linkage, present in Buna-N polymers containing approximately 19, 27.5 and 35 percent acrylonitrile was used to construct a working curve to determine the percentage acrylonitrile in acrylonitrile butadiene co-polymers. The absorbance values for the 4.48 micron blend computed by the base-line technique, together with the known percentage range of acrylonitrile in the Buna-N elastomers used in this determination are shown in Table II. A plot of the absorbance at 4.48 microns versus acrylonitrile content of Buna-N elastomers is shown in Figure 9.

TABLE II.—Absorbance ratios and percentages of the acrylonitrile constituent in butadiene-acrylonitrile co-polymers

Sample No.	Type of elastomer	Range of acrylonitrile given (percent)	Average percent of acrylonitrile	Absorbance of 4.48 micron band
1	Paracril 18	18–20	19	0.259
2	Paracril 26	28–29	27.5	0.537
3	Paracril 35	35	35	0.870
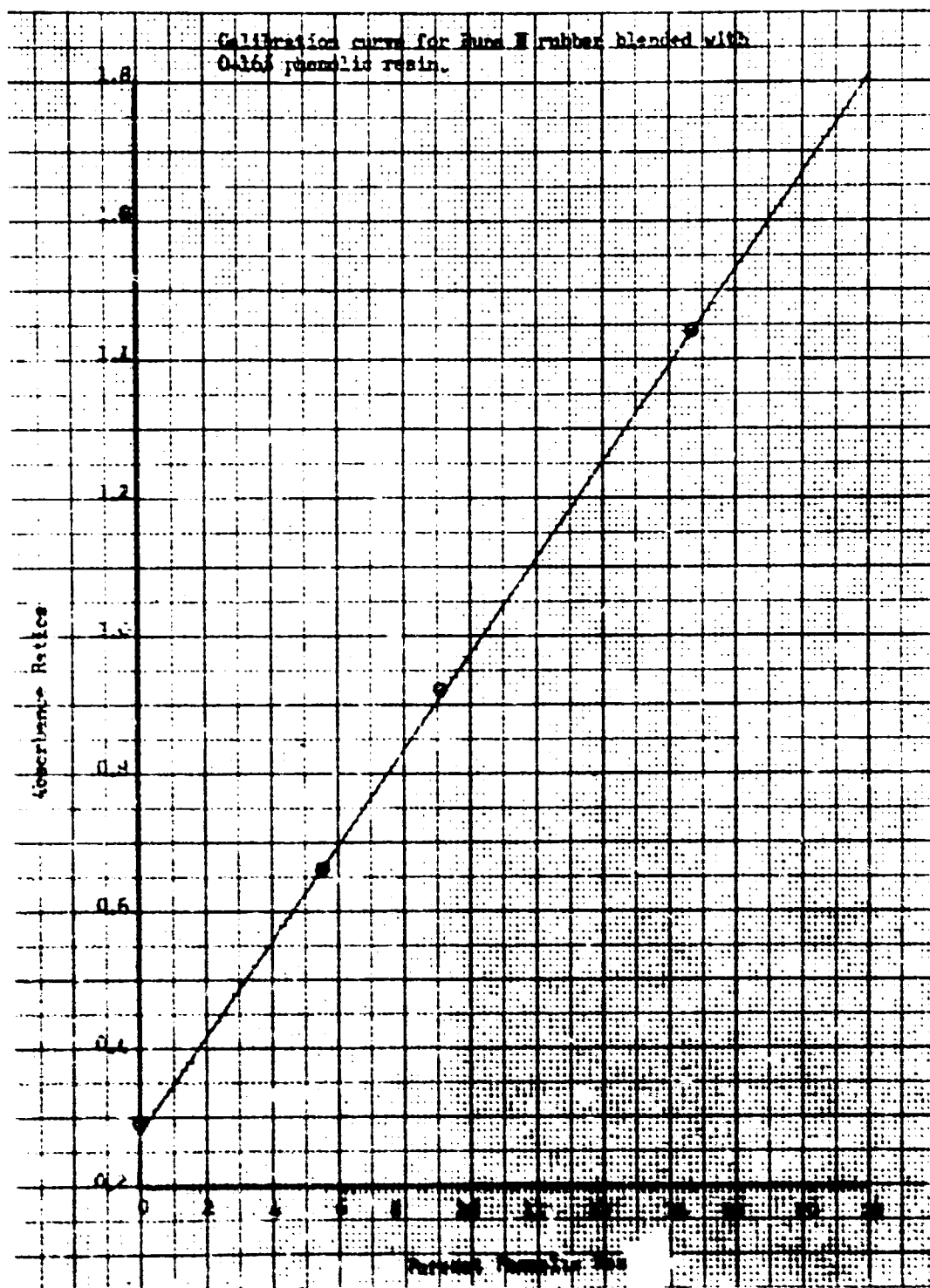
Figure 7—Calibration curve for Buna-N rubber blended with 0.16% phenolic resin.
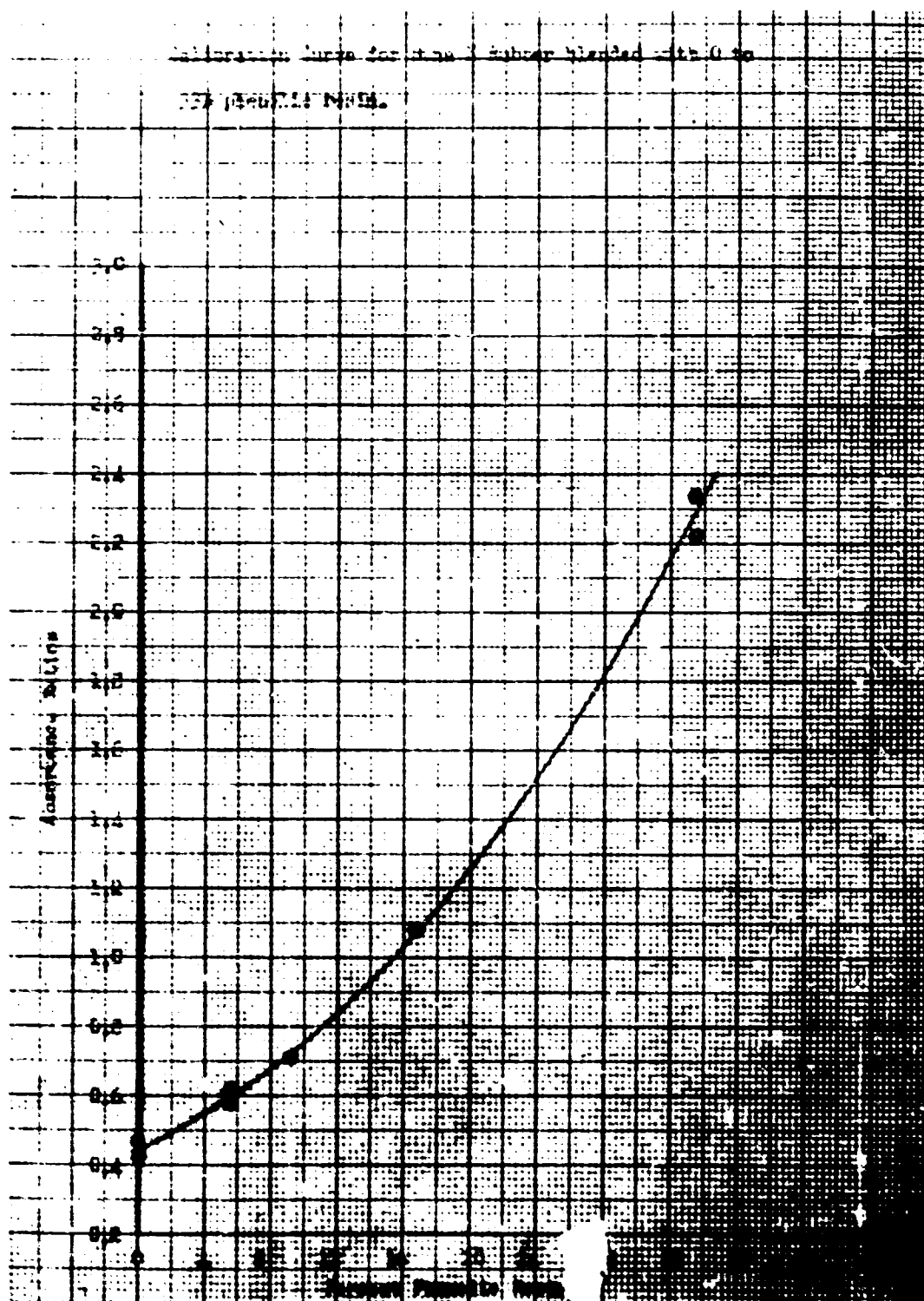
Figure 8 — Calibration curve for Buna-N rubber blended with 0.33% phenolic resin
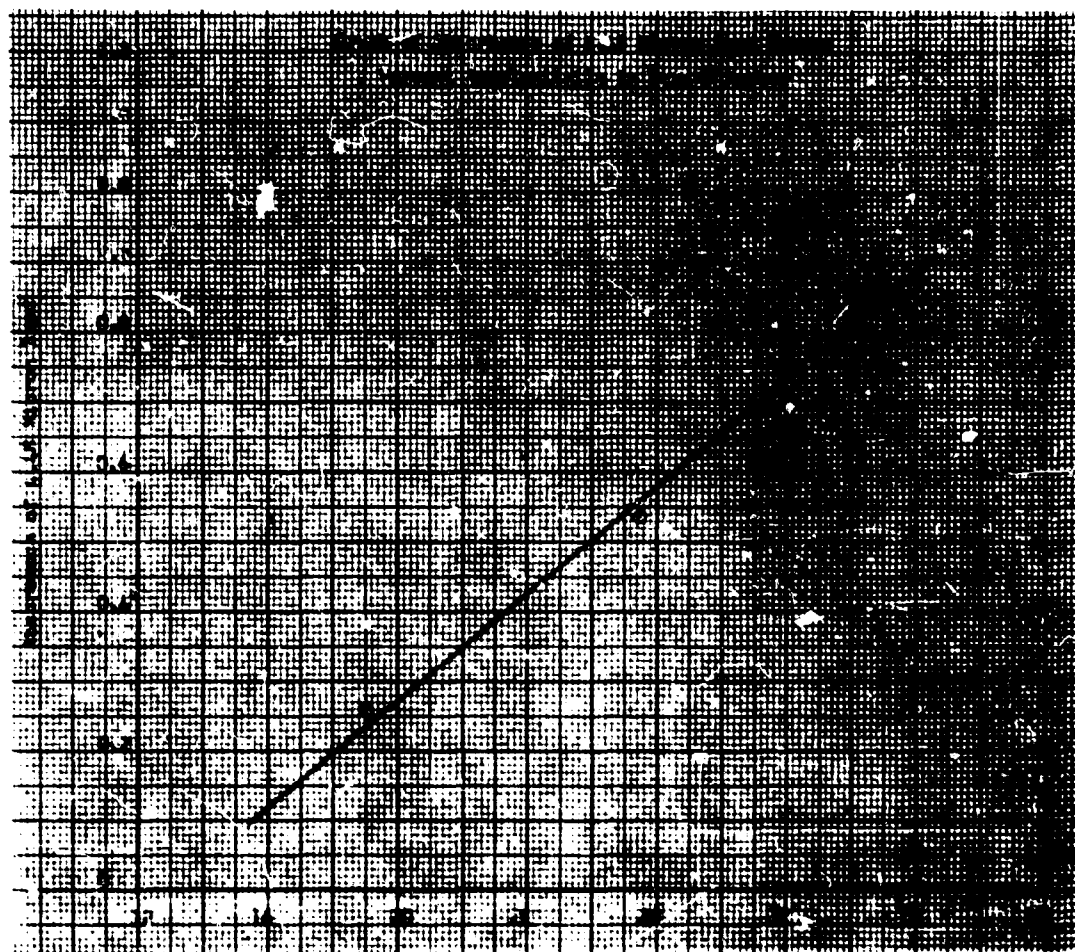
FIGURE 9. Graph of absorbance of 4.48 micron band versus percent acrylonitride in Buna-N rubber

DISCUSSION OF RESULT

This report demonstrates that polymer blends and co-polymers will yield unique and reproducible pyrolyzates, and that their infrared spectra reflect the composition of both the polymer blends and the co-polymer ratios. No exhaustive treatment has been given to evaluate the accuracy of the quantitative results. Observation of the scattering of points on the working curves for Buna-N phenolic resin blends makes it appear that the phenolic resin content of such blends can be estimated with ±2 percent in the 0–33 percent range. An unknown sample of vulcanized Buna-N phenolic resin blend was analyzed by this method on a Baird Infrared Spectrophotometer and a Perkin-Elmer Model 21 Spectrophotometer. The results of these analyses for the phenolic resin content differed by less than one percent. The accuracy of the method is, of course, dependent on the use of essentially identical polymers and compounding ingredients in the unknown and known blends employed in preparing the working curve.

The nominal value of acrylonitrile content of several commercial Buna-N polymers was used to construct the working curve shown in Figure 9. In each case the average value for the normal range of acrylonitrile content was used. This calibration curve appears at least adequate for the identifying commercial Buna-N polymers of varying nitrile content. Even with a nominal value of acrylonitrile cont.   sed as standards in plotting the working curve   acrylonitrile content in the butadiene co-poly.   can be estimated within ±3 percent in the 18 to 40 percent range. The accuracy of the method described does not compare

65

favorably with that of existing methods for the quantitative analysis of polymers. Its advantage lies in its application to systems which cannot be handled by existing methods and in its speed and convenience in determining semiquantitative results which are often sufficient for the use of rubber compounders.

Section 2.

SEMIQUANTITATIVE DETERMINATION OF THE NONCOMBUSTIBLE MATERIALS IN BUNA N-PHENOLIC RESIN BLENDS

A quantitative analysis of the noncombustible material was conducted on several of the phenolic blended Buna-N rubber samples to establish the possibility of determining the ash content along with the elastomer. In the samples analyzed the residue remaining in the combustion tube was transferred to a container and weighed. Inasmuch as the residue of the carbon black and inorganic materials retained the shape of the original rubber sample, it was easily removed by gently tapping the combustion tube. The results of these analyses are shown in Table III.

TABLE III.— *Results of the analysis of the residue in Buna-N phenolic resin blends*

Sample No.	Calculated wt. percent residue	Wt. percent residue found	Difference +
1. –87	40.9	43.9	3.0
2. –88	40.0	43.6	3.6
3. –89	38.1	41.0	2.9
4. –89	38.1	40.8	2.7
5. –XL	33.8	37.1	3.3
6. –XL	33.8	37.7	3.9
Unknown	(38.6)	41.8	....

$$\% \text{ Residue} = \frac{\text{Wt. of Residue} \times 100}{\text{Wt. of Rubber Sample}} - 3.2\%$$

The weight percent of the noncombustible residue found in each determination was somewhat higher than the calculated values. This was expected, inasmuch as a small amount of charring occurred in the combustion tube, particularly at the ground glass connections, during pyrolysis of the sample. Of the six Buna-N phenolic resin blends determined the deviation in the differences of the calculated and measured percentages of noncombustible ash ranged from

2.7 to 3.9 percent. The average value of the differences in the measured and calculated ash content was 3.2 percent. Although the results were somewhat high in each case, the consistency of the values permits the use of a factor so that a semiquantitative estimation of the noncombustible material in the rubber can be adequately made. Although the technique does not compare favorably with existing methods of analyzing noncombustible materials in cured and compounded elastomers quantitatively, its advantage lies in the speed and convenience of determining the residue simultaneously with polymer blends or co-polymer ratios.

Section 3.

CONCLUSIONS

A semiquantitative method of determining polymeric blends and co-polymer ratios in elastomers by the infrared spectra of their pyrolyzates has been established. The applicability of the technique was established through the analysis of blends of phenolic resins in Buna-N rubber, and by determining the percentage acrylonitrile in butadiene acrylonitrile co-polymers.

Although no exhaustive study was made to evaluate the accuracy of the quantitative results, the scattering of points on the working curve for Buna-N phenolic resin blends indicates that the phenolic resin content can be estimated within ±2 percent within the 0–33 percent range investigated. The calibration curve for the determination of acrylonitrile in butadiene co-polymers appears at least adequate for the differentiation of commercial Buna-N co-polymers of varying nitrile content.

A semiquantitative method of determining the noncombustible materials in Buna-N rubber simultaneously with the phenolic blends and co-polymer ratios was also perfected. By using a factor the total noncombustible material can be estimated within ±5 percent.

Conducting the pyrolysis under reduced pressure and with controlled temperatures gives a more reproducible pyrolyzate, with less charring than those prepared at atmospheric conditions using a Bunsen burner. The technique used here partially separates the phenolic resin from the Buna-N rubber permitting a more effective identification of the individual constituents in the elastomer. The technique isolates the inorganic materials

from rubber in a form particularly suitable for spectrographic and X-ray analysis.

BIBLIOGRAPHY

1. Harms, D. L., *Identification of Complex Organic Materials*, Anal. Chem. 25, 1140 (1953).
2. Kruse, P. F., and Wallace, W. B., *Identification of Polymeric Materials*, Anal. Chem. 25, 1156 (1953).
3. Dinsmore, H. L., and Smith, D. C., *The Analysis of Natural and Synthetic Rubber by Infrared Spectroscopy*, Report No. P-2861, August 1946, Naval Research Laboratory, Washington, D.C.
4. Heigl, J. J., Bell, M. J., and White, J. U., Anal. Chem. 19, 293 (1947)

APPENDIX I

Advantages of Preparing Pyrolysis Products Under Controlled Conditions for Qualitative Analysis

The technique of preparing pyrolyzates under controlled conditions is important in the qualitative analysis of commercial mixtures and polymer blends because the organic materials, are removed from the noncombustible residue, and in many instances, partially separated into individual constituents. The technique, therefore, allows the identification of the organic constituents present in the mixture. Pyrolyzates of Buna-N phenolic resin blends collecting in the dry ice trap were found to be richer in phenolic resin content than those collecting in other regions of the combustion assembly, making it possible to identify both the polymer blend and the base elastomer. Other commercial mixtures such as lacquers, paints, adhesives, etc., containing, in addition to carbon black and inorganic fillers, a variety of organic constituents might be sufficiently separated to allow their identification in one operation. Under conditions of reduced pressure and lower temperature a more reproducible pyrolyzate with less cracking or breaking down of the polymers into lower molecular weight components appears possible. Although more time is required to prepare the pyrolyzates under controlled conditions the partial separation of the organic materials with less charring makes this technique attractive from a qualitative aspect.

DAVID ROLLER

An Electrical Conductance Test Method for Measuring Corrosion

1955

69

70

DAVID ROLLER

David Roller was born March 20, 1930, in New Brunswick, New Jersey. He was awarded a B.S. in chemistry at the Massachusetts institute of Technology in 1950. From 1950 to 1951, he was employed by the General Aniline and Film Corporation; and, from 1951 to 1954, he was associated with the Freeport Sulphur Company Freeport, Texas.

Although he had received a direct commission as second lieutenant in the United States Air Force in 1951, he enlisted in the Air Force in 1954 and was assigned to the Materials Central. At the time he received the Cleary Award in 1955, he held the rank of Airman/2C. At the expiration of his military tour in 1956, he remained with the Materials Central in a civilian capacity until June 1959. In 1959, he joined the Magna Corporation, Anaheim, California, where he is currently Manager, New Devices, Research and Development Laboratories.

Mr. Roller is a member of the American Chemical Society, the American Ceramic Society, and the National Association of Corrosion Engineers. He is technical program chairman for the National Meeting of the National Association of Corrosion Engineers. In addition to winning the Cleary Award in 1955, he was the recipient of the Air Force "Outstanding Airman's Award", and in 1956 received the Air Force Commendation Ribbon Award. He is listed in the tenth edition of American Men of Science.

BIBLIOGRAPHY

Thin Metal Film Corrosion Indicators. Corrosion, 14(6): 21-25, June 1958.

With W. M. Spurgeon. Coatings for Protection Against HEF Combustion Products. Paper presented at the Fifteenth Annual National Association of Corrosion Engineers Conference, Chicago, Illinois, March 1959. Published as WADC Technical Report no. 59-11, January 1959.

With C. R. Andrews. Effect of Molten Boron Oxide on Selected High Temperature Alloys. Corrosion, 15(2): 49-60, February 1959.

Detection and Measurement of Corrosion. Paper presented at the Air Force Material Command Corrosion Conference on Aircraft and Missiles. Published in the conference report of the same title, April 1960.

With G. H. Rohrback. Development of Thin Metal Film Corrosion Indicators. Corrosion, 16(8): 103-110, August 1960.

With W. R. Scott, Jr., H. S. Preiser and F. K. Cook. Corrosion Measuring Probes for Marine Applications. Corrosion, 17(10): 107-113, October 1961.

With W. R. Scott. Detecting and Measuring Corrosion Using Electrical Resistance Techniques. Corrosion Technology, 8(2): 71-76, March 1

An Electrical Conductance Test Method
For Measuring Corrosion

D. ROLLER

PURPOSE

To investigate a sensitive test method for determining the rate and amount of corrosion of a metal specimen by measuring the corroding specimen's change in electrical conductance.

FACTUAL DATA

1. Theoretically, the amount and rate of corrosion of a metal can be determined by measuring the change in electrical conductance of the corroding specimen. Since the electrical conductance of a metal depends on its cross-sectional area, a decrease in thickness or cross sectional area of a specimen due to corrosion may be evaluated from the corresponding decrease in conductance. Measuring the rate of corrosion of a metal specimen by measuring the change in electrical conductance has many advantages over older, more conventional, methods such as weight loss, gasometric, or visual means. A discussion of the theoretical aspects of the method is found in Appendix I, Section 1. Appendix I, Section 2 discusses the numerous advantages and the limits of applicability of the electrical conductance method in comparison with other, more conventional, methods.

2. Essentially this method depends on passing a known amount of current through a metal specimen, measuring the voltage drop across the specimen, and then calculating the conductance. The necessary manual or automatic recording equipment for making these measurements is described in Appendix II.

3. Thin ribbon specimens in which the width is proportionately very much larger than thickness

have been found most convenient because of their greater sensitivity and ease of mathematical calculation. Other possible types of specimens could be made from long metal wires or by use of metal deposition techniques. Metal specimens can be placed in almost any environment, either in a laboratory or under actual field conditions. The necessary electrical measurements could be made without moving the specimens by use of either manual or automatic recording equipment. Appendix III describes the use of various metal specimens and corrosive environments possible with this method.

4. The method of making measurements, either manually or with automatic recording equipment was not difficult but the amount of raw data generated was large. To make reliable conclusions, proper techniques of experimental design were necessarily combined with appropriate statistical methods for evaluating test results. Techniques of experimental design and the methods of analyzing experimental data used are shown in Appendix IV and V.

5. To determine with what accuracy and precision corrosion rates could be measured, pure magnesium ribbon specimens were placed in various corrosive environments. These tests showed that reproducible results could be obtained which agreed well with theory and with results available by other techniques. These tests are described in Appendix V.

6. Further test programs have been initiated to aid other research and development investigations. These programs include development of suitable inhibitors in fuming nitric acid, development of new surface treatments for magnesium

alloys, and determining the effect of humidity on the corrosion rate of metals. These future programs are discussed in Appendix VI, Sections 1, 2, and 3.

7. A literature survey indicated that previously a number of investigators have used this principle for the solution of special problems in corrosion research. Appendix VII contains a bibliography of technical articles describing previous investigations in which corrosion rate studies were made by observing the change in electrical conductance of the specimen.

CONCLUSIONS

1. Both theoretically and in practice, measuring the rate of uniform corrosion of a metal specimen by measuring the change in conductance of the specimen will give results of practical significance. The primary advantages of this method over older, more conventional, methods of measuring corrosion are numerous. When measurements are made specimen cleaning is unnecessary; it can be used in any corrosive environment; and measurements are simple, rapid, and precise when corrosion is generally uniform. The method is particularly adaptable to classifying similar media or metals according to their relative corrosivities or corrosion resistance.

2. Statistical analysis of initial tests as described in Appendix V showed that results obtained by this method were comparable to results obtained by other, more conventional, corrosion methods. The equipment used in these tests can accurately measure the change in conductance of the metal specimens.

RECOMMENDATIONS

The Materials Laboratory, Directorate of Research (WCRTH-3), will make further study of the application of this method to measuring corrosion rates as outlined in Appendix VI.

APPENDIX I

Section 1.

The electrical conductance method for measuring the amount and rate of corrosion of a metal utilizes the fact that metals and alloys have, in general, much higher specific electrical conductance than their corrosion products. The electrical conductance of any metal or alloy, at any fixed temperature, is a function of its three dimensions

as shown below where C = Conductance; L, and A are the

$$C = \frac{A}{\rho L} \qquad (1)$$

metal's length and cross sectional area respectively; and ρ is the resistivity, a constant dependent only on the metal and temperature. For simplicity of calculation, a metal specimen is used such that its length is very much greater than its width or thickness, i.e., a ribbon. At any fixed temperature and using a ribbon specimen (assuming length to be constant)

$$\frac{C}{A} = \frac{1}{\rho L} = \text{Constant} \qquad (2)$$

Differentiating this equation with respect to time (t) gives the following equation

$$\frac{C \frac{dA}{dt} - A \frac{dC}{dt}}{A^2} = 0 \qquad (3)$$

which when rearranged shows the relationship between the change in cross-sectional area with time as a function of change in conductance with time

$$\frac{dA}{dt} = \frac{A}{C} \cdot \frac{dC}{dt} \qquad (4)$$

It should be noted that the ratio of (A/C) is a constant and does not vary with time. For a metal specimen in the form of a long ribbon, dA/dt, the reduction in cross-sectional area with time is, by definition, the rate of corrosion of the metal. On integration, Equation 4 shows that a straight line relationship should exist between log conductance and log area. The decrease in cross-sectional area by corrosion

$$\text{Decrease in area} = \frac{C_o - C_1}{C_o} \times A_o \text{ (in inches)}^2 \qquad (5)$$

The relationships determined above can be used to measure the decrease in uniform thickness by corrosion by assuming the ribbon width to be constant. By similar calculations it is also possible to relate weight loss and change in conductance of a corroding metal specimen. The specimen weight is proportional to its dimensions where L,

$$\text{Weight} \quad \text{Density} \times (L \times W \times T) \qquad (6)$$

W, and T are the specimen's three dimensions and

74

D is the metal's density, a constant depending only on the metal and its temperature.

Solving for the area A, substituting in Equation 1., and canceling,

$$\frac{C}{\text{Weight}} = K \qquad (7)$$

where $K = \frac{1}{\rho \times D \times L^2}$ in appropriate units. Using the same techniques as before, it can be shown that the change in conductance has a similar relationship to the change in weight as to the change in thickness or cross sectional area. The use of conductance, the reciprocal of resistance, has provided an exact relationship between rate of corrosion and change in conductance with time. Plotted graphically, the change in conductance of a metal specimen is directly proportional to its change in thickness and its change in weight, where as resistance change is not. If resistance is used in deriving these equations it is necessary to assume that the initial resistance and thickness are equal to the resistance and thickness over the time interval in which measurements are made, that is, that

$$R_o \cong R_t \text{ and } T_o \cong T_t \qquad (8)$$

and this is only an approximation, true up to about a 20 percent change in resistance

If wire specimens were used in place of ribbon specimens, the theoretical equations relating corrosion and conductance change would be similar. A problem with wire specimens is providing for "potential" and "current" leads without introducing uncontrollable errors due to heat treating or cold working of the metal at the junction points. Appendix III is a more detailed discussion on metal specimens as used in the electrical conductance method.

Section 2.

There are a number of methods for determining the amount or rate of corrosion of a metal, each method having its own particular advantages and limitations. The major methods, including certain qualitative aids, are: visual observations, loss or gain in weight, gas evolution or absorption, changes in physical properties (such as tensile strength), optical methods, and electrical measurements (such as electrometric, electrochemical, and electrical conductance methods).

Because the reaction mechanisms associated with corrosion are complex and because of the diverse environmental conditions that may be met, there are many inter-related factors of importance in determining the reproducibility and accuracy of experimentally determined corrosion rates. In general, these factors involve the metal surface, the corrosive environment, and the method of measuring corrosion. The best method is the one which eliminates or reduces random and uncontrollable errors.

The electrical conductance method has many advantages over other methods used for determining uniform corrosion rates. Essentially, it eliminates the need to clean or handle the the corroding specimen prior to measuring the amount of corrosion, thus reducing a major source of error.

Electrical conductance measurements are analogous to "electrical weighing", that is, they are sensitive only to the amount of metal which remains uncorroded. The electrical conductance of the metal specimen is unaffected in most cases by scale, dirt, or other corrosion products. Thus, the sample could be placed in almost any corrosive environment. either in the laboratory or under service conditions; and one need only measure the change in electrical conductance with time to determine the corrosion rate. The method is easily adopted to produce a highly sensitive, continuous record of the progress of corrosion of a metal specimen in situ. It is particularly adaptable to measuring very low corrosion rates where removal of corrosion products might introduce error. The electrical measurements are simple, rapid, and precise; they require no apparatus not ordinarily available.

The method is best applied where the corrosion is reasonably uniform and free of an excessive number of large pits. This is also true of other methods, such as weight loss, which quantitatively measure corrosion rates. If the specimen corrodes fairly uniformly, the reproducibility is, in general, much better than if the attack occurs only at a few discrete points.

As with data from any laboratory test, considerable caution must be exercised in interpreting results in terms of service performance. There is such a wide variance in the behavior of metals in different types of environments that no one or even several accelerated laboratory tests can possibly be strictly interpreted in terms of actual service of such material

APPENDIX II

Measurements used to determine the change in electrical conductance of a specimen consist of passing a known amount of current through the metal, measuring the voltage drop across the specimen, and calculating the conductance using Ohm's law. The measuring circuits required no apparatus not ordinarily available in the laboratory. The primary parts of the circuits consisted of a potentiometer, a current source, variable and standard resistors, a constant temperature bath, and such electrical components as switches, ammeters, and junction boards. Figure 1 is a general pictorial diagram of the measuring circuits; Figure 2 is a schematic drawing of the actual manual circuits used in this investigation; and Figure 3 is a schematic drawing of a continuously recording electrical circuit. Figures 4, 5, 6, and 7 are pictures of the equipment and specimens used in this initial investigation

Current was supplied by a 6 volt, 3 cell, acid storage battery which appeared to be a fairly stable current source. The amount of current is determined by using a 1.00 ohm standard resistor, immersed in oil, and measuring the voltage drop using the potentiometer. The current was then directly equivalent to the voltage drop. Since the amount of current (0.3 to 0.5 amps) was small, the battery did not need frequent recharging, however, a separate recharging circuit was connected to the battery by means of switches. If a high grade electronic DC voltage source is available, a large constant resistor may be placed in series with the specimens. This would provide a fairly stable current source, independent of changes in resistance of the specimen. The current from the battery was adjusted by use of a variable carbon pile resistor. For continuous measurements a metal specimen in a noncorroding media (such as benzene) was placed in the thermostatically regulated bath and used as a standard resistor. In this manner, any fluctuation in temperature or current could be compensated for when calculations were made.

To reduce the possibility of electrically heating the metal specimen, the current used was usually less than 0.35 amperes. This electrical heating effect is the heat in calories developed in a circuit by an electric current of I amperes flowing through a resistance of R ohms for a time, t, seconds, related as shown below

$$\text{Heat (in calories)} = \frac{RI^2t}{4.18}$$

76
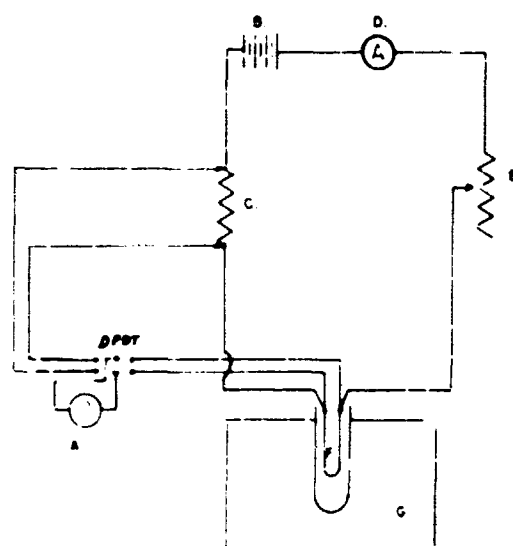
A POTENTIOMETER
B. STORAGE BATTERY
C. STANDARD RESISTOR, 1.00 OHM
D. AMMETER
E. VARIABLE RESISTOR
F SPECIMEN
G. THERMOSTAT

Figure 1   Pictorial diagram of electrical circuits.

The temperature rise, ΔT which occurs in the metal specimen when electrically heated is equal to the heat in calories divided by the mass of the specimen in, m, grams times the specific heat of the specimen, s, or more properly, the thermal capacity of the specimen. This relationship between temperature rise, current, and time is shown below.

$$\Delta T = \frac{RI^2T}{(4.18)sm}$$

Theoretical calculations show that ordinarily temperature changes no greater than 0.25° C should occur from electrical heating effects during the few seconds needed to take a reading. Since most metals have a small resistance change per degree centigrade, the effect of electrical heating of the specimen should be small. To further reduce this source of error, during each test, specimens are placed in a large constant temperature bath

A Leads and Northrup Company K-2 potentiometer was used to measure the voltage drop across the standard resistor or the metal specimen This very sensitive instrument can measure with
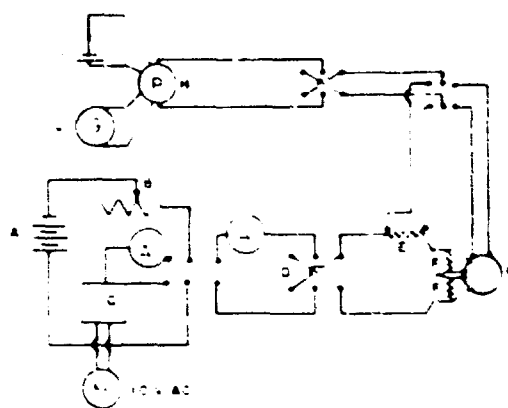
a BATTERY, 6V
b VARIABLE CARBON PILE RESISTOR
  BATTERY CHARGER
c REVERSING SWITCH
e STANDARD 100 OHM RESISTOR
f TEST SPECIMENS
g SELECTOR
h POTENTIOMETER
i STANDARD CELL
  GALVANOMETER

A BATTERY
B VARIABLE RESISTOR
C TEST SPECIMENS
  AMMETER
E MERCURY SWITCH AND COIL
F TIMER
  RECORDER, 10-20 MV RANGE
H SELECTOR, 12 POINT

FIGURE 2   Electrical circuits manual equipment

FIGURE 3   Electrical circuits automatic equipment

great accuracy potentials up to 1.6 volts. A sensitive external galvanometer was used to adjust and balance the potentiometer circuit. A potentiometric circuit was used to reduce any error associated with circuit contact resistance points. By having separate "current" and "potential" leads on a specimen and measuring both the current and voltage drop across the specimen, the effect of any resistance in the circuit other than specimen resistance was removed.

Two constant temperature baths were found useful. The large bath, 18 inches by 36 inches inside could hold 36 specimens at one time and could be conveniently used for long term tests in conjunction with the automatic recording equipment. Equipped with agitators, heating elements and thermo-regulators, it was capable of attaining temperatures up to 100°C with a temperature control of better than ±0.15°C. For manual operation, specimens could be placed in specimen holders attached to short leads which were mounted permanently to terminal boards and connected by cable to a switch box. Thus, by proper switching it was possible to measure the electrical conductance of any specimen in the large bath.

A small round glass jar, 12 inches in diameter, was used for special tests. The bath could attain temperatures of 100°C and by using a sensitive bimetallic thermoregulator, temperature control of ±0.01°C could be attained. Seven specimens could be placed in the bath at once, measurements being made manually. Normally, the bath was used when the corrosive media was conductive and electrical measurements had to be made by placing the specimens in a nonconducting media.

Self contained fully automatic electrical recording equipment has been designed and installed to measure the change in voltage drop of specimens in their particular corrosive environment. A Minneapolis-Honeywell 12 point automatic recording potentiometer was used. It has a range of 10 to 20 millivolts with a sensitivity of 0.15 millivolts. The instrument measured the electrical resistance of twelve metal specimens consecutively. This would include several specimens in benzene being used as standard resistors. A timing circuit was developed to increase flexibility of the equipment. For example, recorder could be adjusted to measure the potential across each of the twelve specimens, sequentially, three times, then it

FIGURE 4.

shuts off for a period adjustable up to two hours
before repeating the operation. By using a suit-
able cam mechanism, the instrument always
stopped and started at the same recording index.
The length of time during and between each oper-
ation could be accurately calculated. A battery
similar to that used with the manual equipment
was used as a current source. An ammeter and
variable carbon pile resistor were used to adjust
qualitatively the current. For mobility, the
recorder and supplementary equipment were
mounted on wheels in a metal frame. Nine foot
electrical leads were provided for each specimen,
all twelve specimens being connected in series.
Small alligator clamps at the end of each lead

could be conveniently attached to the current and
potential leads of a specimen.

APPENDIX III

Theoretically, specimens of any dimension for
which electrical conductance measurements can
be made could be satisfactorily used with this
method. It was convenient to use metal specimens
in the form of long ribbons in which thickness was
proportionately very much smaller than width.
This was done to achieve increased sensitivity and
simplicity of mathematical calculation. The lim-
its of application of this method arose mostly
from the use of these thin specimens, which were
preferably less than 0.020 inch thick.

Most metals and alloys may be obtained com-
mercially as thin ribbon, sheet, or foil; however,
the cost of obtaining some metal alloys in such
form may be prohibitive. Cast metal specimens
could not be used and the very nature of the speci-
mens made them somewhat fragile and easily bent.
There is also the chance of introducing uncon-
trollable errors from the hot or cold rolling, bend-
ing, and cutting of the specimens.

Typical corrosion specimens used for the elec-
trical resistance method are shown in Appendix
II, Figure 7. The specimens were approximately
15-inch by ¼ inch strips with a thickness between
0.005 and 0.015 inch. Slits or "tails" of approxi-
mately 4 inches from either end served as "po-
tential" and "current" leads. By using separate
"current" and "potential" leads, the effect of elec-
trical resistance at the specimen contact points
was removed. Furthermore the exact dimensions
of the specimens could be measured. The actual
specimen length was from the point of one juncture
(formed by the meeting of one set of leads) to the
other. Therefore when duplicate specimens were
used, the resolution of the method was limited
only by the reproducibility of the electrical read-
ings.

The width and length of the specimens can vary
over a wide range but the conductance must be of
an order of magnitude which can be precisely
measured. Specimens should be cut either with a
jig, scissors, or a sharp knife. It was found best
to have a jig which permitted cutting many identi-
cal specimens. This uniformity between speci-
mens facilitate electrical measurements and
mathematical c   arisons made between tests.
To further insu niformity, surface cleaning of
each specimen prior to testing was accomplished
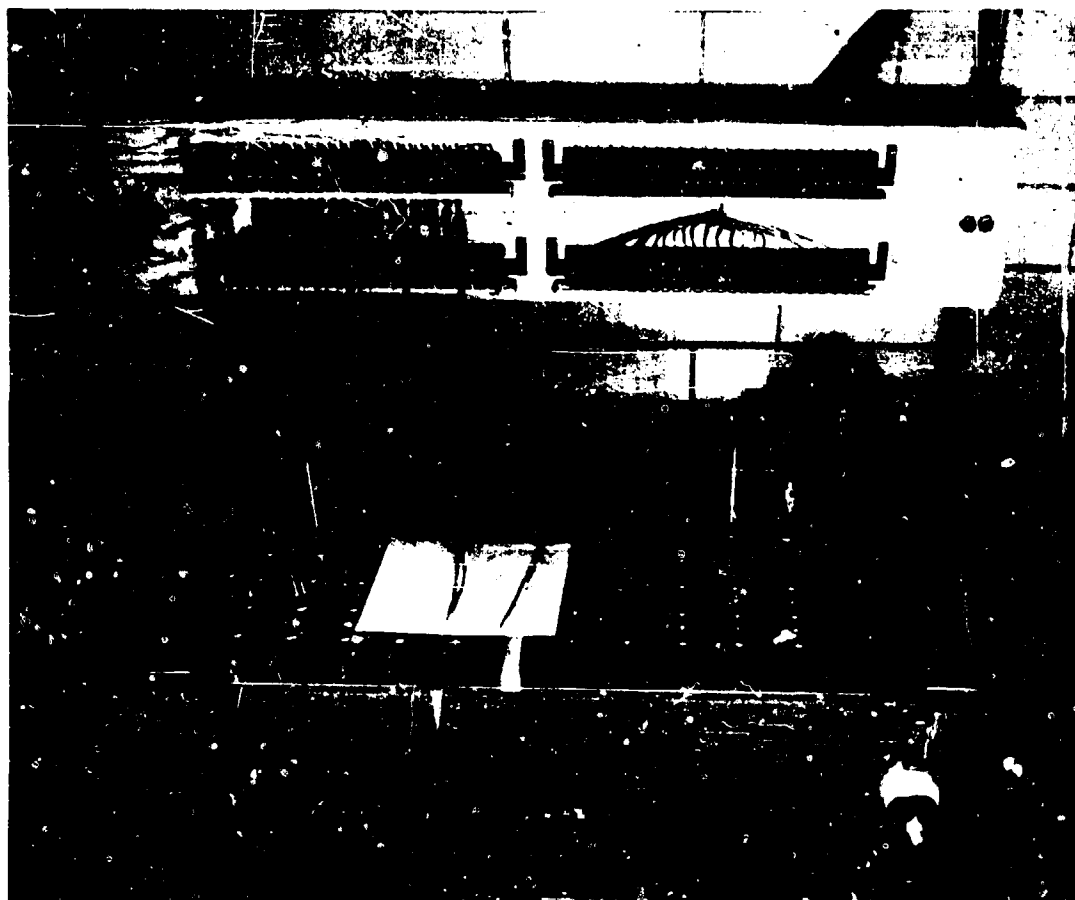
FIGURE 5.

by using a chemical cleaning or pickling treatment. Abrasives or polishes are unnecessary for this test method.

For experiments at high temperature, it would be necessary to determine whether changes in conductance might have resulted from the effect of heat treatment instead of from the reduction in specimen thickness due to corrosion. Extraneous heat treatment effects can be eliminated by making corrections from the results of a test run, or by eliminating these effects by annealing the specimens. Where test temperatures are near room temperature, this effect can be usually neglected.

Corrosion products are rarely conductive to electricity; however, such products would partially compensate for the loss in conductance of the specimen due to corrosion. In such cases, as formation of some sulfide products, it is likely that a correction factor can be obtained and used advantageously. The same is true of measure-ments made in conductive test solutions. A correction can be made for the conductivity of the solution cr the specimen .: its holder can be placed in a nonconducting solution (benzene), electrical measurements made, and the sample replaced in its corrosive environment, proper allowance being made for time in the calculations.

Other types of test specimens could also be quite useful in conjunction with this method. It should be possible to use small diameter wires as specimens and connect "tails" to act as "potential" and "current" leads. The use of metal deposition to furnish ribbons on glass or plastic is also possible. Such specimens should be highly sensitive to small amounts of corrosion and could be used as indicators of corrosive environments such as are found in closed contain At present, the use of metal deposition techni are being investigated to determine whether k films up to approximately 50,000 A°, can be evenly distributed in

79
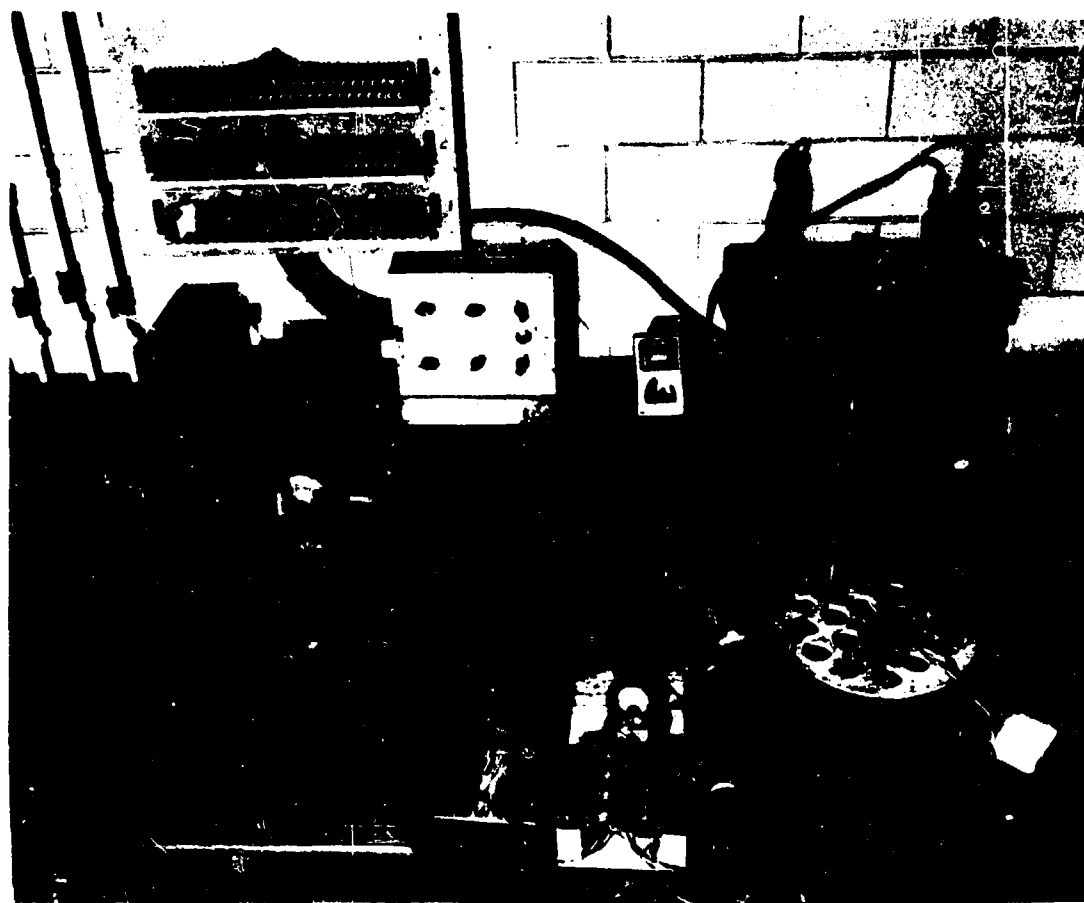
FIGURE 6.

suitable form on a glass or plastic specimen. In using such specimens, however, caution must be observed in interpreting results in terms of field conditions.

Specimens could be placed in almost any corrosive environment either in the laboratory or in actual field conditions. For laboratory accelerated corrosion tests, specimens could be placed in salt spray cabinets, alternate or total immersion equipment, humidity cabinets, or other similar corrosive environments. For field tests, samples in specimen holders could be placed in any environment where corrosion occurred. Continuous measurements of the sample's change in electrical resistance could either be made with portable equipment in the field or the specimen in its holder could be taken to the laboratory, measurements made, and the specimen returned to its original environment.

APPENDIX IV

A series of initial tests were made to determine the applicability of the electrical conductance method. For each test normally four measurements of current and voltage were made alternately, at any predetermined time. Over long time intervals and with low corrosion rates, large amounts of raw data were generated. From this data, calculations were made to determine the amount and rate of corrosion of the metal specimen as outlined in Appendix I, Section 1. Because differences between metals, treatments, and corrosive environments were usually small, it was necessary to resor   statistics to determine if real differences ex   .

The data from each test was first plotted to determine the best fitting straight line. Since

80

UNCORRODED CORRODED   UNCORRODED CORRODED

PERMANENT LEADS   REMOVABLE LEADS

MAGNESIUM RIBBON SPECIMENS IN TWO

TYPES OF HOLDERS

FIGURE 7.

81

the mechanisms of corrosion and film inhibition are fundamentally complex, it was expected that curves of the form

   a. Conductance $= a + b$ (Time)
   b. Log conductance $= a + b$ (Time)
   c. Log conductance $= a + b$ (Log time)

where "a" is the intercept, "b" is the slope of the line and both are calculated constants, would be necessary to obtain good estimates of the rate of corrosion as a function of time. Theoretical justification for using relationships of this type are found in the derivation of equations in Appendix I, Section 1 and from a knowledge of reaction kinetics. Straight line relationships were necessary in order to statistically compare corrosion rates between similar tests.

Regression analysis presented a unique way to determine the best straight line function to fit the experimental data. The principal of Least Squares was used to determine the best straight line to fit the data with an estimate of the variation of the data from the line. The correlation constant, r, is a measure of the variation of the data from the regression line. Assuming positive slopes, it can vary from zero to one, where one is perfect correlation. By determining which function of conductance versus time gave the best straight line with the least variation of the data from the line, "b", the slope of the line, the change of conductance with time could be computed. Assuming similar specimens dimensionally, the change in conductance with time is a direct function of the rate of corrosion. The variation of "i", the slope of the line, due to the variation of the data from the line can be estimated by its variance, s^2_b.

Covariance analysis is a ramification of the analysis of variance developed by Dr. Fisher and his coworkers in the 1920's. Covariance analysis is essentially the comparison of the variation between tests with the variance within the tests. The hypothesis to be tested is that the slopes ("b") of the various lines are actually the same and that the differences are due to random error. These hypotheses can be tested statistically and conclusions drawn from the results can be made with a certain mathematical probability. This statistical method was used to analyze data obtained by the electrical conductance method.

Because of the ease with which tests could be made, the large amounts of data generated, and the number of calculations needed in order to draw meaningful conclusions, the use of punched card techniques and electronic digital computers was warranted. Onto each card was punched the raw data, and by proper programing. all the statistical calculations could be made by the computers. Errors introduced by making the computations on hand calculators were thus eliminated.

A full discussion on the use of statistics in interpreting data is outside the scope of this technical note. Perusal of any standard textbook on statistics such as, *Statistical Methods* by Snedecor, *Statistical Methods for Research Workers* by Fisher, and *Experimental Design* by Cochran and Cox is suggested.

APPENDIX V

Initial tests using the electrical conductance method were made using pure magnesium ribbon as specimens. Test objectives were: 1, to familiarize personnel with the equipment; 2, determine performance characteristics of the method; 3, determine variation within tests and variations between tests; and 4, to compare results obtained using this method with results obtained from similar tests using other methods. Careful analysis of these test results were made using procedures outlined in Appendix IV.

Because of the initial difficulty of obtaining reproducible metal ribbon specimens, readily available pure magnesium ribbon was used. Obtained commercially in long rolls, the 0.125 inch wide ribbon could be easily cut into suitable specimens with scissors. A spectrographic analysis of the ribbon is shown below.

   Mg   99.9%
   Fe   0.04%
   Mn   0.047%
   Traces Si, Ca, Cu, Sn, Pb, Ti, Cd.

Variations within the metal ribbon appeared to be small and this permitted a closer estimate of residual error within a test and between duplicate tests. Corrosion rates obtained from these initial tests were not strictly comparable to other corrosion tests made using other methods due to dissimilarity between specimens, i.e., the infrequent use of pure magnesium as test specimens.

A representative data sheet containing the raw data obtained in T M-1 is shown in Figure 8. The column headed P. refers to the reversing switch positions the manual circuit. The column headed Volts, S.R. and Samp. refer to the

SPECIMEN: Pure Magnesium Ribbon, 18.0″ x 0.125″ x 0.0065″ with 3″ Leads.
TREATMENTS: Precleaned for 10 seconds in acetic nitrate solution, rinsed in distilled water.
TEST CONDITIONS: Total Immersion in Anhydrous Benzene at 25.9° C.
REMARKS: Test to Determine Precision and Reproducibility of Data.

TEST DATA

Time		Temp	S.	Volts	Volts	Conduct.*
Mins	Hrs	° C	P.	S.R.	Samp	mhos.
0.0	0.0	25.0	1	.20630	.008653	23.841
1515	Hrs	....	2	.20702	.008680	23.850
14	Mar		1	.20742	.008677	23.905
	'55		2	.20769	.008698	23.878
			1	.27029	.011350	23.871
			2	.27209	.011408	23.851
			1	.27221	.011401	23.876
			2	.27226	.011394	23.896
	69.5	25.0	1	.33131	.013899	22.853
			2	.33237	.013923	23.872
			1	.33280	.013938	23.877
			2	.33333	.013956	23.885
			1	.34726	.014547	23.871
			2	.34747	.014551	23.880
			1	.34783	.014556	23.896
			2	.35995	.015082	23.866
	208.0	25.0	1	.36015	.015061	23.913
			2	.36030	.015088	23.880
			1	.36075	.015114	23.869
			2	.34817	.014577	23.885
			1	.34747	.014541	23.896
			2	.34813	.014574	23.887

Standard resistor: ---- Ohms
Duplicate test No's: M-2
Comparison test No's: M-9, M-10
Intercept of curve: 23.874
Slope of curve: 0.00

SAMPLE DATA SHEET FROM TEST M-1

*Conductance (in mhos) =
$$\frac{\text{Volts S.R.}}{\text{Resistance S.R. (ohms) X Volts Samp.}}$$

FIGURE 8

voltage readings obtained from the K-2 potentiometer when current is passed through the standard resistor and test specimen respectively. Even though results of some tests did not warrant statistical analysis due to small fluctuations, statistics was used primarily for familiarization of personnel and as a check on technique, both of manual and machine computations.

To insure uniformity between specimens, surface cleaning of each specimen prior to testing was accomplished with a chemical cleaning treatment. This consisted of dipping with agitation each specimen in a 20 percent acetic nitrate solution for ten seconds, then thoroughly rinsing with distilled water. Abrasives and polishes were not used. The specimen was weighed and then randomly assigned to a test environment. After each test and prior to final weighing, the specimen was dipped in a boiling 20 percent chromic acid plus 1 percent silver nitrate, which precipitates any chlorides present. This treatment preferentially removed any corrosion products on the specimen. The treatments used for these tests with pure magnesium are described in Military Specification MIL–M–3171A; Paragraphs 3.3.2 and 3.3.8. The solution compositions and operation used were:

Acetic Nitrate Pickle

Glacial acetic acid	25½ fl. oz.
Sodium nitrate	6⅔ oz.
Water to make	1 gallon
Operating temperature	70–80° F
Immersion time	Approx. 10 sec.

Chromic Acid Pickle

Chromic acid	24 oz.
Silver nitrate	1.3 oz.
Water to make	1 gallon
Operating temperature	190–212° F
Immersion time	1-15 mins.

Tests M-1 and M-2 were made to show the corrosion rate of pure magnesium when totally immersed in anhydrous benzene for periods up to 700 hours (30 days). Even though it is well known that anhydrous benzene will not corrode pure magnesium, it was desired to re-establish this fact using this sensitive corrosion test as well as to determine the variation (or random error within the test). As shown in Figure 8, within any set of readings (up to twenty of current and voltage, made at any one time, the calculated mean conductance had a standard deviation (s) of approximately 20 micromhos. For periods up to a month, specimens did not tarnish or corrode at all. Statistical differences between sets of readings taken during the test were no greater than variations within any particular set of readings. Differences between sets of readings appeared to be due to minor fluctuations in the temperature of the water bath and residual error within the equipment. Results of these and other tests reported in this Appendix are shown in Figure 9.

Tests M-3 and M-4 were made to determine the effect of temperature on conductance. Having determined that anhydrous benzene does not corrode magnesium, but knowing that small changes in temperature did affect the measurements, it was desirable to determine conductance as a function of temperature. Magnesium specimens were totally immersed in benzene and conductance measurements made at 10° intervals up to 65° C. The change in resi e, the reciprocal of conductance, as a funct of temperature is shown in Figure 10.

83

Test No.	Test conditions			Percent change in conductance (mhos)	Percent wt. loss (grms.)	Regression line coefficients [1]		
	Totally immersed in	Temp.	Total time			a	b	r [2]
M-1	Anh. benzene	25° C	700 hours	0.0	0.0	.04189	0.0	0.96
M-2	Anh. Benzene	25° C	700 hours	0.0	0.0	.03965	0.0	0.96
M-3	Anh. Benzene	Variable		14.59	0.0	.033071	1.365×10^{-4}	0.98
M-4	Anh. benzene	Variable		14.23	0.0	.033078	1.322×10^{-4}	0.98
M-5	Acetic Nitrate Solution	25° C	Artificially corroded.	79.96	51.03	See Fig. 11 & 12.	See Fig. 11 & 12.	0.99
M-6	Approx. 0.1 N KCl.	50° C	5.67 hours	19.1	12.1	.03927	1.639×10^{-3}	0.96
M-7	Approx. 0.1 N KCl.	50° C	4.77 hours	17.1	10.3	.03937	1.711×10^{-3}	0.95

[1] Using the method of Least Squares to determine the best fitting regression line of resistance versus Time or Temperature where "a" is the intercept and "b" is the slope.

[2] The correlation coefficient, r, is a measure of the dispersion of the data from the calculated line, where r = 1.0 is perfect correlation.

FIGURE 9.

CHANGE IN RESISTANCE VERSUS TEMPERATURE FOR MAGNESIUM RIBBON TOTALLY IMMERSED IN BENZENE
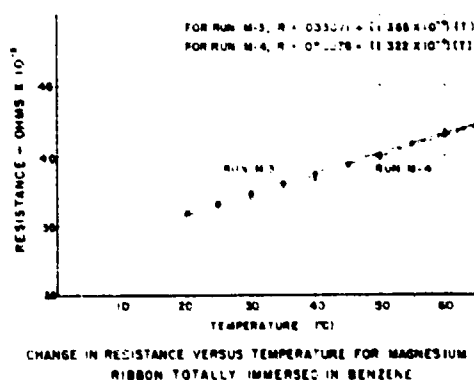
FIGURE 10.

It was noted that correlation between tests was good. The two straight line relationships were displaced (different "a" values, or y intercept) due to slightly different specimen lengths. The two best fitting lines appeared to have the same slopes and this was shown by the calculated slope constants "b" which were .0001365 and .0001322. Statistical analysis showed that no real differences existed between the duplicate tests and that both tests could be represented by one average line with a slope of .0001343 and an "a" value of 0.033075. The calculated correlation coefficient for the average regression line obtained from both tests was 0.95, where perfect correlation between the calculated regression line and the data would be 1.0.

The temperature resistance coefficient of a metal is defined as the ratio of the change in resistance due to a change in temperature of 1° C to its resistance at 0° C. Using the average calculated "a" which is the resistance of magnesium at 0° C,

this coefficient can be calculated from the results of these two tests. A value of 0.00412 per degree Centigrade was obtained which compares favorably with the value of 0.004 per degree Centigrade obtained by the Bureau of Standards for pure magnesium metal.

Most quantitative corrosion tests make use of a metal's loss in weight as a measure of corrosion. Test M-5 was made to try and correlate change in conductance with change in the specimen's thickness and loss in weight. Acetic nitrate solution was used as the corroding agent as it will rapidly and uniformly attack magnesium. The conductance, thickness, and weight of the magnesium ribbon specimen was determined prior to and after each successive rapid dip into the acetic nitrate solution. After each dip into the nitrate solution, the specimen was thoroughly washed with water and dried prior to making measurements. Thickness measurements were made using a micrometer; a large number of measurements being made along the specimen's length and an arithmetic average computed. The averages of two weight measurements, which were made on an analytical balance, and of four or more conductance measurements were used. All measurements were made at approximately 25° C.

As shown theoretically in Appendix I, Section 2, a plot of conductance versus weight loss should be a straight line when plotted on rectangular coordinates. As shown in Figure 11, when the experimental data from Test M-5 was plotted, excellent correlation found. The variation of the data from the lated regression line was very small; the ca ted correlation coefficient being 0.99.

84

CHANGE IN CONDUCTANCE VERSUS CHANGE IN WEIGHT FOR AN
ARTIFICIALLY CORRODED MAGNESIUM RIBBON SPECIMEN

FIGURE 11.

A plot of resistance change versus weight loss
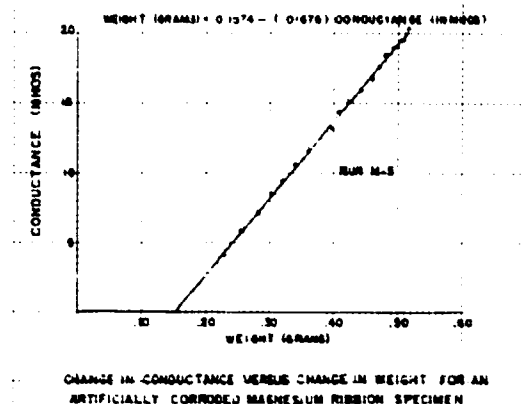was a curve which approximated a straight line
up to a 22 percent change in resistance. Beyond
that point deviations of resistance change versus
weight loss from a straight line were appreciable
and continuously increasing. The percent change
in resistance was equal to the percent change in
thickness up to a 30 to 40 percent change in resist-
ance. Beyond this point, the percent change in
width was appreciable, increasingly so as corrosion
continued. When an 80 percent change in resist-
ance had occurred, the average measured specimen
thickness had changed approximately 66 percent.
Visual observation showed that the specimen's
width had decreased appreciably and this would
account for the difference of 14 percent

A measure of corrosion which is unaffected by
specimen size is the use of percent weight loss. In
many corrosion tests, percent weight loss has been
correlated with tensile strength, change in elonga-
tion, and other mechanical tests. In Figure 12, is
shown a graph of percent change in resistance
(equal to the percent change in conductance)
versus percent change in weight for Test M 5.
A calculated straight line with a correlation coeffi-
cient of 0.987 and the equation of the line relating
the two functions are shown. The constants
relating the percent change in weight are the re-
sistivity coefficient and the density of the metal.
At this one temperature and for similar specimens
of this same metal, magnesium, this relationship
should not change. Thus it should be possible to
determine percent change in weight from the per-
cent change in resistance whenever similar mag-
nesium specimens are experimentally corroded at
this temperature. Since magnesium and magne-

PERCENT CHANGE IN RESISTANCE VERSUS PERCENT CHANGE IN WEIGHT
FOR PURE MAGNESIUM RIBBON ARTIFICIALLY
CORRODED
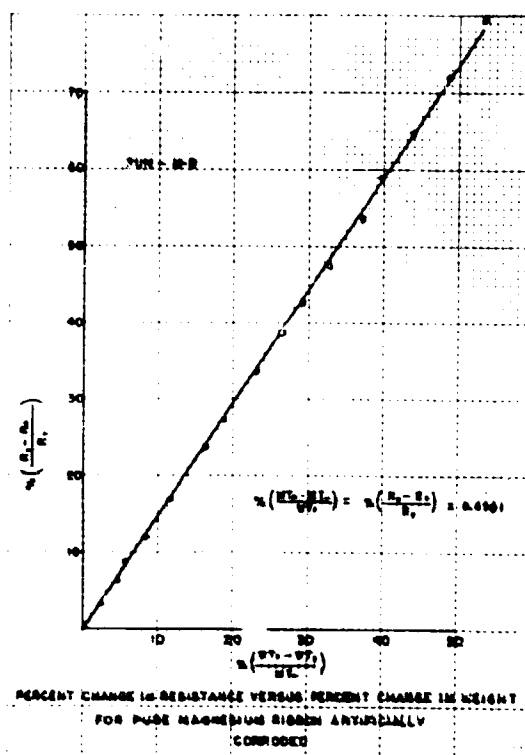
FIGURE 12.

sium alloys tend to pit in a corrosive environment
rather than uniformly etch, the need for a uniform
etchant was recognized. From previous experi-
ence, it was felt that dilute salt solutions might
satisfactorily etch pure magnesium.

Tests M 6 and M 7 were made to determine the
amount, rate, and type of corrosion of a salt solu-
tion on pure magnesium ribbon specimens. Both
tests, run simultaneously, were made by totally
immersing the specimens in 0.1 NKCl at 30° C.
Since salt solutions of this strength are good elec-
trical conductors, the electrical measurements
were made in benzene, compensation being made
for the amount of time the specimens were not in
the corroding media. A graph of change in con-
ductance versus time for the two tests is shown
in Figure 13.

Microscopic examination of each specimen after
the test showed little pitting; reasonably uniform
corrosion of the specimens was apparent. Varia-
tion of the experimental data on the calculated
regression line was small; the correlation coefficient
was greater than 0.95. Statistically, both tests
could be represented by one regression line with

85

Figure 13.

the average corrosion rate was 0.947 inches per year. Though no similar tests could be found in the literature with which to compare results, this value appears reasonable.

APPENDIX VI

Because of the many advantages of the electrical conductance method for determining corrosion rates, it is planned to adopt these techniques to other Air Force research problems. Though the method could be adopted for use in many programs, it will be used at present with only three. These programs are: development of suitable inhibitors for red fuming nitric acid, development and comparison of new surface treatments for magnesium alloys, and determining the effect of humidity on corrosion rate. In order to use these new techniques to advantage, close coordination with the project engineers of the aforementioned programs has been initiated. Working jointly with each project engineer, test programs have been devised, most equipment obtained, and work scheduled. Each program will be discussed more fully in the following three sections.

Further work will also be done to investigate the use of different types of specimens (ribbon, wire, and deposited films) in different corrosive environments. The effect of temperature, concentration, and flowing versus nonflowing solutions on corrosion will be investigated.

Section I.

Because of the increased use of red-fuming nitric acid in aircraft propulsion equipment, there is great need in the Air Force for a corrosion resistant nonscaling metal to contain this media under a range of conditions. At present, there are several subtasks which have been initiated to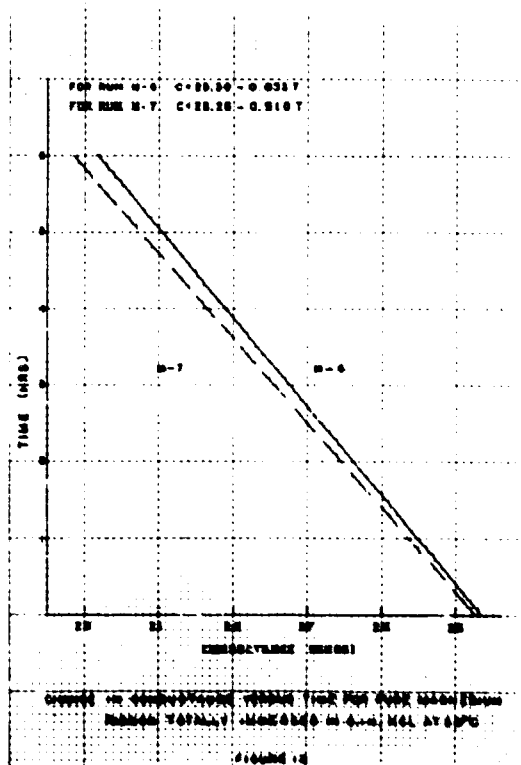 solve the corrosion problems which occur when fuming nitric acid is used. Programs have been initiated to develop both suitable inhibitors to reduce the corrosiveness of fuming nitric acid and materials to resist either uninhibited or inhibited acid.

The electrical conductance method is well suited to classifying the relative corrosivities of different inhibitors in nitric acid and the relative corrosion resistance different metals to these inhibited acid solut. Because temperature appears to greatly the rate and types of corrosion, tests must be made at several different

---

high probability. The small difference between the calculated intercept values ("a") was due to the reproducibility in preparing the specimens dimensionally.

Both specimens were weighed before and after the test as described previously. The percent change in weight for tests M-6 and M-7 respectively were 12.1 and 10.3 percent. Using the percent change in weight to calculate an expected percent change in conductance according to the calculated equation from Figure 12, values of 17.7 and 15.1 percent were obtained. The actual values of percent change in conductance were 19.1 and 17.1 percent, respectively, which are in good agreement. A likely source of error is the fact that in these tests the specimens had to be cleaned in hot chromic acid solution prior to final weighing. This was not a factor in test M-4 when the equation above was determined since etching with acetic nitrate solution leaves no corrosion products.

The average corrosion rate can be calculated using the equations derived in Appendix I, Section I. For pure magnesium ribbon specimens totally immersed in approximately 0.1 NKCl at 50° C,

temperature levels. Metal specimens will be placed in both the vapor and liquid regions, thereby obtaining vapor and liquid corrosion rates simultaneously. By threading the electrical leads through Kel F sleeves running outside the Kel F lined pressure vessel, continuous recording equipment can measure the change in electrical conductance of the specimen while corrosion occurs. Figure 14 shows the experimental design of the first series of planned tests It tests the effect of five inhibitors in 84 percent fuming nitric acid on 3 types of metals to both liquid and vapor at two different temperatures. After the data obtained from these tests have been carefully analyzed, other similar tests will be made.
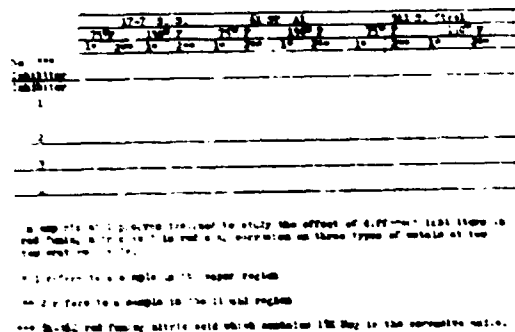

Figure 14

Section 2.

During the last decade, the use of magnesium and its alloys in Air Force equipment has increased manyfold. However, magnesium alloys corrode in many environments. Maximum protection from corrosion may be obtained through the use of chemical treatments followed by painting. The need exists for a surface chemical treatment which will protect magnesium from corrosion by forming an adhering film, which will also be a good paint base. The electrical conductance method is well suited for classifying the protection afforded by different surface treatments on different types of magnesium alloy.

The experimental design of the first set of tests is shown in Figure 15 Six types of treatments will be applied to duplicate specimens from each of three types of magnesium alloy. Each specimen will then be totally immersed in a standard salt solution (0.05 NKCl) at 25° C From previous tests, this corrosive environment appears to uniformly corrode pure magnesium without excessive pitting at a reasonable rate. Measure-

Figure 15.

ments will be made at regular intervals and the data statistically analyzed to determine if there are real differences between metals and between treatments.

As new treatments and alloys are devised these will be compared with older ones in the same manner. It is possible that this method of determining corrosion rates can be standardized and used as the basis for an Air Force specification in qualification testing.

Section 3.

It is well known that in the absence of other corrosive agents, steel will not corrode in a dry atmosphere. It is also true that in the presence of moisture steel will readily corrode. The relationship between rate of corrosion of steel and percent humidity is not clearly known. Because the electrical conductance method can accurately measure very small changes in electrical conductance and therefore low rates of corrosion, it could accurately determine this relationship.

Two types of mild steel, 24ST3 unclad aluminum, and FS-1 magnesium specimens will be exposed to relative humidities ranging from zero to one hundred percent in 10 percent steps. A constant known humidity can be effected by using different aqueous solutions of sulfuric acid. Different acid solutions will be placed in the bottom of large mouthed one gallon glass jars. The specimens will hang in the vapor space of the jar with the leads passing through porcelain sleeves inserted in the lid. The jar lid can then be sealed to prevent evaporation and measurements made at regular intervals by simply connecting electrical leads to the specimen leads which are outside the jar The jars will be kept at a constant temperature of 25° C though measurements could as easily be made at other temperatures.

From experiments of this kind formation can be obtained as to packaging c ions needed to prevent corrosion. It might b. possible to insert sensitive metal specimens in packages and by

87

suitable measurements to determine if the environment within becomes corrosive.

APPENDIX VII

Bibliography

Measuring the change in conductance of a metal specimen in order to determine its rate of corrosion has not been widely used. However, this principle has been used by some investigators to solve special problems in corrosion research. A list of articles relating to this method are given below.

1. N. B. Pilling, R. E. Bedworth, J. Inst. Metals (London) 29, 529 (1923)

2. J. S. Dunn, Proc. Roy. Soc. London A 111, 210 (1926)

3. R. R. Seeber, Symposium on Corrosion Testing Procedures, ASTM, (1947)

4. A. Dravnieks, J. Am. Chem. Soc. 72, 3761 (1950)

5. A. Dravnieks and H. A. Cataldi, Corrosion, 10, 224, (1954)

6. A. Dravnieks, Ind. Eng. Chem. 43, 2897, (1951)

7. F. Wormwell and D. M. Brasher, J. Iron Steel Inst. (London) 164, Pt. 2 141 (1950)

8. M. A. Arthur, ASTM Bull. 57 (1949) Sept.

9. W. E. Shaw and D. L. Hawke, Org. Finishing, 10, No. 10, 19 (1949)

10. W. E. Shaw and D. L. Hawke, Can. Paint and Varnish Mag. 23, No. 6, 18 (1949)

11. Progress Report under contract H-219, OEMSR-211, Report OSRD No. 4847, 23 Mar. 45, Bakelite Corp.

12. J. C. Hudson, Proc. Phys. Soc (London) 40, 107, (1928)

13. R. M. Burns and W. E. Campbell, Trans. Electrochem. Soc. 55, 271, (1929)

14. J. Rutherford and R. Aborn, Trans. Am. Inst. Mining and Met. Engs., 100, 293 (1932)

DOUGLAS A. RAUSCH
ALAN M. LOVELACE

The Preparation and Properties of Some New
Fluorine-Containing 1,2-Epoxides

1956

DOUGLAS A. RAUSCH

Douglas A. Rausch was born July 26, 1928, in Fort Wayne, Indiana. He received a B.S. in chemistry from Indiana University in 1950, and a Ph. D. in organic chemistry from the University of Colorado in 1954. During the time he was at the University of Colorado, he was employed as a teaching assistant of chemistry from 1950 to 1952 and research assistant of chemistry from 1952 to 1953. He was employed as a research chemist by the E. I. du Pont de Nemours Company from 1953 to 1954, when he entered the military service. He was assigned to the Nonmetallic Materials Laboratory, Materials Central, in December 1954 as a project officer in the Polymer Branch.

While Mr. Rausch was in the military service, he coauthored an American Chemical Society monograph on aliphatic fluorine compounds and coauthored four technical publications. Upon separation from military service, he joined the Dow Chemical Company. His principle area of research is fluorine chemistry.

Mr. Rausch is a member of the American Association for the Advancement of Science, the American Chemical Society, and the Research Society of America. He is listed in the tenth edition of *American Men of Science*.

BIBLIOGRAPHY

With J. D. LaZerte, R. J. Koshar, J. D. Park, W. H. Pearlson, and J. R. Lacher. Perfluoroacrylonitrile and its Derivatives. Journal of the American Chemical Society, 78 (21), 5639-5641, November 5, 1956

With A. M. Lovelace and L. E. Coleman. The Preparation and Properties of Some Fluorine-Containing Epoxides. Journal of Organic Chemistry, 21 (11), 1328-1330, November 1956

With L. E. Coleman and A. M. Lovelace. Unsaturated Ketones. I. The Preparation and Polymerization of Perfluoroalkyl Propenyl Ketones. Journal of the American Chemical Society, 79 (18), 4983-4985, September 20, 1957

With F. B. Jones, P. B. Stickney, L. E. Coleman, and A. M. Lovelace. Polymerization of Some Fluorine-Containing Olefin Oxides. Journal of Polymer Science, 26 (113), 51-58, October 1957

With L. E. Coleman and W. R. Griffin. Polymerization of Some 1-Alkyl-1-Hidroperfluoroalkyl Acrylates. Journal of Chemical and Engineering Data, 3 (1), 113-17, April 1958

With A. M. Lovelace and W. Postelnek. American Chemical Society Monograph No. 138. Aliphatic Fluorine Compounds. New York, Reinhold Publishing Company, 1958

ALAN M. LOVELACE

Alan M. Lovelace was born in St. Petersburg, Florida, on September 4, 1929. He attended the University of Florida and received the B.S. in chemistry in 1951, the M.S. in organic chemistry in 1952, and the Ph. D. in organic chemistry in 1954. During the time he was in college, he worked in the university's Nutritions Laboratory doing radioactive tracer work related to nutrition in animals. Upon receiving his doctorate, he joined the research department of the E.I. du Pont de Nemours Company in Kinston, North Carolina.

He entered active military duty as a lieutenant in the Air Force in August 1954, and was assigned to the Nonmetallic Materials Laboratory. After separation from the service, he remained with the Materials Central and became Chief of the Polymer Branch in 1959. He served in that capacity until the early part of 1962 when he was appointed Technical Director, Materials Central.

In addition to the Cleary Award, Dr. Lovelace was the recipient of the Arthur S. Flemming Award as one of the outstanding young men in government in 1958, and the Meritorious Civilian Service Award in 1959. He is a member of Phi Kappa Phi, the American Chemical Society, the Southern Ohio Rubber Group, Sigma Xi, and Gamma Sigma Epsilon. He serves on a number of committees including the Board of Reviewers, Journal of Polymer Science; Board of Editors, Chemical Propulsion Journal; Materials Advisory Board, Basic Research Committee, Department of Defense Solid Propellant Committee; and, the Organizing Committee of the Second International Fluorine Symposium, co-sponsored by the Materials Central and the American Chemical Society. He has been chosen Chairman-Designate by the Fluorine Subdivision, Industrial and Engineering Chemistry Division of the American Chemical Society for the year 1962.

BIBLIOGRAPHY

Synthesis of Some Fluorine-Containing Acrylic Acids. Paper presented at the American Chemical Society Meeting in Miniature, 1952

The Synthesis of 1,1-difluoro-3-methylbutadiene. Paper presented at the One Hundred Twenty-fourth Meeting of the American Chemical Society, Chicago, Ill., September 1953

With P. Tarrant and J. Attaway. Fluorobutadienes. V. The Synthesis of 1,1-difluoro-3-methylbutadiene. Journal of the American Chemical Society, 75, 2345, April 1954

With P. Tarrant. Free Radical Additions Involving Fluorine Compounds I. The Addition of Dibromodifluoromethane to Hydrocarbon Olefins. Journal of the American Chemical Society, 76, 12, 3466-3468, July 5, 1954

Free Radical Additions of Dibromodifluoromethane to Fluoroolefins. Paper presented at the One Hundred Twenty-Sixth Meeting of the American Chemical Society, New York, N.Y., September 1954

Free Radical Addition of Dibromodifluoromethane to Hydrocarbon Olefins. Paper presented at the One Hundred Twenty-sixth Meeting of the American Chemical Society, New York, N.Y., September 1954.

With P. Tarrant. Free Radical Additions Involving Fluorine Compounds. III. The Addition of Chlorobromodifluoromethane to Olefins. Journal of the American Chemical Society, 77(3):768-770, February 5, 1955.

With P. Tarrant and M. R. Lilyquist. Free Radical Additions Involving Fluorine Compounds. IV. The Addition of Dibromodifluoromethane to some Fluoroolefins. Journal of the American Chemical Society, 77(10):2783-2787, May 20, 1955.

Gamma Ray Induced Addition of Bromotrichloromethane to Olefins. Paper presented at the One Hundred Twenty-eighth Meeting of the American Chemical Society, Minneapolis, Minn., September 1955.

Internal Program on Fluoro-Organic Polymers. Paper presented at the WADC-Polymer Section Contractors' Conference, Dayton, Ohio, March 1956.

Orientation in Free Radical Addition of Perhaloalkanes to Fluorine-Containing Olefins. Paper presented at the One Hundred Thirtieth Meeting of the American Chemical Society, Atlantic City, N.J., September 1956.

Polymerization Reactions of Some Perfluoroalkyl Propenyl Ketones. Paper presented at the One Hundred Thirtieth Meeting of the American Chemical Society, Atlantic City, N.J., September 1956.

The Preparation of Some Fluorinated Unsaturated Ketones. Paper Presented at the One Hundred Thirtieth Meeting of the American Chemical Society, Atlantic City, N.J., September 1956.

With D. A. Rausch and L. E. Coleman. Synthesis of Some Fluorine-Containing 1,2-Epoxides. Journal of Organic Chemistry, 21(11):1328-1330, November 1956.

Review of Materials Laboratory Transparent Material Programs. Paper presented at the WADC-University of Dayton Conference on Transparent Materials for Aircraft Enclosures, Dayton, Ohio, December 1956.

With D. A. Rausch. Preparation of Perfluoroalkyl Propenyl Ketones. Paper presented at the One Hundred Thirty-first Annual Meeting of the American Chemical Society, Minneapolis, Minn., April 1957.

With D. A. Rausch and L. E. Coleman. Unsaturated Ketones. I. The Preparation and Polymerization of Perfluoroalkyl Propenyl Ketones. Journal of the American Chemical Society, 79(18):4983-4984, September 20, 1957.

Polymer Section Internal Research Program. Paper presented at the WADC-University of Dayton Conference on High Temperature Polymer and Fluid Synthesis, Dayton, Ohio, October 1957.

With F. B. Jones, P. H. Stickney, L. E. Coleman and D. A. Rausch. Polymerization of Some Fluorine-Containing Olefin Oxides. Journal of Polymer Science, 26(112):81-88, October 1957.

With M. Rausch, P. Shaw, and D. Mayo. Derivatives of Ferrocene. V. The Preparation of Some N-Substituted Ferrocene-carboxamides. Journal of Organic Chemistry, 23(3):505-507, March 1958.

With W. Postelnek and D. A. Rausch. American Chemical Society Monograph No. 138. Aliphatic Fluorine Compounds. New York, Reinhold Publishing Company, 1958.

With W. Postelnek and L. E. Coleman. Fluorine-Containing Polymers. I. Fluorinated Vinyl Polymers with Functional Groups, Condensation Polymers, and Styrene Polymers. Fortschritte Der Hochpolymeren Forschung, 1958.

The Air Force Inorganic Polymer Program. Paper presented at the Gordon Research Conference on Polymer Research, July 1959.

With H. K. Reimschuessel and J. M. Hagerman. Linear Polymers Containing the 1,3,5-Triazine Nucleus. Journal of Polymer Science, 49:136:270-272, October 1959.

With W. Darrell and R. L. Adamczak. Some Reactions of Vinyl and Allyl Acetate with Haloalkanes. Journal of Organic Chemistry, 25(9): 1661-1662, September 1960.

With D. A. Rausch. Gamma Ray Induced Additions of Bromotrichloromethane to Olefins. Journal of the American Chemical Society. (Pending.)

With P. D. Shaw and D. W. Mayo. Studies on the Lithiation of Ferrocene. Journal of the American Chemical Society. (Pending.)

With W. Postelnek and D. A. Rausch. Orientation in Free Radical Additions of Perhaloalkanes to Fluorine-Containing Olefins. Journal of the American Chemical Society. (Pending.)

The Preparation and Properties of Some New Fluorine-Containing 1, 2-Epoxides

D. A. RAUSCH

A. M. LOVELACE

ABSTRACT *The interest in fluorine-containing polyethers for possible application as thermally stable elastomers prompted research on the preparation of new epoxide monomers.*

Six new epoxides were prepared and characterized. The utilization of these monomers in new polymer system is being investigated.

I. INTRODUCTION

The research described here was undertaken to prove out a general procedure for the preparation of fluorinated epoxides and to prepare a type of epoxide hithertofore unreported for evaluation as a monomer in the synthesis of new experimental elastomers and base stock fluids.

II. SUMMARY AND CONCLUSIONS

The general procedure as outlined previously for the preparation of epoxides appears to be a general method for the preparation of epoxides substituted in the 1- and 1,2-positions. The preparation of the alkyl perfluoroalkyl ketones using the lithium salt of the perfluorocarboxylic acid appears to offer certain advantages.

No data were available at the time this report was written as to the polymerization characteristics of the substituted epoxides.

III. DISCUSSION

Until this research was undertaken no fluorine-containing epoxides had been prepared which were substituted with alkyl and perfluoroalkyl groups in the one and two positions. McBee and Burton (1) prepared trifluoropropylene oxide and trifluoroisobutylene oxide by reduction of the corresponding alphabromoketones followed by epoxidation with aqueous sodium hydroxide. This procedure had never been applied to the synthesis of the aforementioned 1,2-disubstituted epoxides since the procedure for the preparation of the starting ketones was rather lengthy. Recently, however, it has been reported by McGrath (2) and co-workers that the desired ketones can be prepared by the addition of the perfluorocarboxylic acid to an excess of the alkyl Grignard reagent.

In the course of this investigation, it was discovered that an alternate procedure could be employed for the preparation of the ketones. This procedure utilized the lithium salt of the perfluorocarboxylic acid and the alkyl Grignard reagent using the reverse addition technique. This modified procedure offers several advantages over the one in which the perfluorocarboxylic acid is employed. These advantages are firstly, less alkyl Grignard reagent is required and thereby the hydrolysis of the reaction mixture is simplified. Secondly, greater economy in the utilization of the

acid has been found. Finally, no fluorine-containing alcohols were isolated which result from the reduction of the ketone by the excess Grignard reagent. The unreacted acid is recovered as the ether complex (3) which can be regenerated by treatment with dilute acid.

The following will summarize the reactions employed in the preparation and proof of structure of the fluorine-containing epoxides.

$$C_3F_7COOH + C_2H_5MgBr \rightarrow C_3F_7COC_2H_5 \quad I$$
$$C_3F_7COOH + CH_3MgBr \rightarrow C_3F_7COCH_3 \quad II$$
$$C_3F_7COCH_3 + Br_2/H_2SO_4 \rightarrow C_3F_7COCHBrC_2H_5 \quad III$$
$$C_3F_7COCHBrC_2H_5 + LiAlH_4 \rightarrow C_3F_7CHOHCHBrC_2H_5 \quad IV$$
$$C_3F_7CHOHCHBrC_2H_5 + NaOH/H_2O \rightarrow C_3F_7CH—CHC_2H_5 \quad V$$
$$C_3F_7CH—CHC_2H_5 + H_2SO_4/H_2O \rightarrow C_3F_7CHOHCHOHC_2H_5 \quad VI$$
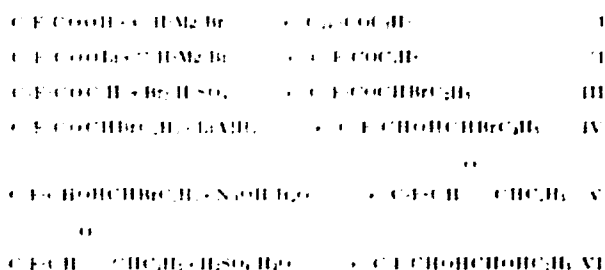
Reactions I and II represent the procedures used in preparing the starting ketones. The bromination reaction III was carried out in concentrated sulfuric acid. In the case of each ketone a single monobromo-derivative was obtained which was subsequently shown to be the alpha isomer by conversion to the 1,2-epoxides.

The reduction of the bromoketones reaction IV was effected with an ether slurry of lithium aluminium hydride. Some reductive elimination occurred as evidenced by the presence of bromide ion in the reaction mixture.

The bromoalcohols were then added dropwise to hot 50 percent aqueous sodium hydroxide solution reaction V. The epoxide steam distilled from the reaction mixture. Treatment of the epoxides with 6M sulfuric acid gave the corresponding vicinal diols as shown in reaction VI. A positive periodic acid test (4) was obtained with each glycol.

Using the procedure described the following epoxides were prepared:

$$C_3F_7CH—CHCH_3, C_3F_7CH—CHC_2H_5, C_3F_7CH—C(CH_3)_2,$$
$$CF_3CH—CHCH_3, CF_3CH—CHC_2H_5, CF_3CH—C(CH_3)_2$$

The physical properties, analysis and yields of the new compounds are given in Table I.
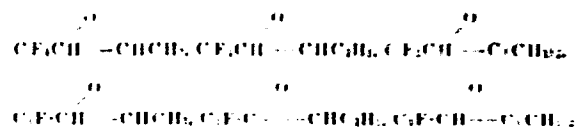
TABLE I. *Physical properties of new compounds*

Compound	Yield, percent	B.P./mm °C	n_D^{20}	d_4^{20}	AR_F	Percent carbon		Analysis [a] Percent hydrogen		Percent fluorine	
						Calc	Fd	Calc	Fd	Calc	Fd
$C_3F_7COCHBrCH_3$	60	57/85	1.3491	1.686	1.25	23.62	23.74	1.38	1.38	43.60	43.60
$C_3F_7COCHBrC_2H_5$	72	52/31	1.3594	1.627	1.23	26.35	26.37	1.89	1.96	41.69	41.76
$C_3F_7COCBr(CH_3)_2$	66	62.1/61	1.3628	1.631	1.26	26.35	26.36	1.89	2.03	41.69	41.83
$CF_3COCHBrCH_3$	82	93/748	1.3805	1.640	1.25	23.41	23.40	1.95	2.04	27.80	27.89
$CF_3COCHBrC_2H_5$	83	61/124	1.3905	1.554	1.25	27.42	27.47	2.73	2.86	26.03	25.87
$CF_3COCBr(CH_3)_2$	63	57.5/135	1.3920	1.547	1.31	27.42	27.41	2.73	2.80	26.03	26.00
$C_3F_7CH(OH)CHBrCH_3$	56	85/81	1.3709	1.748	1.16	23.45	23.37	1.95	2.01	43.32	43.35
$C_3F_7CH(OH)CHBrC_2H_5$	65	75.0–75.8/32	1.3770	1.674	1.14	26.16	26.16	2.49	2.30	41.43	41.52
$C_3F_7CH(OH)CBr(CH_3)_2$	54	83.9/62	1.3798	1.564	1.17	26.16	25.70	2.49	2.47	41.43	41.56
$CF_3CH(OH)CHBrCH_3$	78.5	65.5/63	1.4080	1.697	1.15	23.19	23.23	2.90	2.90	27.54	27.72
$CF_3CH(OH)CHBrC_2H_5$	34	94.0–94.5/116	1.4148	1.602	1.08	27.17	27.15	3.65	3.75	25.79	25.69
$CF_3CH(OH)CBr(CH_3)_2$	42	67.5/47	1.4159	1.591	1.18	27.17	27.20	3.65	3.66	25.79	25.86
$C_3F_7CHCHO(CH_3)$	76	93.5/748	1.3091	1.424	1.26	31.86	31.86	2.21	2.25	58.84	58.93
$C_3F_7CHCHO(C_2H_5)$	83	110.5–111/749	1.3218	1.358	1.22	35.00	35.01	2.92	3.02	55.42	55.42
$C_3F_7CHCO(CH_3)_2$	85	102.5–103/747	1.3187	1.351	1.26	35.00	35.03	2.92	2.93	55.42	55.39
$CF_3CHCHO(CH_3)$	90	58.5–59.0/747	1.3107	1.207	1.12	38.10	38.10	3.97	3.91	45.21	45.34
$CF_3CHCHO(C_2H_5)$	83	78.8–79/745	1.3340	1.146	1.23	42.86	42.80	5.00	4.87	40.71	40.83
$CF_3CHCO(CH_3)_2$	81	71.3–71.9/747	1.3292	1.125	1.26	42.86	43.03	5.00	5.03	40.71	40.64
$C_3F_7CH(OH)CH(OH)C_2H_5$		[b]88				32.55	32.89	3.49		31.55	32.60

[a] Analyses were carried out by the Schwarzkopf Microanalytical Laboratory, Woodside, N.J.
[b] Uncorrected melting point.

IV. EXPERIMENTAL

A. Preparation of Alkyl Perfluoroalkyl Ketones

1. From perfluorocarboxylic acids—general procedure

The ketones were prepared by the general procedure described by McGrath et al. (2) To three moles of alkyl Grignard reagent in one liter of ether cooled in an ice bath was added dropwise with stirring one mole of perfluorocarboxylic acid in an equal volume of ether. After stirring overnight, the reaction mixture was hydrolyzed by pouring into ice-concentrated hydrochloric acid. The ether layer was separated and the water layer extracted with three-100 ml portions of ether. The combined ether layers were dried over Drierite and distilled to remove the ether; the residual liquid was then dried over phosphorus pentoxide and fractionally distilled at atmospheric pressure through an efficient column.

2. From the salt of perfluorocarboxylic acid

The lithium salt of perfluorobutyric acid was prepared by slowly adding one mole of the acid to one-half mole of lithium carbonate in 20 cc of water. The salt was then dried thoroughly in a vacuum oven at 80–100° C.

One mole of lithium perfluorobutyrate was dissolved in one liter of dry ether and cooled in an ice bath. To this vigorously stirred solution was added dropwise 1.10 moles of ethyl magnesium bromide in 400 cc ether over a period of two hours. The reaction mixture was stirred for an additional two hours at room temperature, then cooled in an ice bath, and finally hydrolyzed by the dropwise addition of 200 cc of 20 percent sulfuric acid. The ether layer was separated and the water layer extracted with three 100 ml portions of ether. The combined ether layers were dried over Drierite and the ether removed by distillation. The residual liquid was dried with phosphorus and rectified to give 105 g (44 percent yield) of ethyl heptafluoropropyl ketone b.p. 82–83°, n_D^{25} 1.3030 and 70 g of $2C_3F_7C(O)H$ $(C_2H_5)_2O$ b.p. 129° C.

B. α-Bromoalkyl perfluoroalkyl ketones—general procedure

To 400 ml of concentrated sulfuric acid was added rapidly 0.5 mole of the alkyl perfluoroalkyl ketone. Then 0.25 mole of bromine was added to the vigorously stirred suspension, at such a rate

that the bromine concentration was kept low (several hours to one day may be required for the addition depending on the ketone being brominated). After addition, the stirring was continued for two additional hours and the crude product was removed from the sulfuric acid by distillation under reduced pressure. The crude brominated ketone was then fractionally distilled at reduced pressure.

C. Reduction of α-bromoketones—general procedure

Lithium aluminum hydride (10 percent excess) was stirred with dry ether overnight to give a slurry of the hydride. The hydride slurry was then cooled in an ice bath and the α-bromoketone in an equal volume of ether was added dropwise at such a rate that no reflux took place. After four additional hours of stirring at room temperature, the flask was cooled in an ice bath and the excess hydride was destroyed by the addition of a small amount of ethanol followed by hydrolysis with 20 percent sulfuric acid. The ether layer was separated, the water layer extracted with ether, and the combined ether layers were dried with Drierite. The ether was removed by distillation and the residual liquid was fractionated at reduced pressure to yield the α-bromo alcohols.

D. 1,2-epoxides—general procedure

The α-bromo alcohol was added dropwise to a vigorously stirred 50 percent sodium hydroxide solution (10 molar excess) at 100° C. The epoxide rapidly steam distilled out of the reaction mixture and was then separated from the water layer, dried over Drierite, and fractionally distilled at atmospheric pressure.

E. Hydrolysis of 1,2-epoxides

Two grams of 1,1,1,2,2,3,3-heptafluoro-4,5-epoxyheptane was heated in a sealed tube with 6 ml of 20 percent sulfuric acid at 105° C for sixty hours. Upon cooling a white solid crystallized out which was recrystallized from benzene to yield 1,1,1,2,2,3,3-heptafluoro-4,5-heptanediol, m.p. 55° C. The diol gave a positive periodic test (4).

Similar treatment of 1,1,1,2,2,3,3-heptafluoro-4,5-epoxyhexane and 1,1,1,2,2,3,3-heptafluoro-5-methyl-4,5-epoxyhexane gave oils which were the corresponding glycols, each of which gave a positive periodic acid test.

V. BIBLIOGRAPHY

1. E. T. McBee and T. M. Burton, J. Am. Chem. Soc. 74, 3022 (1952).

2. T. F. McGrath, K. J. Dishart, and R. Levine, Abstracts of papers, 127th meeting, American Chemical Society, Cincinnati, Ohio, March 1955. 9n.p

3. M. Hauptschein and A. V. Grosse, J. Am. Chem. Soc. 73, 5139 (1951).

4. R. L. Shriner and R. C. Fuson, "The Systematic Identification of Organic Compounds", John Wiley & Sons, Inc., New York 1948. p. 115.

MARVIN D. RAUSCH

MARTIN VOGEL

HAROLD ROSENBERG

Derivatives of Ferrocene

1957

MARVIN D. RAUSCH

Marvin D. Rausch was born June 27, 1930, in Topeka, Kansas. He received a B.S. in organic chemistry in 1952 and a Ph. D. in 1955 from the University of Kansas. He entered the military service as a lieutenant in the United States Air Force in September 1955, and was assigned to the Nonmetallic Materials Laboratory, Materials Central. Upon completion of his military tour in 1957, he was awarded a National Science Foundation Post-Doctoral Fellowship for one year at the University of Munich, Germany.

Mr. Rausch was with the Monsanto Chemical Company in St. Louis prior to entering the military service. At the conclusion of his post-doctoral studies in Munich, he returned to the Research and Engineering Division of Monsanto. During the fall semester, 1961-1962, Mr. Rausch was Visiting Professor of Chemistry at the University of Kansas, Lawrence, Kansas. He is now once again with Monsanto as a Senior Research Chemist, Research and Engineering Division, St. Louis, Missouri.

Mr. Rausch is a member of the American Chemical Society and is listed in the tenth edition of *American Men of Science*.

BIBLIOGRAPHY

With W. E. McEwen and J. Kleinberg. Anodic Reductions. I. Conversion of Benzophenone to Benzopinacol by Unipositive Magnesium. Journal of the American Chemical Society, 76:14:3622-3625, July 20, 1954.

With W. E. McEwen and J. Kleinberg. The Anodic Oxidation of Some Active Metals in Pyridine. Journal of the American Chemical Society, 77:8:2093-2096, April 20, 1955.

With F. D. Popp, W. E. McEwen, and J. Kleinberg. Anodic Reductions. II. Conversion of 2-Methoxyphenyl Mesityl Ketone to 2,2-Dimesitoylbiphenyl by Unipositive Magnesium. Journal of Organic Chemistry, 21:2:212-214, February 1956.

With M. Vogel and H. Rosenberg. Ferrocene: A Novel Organometallic Compound. Journal of Chemical Education, 34:6:268-272, June 1957.

With W. E. McEwen and J. Kleinberg. Reductions Involving Unipositive Magnesium. Chemical Review, 57:3:417-437, June 1957.

With M. Vogel and H. Rosenberg. Derivatives of Ferrocene. I. The Metalation of Ferrocene. Journal of Organic Chemistry, 22:8:900-903, August 1957.

With M. Vogel and H. Rosenberg. Derivatives of Ferrocene. II. Some Reduction Products of Benzoylferrocene and 1,1-Dibenzoylferrocene. Journal of Organic Chemistry, 22:8:1013-1016, August 1957.

With M. Vogel and H. Rosenberg. Derivatives of Ferrocene. III. The Preparation of Some Alkylferrocenes and Arylferrocenes. Journal of Organic Chemistry, 22:9:1016-1018, September 1957.

With D. W. Mayo and P. D. Shaw. Effect of Tetrahydrofuran on the Lithiation of Ferrocene. Chemistry and Industry, London, pp. 1388-1390, October 19, 1957.

With L. L. Coleman. Derivatives of Ferrocene. IV. Ferrocene-Containing Unsaturated Ketones. Journal of Organic Chemistry, 23:1:107-109, January 1958.

With L. L. Coleman. Alpha Beta Unsaturated Ketones. II. Copolymerization Reactions of Cinnamoylferrocene. Journal of Polymer Science, 28:116:207-211, February 1958.

With P. Shaw, D. Mayo, and A. M. Lovelace. Derivatives of Ferrocene. V. The Preparation of Some N-Substituted Ferrocenecarboxamides. Journal of Organic Chemistry, 23:3:505-507, March 1958.

With E. O. Fischer and H. Grubert. Ring Substitution Reactions of Dicyclopentadienylruthenium and Dicyclopentadienylosmium. Chemistry and Industry, London, pp. 756-757, June 21, 1958.

With S. I. Goldberg, D. W. Mayo, M. Vogel, and H. Rosenberg. Derivatives of Ferrocene. VI. Heteroannular Disubstitution of Ferrocene. Journal of Organic Chemistry, 24:6:824-826, June 1959.

With G. N. Schrauzer. Ferrocene and Related Organometallic π-Complexes. II. Cyclooctatetraene-Iron Tricarbonyl and Cyclooctatetraene-Diiron Hexacarbonyl. Chemistry and Industry, London, pp. 957-958, July 25, 1959.

With E. O. Fischer and H. Grubert. Ferrocene and Related Organometallic π-Complexes. I. The Aromatic Reactivity of Ferrocene, Ruthenocene, and Osmocene. Journal of the American Chemical Society, 82:1:76-82, January 5, 1960.

Ferrocene and Related Organometallic π-Complexes. III. An Unequivocal Synthesis of Rubrocene. Journal of the American Chemical Society, 82:8:2000-2001, April 20, 1960.

Cyclopentadienyl Compounds of Metals and Metalloids. Journal of Chemical Education, 37(11), 568–578, November 1960.

Ferrocene and Related Organometallic π-Complexes. IV. Some Ullman Reactions of Haloferrocenes. Journal of Organic Chemistry, 26(6):1802–1805, June 1961.

Ferrocene and Related Organometallic π-Complexes. V. Convenient Synthesis of Ferrocenyl Aryl Sulfides. Journal of Organic Chemistry, 26(9):3579–3580, September 1961.

Ferrocene and Related Organometallic π-Complexes. VI. Thermal Decomposition of Diferrocenylmercury. Inorganic Chemistry, 1(2):414–417, May 1962.

Addition of Alcohols to Methyl Propiolate. Journal of the American Chemical Society. (Pending.)

American Chemical Society Monograph on Reactions of Coordinated Ligands. Chapter on Ring Substitution Reactions of Metal Cyclopentadienyls and Metal Arenes. (Pending.)

Ferrocene and Related Organometallic π-Complexes. VII. Mercury-Bridged Ferrocenes. Journal of Organic Chemistry. (Pending.)

106

MARTIN VOGEL

Martin Vogel was born in Los Angeles, California, on March 7, 1935. He received a B.S. in chemistry in 1955 and a Ph. D. in chemistry in 1961 from the California Institute of Technology, Pasadena, California. Prior to receiving his bachelor's degree, he was employed in the chemical department of the California Institute of Technology. From July 1955 until October 1955 he was employed as a chemist by the Hughes Aircraft Company. At this time he entered the military service as a lieutenant in the United States Air Force, and was assigned to the Nonmetallic Materials Laboratory, Materials Central. At the conclusion of his military tour in October 1957, he returned to the California Institute of Technology where he received his Ph. D. on a National Science Foundation Predoctoral Fellowship. He is currently Assistant Professor of Chemistry at Rutgers University, New Brunswick, New Jersey.

Mr. Vogel is a member of the American Chemical Society, Sigma Xi, and Tau Beta Pi.

BIBLIOGRAPHY

With M. D. Rausch and H. Rosenberg. Ferrocene A Novel Organometallic Compound. Journal of Chemical Education, 34(6):268-272, June 1957.

With S. I. Goldberg, D. W. Mayo, H. Rosenberg, and M. D. Rausch. Derivatives of Ferrocene. VI. Heteroannular Disubstitution of Ferrocene. Journal of Organic Chemistry, 24(6):824-826, June 1959.

With P. R. Shafer, D. R. Davis, K. Nagarajan, and J. D. Roberts. Nuclear Magnetic Resonance Spectroscopy: Abnormal Splitting of Ethyl Groups Due to Molecular Asymmetry. In: Proceedings of the National Academy of Sciences 47:49, 1961.

HAROLD ROSENBERG

Harold Rosenberg was born June 27, 1923, in Chicago, Illinois. He received a B.S. in chemistry from Roosevelt College, Chicago, Illinois, in 1946. He was awarded the M.S in 1947 and the Ph. D in 1950 from the University of Illinois, Urbana, Illinois. From 1950 to 1951, he held the Air Force Post-Doctoral Fellowship with the Purdue Research Foundation at Purdue University. He carried out research there in fluorine chemistry under Professor E. T. McBee.

Mr. Rosenberg was employed by the General Luminescent Corporation, Chicago, Illinois, from 1941 to November 1942 when he enlisted in the United States Army. After separation from the service in 1945, he returned to Luminescent Corporation as Supervisor of Chemical Production From 1947 to 1950, he was employed as a teaching assistant at the University of Illinois. At the expiration of his post-doctoral fellowship at Purdue, in 1951, he came to the Materials Central. He is currently Senior Research Chemist in the Polymer Branch, Nonmetallic Materials Laboratory.

Mr Rosenberg is listed in the ninth and tenth editions of American Men of Science and in Who's Who in the Midwest. He is a Fellow of the Chemical Society, London, the American Institute of Chemists, and the New York Academy of Science. He is a member of Sigma Xi, the American Chemical Society, and the American Society for the Advancement of Science. He is a Consultant Member of the Chemistry Section, Research Division, American Ordnance Association and was the 1961 Chairman of the Professional Practices Committee, Dayton Section of the American Chemical Society. He was a member of the United States Scientific Advisory Committee for the 1958 Brussels International Exposition. His model of the ferrocene molecule was included among the United States scientific exhibits in the Science Pavilion of the Exposition. In 1959, he received the United States Department of State Public Service Scroll.

BIBLIOGRAPHY

Further Evaluation of Organofluorine Compounds for Use in Military Aircraft Paper presented at the One Hundred Twenty-second National Meeting of the American Chemical Society, Atlantic City, N J, September 1952

With J C Montelier Evaluation of Organic Fluorine Compounds for Use in Military Aircraft Industrial and Engineering Chemistry, 45 2283 2286 October 1953

Organic Derivatives of Germanium ortho Esters of 2-Alkoxyethanols Paper presented at the One Hundred Twenty-fourth National Meeting of the American Chemical Society, Chicago Ill, September 1953

Synthetic Materials for Future Engine Lubricants Paper presented at the Conference on Aircraft Power Plant Lubricants, Dayton, Ohio, Ma, 1956

With M. D. Rausch and M. Vogel. Ferrocene—A Novel Organometallic Compound. Journal of Chemical Education, 34(6): 268–272, June 1976.

Synthesis of New Base Stock Fluids. Paper presented at the Air Force-Navy-Industry Conference on Aircraft Lubricants, San Antonio, Tex., November 1956.

With M. D. Rausch and M. Vogel. Derivatives of Ferrocene. I. The Metalation of Ferrocene. Journal of Organic Chemistry, 22(8): 900–903, August 1957.

With M. D. Rausch and M. Vogel. Derivatives of Ferrocene. II. The Preparation and Reduction of Benzoyl and 1,1-Dibenzoylferrocene. Journal of Organic Chemistry, 22(8): 903–906, August 1957.

With M. D. Rausch and M. Vogel. Derivatives of Ferrocene. III. The Preparation of Some Acylferrocenes and Alkylferrocenes. Journal of Organic Chemistry, 22(9): 1016–1018, September 1957.

With S. I. Goldberg, D. W. Mayo, M. Vogel, and M. D. Rausch. Derivatives of Ferrocene. VI. Heteroannular Disubstitution of Ferrocene. Journal of Organic Chemistry, 26(6): 824–826, June 1959.

Some New Derivatives of Ferrocene. Paper presented at the Seventeenth International Congress of Pure and Applied Chemistry, Munich, Germany, September 1959.

With I. D. Groves and C. Tamborski. Organosilicon Compounds. I. Synthesis of Some Long-Chain Tetraalkylsilanes. Journal of Organic Chemistry, 25(2): 243–245, February 1960.

With C. Tamborski. Organosilicon Compounds. II. 1,1-Disubstituted Silacyclohexanes. Journal of Organic Chemistry, 25(2): 246-248 February 1960.

Functional Ferrocenes. Paper presented at the Forty-seventh National Meeting of the American Institute of Chemical Engineers, Baltimore, Md., May 1961.

Derivatives of Ferrocene

M. RAUSCH, M. VOGEL, and H. ROSENBERG

Part I. The Metalation of Ferrocene

ABSTRACT *The metalation of ferrocene by means of n-butyl-lithium and mercuric acetate has been further investigated. The lithiation reaction has been extended for the preparation of tri-methylsilylferrocene and 1,1'-di(trimethylsilyl)ferrocene. In the mercuration reaction, the ratio of starting materials has been varied in order to obtain optimum yields of either chloromercuri-ferrocene or 1,1'-dichloromercuriferrocene. Chloromercuriferro-cene has been converted to diferrocenylmercury by means of dispersed sodium, sodium stannite, and sodium iodide in ethanol.*

Since the discovery of ferrocene [1-3] in 1951, over one hundred technical publications have appeared in the literature concerning cyclopentadienyl-metal compounds.[4] In this and subsequent papers we wish to report some new derivatives of ferro-cene, as well as discuss the various synthetic methods by which substituted ferrocenes can be made.

One method for the preparation of ferrocene derivatives is by metalated intermediates. Ben-keser, Goggin, and Schroll,[5] and Nesmeyanov et al.[6] have lithiated ferrocene using n-butyllithium to produce a mixture of mono- and dilithioferrocene. These metalated intermediates have been con-verted to carboxy,[5,6] triphenylsilyl,[5] and amino[7] derivatives. Nesmeyanov et al. have also mercu-rated ferrocene[8] and have converted the mercu-rated intermediates to bromo and iodo derivatives.[9]

The present investigation was undertaken to determine the usefulness of these two reactions as practical methods for the preparation of mono- and disubstituted derivatives of ferrocene; part of our results are discussed herein. Initial experi-ments were directed toward improving the yields of mono- and dilithioferrocene, these metalated derivatives being characterized by carbonation to

the mixed mono- and dicarboxyferrocenes. In numerous experiments in which experimental con-ditions were varied, however, the total yield of mixed acids could not be increased to more than about 30%. These yields are consistent with the yields of ferrocene acids reported by the other investigators.[5,6]

Benkeser et al.[5] have also reported that the mix-ture of mono- and dilithioferrocene obtained from the reaction of ferrocene and n-butyllithium in ether reacts with triphenylchlorosilane to produce triphenylsilylferrocene and 1,1'-di(triphenylsilyl)-ferrocene. These two compounds were obtained in yields of 27% and 7%, respectively, or a total yield of 34%.

We have found that this reaction can also be applied to the synthesis of trialkylsilylferrocenes, and wish to report here the synthesis of trimethyl-silylferrocene (I) and 1,1'-di(trimethylsilyl)ferro-cene (II). Both I and II were isolated as mobile, distillable, orange-red liquids, possessing mild odors. Both appeared to be completely st   in light and in air, in contrast to several low   le-cular weight alkyl derivatives of ferroc   [?-??] The yields of I and II obtained were somewhat higher than the yields of carboxy- and triphenyl-

111
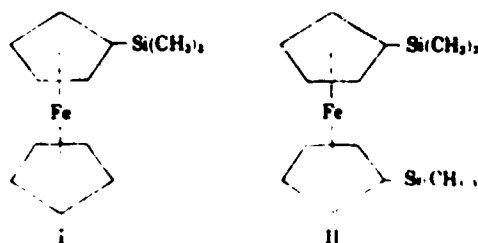
silylferrocene obtained by this method. It is also interesting to note that more disubstituted product was obtained than monosubstituted product, in contrast to the above results.

The infrared spectra of I and II were very similar, the only notable difference being strong absorption bands at 9.00 and 9.95 μ in the spectrum of I. Both bands were totally absent in the spectrum of II. These results are in good accord with the data of Rosenblum[ ] and of Pauson[ ] who have found that the bands at 9.00 and 9.95 μ are present in both ferrocene itself and in derivatives in which only one cyclopentadienyl ring is substituted, but are absent in derivatives in which both rings are substituted. Among the absorption bands in both spectra were strong bands at 8.0 μ, 13.2 μ, and strong absorption from 11.6 to 12.1 μ. These three regions of absorption may be assigned to CH₃ Si stretching and rocking vibrations.[ ]

The mercuration of ferrocene in either ether-alcohol or benzene-alcohol has been reported by Nesmeyanov et al. to produce a mixture of both chloromercuriferrocene (III) and 1,1'-dichloromercuriferrocene (IV).[ ] A study of this reaction indicates that the relative proportions of III and IV
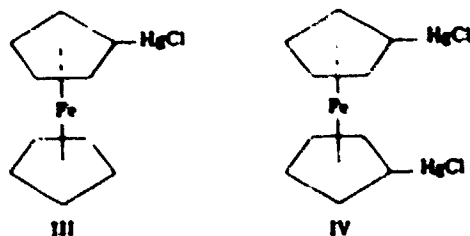
produced can be conveniently controlled by varying the ratio of the starting materials. Table I summarizes these results.

The mercuration of ferrocene to form III and IV can likewise be carried out in glacial acetic acid. This reaction requires no pressure vessel or additional high boiling solvent as does the well-known mercuration of benzene.[ ] Under these condi-

112

tions, however, some oxidation of ferrocene to the ferricinium ion, FeC₁₀H₁₀⁺, occurred, and the combined yield of III and IV was low. The use of ether-methanol as the solvent offers many advantages, avoiding oxidation of ferrocene and producing an excellent combined yield of III and IV. The facile formation and separation of these mercurated derivatives suggest them as useful intermediates in the preparation of additional ferrocene compounds in which either one or both cyclopentadienyl rings are substituted. Further studies along these lines are currently in progress in this laboratory.

The direct reaction of organomercury compounds with active halogen compounds such as alkyl halides, acid halides, etc., has been reported in only a few instances to yield the desired derivatives,[ ] these compounds being among the least reactive organometallics known.[ ] Attempts to react III with acetyl chloride and trimethylchlorosilane in toluene solution were likewise not successful and considerable oxidation occurred. In both instances, insoluble blue solids separated which were identified as ferricinium salts by means of their solubility characteristics, reactions, and ultraviolet spectra.

In an attempt to trans-metalate III using dispersed sodium, several unexpected results were obtained. When III was reacted with a 10-molar excess of dispersed sodium (40% in n-nonane) diluted with benzene and the reaction mixture hydrolyzed at room temperature, quantitative yields of ferrocene were obtained. In a similar experiment in which the reaction mixture was first carbonated with a dry ice-ether mixture and then hydrolyzed, a 70% yield of diferrocenyl-mercury (V) was isolated. This result is not entirely anomalous, since both sodium and sodium amalgam have been reported to convert compounds of the type RHgX to the symmetrical R₂Hg derivatives.[ ] It was subsequently found

V
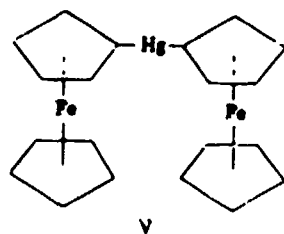
that contact of the reaction mixture with dry ice-
ether was not necessary to obtain V; direct
hydrolysis at the low temperatures afforded by
this refrigerant produced comparable results. No
carboxyferrocene was isolated from these re-
actions, indicating that probably *trans*-metalation
did not occur.

In a manner analogous to other compounds of
the type RHgX,[19,20] III reacted readily with a
solution of sodium stannite to produce V in good
yield. III also reacted rapidly with sodium iodide
in ethanol, another reagent which is frequently
used to convert RHgX compounds to R₂Hg com-
pounds.[18] In this reaction, two stable forms of V
with different melting points were isolated.

Attempts to metalate ferrocene directly using
either lithium metal in *n*-butyl ether or dispersed
sodium in tetrahydrofuran were unsuccessful. In
the latter reaction considerable destruction of
ferrocene occurred, and small amounts of ferric
oxide were isolated.

EXPERIMENTAL [21]

Lithiation of ferrocene and subsequent carbonation. In
general, the procedure followed was similar to that de-
scribed by Benkeser, Goggin, and Schroll.[1] For example,
in a typical experiment in which 0.123 mole of *n*-butyl-
lithium in 175 ml. of anhydrous ethyl ether was reacted
with 17.7 g. (0.095 mole) of ferrocene in 200 ml. of ether,
11.0 g. of ferrocene and 5.0 g. of the crude acid were ob-
tained. The neutralization equivalent of the crude acid,
determined potentiometrically in aqueous ethanol solution,
was 196, indicating a mixture of about 3 parts carboxy-
ferrocene to 1 part dicarboxyferrocene, assuming these
are the only two acids present.

*Trimethylsilylferrocene (I) and 1,1'-di(trimethylsilyl)ferro-
cene (II).* A suspension of 139.5 g. (0.75 mole) of ferrocene
in 1200 ml. of anhydrous ethyl ether (dried and distilled
over sodium) was placed in a 3-liter, 3-necked flask, fitted
with a stirrer, reflux condenser, addition funnel, and nitro-
gen inlet. Over a 1-hr. period was added 1000 ml. of a
1.55-molar solution of *n*-butyllithium in anhydrous ether.
Following the addition, all the ferrocene appeared to be
dissolved. The reaction mixture was then stirred under a
nitrogen atmosphere for 44 hr. at room temperature, during
which time an orange precipitate separated from the ether
solution. With stirring, 163.0 g. (1.50 moles) of trimethyl-

chlorosilane was added over a period of about 5 hr., in
order to maintain gentle reflux. The reaction mixture was
then refluxed for 15 hr., hydrolyzed with ice, and the aque-
ous and ether phases separated. The aqueous layer was
extracted once with ether and the combined ether phase
washed repeatedly with water to neutrality and dried over
Drierite.

The ether was evaporated leaving a dark orange-red
liquid and precipitated ferrocene. This mixture was chilled
in a dry ice-acetone bath in order to freeze out as much
ferrocene as possible, filtered, and the ferrocene washed
with a little ether. After drying the ferrocene weighed
35.1 g., m.p. 173–174°. The filtrate was placed in a 500-
ml. flask fitted with a 12-inch Vigreux column and warmed
under a pressure of 0.1 to 0.2 mm. of mercury. After
about 1 hr. additional unreacted ferrocene had sublimed
onto the column. Atmospheric pressure was then restored
and the column was removed, rinsed with acetone, dried,
and replaced. This procedure was repeated several times
until all the ferrocene appeared to have sublimed, and only
refluxing liquid was observed. From the acetone washings
an additional 6.5 g. of ferrocene was isolated, for a total
recovery of 41.6 g.

The remaining liquid was fractionally distilled using a
packed column and a distillation head equipped for total
reflux. After initial separation into low and high boiling
fractions, both fractions were redistilled through a 12-inch
Vigreux column equipped with a straight take-off head.

Following redistillation, 36.9 g. (19% yield) of I was
obtained as a dark orange-red mobile liquid possessing a
mild cedar-like odor, b.p. 64–65° (uncorr.) at 0.045 mm.
of mercury, m.p. 23°, n_D^{22} 1.5696.

Anal. Calcd. for C₁₃H₁₈SiFe: C, 60.47; H, 7.03; Fe,
21.63; Si, 10.88. Found: C, 60.58, 60.69; H, 7.17, 7.17;
Fe, 21.95, 21.69; Si, 10.64, 10.89.

The higher boiling fraction produced 66.5 g. (27% yield)
of II, b.p. 87–88° (uncorr.) at 0.060 to 0.070 mm. of mer-
cury, m.p. 16°, n_D^{22} 1.5454. II was similar in appearance
to I, although its odor was very faint.

Anal. Calcd. for C₁₆H₂₆Si₂Fe: C, 58.16; H, 7.93; Fe,
16.90; Si, 17.00. Found: C, 58.50, 58.13; H, 7.97, 7.98;
Fe, 16.63, 16.60; Si, 16.80, 16.82.

*Chloromercuriferrocene (III) and 1,1'-di(chloromercuri)-
ferrocene (IV).* (A) *Methanol-ethyl ether as the solvent.* In
general, modifications of the procedure described by Nes-
meyanov *et al.*[4] were used, by varying the ratio of the re-
actants as illustrated in Table I. III was obtained in the
form of golden-yellow leaflets, m.p. 193–194°, with decomp.
(lit.[4] m.p. 194–196°). IV was isolated as a yellow powdery
solid which did not melt at temperatures up to 300°. When
heated at elevated temperatures over a period of time, how-
ever, slow decomposition was observed with ferrocene sub-
liming on the tube.

(B) *Glacial acetic acid as the solvent.* A solution of 18.6 g.
(0.10 mole) of ferrocene in 400 ml. of glacial acetic acid was
heated to reflux, and a solution of 15.9 g. (0.05 mole) of
mercuric acetate in 100 ml. of hot glacial acetic acid was
added with stirring over a period of 1.25 hr. Following
the addition the reaction mixture was refluxed for 0.5 hr.
and then stirred for 16 hr. at room temperature. After
filtering from a small amount of metallic mercury which
had separated (0.4 g.), the filtrate was mixed with a solu-
tion of 4.1 g. (0.055 mole) of potassium chloride in 100 ml.

113

of a 1:1 mixture of ethanol and water. A brown solid separated (A), which was washed with benzene to remove ferrocene; after drying the solid weighed 9.5 g

The blue acidic filtrate was diluted with 500 ml. of water and a yellow solid separated, which after filtering, washing with water, and recrystallizing from cyclohexane produced a small amount of ferrocene. The filtrate was stirred with 50 g. of powdered zinc for about 2 hr. during which time the blue color was discharged. Extraction with benzene and removal of the solvent produced an additional 1.4 g. of ferrocene. From A, both III and IV were obtained by recrystallization from hot 1-butanol. The total amount of III isolated was 3.9 g., m.p. 192-193°, with decomp., or a yield of 14%. The total amount of IV isolated was 2.2 g., or a total yield of 14%.

Attempted reaction of III with trimethylchlorosilane. To a warm solution of 2.1 g. (0.005 mole) of III in 100 ml. of toluene (dried over sodium) was added 5.4 g. (0.05 mole) of trimethylchlorosilane. The reaction mixture was stirred under a nitrogen atmosphere for 3 hr. at 70°. During this period the solution darkened and a blue solid separated. The reaction mixture was diluted with 100 ml. of cold water and filtered. The light blue solid which was collected was washed with water and with toluene and dried, weighing 1.2 g. This solid was insoluble in common organic solvents, only slightly soluble in water, and was moderately soluble in dilute hydrochloric acid, forming a blue solution. The blue color was readily discharged upon addition of an excess of sodium hydroxide solution. The ultraviolet spectrum of a small sample in dilute hydrochloric acid was similar to that reported for the ferricinium ion.[16] From the toluene layer 0.7 g. of ferrocene was recovered.

A similar experiment was carried out using acetyl chloride in place of trimethylchlorosilane. In this reaction also, a similar blue solid was isolated and ferrocene was recovered.

Reaction of III with dispersed sodium. (A). *Isolation of ferrocene.* In a 3-necked 250 ml. flask was placed 2.9 g. (0.05 mole) of sodium dispersion (40% in n-nonane), and the dispersion diluted with 50 ml. of benzene (dried over sodium). With stirring and under a nitrogen atmosphere, 2.1 g. (0.005 mole) of III in 100 ml. of warm dried benzene was added over a period of 15 min., and the reaction mixture stirred at 25° for 3.5 hr. At the end of this period 35 ml. of 95% ethanol was cautiously added, followed by 50 ml. of water. The hydrolyzed mixture was filtered with suction and washed thoroughly with hot water and with benzene. The residue which remained (0.82 g.) appeared to be a gray powder containing small globules of mercury. The filtrate was separated into layers, the aqueous phase extracted with benzene, the combined benzene portion washed with water, and then the benzene solution dried over anhydrous magnesium sulfate. Filtration of the drying agent and evaporation of the solvent left 0.92 g. (99% yield) of ferrocene, m.p. 171-174° (uncorr.).

(B). *Isolation of diferrocenylmercury* (V). The apparatus and quantities of reactants were the same as outlined in (A). After stirring at 25° for 3.5 hr., the reaction mixture was poured onto a mixture of dry ice and ether. After cautious hydrolysis with 95% ethanol and with water, the mixture was vacuum-filtered. The aqueous and benzene phases were separated, and the benzene phase washed and dried over anhydrous magnesium sulfate. Removal of the

solvent by evaporation left a yellow-orange solid. This solid and the initially insoluble material were extracted with a small quantity of boiling xylene, filtered, and the filtrate cooled to produce 1.0 g. (70% yield) of orange crystals of V, m.p. 235-236°, with decomp. (lit.[4] m.p. 235-234°). Acidification of the basic aqueous phase produced no trace of solid acidic material.

When the above reaction was carried out at 50° instead of 25°, carbonation and hydrolysis produced some V and some light yellow powdery solid which was insoluble in hot xylene and in dilute potassium hydroxide solution, but which did react with hydrochloric acid to give a blue solution. Acidification of the aqueous layer produced a trace of insoluble yellow material.

Reaction of III with sodium stannite. To a suspension of 2.1 g. (0.005 mole) of III in 20 ml. of 95% ethanol and 50 ml. of water was added a solution of sodium stannite, previously prepared by mixing 5.0 g. of sodium hydroxide in 25 ml. of water with 1.8 g. of stannous chloride dihydrate in 25 ml. of water. The yellow-orange color was immediately discharged and a gray-black solid separated. After stirring for 3 hr., the mixture was vacuum filtered, the solid washed well with water, dried, and digested with a little boiling xylene. The residue consisted of a dark gray solid containing globules of mercury. Upon cooling the xylene solution, 1.0 g. (70% yield) of V separated as yellow-orange crystals, m.p. 230-233° (uncorr.). Recrystallization from xylene raised the melting point to 234-235°, with decomp.

Reaction of III with sodium iodide in ethanol. A mixture of 600 ml. of 95% ethanol, 10.5 g. of sodium iodide, and 2.1 g. (0.005 mole) of III was refluxed for 2 hr. After filtering the hot mixture a yellow-orange solid separated, m.p 215-225° (uncorr.). Two recrystallizations from xylene produced 0.9 g. (64% yield) of V, m.p. 235-236°, with decomp. Upon cooling and concentrating the ethanolic filtrate there was obtained 0.5 g. (35% yield) of an orange crystalline solid, m.p. 245-248°. Recrystallization from xylene produced a second form of V, m.p. 248-249°, with decomp.

Anal. Calcd. for $C_{20}H_{18}Fe_2Hg$: C, 42.09; H, 3.18; Fe, 19.57; Hg, 35.16. Found: C, 42.01, 41.99; H, 3.28, 3.15; Fe, 19.46, 19.41; Hg, 35.10, 35.24.

In two additional experiments both forms of V were obtained in each case. The infrared spectra of both forms of V (mulls in Nujol) were completely identical.

BIBLIOGRAPHY

(1) T. J. Kealy and P. L. Pauson, *Nature*, 168, 1039 (1951).

(2) S. A. Miller, J. A. Tebboth, and J. Tremaine, *J. Chem. Soc.*, 632 (1952).

(3) In this and subsequent papers from this laboratory, the generic name *ferrocene* will be used instead of

the more formal dicyclopentadienyliron (II). Furthermore, the system of nomenclature as outlined by Rosenblum [10] has been adopted.

(4) For excellent reviews on the subject, see: E. O. Fischer, *Angew. Chem.*, 67, 475 (1955); P. L. Pauson, *Quart. Revs. (London)*, 9, 391 (1955).

(5) R. A. Benkeser, D. Goggin, and G. Schroll, *J. Am. Chem. Soc.*, 76, 4027 (1954).

(6) A. N. Nesmeyanov, L. G. Perevalova, R. V. Golovnya, and O. A. Nesmeyanova, *Doklady Akad. Nauk SSSR*, 97, 459 (1954).

(7) A. N. Nesmeyanov, E. G. Perevalova, R. V. Golovnya, and L. S. Shilovtseva, *Doklady Akad. Nauk SSSR*, 102, 535 (1955).

(8) A. N. Nesmeyanov, E. G. Perevalova, and O. A. Nesmeyanova, *Doklady Akad. Nauk SSSR*, 100, 1099 (1955).

(9) The structural configuration which is shown for ferrocene is used for convenience only; the exact nature of the bonding is still in dispute.[4]

(10) M. Rosenblum, Ph. D. Thesis, Harvard University, 1953.

(11) A. N. Nesmeyanov and N. A. Vol'kenau, *Doklady Akad. Nauk SSSR*, 107, 262 (1956).

(12) M. Vogel, M. D. Rausch, and H. Rosenberg, unpublished results

(13) P. L. Pauson, *J. Am. Chem. Soc.*, 76, 2187 (1954).

(14) L. J. Bellamy, *The Infrared Spectra of Complex Molecules*, pp. 274–277, John Wiley and Sons, Inc., New York (1954).

(15) F. C. Whitmore, *Organic Compounds of Mercury*, pp. 35, 171, Chemical Catalog Co., New York (1921).

(16) K. A. Kobe and P. F. Lueth, *Ind. Eng. Chem.*, 34, 309 (1942).

(17) For example, see W. D. Schroeder and R. Q. Brewster, *J. Am. Chem. Soc.*, 60, 751 (1938).

(18) F. C. Whitmore, *Organic Compounds of Mercury*, pp. 38–84, Chemical Catalog Co., New York (1921).

(19) H. Gilman, *Organic Chemistry*, Vol. I, p. 550, John Wiley and Sons, Inc., New York (1943).

(20) J. L. Maynard, *J. Am. Chem. Soc.*, 46, 1510 (1942).

(21) All melting points and boiling points are corrected unless otherwise noted. Analyses were made by Schwarzkopf Microanalytical Laboratory, Woodside 77, N.Y.

Part 2. Some Reduction Products of Benzoylferrocene and 1,1'-Dibenzoylferrocene [1]

ABSTRACT —*The reduction of benzoyl- and 1,1'-dibenzoylferrocene to benzyl- and 1,1'dibenzylferrocene has been accomplished by either catalytic hydrogenation or by reduction with sodium and ethanol. 1-Hydroxybenzylferrocene has been prepared by the sodium borohydride reduction of benzoylferrocene, while the reduction of 1,1'-dibenzoylferrocene with lithium aluminum hydride has produced 1,1'-di(1-hydroxybenzyl)ferrocene. The action of a number of other reducing agents on these aryl ferrocenyl ketones is discussed.*

In the Friedel-Crafts reaction of ferrocene, benzoyl chloride and aluminum chloride, both benzoylferrocene (I)[2,3] and 1,1'-dibenzoylferrocene (II)[2,4,5] have been reported to be formed. We have further investigated this reaction and have found that by varying the method of addition and the molar ratio of the reactants, both I and II can be prepared in yields more satisfactory than any thus far reported.

Although Csendes[2] has reported the preparation of benzoylferrocene oxime, our attempts to prepare oximes, phenylhydrazones, and p-nitrophenylhydrazones by the usual methods were not successful. By resorting to more drastic conditions, however, both benzoylferrocene oxime and 1,1'-dibenzoylferrocene dioxime were obtained.

The Clemmensen reduction has successfully been applied to the preparation of ethyl-,[3,4] n-propyl-,[3] n-butyl-,[5] and long chain alkylferrocenes[7] from the corresponding ketones, as well as to the preparation of 1,1'-dibenzylferrocene (III)[5] from II. The reduction of I by the Clemmensen method proceeded anomalously, however. Upon extensive refluxing, a small yield of the expected product, benzylferrocene (IV), was obtained, although the primary reduction product was an as yet unidentified high melting orange-red solid (V). In several experiments V was the only product isolated from the reaction.

III IV
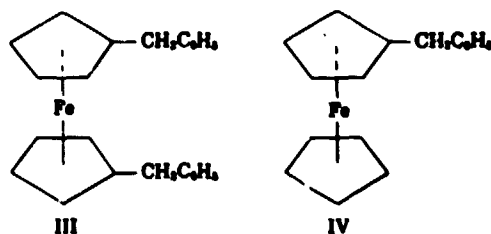
The reaction of I with the binary mixture, magnesium-magnesium iodide, has been carried out in this laboratory and elsewhere[3] to produce small yields of a reduction product (VI) similar in appearance and properties to V. The ultraviolet and visible spectra of V and VI are completely identical, while the infrared spectra are very nearly identical.

It was initially suspected that the reduction products V and VI were the *sym*-pinacol, since the magnesium-magnesium iodide mixture is commonly used for the preparation of pinacols from aromatic ketones[3,9] and the Clemmensen reduction of aromatic ketones occasionally produces pinacols rather than hydrocarbons.[10] Numerous elemental analyses of both V and VI have indicated, however, that only carbon, hydrogen, and iron are present, eliminating the possibility of a pinacol or other oxygen-containing compound. The structures of

117

V and VI are currently being investigated and detailed information will be published later.

Attempts to reduce II using magnesium-magnesium iodide in ethyl ether-benzene solution either at room temperature or at reflux resulted in the formation of an insoluble complex, and after hydrolysis only tarting ketone could be recovered. Preliminary experiments indicate that reduction of II does occur when solvents capable of producing higher temperatures are used.

While I did react with magnesium-magnesium iodide, it failed to undergo two other reactions which are commonly used to reduce aromatic ketones to bimolecular derivatives.[11-13] When I was stirred several days at 25° with powdered zinc and glacial acetic acid, only starting ketone was recovered. In an attempted photochemical reduction of I in 2-propanol, nearly all the ketone was recovered after 10 days exposure to sunlight, and only a very small amount of insoluble material resulted. This appeared to contain mostly iron oxide together with a trace of carbonaceous material. It has since been observed in this laboratory that certain derivatives of ferrocene in hydroxylic solvents are subject to photochemical decomposition. In a control photochemical experiment using benzophenone, a 97% yield of benzopinacol was obtained.

Both I and II could be reduced to the corresponding hydrocarbons IV and III by either catalytic hydrogenation or by "chemical" hydrogenation using sodium and ethanol. Although both reactions proceeded smoothly, the latter was more rapid and produced much better yields.

It has been reported[3] that the reaction of I with aluminum isopropoxide in isopropanol produced 1-propoxybenzylferrocene. In a similar experiment in which the reaction was carried out at higher temperatures using xylene as the solvent, we isolated a small yield of IV. In only one other case has the reduction of a ketone by aluminum isopropoxide been reported to yield a hydrocarbon, namely, the reduction of 9,9-dimethylanthrone-10 in xylene solution to 9,9-dimethyl-10,10-dihydroanthracene.[14]

The reduction of I with sodium borohydride in aqueous methanolic solution proceeded smoothly to produce the expected carbinol, 1-hydroxybenzylferrocene (VII). II was likewise reduced readily with lithium aluminum hydride in ether-benzene solution, and the tarry residue which resulted was purified to yield 1,1'-di(1-hydroxybenzyl)ferrocene (VIII).

118

VII   VIII
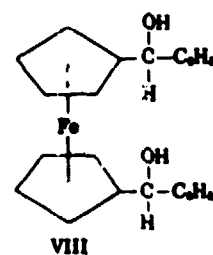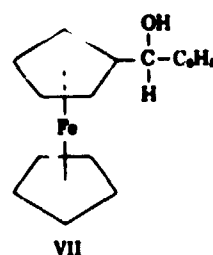
EXPERIMENTAL[15]

Benzoylferrocene (I). I was best prepared by the dropwise addition of a solution of equimolar quantities of benzoyl chloride and aluminum chloride to an equimolar quantity of ferrocene, using methylene chloride as the solvent. After hydrolysis and product workup, 70-75% yields of dark red needles of I were obtained by recrystallization from methanol, m.p. 108.1-108.3° (lit.[3] 111.5-112.0°). Extensive refluxing following the addition usually resulted in lower yields of I accompanied by increased amounts of tars.

1,1'-Dibenzoylferrocene (II). A modification of the procedure already reported[4] was adopted by adding the ferrocene in methylene chloride solution to slightly greater than two equivalent each of benzoyl chloride and aluminum chloride in the same solvent. In this manner, 81-91% yields of II were obtained in the form of purple needles, m.p. 106.5-106.7° (lit.[4] 103-106°).

1,1'-Dibenzoylferrocene dioxime. A solution of 2.0 g. of II, 4.0 g. of hydroxylamine hydrochloride, and 16.0 g. of potassium hydroxide in 100 ml. of 95% ethanol was refluxed for 4 hr. The reaction mixture was poured into 400 ml. of water and acidified with dilute hydrochloric acid. A yellow solid weighing 1.8 g. separated, m.p. 164-165° (uncorr.), with decomp. After several recrystallizations from methanol and water, the dioxime was collected in the form of golden-yellow crystals, m.p. 172-173°, with dec.

Anal. Calcd. for $C_{24}H_{20}FeN_2O_2$: C, 67.94; H, 4.75; Fe, 13.16; N, 6.60. Found: C, 68.12, 68.07; H, 4.63, 4.73; Fe, 12.86, 12.90; N, 6.36, 6.48.

Benzoylferrocene oxime. In a manner similar to the preparation of the dioxime, benzoylferrocene oxime was obtained as golden-yellow crystals, m.p. 139.6-160.0° (lit.[3] 160°).

Reduction of I by the Clemmensen method. A mixture of 60 g. of zinc dust, 4.5 g. of mercuric chloride, 3 ml. of concentrated hydrochloric acid and 75 ml. of water were stirred for 10 min. in a 1,000-ml., 3-necked flask fitted with stirrer and reflux condenser. The aqueous phase was removed by a pipet and the amalgamated zinc was covered with 30 ml. of water, 60 ml. of concentrated hydrochloric acid and 100 ml. of toluene. There was then added 17.4 g. (0.06 mole) of I and the mixture was stirred under reflux for 72 hr. During this period, five 25-ml. portions of concentrated hydrochloric acid were added occasionally in order to replenish the concentration of acid. Upon cooling to room temperature an appreciable amount of yellow solid has separated, and the reaction mixture was filtered and washed with hot toluene. The combined toluene portion washed to neutrality with water and dried over anhydrous magnesium sulfate. The solid which remained after evaporation of the solvent was extracted with 200 ml. of hot methanol, the

methanol solution was concentrated, and water was added to the cloud point. Upon cooling, 3.7 g. of benzylferrocene (IV) separated. IV was recrystallized from ethanol and water and was isolated as yellow crystals, m.p. 73-74° (lit.[10] 76°).

The methanol insoluble portion was recrystallized several times from either xylene and heptane, cyclohexane, or n-heptane to produce 5.0 g. of an orange-red solid (V). V did not melt when a melting point determination was made in the usual manner, but did slowly decompose when heated above 250°.

Anal. Found: C, 74.26, 74.38; H, 5.35, 5.43; Fe, 19.88, 19.92.

When the above reaction was carried out using less ketone and a shorter time of reaction, V was the only reduction product isolated.

Reduction of I by the binary mixture, magnesium-magnesium iodide. To a mixture of 1.7 g. (0.070 g. atom) of powdered magnesium in 50 ml. of ethyl ether and 50 ml. of dried benzene was added 5.6 g. (0.022 mole) of iodine with stirring. After the first few iodine crystals had been added the reaction mixture was warmed to initiate the reaction, which proceeded exothermically thereafter. After about 30 min. the reaction was complete and the mixture was nearly colorless. To this mixture was added 9.3 g. (0.032 mole) of I in 50 ml. of benzene. A deep violet color formed immediately upon contact of the ketone with the mixture, reminiscent of the color of the metal ketyls reported by Gomberg and Bachmann[4] and later workers. After shaking on a mechanical shaker overnight, the reaction mixture was hydrolyzed with 300 g. of ice containing 25 ml. of concentrated hydrochloric acid. The ether-benzene layer was washed with dilute sodium bicarbonate solution, dilute sodium bisulfite solution, water, and dried overnight over Drierite. The solvent was evaporated and the solid residue was extracted with 150 ml. of hot methanol. From the methanol extract, 7.5 g. of crude I was obtained, m.p. 102-106° (uncorr.).

The methanol insoluble material was recrystallized several times from hot n-heptane to produce 0.7 g. of VI. VI was obtained as fine orange-red crystals, which did not melt but slowly decomposed at elevated temperatures.

Anal. Found: C, 74.15, 74.28; H, 5.08, 5.23; Fe, 19.92, 20.06.

Catalytic hydrogenation of I. In a 500-ml. hydrogenation bottle were placed 8.70 g. (0.03 mole) of I, 1.0 g. of 5% platinum on charcoal, and 250 ml. of redistilled 1-butanol. The mixture was placed on a Parr hydrogenation apparatus under a pressure of 35 psi.; after about 30 hr. a theoretical uptake of hydrogen was noted. The catalyst was filtered and the butanol solution was concentrated almost to dryness. Several recrystallizations of the residue from ethanol and water produced 6 g. (70% yield) of IV in the form of yellow leaflets, m.p. 72-73°.

Catalytic hydrogenation of II. A mixture of 11.5 g. (0.03 mole) of II, 2.0 g. of 5% platinum on charcoal and 250 ml. of redistilled 1-butanol was hydrogenated as described above under a pressure of 65 psi. After 17 hr. a theoretical hydrogen uptake was noted and the catalyst was filtered. Removal of the solvent and several recrystallizations of the residue from hot methanol produced long yellow needles of III weighing 3.4 g. (65% yield), m.p. 97-99° (lit.[10] 102°).

Reduction of I by sodium and ethanol. A mixture of 1.50 g. (0.0052 mole) of I and 50 ml. of absolute ethanol was warmed to about 60° during which time all the ketone dissolved. With stirring, about 5 g. of small clean chunks of sodium metal was added at such a rate as to maintain the reaction temperature between 60° and 70°. During the addition the reaction mixture changed from a red color characteristic of the ketone to a thick yellow-orange solution. Following addition of all of the sodium, 25 ml. of additional ethanol was added and the solution was stirred at room temperature for an additional hour. Water was then added until the solution became cloudy, and the solution was cooled. After filtering and drying, 1.40 g. (98% yield) of yellow leaflets of IV was collected, m.p. 72-73°. One recrystallization from ethanol and water raised the melting point to 73.5-74.0°.

Anal. Calcd. for C₁₇H₁₆Fe: C, 73.93; H, 5.85; Fe, 20.22. Found: C, 74.07, 74.01; H, 6.06, 6.08; Fe, 20.11, 20.36.

In another experiment, a 95% yield of IV was obtained by this procedure.

Reduction of II by sodium and ethanol. In a manner similar to that described for the reduction of I, about 7.5 g. of sodium was added to a solution of 2.00 g. (0.0051 mole) of II in 75 ml. of absolute ethanol at 60-70°. Following addition of the sodium, 25 ml. of additional ethanol was added to the thick yellow solution and the mixture was stirred for 1 hr. at room temperature. Water was added and the yellow crystals which separated were dried and recrystallized from hot ethanol. Long yellow needles of III were obtained weighing 1.00 g., m.p. 105-106°. From the methanol mother liquor an additional 0.49 g. of III was recovered, for a total yield of 80%.

Anal. Calcd. for C₂₃H₂₀Fe: C, 78.70; H, 6.06; Fe, 15.24. Found: C, 78.40, 7.35; H, 6.16, 6.16; Fe, 15.05, 15.02.

A mixed melting point test of a sample of III prepared above and a sample obtained by means of catalytic hydrogenation melted intermediate between the two melting points. The infrared spectra of the two samples were identical.

In another experiment, a 72% yield of III was obtained by this procedure.

Reduction of II by lithium aluminum hydride. To a slurry of 1.32 g. (0.04 mole) of powdered lithium aluminum hydride in 250 ml. of ether was added 11.5 g. (0.030 mole) of II in 150 ml. of benzene and 50 ml. of ether over a 1 hr. period. The reaction mixture was refluxed with stirring for 16 hr., cooled, and most ether followed by dilute ammonium chloride solution was added. After filtering, the ether phase was washed with water and dried over Drierite. The solvent was evaporated leaving a dark viscous oil which was induced to crystallize by dissolving it in hot methanol and rapidly cooling in a dry ice-acetone bath. Seven g. of a yellow solid was thus obtained, m.p. 113-123° (uncorr.). After repeated crystallization from either methanol or ethanol, 5.0 g. of VIII was obtained in the form of yellow leaflets, m.p. 136-137°.

Anal. Calcd. for C₂₃H₂₂Fe: C, 72.37; H, 5.37; Fe, 14.02. Found: C, 72.02, 72.02; H, 5.43, 5.46; Fe, 14.01, 11.04.

Reduction of I by sodium borohydride. To a solution of 2.90 g. (0.01 mole) of I in 50 ml. of methanol was added 2.8 g. (0.10 mole) of sodium borohydride in 20 ml. of water

The mixture was stirred for 2 hr. and then filtered. The filtrate was cooled in ice and the excess sodium borohydride was decomposed with acetone. Following the addition of 50 ml. of water and 100 ml. of ether, the ether portion was washed with water and dried over anhydrous sodium sulfate. Removal of the solvent and two recrystallizations from ether-petroleum ether produced 1.9 g. (66% yield) of yellow crystals of VII, m.p. 80.3-80.5°.

Anal. Calcd. for C$_{17}$H$_{16}$FeO: C, 69.88; H, 5.52; Fe, 19.12. Found: C, 70.10, 69.92; H, 5.57, 5.67; Fe, 19.18, 19.22.

Reduction of I by aluminum isopropoxide. A solution of 1.37 g. (0.015 mole) of I and 7.1 g. (0.036 mole) of aluminum isopropoxide in 150 ml. of redistilled isopropyl alcohol was slowly distilled for 1 hr.; however, the presence of acetone in the distillate could not be detected. In order to raise the reaction temperature, 300 ml. of xylene was added and the isopropyl alcohol was removed by distillation. Continued slow distillation at 131-135° produced a distillate containing acetone. After hydrolysis with 150 ml. of 10% hydrochloric acid, the organic phase was washed with water and the solvent evaporated. Recrystallization of the residue produced 0.6 g. of benzylferrocene (IV), m.p. 73-74°. A mixed melting point test with an authentic sample was not depressed.

(1) Presented in part at the 131st Meeting of the American Chemical Society, Miami, Fla., April 7 to 12, 1957; see Abstracts of Papers, p. 47-O.

(2) M. Rosenblum, Ph.D. Thesis, Harvard University, 1953 (see Appendix).

(3) N. Weliky and E. S. Gould, New York Section, American Chemical Society, Meeting in Miniature, March 16, 1956.

(4) R. Riemschneider and D. Helm, *Ber.*, 89, 155 (1956).

(5) A. N. Nesmeyanov and N. A. Vol'kenau, *Doklady Akad. Nauk SSSR*, 107, 262 (1956).

(6) F. S. Arimoto and A. C. Haven, Jr., *J. Am. Chem. Soc.*, 77, 6295 (1955).

(7) M. Vogel, M. D. Rausch, and H. Rosenberg, unpublished results.

(8) M. Gomberg and W. E. Bachmann, *J. Am. Chem. Soc.*, 49, 236 (1927).

(9) M. D. Rausch, W. E. McEwen, and J. Kleinberg, *Chem. Revs.*, in press.

(10) R. C. Fuson, *Advanced Organic Chemistry*, John Wiley and Sons, Inc., New York (1950), p. 361.

(11) W. E. Bachmann and F. H. Moser, *J. Am. Chem. Soc.*, 54, 1124 (1932).

(12) R. P. Zelinski and M. Jurisch, *J. Am. Chem. Soc.*, 78, 1012 (1956).

(13) W. E. Bachmann, *Org. Syntheses*, Coll. Vol. II, 71 (1943).

(14) N. L. Wilds, *Org. Reactions* II, 178 (1944).

(15) All melting points are corrected unless otherwise noted. Analyses were made by Schwarzkopf Microanalytical Laboratory, Woodside 77, N. Y.

(16) B. F. Hallam and P. L. Pauson, *J. Chem. Soc.*, 3030 (1956).

Part 3. The Preparation of Some Acylferrocenes and Alkylferrocenes[1]

ABSTRACT   Several new acylferrocenes and 1,1'-diacylferrocenes
have been prepared and reduced to the corresponding alkylferro-
cenes and 1,1'-dialkylferrocenes.   Attempts to directly alkylate
ferrocene resulted in mixtures of polyalkylated products.

One of the first reactions of ferrocene[2,3] to be
investigated was the Friedel-Crafts acylation with
acid chlorides and anhydrides in the presence of
a suitable Lewis acid catalyst[4] under conditions
similar to those used for preparing acylbenzenes.
However, at the time of the inception of the
present investigation, no successful attempts to
directly alkylate ferrocene had been reported in
the literature.[?]

In order to prepare a series of alkylferrocenes
the direct alkylation of ferrocene was first inves-
tigated and found to be an unsatisfactory syn-
thetic method   The acylation of ferrocene and
subsequent reduction was then studied and many
new acylferrocenes and alkylferrocenes synthesized

It has been found that both acylferrocenes (I
and 1,1'-diacylferrocenes (II) can be prepared in
satisfactory yield by varying the ratio of ferro-

I   II

cene, acid chloride, and aluminum chloride, and
also the mode of addition   Compounds of type
I are prepared by the dropwise addition of the
acid chloride-aluminum chloride complex to the

ferrocene solution, using equimolar amounts of
acid chloride, catalyst and ferrocene.   The disub-
stituted derivatives, II, were prepared by adding
the ferrocene solution to the complex, using a
molar ratio of both the acid chloride and the alu-
minum chloride to ferrocene of greater than 2:1.

The preparation of both I and II by these pro-
cedures appears to be a very satisfactory synthetic
method   Using the appropriate procedure, either
was obtained uncontaminated by the other or by
unreacted ferrocene   The unaccounted ferrocene
was present in the form of tars   If the reaction
was carried out at room temperature instead of
at reflux, the amount of tar produced was con-
siderably decreased.   The yields of the diketones
tended to decrease with increasing molecular
weight, probably due to steric factors as well as
decreased reactivity of the acid chlorides   The
properties and analyses of the acylferrocenes and
1,1'-diacylferrocenes are summarized in Table 1

The catalytic hydrogenation of 1,1'-diacetyl-
ferrocene to 1,1'-diethylferrocene was successfully
carried out by Rosenblum   However, it was no
possible to extend this reaction to the higher
homologues under similar as well as stronger con-
ditions, although it was possible to duplicate
Rosenblum's work   This is in marked contras.
to aryl alkyl ketones which in general are readily
hydrogenated to hydrocarbons[?]   Consequently,
the Clemmensen reduction was used for the re-
duction of the higher homologs   Recently, Nes-
meyanov and Volkenau have used this same
method for the reduction of some lower 1,1'-

TABLE I.— Acylferrocenes

Ferrocene	M.P., °C.	Yield, %	C	Calcd. H	Fe	Analyses C	Found H	Fe
1,1'-Diacetyl-[a]	127.0-127.5	74	62.26	5.22	20.67	61.96, 61.98	5.29, 5.16	20.83, 20.91
1,1'-Dicaprylyl-[b]	54.8-56.0	65	71.23	8.74	12.74	71.55, 71.79	8.80, 8.89	13.00, 12.98
1,1'-Dicaprylyl-[b]	68.6-69.8	41	72.86	9.38	11.29	73.00, 73.17	9.38, 9.27	11.57, 11.46
1,1'-Dilauroyl-[b]	76.6-77.1	44	74.17	9.88	10.14	74.38, 74.37	9.75, 9.75	10.06, 10.05
1,1'-Ditridecanoyl	80.0-80.4	15	74.71	10.11	9.65	74.87, 74.77	10.19, 10.07	9.88, 9.84
1,1'-Dipalmitoyl-[c]	82.4-83.4	12	76.10	10.65	8.43	76.29, 76.19	10.30, 10.16	8.79, 9.01
Palmitoyl-[d]	59.0-59.8	46	73.57	9.50	13.16	74.07, 74.07	9.55, 9.36	13.20, 13.27

[a] Red crystalline solid. [b] Red-orange crystalline solid. [c] Salmon-colored solid. [d] Yellow crystalline solid.

TABLE II. Alkylferrocenes

Ferrocene	M.P., °C.	B.P., °C.	n_D^{25}	Yield, %	C	Calcd. H	Analyses Fe	C	Found H	Fe
1,1'-Diethyl-[a]	−35.0[b]	87-89 0.15 mm.	1.5761	60	69.45	7.49	23.06	69.12, 69.11	7.36, 7.28	23.10, 22.86
1,1'-Dioctyl-[a]	−16.0[c]	190-193 0.15 mm.	1.5214	58	76.07	10.32	13.61	76.30, 76.10	10.27, 10.49	13.09, 13.01
1,1'-Didecyl-[a]	11.5[d]	197-205 0.04 mm.	1.5142	50	77.23	10.80	11.97	78.01, 77.78	10.89, 10.69	11.47, 11.43
1,1'-Didodecyl-[e,f]	30.6-30.8				78.13	11.19	10.68	77.89, 77.93	11.01, 10.98	10.72, 10.93
1,1'-Ditridecyl-[e]	38.0-39.0			32	78.51	11.35	10.14	78.15, 78.17	11.07, 11.01	10.40, 10.41
1,1'-Dihexadecyl-[e]	41.2-42.4			33	79.45	11.75	8.80	79.59, 79.27	11.56, 11.65	8.82, 9.13
Hexadecyl-[e]	55.0-55.6			77	76.08	10.32	13.61	76.00, 76.26	10.32, 10.20	13.43, 13.65

[a] Dark-red liquid. [b] Melting point value obtained from reference 7. [c] d_4^{25} 1.0076; M.R. 124.12. [d] d_4^{25} 0.9863; M.R. 140.91. [e] Yellow crystalline solid. [f] Two unsaturated compounds, melting points 32.4-33.4° and 37.2-38.8° (uncorr.), were the only products isolated from the initial Clemmensen reduction. Both exhibited strong absorption in the trans double-bond region of the infrared (10.3 microns) and both could be hydrogenated to the expected compound. In a repeat experiment, 1,1'-didodecylferrocene was obtained directly.

diacylferrocenes. The properties and analyses of the alkylferrocenes and 1,1'-dialkylferrocenes are summarized in Table II.

1,1'-Diethylferrocene decomposed to a considerable extent after standing for several months, even in the absence of light and air. This is in accord with observations by other workers[7,8] concerning this and other low molecular weight liquid alkylferrocenes. On the other hand, 1,1'-dioctylferrocene and 1,1'-didecylferrocene, both liquids, appeared completely stable to air and light after several months storage.

A point worth noting is the unusual melting point of hexadecylferrocene (55.0-55.6°) compared to those of 1,1'-dioctylferrocene (−16.0°) and 1,1'-dihexadecylferrocene (41.2-42.4°). Hexadecylferrocene would be expected to have a lower melting point than its symmetrical isomer, 1,1'-dioctylferrocene, but it does not. Also, hexadecylferrocene is higher melting than even 1,1'-dihexadecylferro-

cene, the corresponding disubstituted derivative, which is very unusual among substituted aromatic compounds.

The question arises whether the diacylferrocenes and dialkylferrocenes are symmetrically or unsymmetrically substituted. Since none of these compounds absorb in the infrared in the region of 9.00 or 9.95 microns (peaks in these regions being indicative of unsymmetrical substitution according to the data of Rosenblum[9] and of Pauson[10]), it was concluded that these compounds were symmetrically substituted. The two monosubstituted compounds, palmitoylferrocene and hexadecylferrocene, did absorb in these regions as expected.

Three methods of direct alkylation of ferrocene were attempted; alcohols and 100% phosphoric acid, as successfully used for alkylating biphenyl[11]; alcohols and aluminum chloride, and alkyl es and aluminum chloride. All were successful the extent that little or no unreacted ferrocene could

be recovered by steam distillation. However, the product was always a mixture of polyalkylated liquid ferrocenes, boiling over a wide range, or undistillable tars. We were unable to obtain any pure fractions upon distillation, and it appeared that the yield of any one product was small. Nesmeyanov and Kochetkova [2] have recently reported similar work using alkyl halides and aluminum chloride. They were able to isolate by distillation mono-, di-, and penta-alkylated ferrocenes in very small yields.

EXPERIMENTAL [3]

1,1'-Diacylferrocenes (II). All 1,1'-diacylferrocenes were prepared by the reaction of the appropriate acid chloride with aluminum chloride and ferrocene. As a typical example, 1,1'-dicaprylylferrocene was prepared by adding 120 g. (0.90 mole) of anhydrous aluminum chloride to 350 ml. of methylene chloride (dried over calcium hydride) in a 2-liter, 3-necked flask equipped with stirrer, reflux condenser, and additional funnel. A nitrogen atmosphere and stirring were maintained throughout the reaction. Through the addition funnel, 146.5 g. (0.90 mole) of caprylyl chloride (prepared from caprylic acid and thionyl chloride in 80% yield) was slowly added, dissolving the aluminum chloride. A solution of 65.1 g. (0.35 mole) of ferrocene in 350 ml. of methylene chloride was added dropwise over a period of 2 hrs. Reaction was immediate as evidenced by the evolution of hydrogen chloride and the formation of a dark purple complex. After 70 hr. of stirring, hydrogen chloride evolution had ceased and the reaction mixture was hydrolyzed by pouring it onto 500 g. of ice. The two-phase system, which was badly emulsified, was filtered under vacuum and the phases were separated. The organic phase was washed until neutral and dried over anhydrous calcium sulfate. The methylene chloride solution was filtered free of drying agent and the solvent evaporated under an air stream. The crude product was recrystallized twice from methanol yielding 100.0 g. (65% yield) of orange-red crystals, m.p. 50–52° (uncorr.). An analytical sample was obtained after two additional recrystallizations from methanol, m.p. 51–56.0°. See Table I for the analysis.

Palmitoylferrocene. The equipment and procedure used were the same as for the preparation of the 1,1'-diacylferrocenes with the exception that the mode of addition was reversed. A solution of 133.1 g. (0.358 mole) of palmitoyl chloride (prepared in 88% yield from palmitic acid and thionyl chloride) and 77.5 g. (0.358 mole) of aluminum chloride in 200 ml. of anhydrous methylene chloride was added dropwise over a 2.5 hr. period to 101.8 g. (0.358 mole) of ferrocene dissolved in 600 ml. of methylene chloride. After stirring overnight the reaction mixture was worked up and the crude product isolated. One recrystallization from methanol produced 116.4 g. (43.8% yield) of yellow crystals, m.p. 57.0–58.7°. An analytical sample was obtained after one recrystallization from methanol, m.p. 59.0–59.8°. See Table I for the analysis.

Hydrogenation of 1,1'-diacetylferrocene. In a 500-ml hydrogenation bottle were placed 10.8 g. (0.040 mole) of 1,1'-diacetylferrocene dissolved in 300 ml. of methanol and 1 g. of 5% platinum on charcoal. The mixture was placed in a Parr hydrogenation apparatus at a pressure of 50 p.s.i. After 24 hr. the hydrogen uptake had reached the theoretical value. The solution was filtered free of catalyst and the methanol stripped off. Distillation of the crude product at reduced pressure gave 5.7 g. (60% yield) of a dark-red liquid with a strong camphoraceous odor, b.p. 87–89° at 0.15 mm., n_D^{25} 1.5761. Rosenblum reports b.p. 130–131° at 9 mm., n_D^{25} 1.760.[7]

Attempts to hydrogenate the higher 1,1'-diacylferrocenes under similar conditions and also at elevated temperatures gave starting material as the only isolatable product.

Clemmensen reduction of acyl- and 1,1'-diacylferrocenes. The acyl- and 1,1'-diacylferrocenes were reduced to the corresponding alkyl derivatives by refluxing with dilute hydrochloric acid and amalgamated zinc. In a typical experiment, 200 g. of granular zinc was amalgamated by stirring 5 min. with 15 g. of mercuric chloride, 250 ml. of water, and 10 ml. of concentrated hydrochloric acid in a 1-liter, 3-necked flask equipped with a stirrer and reflux condenser. The aqueous phase was pipetted off and 100 ml. of water, 200 ml. of concentrated hydrochloric acid, 43.8 g. (0.10 mole) of 1,1'-dicaprylylferrocene, and 100 ml. of benzene were added quickly in that order. The mixture was brought to reflux and stirred vigorously so that the amalgam was in contact with both phases. At intervals during the reaction, four 50-ml. portions of concentrated hydrochloric acid were added to maintain the acidity of the solution. After 52 hr. the mixture was brought to room temperature and filtered free of amalgam. The amalgam was washed with ether and the combined organic phase extracted with water to neutrality and dried over anhydrous calcium sulfate. After filtration from the drying agent, the solvent was concentrated under an air stream. The crude product was distilled twice under reduced pressure through a heated 9-inch Vigreux column yielding 23.8 g. (58% yield) of a dark red liquid b.p. 190–193° at 0.15 mm. See Table II for the analysis.

The solid alkyl- and 1,1'-dialkylferrocenes were purified by recrystallization from acetone.

Direct alkylation of ferrocene. As a typical example, 35.8 g. (0.192 mole) of ferrocene, 40.0 g. (0.30 mole) of anhydrous aluminum chloride, and 100 ml. of dry methylene chloride were placed in a 250-ml. 3-necked flask equipped with stirrer, reflux condenser and addition funnel. Stirring and a nitrogen atmosphere were maintained throughout the reaction. A solution of 17.6 g. (0.20 mole) of t-amyl alcohol in 50 ml. of dry methylene chloride was added over a period of 1.5 h. After 18 hr., the mixture was hydrolyzed with ice water and neutralized with sodium hydroxide solution. A steam distillation failed to produce any unreacted ferrocene. The residue from the steam distillation was extracted with benzene, the benzene solution washed with water, and dried over calcium chloride. After filtration from the drying agent, the solvent was evaporated under an air stream. The crude product was distilled twice under reduced pressure through a 24-inch column

123

packed with 0.25-inch glass helices. The main fraction, a dark-red liquid, weighed 5.0 g., b.p. 62 64° at 0.1 mm., n_D^{42} 1.5683. The elemental analysis was intermediate between those calculated for the mono- and disubstituted derivatives.

Anal. Calcd. for $C_1H_{20}Fe$: C, 70.34; H, 7.87; Fe, 21.79. Calcd. $C_{20}H_{30}$ Fe: C, 73.62; H, 9.27; Fe, 17.11. Found: C, 72.17, 72.28; H, 8.19, 8.23; Fe, 19.57, 19.55.

Similarly, ferrocene was alkylated with *n*-decyl alcohol and with *n*-decyl chloride by refluxing several days with excess aluminum chloride in methylene chloride solution. The reaction of ferrocene with either *t*-amyl alcohol or *n*-amyl alcohol for several hours at 110-115° with 100% phosphoric acid as the solvent also produced alkylated derivatives. The products in every case were mixtures of liquid alkylferrocenes, none of which could be readily separated into pure compounds by distillation or by chromatography on alumina.

BIBLIOGRAPHY

(1) Presented in part at the 131st Meeting of the American Chemical Society, Miami, Fla., April 7 to 12, 1957; see Abstracts of Papers, pp. 47-50.

(2) T. J. Kealy and P. L. Pauson, *Nature*, 168, 1039 (1951).

(3) S. A. Miller, J. A. Tebboth, and J. F. Tremaine, *J. Chem. Soc.*, 632 (1952).

(4) R. B. Woodward, M. Rosenblum, and M. C. Whiting, *J. Am. Chem. Soc.*, 74, 3458 (1952).

(5) V. Weinmayr, *J. Am. Chem. Soc.*, 77, 3009 (1955).

(6) P. L. Pauson, *Quart. Revs.*, 9, 391 (1955).

(7) M. Rosenblum, Ph. D. Thesis, Harvard University, 1953.

(8) W. H. Hartung and R. Simonoff, *Org. Reactions*, *VII*, 263-326 (1953).

(9) A. N. Nesmeyanov and N. A. Vol'kenau, *Doklady Akad. Nauk SSSR*, 107, 262 (1956).

(10) P. L. Pauson, *J. Am. Chem. Soc.*, 76, 2187 (1954).

(11) I. A. Romadan and V. K. Berzinya, *J. Gen. Chem. USSR*, 25, 265 (1955).

(12) A. N. Nesmeyanov and N. S. Kochetkova, *Doklady Akad. Nauk SSSR*, 109, 543 (1956).

(13) All melting points are corrected unless otherwise noted; boiling points are not corrected. Analyses were made by Schwarzkopf Microanalytical Laboratory, Woodside 77, N.Y.

WARREN R. GRIFFIN

A Room Temperature Vulcanization System for Selected Fluorine-Containing Polymers

1958

WARREN R. GRIFFIN

Warren R. Griffin was born January 1, 1932, in Rochester, New Hampshire. He was awarded a B.S. in chemical engineering by the University of New Hampshire in 1954. He then joined the Goodyear Tire and Rubber Company in Akron, Ohio, until December 1954 when he entered active military duty as a lieutenant in the United States Air Force. He was assigned to the Materials Central, and, at the expiration of his military tour, elected to remain with the Materials Central in a civilian capacity. He is currently assigned to the Elastomers Section of the Elastomers and Coatings Branch, Nonmetallic Materials Laboratory.

Mr. Griffin is a member of the American Chemical Society and was Chairman of the Fall (1961) Technical Session of the Southern Ohio Rubber Group, a division of the American Chemical Society.

His inventions include "Room Temperature Vulcanization of Elastomers" and a "Reclaiming Process for Fluorocarbon Elastomers" He was presented an Outstanding Inventor Award in 1960.

BIBLIOGRAPHY

Rubber in a Nuclear Environment. Paper presented at the First Semi-Annual Radiation Effects Symposium, May 1957.

WADC Evaluation of Experimental Polymers. Paper presented at the Joint WADC-UD Conference, March 1957. Published in Rubber World, 136(5): 687-694, August 1957.

With L. E. Coleman and D. A. Rausch. Polymerization of Some 1-Alkyl-1-Hydroperfluoroalkyl Acrylates. Journal of Chemical and Engineering Data, 3(1): 113-171, April 1958.

Radiation Effects on Elastomers. Paper presented before the New York Rubber Group of the American Chemical Society, October 1958. Abstract published in Rubber World, 139(2): 379, November 1958.

A Room Temperature Vulcanization System for Selected Fluorine-Containing Elastomers. Paper presented at the WADC Science Engineering Symposium, October 1959.

Characterization of New Elastomers. Paper presented at the Air Force Materials Symposium, Phoenix, Arizona, September 1961. Published in the proceedings of the conference.

Elastomer Research at WADD. Paper presented at the Joint Army-Navy-Air Force Conference on Elastomer Research, October 1960. Published in the proceedings of the conference.

Fluoroelastomers--Their Status as Engineering Materials. To be published as a chapter of the Encyclopedia of Engineering Materials and Processes. In preparation by the Reinhold Publishing Corporation, New York, N.Y.

A Room Temperature Vulcanization System for Selected Fluorine-Containing Polymers

W. R. GRIFFIN

ABSTRACT—*The development of a room temperature vulcanization system for selected fluorine-containing polymers is described. A theory is postulated to explain the vulcanization involving attachment of reactive sites to the polymers at elevated temperatures followed by cross-linking through these sites at room temperatures. The formulation, characteristics and test data are given for a hexafluoropropylene-vinylidene fluoride copolymer (Viton A*) vulcanized by this system. The technique appears applicable to the preparation of sealants, aerodynamic smoothers and other related materials urgently required by the Air Force for advanced vehicles.*

Section 1

INTRODUCTION

This report concerns the development of a room temperature vulcanization system for fluorinated hydrocarbon polymers.

Room temperature vulcanization is a necessary feature of the polymeric liquids used for fuel tank and cabin pressurization sealants, potting compounds and many other related products. Without this feature, delicate electronic equipment, large wing and cabin structures, and perhaps whole aircraft would require exposure to normal vulcanization temperatures (275° to 320° F). While such exposures are not impossible, the need for high vulcanizing temperatures has discouraged the use of many elastomeric polymers which would have otherwise provided a basis for sealant materials.

Subsonic aircraft operating under the environments encountered during world wide operation (−65° to 160° F) have employed sealant materials based on liquid polysulfide polymers and have been generally satisfactory. However, they are limited in thermal stability to 275° F and with the advent of supersonic aircraft, the need for sealant materials in the 500°-600° F range became urgent.

The fluorinated hydrocarbon elastomers were known to possess the necessary thermal stability and fluid resistance, (1) but prior to the investigation described in this report required 300° and 400° F temperatures with applied pressure for complete vulcanization. Although liquid polymers of this type were not available during the investigation, the room temperature vulcanization of dry polymers prepared from solvent solution was believed feasible and would be a useful contribution.

The approach was based upon the assumption that reactive "handles" attached to polymers at normal vulcanization temperatures (275°-320° F) could provide reactive sites for room temperature cross-linking by another agent. The commercially available fluorinated polymer, Viton A (2) (a copolymer of hexafluoropropylene-vinylidene

fluoride) was selected for study. It was modified by a reaction with diallylamine in the presence of magnesium oxide, followed by attempts at vulcanization with a variety of cross-linking agents. The materials, methods of preparation, and the physical properties of Viton A vulcanized by this system are described.

While information presented on actual preparation of sealant materials is quite preliminary, with many facets yet to be explored, this discovery could provide a major break-through in the development of sealant materials for the 500° to 600° F range.

Section 2.

EXPLORATORY CROSS-LINKING STUDIES

The general approach used in this development was based upon the assumption that reactive sites could be attached at elevated temperatures to the polymer and attacked at room temperature by a suitable cross-linking agent.

Early attempts to vulcanize Viton A at room temperature were through chelation. The polymer was reacted for one hour at 300° F with two parts of diethanolamine in the presence of magnesium oxide. Following this treatment, the modified polymer was refined on a tight mill to insure a uniform dispersion. This product was then dissolved in methyl ethyl ketone, mixed with one part of cobaltous chloride and flowed out on a steel plate. After five days at room temperature, the flowout attained a good state of vulcanization. The cobaltous ion was erroneously assumed to have been chelated by the attached diethanolamine and the cross-linking to have resulted because the ligand was attached to the polymer chain.

While the early work yielded much valuable information on solvents, processing techniques and reactions of fluorinated polymers, cross-linking through chelation appeared to be plagued by too many complex variables to emerge as a practical system. However, much evidence supported the original assumption that the secondary amine of diethanolamine would react with selected fluorinated polymers and result in an adduct to the polymer chain. The eventual solution to the problem of a practical room temperature cross-linking system employed this reaction to attach pendant groups which contained carbon-carbon unsaturation.

Section 3.

THE ROOM TEMPERATURE VULCANIZATION SYSTEM

Introduction— The exploratory investigation suggested that a secondary amine structure would attach to the polymer chains without causing vulcanization. Diallylamine, for example, possesses the necessary secondary amine for attachment and carbon-carbon unsaturation for low temperature cross-linking sites. Therefore, after considerable experimentation, a system was devised for investigating this amine as a method of introducing reactive sites

Formulation— The principle ingredients of this system were the fluorinated polymer, magnesium oxide, medium thermal carbon black, diallylamine, and hexamethylene dithiol. As previously stated, the fluorinated polymer was Viton A. Briefly, the intended functions of the various ingredients of this system are as follows:

Magnesium—decomposes the amine hydrohalide salt which is formed when the amine and the polymer react and stabilizes the polymer during high temperature exposure.

Carbon black—provides high solids content solutions with reduced nerve and enhances the physical properties of the vulcanizate.

Diallylamine—provides in the polymer chains reactive sites for room temperature cross-linking.

Hexamethylene dithiol—serves as a cross-linking agent by adding to the unsaturation of the reactive sites.

Evidence supported the need also for a basic catalyst and the presence of moisture for the room temperature reaction.

While it would have been more disirable to use a true liquid polymer, this system was demonstrated with a solvent solution. The total system was separated into two parts as shown in the following formulation. This separation resulted in storage stability for each part.

Part A	Parts per hundred of polymer by weight
Viton A	100
Medium Thermal Carbon Black	30
Magnesium Oxide	10
Diallylamine	4
Methyl Ethyl Ketone	

Part B	
Hexamethylene Dithiol	1.5
Tri-n-amylamine	0.5

130

Preparation of Part A—The ingredients of Part A, exclusive of the solvent, were weighed to an accuracy of plus or minus one percent. The liquid diallylamine was absorbed into the carbon black on the balance to minimize loss and to provide faster mixing. The polymer was banded on a water cooled 3" x " laboratory mill with the roll separation adjusted to provide a rolling bank in the nip of the rolls. The carbon black containing the diallylamine was added and followed immediately by the magnesium oxide. The presence of dry carbon black prevented the magnesium oxide from caking on the unbanded roll. The "drop through" was returned to the nip until all ingredients were in a single mass. The mass was then cut from the roll, and passed through close set rolls four to six times to provide a uniform dispersion and sheeted from a wider roll separation to a convenient thickness for the next operation.

The sheet was placed in a standard ASTM mold which had been liberally coated with surfactant mold release. The mold was then placed in a hydraulic laboratory press at 300° F under sufficient pressure to keep it tightly closed. After a reaction time of two hours, the rubber sheet was stripped from the hot mold and the surfactant removed with water. After the flash was removed and discarded, the sheet was refined on a tight mill to break up any agglomerates and to prepare the stock for rapid attack by the solvent.

The ribbon of heat-treated stock was weighed and placed in a suitable container with an equal amount of methyl ethyl ketone. The stability of Part A prepared under these conditions exceeded three months at ambient laboratory temperatures. During longer storage, the magnesium oxide or carbon black may form an unstable gel with the polymer but this could perhaps be removed by passing through a paint mill.

Preparation of Part B—As indicated in the formulation, Part B was a mixture of hexamethylene dithiol and tri-n-amylamine. The hexamethylene dimercaptan was selected in preference to others because it had liquid state, low vapor pressure, and mild odor at normal laboratory temperatures. Tri-n-amylamine was chosen as the basic catalyst because it was liquid at room temperature, strongly basic, and found to have little effect in the vulcanizate after high temperature exposure.

Preparation of the Vulcanizate—The vulcanizate was prepared from a uniform dispersion of Part B into Part A. Air entrapped during this mixing operation was allowed to escape before a flowout was made on a clean steel plate. After 24 hours at room temperature, the flowout had sufficient strength to be stripped from the plate. Partial vulcanization had occurred during this period as indicated by insolubility in methyl ethyl ketone.

The catalyzed solution remaining in the container retained fluid properties for three days. The absence of moisture was assumed to have been the cause of the long pot life.

Properties of the Vulcanizate—The properties of the flowout were determined during the cross-linking period. The rate of vulcanization at room temperature was traced by measurements of tensile strength, percent elongation, hardness and permanent set after break of the specimen. The test specimens were microdumbbells measuring ⅛" x ⅛" in the constricted section with ½" tabs. (3) The tests, except hardness, were performed on a modified Twing-Albert paper tensile tester, used because of its sensitivity to small changes in tensile strength. These measurements are displayed graphically in Figure 1. The test data obtained are presented in the Appendix, Table I.

These periodic measurements indicated a good state of vulcanization after seven days at room temperature. Therefore, test specimens, exhibiting this state of vulcanization were selected for high temperature tests. Dumbbells were exposed to JP-4 jet engine fuel in a pressure bomb at 400° F for 70 hours. The room temperature vulcanized elastomer displayed excellent resistance to the hot fluid and also showed little additional vulcanization occurring at this higher temperature. Similar samples were exposed to 500° F air for 70 hours in a circulating air oven. The samples retained most of their original properties, but results indicated that oxidation resistance was less than that possessed by conventional Viton A vulcanizates.(4) A summary of these tests is presented in the Appendix, Table II.

Section 4.

PROCESS REFINEMENTS

During the investigation of the diallylamine-dimercaptan system, several undesirable features were recognized:

A portion of the diallylamine was lost through evaporation during the processing of Part A.

The stock tended to stick to the mold during the 300° F treatment.

131
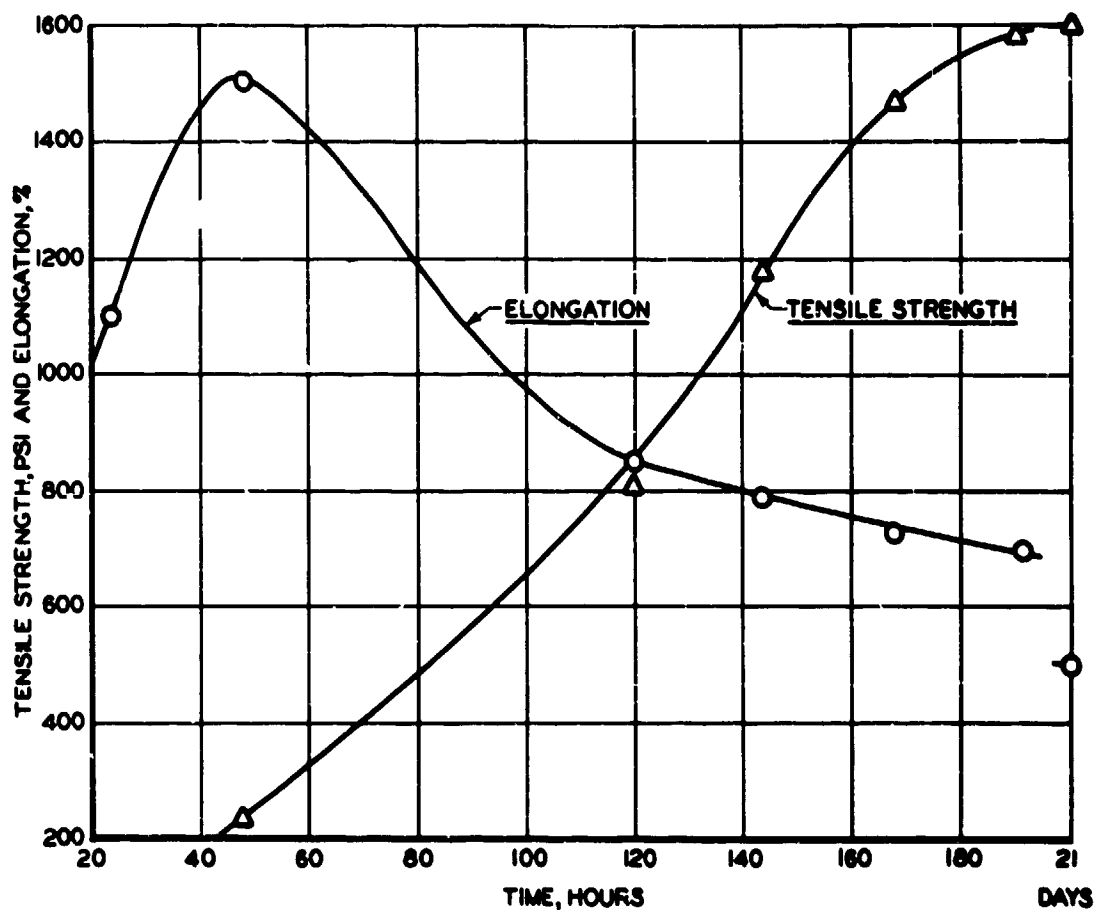
Figure 1. Tensile strength and elongation as a function of time for room temperature vulcanizing Viton A.

The use of water to remove the release agent caused a variable rate of vulcanization.

Methyl ethyl ketone as the solvent tended to form blisters in flowouts.

Hexamethylene dithiol was not commercially available.

Attempts have been made to overcome these difficulties. For example, the partial loss of diallylamine during the milling operation, prior to the heat treatment, was recognized as a large variable in the formulation. This difficulty was overcome by forming the less volatile hydrochloride of the diallylamine. Since the strongly basic magnesium oxide used in the original formulation decomposed the hydrochloride during the milling operation, it was replaced by magnesium carbonate.

Methods to eliminate the use of water for removing mold release materials were also studied since moisture directly affected the rate of room temperature vulcanization and the length of pot life for the catalyzed solution. Cellophane was found to be an excellent release material for the stock during the press treatment. The use of a hot air autoclave could also eliminate the need for mold release, but has not as yet been studied.

Studies to replace the hexamethylene dithiol, which was not commercially available, were undertaken. Glycol dimercapto-acetate exhibited desirable chemical and physical characteristics and demonstrated the capability of vulcanizing the modified polymer to good physical properties. High temperature tests have not been completed

but a suggested formulation for future investigation could be:

Part A	Parts per hundred of polymer by weight
Fluorinated Polymer	100
Medium Thermal Carbon Black	30
Magnesium Carbonate (C.P.)	20
Diallylamine Hydrochloride	1
Ethylacetate	Dependent upon desired viscosity

Part B

Glycol Dimercapto-acetate	1.5
Tri-n-amylamine	0.1-.25 dependent upon desired rate of vulcanization.
Acetone	As needed to make a homogeneous solution.

Section 5.

THEORETICAL

This approach outlined for a room temperature vulcanization system is based upon the assumption that chemically active sites, through which cross-linking with other chemicals can take place at lower temperatures, can be attached to the polymer. Many systems can be envisioned using this basic approach, but few emerge as being practical. The diallylamine-dimercaptan combination as described in this report is a practical system for certain fluorine-containing polymers.

The formation of the active site was the important first step. Amines as a class of chemicals were known to be reactive toward fluorinated hydrocarbon polymers. Diamines have been recommended in conventional dry rubber compounding as cross-linking agents for these polymers. (4) The mechanism of this cross-linking reaction has been partially established as the dehydrohalogenation of the polymer followed by the addition of free amine to the resulting double bond.(5) An acid acceptor decomposes the amine hydrohalide formed and allows the reaction to go to completion. The vulcanization of hexafluoropropylene-vinylidene fluoride copolymer with monoamines such as n-butyl amine suggests that a primary amine structure possesses a difunctional character. Thus, a secondary amine is necessary in order that the reactive site may be attached without cross-linking the polymer. It is theorized

that diallylamine will react with fluorinated polymers, which normally cross-link with diamines, and become a pendant group as shown in the first reaction

Reaction No. 1 Reactive Site Formation
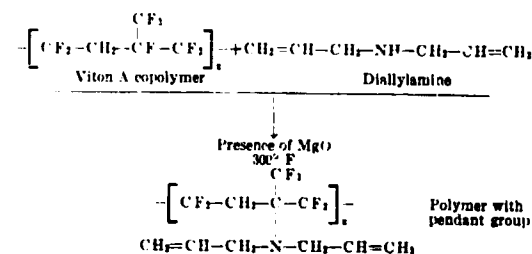
The polymer did not cross-link during reaction at 300° F. However, treatment at 320° F cause partial vulcanization, showing that the allylic unsaturation was present after the treatment, and at 320° F, it became active. The polymer thus modified was extremely reactive toward diamines. Hexamethylene diamine gelled a solution before complete mixing could take place. Para-phenylene diamine was found to be slower, but continued to cross-link at high temperatures. The presence of a secondary amine, which could further react with the polymer, could have resulted from the addition of a primary amine structure to the allylic unsaturation. Piperazine was also able to affect vulcanization while attempts to vulcanize the unmodified polymer at room temperature with piperazine met with failure.(6) Based upon this evidence, the diallylamine is assumed to be adducted to the polymer chain and to be somewhat activated by the fluorinated structure.

A room temperature cross-linking agent, which would be active toward this unsaturation was the next important feature of the system described. Since secondary amine structures continued to cross-link at elevated temperatures, the agent must be difunctional and lose its activity after adding to the allylic unsaturation.

Piperazine and dimercaptans were found to possess these qualities, but hexamethylene dithiol was selected as being more stable and easier to control. The proposed cross-linking reaction is depicted as follows:

Reaction No. 2   Cross-link Formation

Polymer with
pendant group +HS –CH₂–CH₂–CH₂–CH₂–CH₂–CH₂– SH
Hexamethylene dithiol

Presence of tri-n-propylamine and moisture
75° F

$$-\left[CF_2-CH \quad N-CF_3\right]_x-$$
CF₃

CH₂–CH–CH₂–N–CH₂–CH–CH₃

S

(CH₂)₆

S

Additional site
for cross-linking

CH₃–CH–CH₂–N–CH₂–CH=CH₂

$$-\left[CF_2-CH₂-C-CF_3\right]_x-$$
CF₃
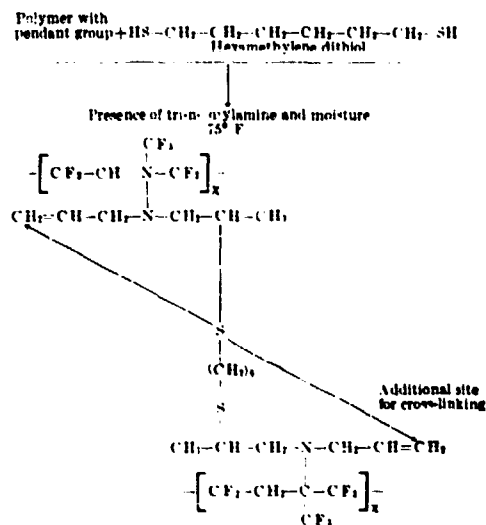
No sponging occurred during the vulcanization, and as has been demonstrated, the seven day vulcanized sheet was stable to 400° and 500° F temperatures with little additional cross-linking occurring. It is, therefore, postulated that dimercaptans, in the presence of a tertiary amine and moisture, add to the allylic unsaturation of the reactive sites and complete the vulcanization reaction at room temperature without by-product formation.

Section 6.

SUMMARY

To satisfy an urgent Air Force requirement for sealant materials and related products capable of withstanding high temperatures, a research program was begun on room temperature vulcanization systems for the fluorinated polymers. The successful results obtained under this program should provide a sound basis for the rapid development of the required products since a practical system for room temperature cross-linking has evolved.

This system is based upon the principle that active unsaturation could be attached to the polymer chain by a reaction with diallylamine in the presence of magnesium oxide. Through these sites, dimercaptans such as hexamethylene dithiol and glycoldimercapto-acetate, when aided by

tertiary amines and moisture, were shown to cross-link the polymer at room termperature.

The vulcanizate developed essentially full properties in seven days and demonstrated excellent resistance to jet engine fuel at 400° F and air at 500° F after a period of 70 hours.

It is recognized that the system described is one of many, and that it is in need of further refinements. For example, the end products required are usually based upon liquid polymers, rather than solvent solutions as used in this study. Adhesion to aircraft construction materials is poor and requires improvement. The laboratory method of preparation is also in need of refinements for larger volume production.

In spite of its deficiencies, this system is considered to be of major importance because it is the first to be disclosed in publications for cross-linking the fluorinated hydrocarbon polymers at room temperatures.(4) Immediate application in the area of fuel tank and structure sealants, followed by its investigation in bladder type fuel cells, fill and drain type of sealants for rocket fuel tanks, coated fabrics and dampening materials for electronic instruments, is anticipated.

APPENDIX

TABLE I.—Rate of cross-linking of room temperature vulcanizing Viton A

Time after catalyzing, hrs.	Tensile strength, psi	Elongation, percent	Break set, percent	Hardness shore A
24	73	1100	240	30
48	235	1500	200	45
120	610	850	90	55
144	1180	790	70	55
168	1470	730	54	57
192	1500	770	40	58
21 days	1600	500	20	62

TABLE II.— Aging resistance of room temperature vulcanizing Viton A

Aging conditions	Tensile strength, psi	Elongation, percent	Hardness shore A	Volume change percent
Original*	1500	700	57	....
70 hours at 400° F JP-4 fuel	1800	550	53	+ 7
70 hours at 500° F air oven	1450	320	6	– 13

*Vulcanized 168 hours at room temperature.

TABLE III.—*List of materials*

Material	Source
n-Butylamine	Eastman Organic Chemicals
Cobaltous chloride	Fischer Scientific Company
Diallylamine	Shell Chemical Corporation
Diallylamine hydrochloride	Prepared from Diallylamine
Diethanolamine	Dow Chemical Company
Glycol dimercapto-acetate	Evans Chemetic Inc.
Hexamethylene diamine	Mathieson Company, Inc.
Hexamethylene dithiol	Aldrich Chemical Company
Magnesium carbonate	
Magnesium oxide	Mallinckrodt Chemical Works
Medium thermal carbon black	Godfrey L. Cabot, Inc.
p-Phenylene diamine	Eastman Organic Chemicals
Piperazine	Wyandotte Chemicals Corporation
Tri-n-amylamine	Eastman Organic Chemicals
Viton A	E. I. du Pont de Nemours, Inc.

BIBLIOGRAPHY

1. Griffin, W. R., "WADC Evaluation of Experimental Polymers", *Rubber World*, Vol. 136, No. 5, pp. 601 and 692, August 1957.

2. Dixon, S. and Rexford, D. R., "Vinylidene Fluoride-Hexafluoropylene Copolymer, A Thermally Stable Elastomer," Jackson Laboratory, E. I. du Pont de Nemours and Co. (Contribution No. 223)

3. Schwarz, E. G., "The Micro-compounding and Evaluation of Rubber-like Polymers," Wright Air Development Center Technical Report 57-247, p. 2, July 1957.

4. Kelble, J. M. and Griffin, W. R., "Compounding of Fluoroelastomers for Aeronautical Applications," Wright Air Development Center. Paper published in the Proceedings of the 1958 Joint Army-Navy-Air Force Conference on Elastomer Research and Development.

5. Preiorek, K. L. et al., "Mechanism of Cross-Linking in the Vulcanization of New Fluoroelastomers," Progress Reports 1 and 2, Contract AF 33(616)5642, 15 July and 15 October 1958.

6. Fujiwara, E. J. et al., "Development and Physical Testing of Elastomeric Compounds Resistant to Petroleum Base Fuels at Elevated Temperatures," WADC Technical Report 55-492, Pt. III, March 1957.

BENJAMIN A. WILCOX

Strain Aging Effects in Columbium Due to Hydrogen

1959

138

BENJAMIN A. WILCOX

Benjamin A. Wilcox was born in Anaconda, Montana, June 18, 1934. He was awarded a scholarship at Washington State University where he received a B.S. in physical metallurgy in 1956. Following this, he won an engineering tuition scholarship to Stanford University where he received a M.S. in metallurgical engineering in 1958.

During his military service from August 1958 to August 1961 he was a lieutenant in the United States Air Force and was assigned to the Applied Mechanics Section, Strength and Dynamics Branch, Metals and Ceramics Laboratory, Materials Central. At the expiration of his military tour, he returned to Stanford University where he received his doctorate degree in August 1962.

Mr. Wilson has been awarded a twelve month National Science Foundation Post-Doctoral Fellowship to Cambridge University, England, beginning September 1962.

In addition to the Cleary Award, Mr. Wilcox received the Air Force Commendation Medal for meritorious service in metallurgical research. He is a member of Sigma Xi

BIBLIOGRAPHY

With W. H. Hill and K. D. Shimmin. Elevated Temperature Dynamic Moduli of Metallic Materials.

With R. A. Huggins. Strain Aging Effects in Columbium Due to Hydrogen. Columbium Metallurgy, pp. 257-278. New York, Interscience Publishing Company, 1961.

With R. A. Huggins. Effect of Hydrogen on Dislocation Locking in Niobium. Journal of the Less Common Metals, Special Conference Issue, 2(2-4): 292-303, April-August 1960.

With T. E. Tietz and J. W. Wilson. Mechanical Properties and Oxidation Resistance of Certain Refractory Metals. Stanford Research Institute Report No. SU-2436, January 30, 1959. AD214829.

With W. H. Hill. Elevated Temperature Dynamic Moduli of Vanadium, Titanium and V-Ti Alloys. WADD Technical Report No. 60-243, May 1960.

With F. H. Beck. The Effect of Concurrent Stressing on the Air Oxidation of Tantalum. WADD Technical Report No. 60-839, 1961.

With A. W. Brisbane and R. F. Klinger. The Effects of Strain Rate and Hydrogen Content on the Ductile-Brittle Transition of Columbium. WADD Technical Report No. 61-44, May 1961. Published in the Transactions of the American Society for Metals, 55: 179, 1962.

Strain Aging Effects in Columbium Due to Hydrogen

B. A. WILCOX

ABSTRACT—The strain aging tendencies of recrystallized, fine-grained arc cast columbium have been investigated using two different experimental techniques, the feasibility and accuracy of both methods having first been evaluated by tests on 1020 steel. Tensile straining (up to about one percent strain) at $-50°$ C revealed the characteristic upper and lower yield point found in BCC metals, this effect being attributed to "Cottrell Locking" of dislocations by atmospheres of interstitial atoms. Immediate re-straining of the samples showed no yield point effect since the dislocations were already unpinned, but suitable aging treatments ($121-260°$ C) caused the yield point to return as a result of dislocations being relocked. The aging temperature dependence of the rate of yield point return was evaluated, and an activation energy of 10,500 cal/mole was determined for the process. This value is considerably lower than the activation energies for diffusion of carbon, oxygen, and nitrogen in columbium, but in good agreement with the value given by Albrecht for hydrogen diffusion in Cb ($Q = 9370$ cal/mole). It is therefore concluded that hydrogen can be responsible for strain aging in columbium. This finding disagrees with the results of Begeley who used a similar technique to determine an activation energy of 27,100 cal/mole for the temperature dependence of the rate of yield point return in columbium. His conclusion was that oxygen was responsible for the strain aging effects.

The ability of hydrogen to cause dislocation pinning in columbium was further substantiated by using dynamic modulus measurements to study the strain aging process. Samples of Cb from the same heat as those used in yield point return studies, and samples which had been hydrogen charged at 650° C for 7 hours were deformed 2-3 percent in compression. The dynamic modulus (measured at room temperature) was decreased as a result of dislocation unpinning during deformation, but increased toward the original unstrained value as a result of aging at temperatures from 24 to 97° C. Activation energies for the strain aging process were determined for the uncharged and the hydrogen charged material ($Q = 7830-8280$ cal/mole uncharged; $Q = 8080-9920$ cal/mole, hydrogen charged). While hydrogen charging did not significantly affect the activation energy, the treatment did cause a fourfold increase in the frequency factor, A, of the rate equation,

$$\text{rate} = A e^{-Q/RT}$$

It was further noted that the hydrogen charging treatment greatly embrittled the columbium. The reduction in area of tensile samples tested at 24° C and a strain rate of 0.005 min^{-1} was decreased from 79 to 2 percent as a result of hydrogen charging.

INTRODUCTION

The refractory metals of Group 5A of the Periodic Chart (V, Cb, and Ta) and of Group 6A (Cr, Mo, and W) have in recent years received considerable attention as a result of their high melting point and their high temperature strength. Researchers have found, however, that in order to minimize harmful oxidation, fabrication should be carried out at the lowest feasible temperatures. Many investigations have therefore been undertaken to evaluate the mechanical behavior of these metals at lower temperatures. Such studies have revealed that these BCC refractory metals behave in many ways like alpha iron and mild steel. In particular, the intraction of dislocations with impurity interstitial elements has been found to affect in a similar fashion many mechanical properties of both alpha iron and the BCC refractory metals.

Among the properties and phenomena which have been influenced by or attributed to the interaction of interstitial elements with dislocations, are the following:

(1) Upper and lower yield point effect; steel (1), V (2), Cb (3), Ta (4), Cr (5), Mo (6), W (7).

(2) The strong temperature dependence of the tensile and yield strengths at low temperatures; iron (8), V, Cb, Ta, Cr, Mo, and W (9).

(3) Delayed yielding and preyield microcreep; mild steel (10, 11, 12), Cb and Ta (13), Mo (13, 14, 15).

(4) The dependence upon strain rate (or cycling rate) of the following:

  (a) The "blue brittle temperature; i.e. the temperature at which a maximum occurs in a plot of strength vs. temperature; mild steel (16), Cb, V, Ta, Cr, and W (9).

  (b) The temperature at which a maximum is observed in a plot of cycles to failure (by fatigue) vs. test temperature; steel (17), Mo (18).

  (c) The ductile-brittle transition temperature; V, Cb, Ta, Cr, Mo, and W (19).

(5) Strain aging, which can be measured by observing changes in the following properties during aging after plastic deformation:

  (a) Hardness; steel (1).

  (b) Yield point return; steel (20, this work), Cb (3, this work).

(c) Electrical resistivity; iron (21, 22).

(d) Notched bar impact strength; steel (23).

(e) Internal friction; iron (24, 25), Mo (26).

(f) Dynamic modulus; steel, Cb (this work).

The most widely accepted explanation of the mechanism of dislocation-interstitial interaction is based upon the classical papers of Cottrell (27), and Nabarro (28), and the later enlargement by Cottrell and Bilby (29). In essence the theory states that the stresses around a dislocation may be relieved by the migration of solute atoms to the vicinity of the dislocation. The "atmosphere" formed then pins the dislocation until a sufficient driving force (e.g. applied stress) is exerted to break the dislocation free. The concept of strain aging arises from the fact that aging after plastic deformation allows the solute atoms to diffuse to the unpinned dislocations, thereby relocking them.

It is well known that carbon, and nitrogen are capable of causing dislocation pinning in α-iron and steel. Rogers (30, 31) has shown, in addition, that hydrogen can cause dislocation locking in steel at low temperatures and in the absence of carbon and nitrogen. However, no thorough investigations have been made to determine which interstitial elements are responsible for the strain aging behavior in the refractory metals. Begley (3) has obtained preliminary data from yield point return studies which indicate that oxygen may be responsible in Cb, and Loomis and Carlson (2) have observed that hydrogen is more effective than C, O, or N in raising the ductile-brittle transition temperature of vanadium. Maringer and Schwope (26) have postulated that strain aging in Mo is due to carbon. However the activation energy for strain aging, (15,600/cal/mole), does not agree with the activation energy for the diffusion of carbon in Mo ($Q = 33,400$ cal/mole, Ref. 32).

It has therefore been the objective of this program to investigate quantatively the strain aging behavior of columbium, in order to determine which interstitial element (s) can cause dislocation locking. The technique of measuring yield point return as a function of aging time and temperature has previously been used to study strain aging (3, 20). To the authors knowledge, dynami modulus measurements have not previously been used to measure strain aging, although workers at Brown University (33) have used this method to examine changes after deformation of Al and Cu.

142

MATERIAL

The arc melted columbium used in this investigation was procured from Fansteel Metallurgical Corp. in the form of ½ inch diameter recrystallized rod, having a very fine grain size of approximately 700 grains per sq. mm. The chemical analysis of the as-received material is shown in Table I.

TABLE I.—*Chemical analyses of materials, weight percent*

Material	H	C	O	N
Comm. arc cast Cb	<0.0010	<0.0050	0.0117	0.0049
Hydrogenated Cb.	0.0779		0.0848	0.0546
1020 steel		0.21		0.007

Hydrogenation of the arc melted Cb was accomplished by annealing in a dry hydrogen atmosphere for 7 hr. at 650° C. This annealing treatment was sufficient to cause a hydride second phase to form throughout the material. The analysis in Table I shows that the treatment raised the hydrogen content from less than 10 ppm to 779 ppm.

The ¼ inch dia. 1020 steel rod, which was used to evaluate the feasibility of the experimental techniques, was annealed for 3 hours at 700° C in air and furnace cooled prior to specimen preparation.

EXPERIMENTAL PROCEDURE

Yield Point Return: Experiments using yield point measurements were performed on 1020 steel and as-received Cb. The tensile samples were 3½ inches long with a 1 inch gage length and a gage diameter of 0.215 inch. All tensile tests were made on a "hard" Baldwin-Emery SR-4 Testing Machine, Model FGT, using a constant strain rate of 0.005 in in min, the load-strain curves being recorded autographically. A temperature of −78° C was used for testing the 1020 steel, and a test temperature of −50° C was selected for the columbium experiments in order to more closely duplicate the test conditions used by Begley (3). The low temperature testing not only promoted the yield point drop, but minimized interstitial diffusion during testing and during the time it took to transfer the sample from the test machine to the aging environment. Aging between room temperature and 98° C was accomplished in a water bath with a temperature control of ±0.5° C. At higher temperatures (to 260° C), aging was per-
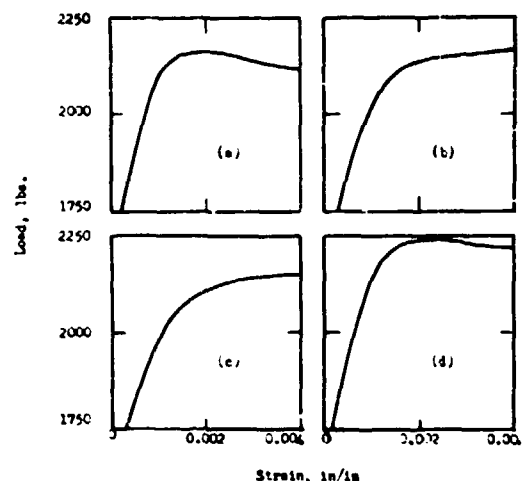
FIGURE 1. Load-strain curves for one sample of commercial arc melted Cb, tested at −50° C and a strain rate of 0.005 min.$^{-1}$. Critical aging time taken as 4 min.
(a) Initial loading
$D_a = 0.2152''$
(b) Immediate reloading
$D_a = 0.2125''$
(c) Aged 260° C, 3 min.
$D_a = 0.2123''$
(d) Aged 260° C, 4 min.
$D_a = 0.2120''$

formed in a Precision Scientific Co. furnace, with a temperature control of ±2° C.

Initial plastic straining of specimens (to about 1% strain) resulted in the characteristic upper and lower yield points, the upper yield point being that stress required to break an "avalanche" of dislocations free from their pinning atmosphere, and the lower yield point being the stress required to maintain the motion of the dislocations in their slip planes once they had been torn free. Immediate reloading produced load-strain curves which exhibited no yield drop. The samples were then repeatedly strained and aged until the time at which the yield drop just barely returned was determined. A load drop of approximately 20 pounds (about 550 psi) was arbitrarily selected as being evidence of the yield point return. Figure 1 illustrates a typical series of load strain curves in the region of the yield point for a sample of Cb aged at 260° C.

Five samples of steel, and four samples of as-received columbium were tested, and critical times of aging as a function of temperature were found to be: steel, 23° C, 435 min; 36° C, 70 min; 50° C, 15 min; 61° C, 5.3 min; 98° C, 0.17 min; columbium, 121° C, 145 min; 149° C, 50 min; 204° C, 12 min; 260° C, 4 min. The temperature dependence of the rate of yield point return was

143
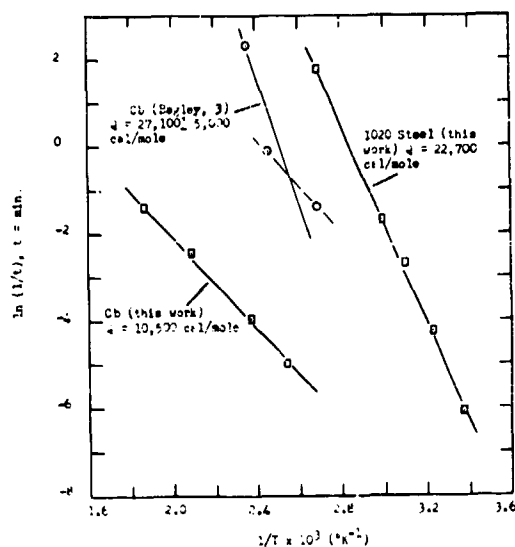
Figure 2. Arrhenius plots of yield point return strain aging data for commercial Cb and 1020 steel.

found to be adequately expressed by an Arrhenius-type rate equation of the form:

$$rate = Ac^{-Q/RT} \qquad (Eq\ 1)$$

where A = frequency factor, Q = activation energy, R = gas constant, and T = absolute temperature. The data is plotted in figure 2 as the natural logarithm of the rate of yield point return versus reciprocal absolute temperature. The results of Begley are also shown for comparison purposes.

An activation energy of 22,700 cal/mole was determined for the strain aging of 1020 steel, and a value of 10,500 cal/mole was determined for columbium. The value for steel is in reasonable agreement with the activation energy for the diffu-

sion of C in α-Fe (Q=20,100 cal/mole, see Table II). The activation energy for strain aging of Cb is considerably lower than values for the diffusion of C, O, and N in Cb (see Table II), but is in good agreement with the Q value for the diffusion of hydrogen in Cb (Albrecht, et al. (35) give Q (H in Cb) as 9,370 cal/mole). It is therefore reasonable to conclude that hydrogen can be responsible for strain aging in columbium.

Dynamic Modulus: In order to further validate the thesis that hydrogen can cause dislocation locking in Cb, samples of as-received columbium and hydrogen charged columbium were tested using dynamic modulus as a means of measuring strain aging. The feasibility and accuracy of this technique was first evaluated by tests on 1020 steel.

Dynamic moduli of the various specimens were calculated from resonant frequency measurements, a free-free beam technique being used to determine resonant frequency. A transverse sonic wave was propogated the length of a sample, having nominal dimensions of 3″ x ½ x ¼″, the ¼″ dimension being in the plane of vibration. All resonant frequency measurements were made at room temperature, the temperature of the room being controlled to about ±1° C. An E-Scope Sonic Analyser was used to excite the specimen, and the pick-up was transmitted directly to a Berkeley Eput Meter where the resonant frequency was counted in cycles per second.

The dynamic modulus of elasticity was calculated using the following relationship:

$$E = CWF_r^2 \qquad (Eq.\ 2)$$

where E = modulus in psi, F_r = resonant frequency in cps, W = weight of specimen in pounds and

TABLE II.—*Summary of diffusion data for interstitials in columbium and iron*

Base metal	Diffusing element	D_0, cm²/sec	Q, cal/mole	Ref.
Columbium	Oxygen	0.0147	27,600	Ang (36)
Columbium	Oxygen	0.00407	24,000	Klopp et al. (37)
Columbium	Oxygen	0.014	26,600	Powers and Doyle (38)
Columbium	Oxygen		22,000	Marx et al. (39)
Columbium	Nitrogen	0.098	38,600	Ang (36)
Columbium	Nitrogen	0.0072	34,800	Powers and Doyle (40)
Columbium	Nitrogen	0.061	38,800	Albrecht and Goode (41)
Columbium	Nitrogen		35,700	Marx et al. (39)
Columbium	Carbon	0.0046	33,000	Powers and Doyle (40)
Columbium	Carbon	0.015	27,000	Wert (42)
Columbium	Hydrogen	0.0215	9,370	Albrecht et al. (35)
Columbium		0.02	20,100	Wert (43)
Iron	Carbon	0.003	18,200	Wert (42)
Iron	Nitrogen			

$$C=\frac{2.45\times10^{-3}L^3T}{bt^3},\ L,\ b,\ \text{and}\ t,\ \text{being respectively}$$

the length, width, and thickness in inches. The term T is a correction factor given by $T=\phi(\nu,$ $K/L)$, where ϕ designates a function, $\nu=$ Poisson's ratio, and $K=$ radius of gyration $=0.298\ t$ for a prism. The values of T were determined with the aid of Ref. 34, in which T is plotted versus K/L for various values of ν.

Plastic deformation was achieved by compressing the samples in the $\frac{1}{4}$ inch direction, using a head travel rate of 0.005 in/min, i.e. approximate strain rate of 0.02 in/in/min. The as-received Cb and 1020 steel were compressed 3 percent, but the hydrogenated Cb was deformed only 2 percent, since the charging treatment was found to cause considerable embrittlement.

The dynamic modulus was determined before deformation, immediately after deformation, and after various times of aging at temperatures from 24° C to 99° C. All aging was done in a constant temperature water bath. It was found that plastic deformation decreased the modulus of steel by about $0.3-0.5\times10^6$ psi. A similar decrease of about $0.1-0.3\times10^6$ psi was noted for the as-received columbium, the modulus lowering in both cases being attributed to creating free dislocations, both by unpinning locked ones and by generating fresh ones. Plastic deformation caused

a rather sporadic effect on the modulus of the hydrogenated Cb, sometimes slightly raising it above the unstrained value and other times slightly lowering it. This erratic behavior is probably associated with the presence of the

TABLE III.—*Data for commercial columbium, hydrogenated columbium, and 1020 steel, showing the effects of deformation and subsequent aging on the dynamic modulus. All modulus measurements made at room temperature*

Material	E', mod. of undeformed spec. (10^{-6} psi)	E_o, mod. immed. after deformation (10^{-6} psi)	E_m, max. recovered mod. (at aging peak) (10^{-6} psi)	Aging temp., °C.
Comm. Cb	15. 861	15. 764	15. 854	24
Comm. Cb	16. 053	16. 033	16. 092	37
Comm. Cb	15. 997	15. 727	15. 798	53
Comm. Cb	16. 002	15. 878	15. 954	73
Comm. Cb	15. 935	15. 638	15. 697	94
Hydrogenated Cb	13. 839	15. 024	15. 949	24
Hydrogenated Cb	14. 857	15. 232	16. 234	53
Hydrogenated Cb	15. 607	15. 100	16. 059	73
Hydrogenated Cb	13. 446	14. 817	16. 338	94
1020 steel	30. 719	30. 221	30. 409	24
1020 steel	30. 582	30. 267	30. 391	29
1020 steel	30. 614	30. 209	30. 341	35
1020 steel	30. 704	30. 305	30. 403	46
1020 steel	30. 603	30. 137	30. 248	55
1020 steel	30. 688	30. 390	30. 611	66
1020 steel	30. 688	30. 374	30. 497	79
1020 steel	30. 641	30. 335	30. 478	99
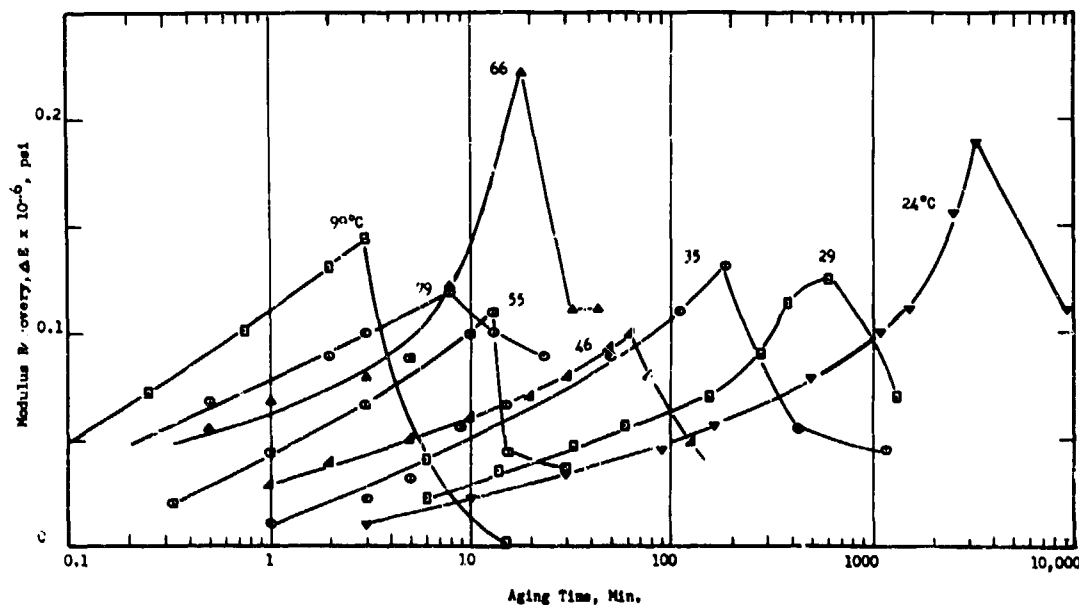
FIGURE 3. Recovery of dynamic modulus of 1020 steel as a function of aging time and temperature after 3% deformation by compression. All modulus measurements at room temperature.
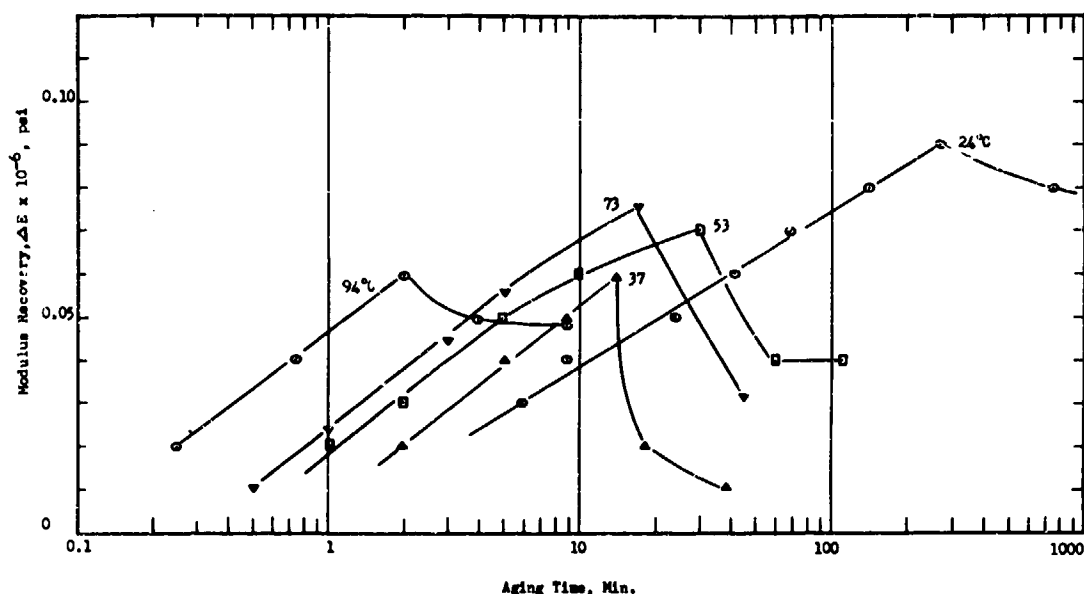
Figure 4. Recovery of dynamic modulus of as-received commercial Cb as a function of aging time and temperature, after 3 percent deformation by compression. All modulus measurements at room temperature.

brittle second phase of columbium hydride. The values of E', the undeformed modulus and E_o, the modulus immediately after deformation, are listed in Table III for all three materials tested.

Aging after deformation was found to increase the modulus above that of the freshly deformed material, the rate of recovery being faster, the higher the aging temperature. The modulus recovery is defined as $\Delta E = E_t - E_o$, where E_t is the modulus after aging time t. The moduli recoveries as a function of aging time and temperature are illustrated in Figures 3, 4, and 5 for 1020 steel, as-received Cb, and hydrogenated Cb respectively. In each case it is noted that an aging peak is present. The moduli values at the aging peaks, E_m, are given in Table III. It is noted in Table III that for 1020 steel the maximum modulus increase due to aging (i.e. at the aging peak) is about 30 to 50 percent of the total decrease caused by deformation, and in the case of as-received columbium, aging causes 20 to 100 percent recovery. The hydrogenated Cb again behaves unusually, the degree of modulus recovery being more than an order of magnitude greater than that of the steel or as-received Cb.

The temperature dependence of the modulus recovery rate was found to be satisfactorily expressed by an Arrhenius-type rate equation. Fig. 6 shows Arrhenius plots for 1020 steel, at isomodulus recovery values of $\Delta E = 0.10 \times 10^6$ psi

and 0.05×10^6 psi, as taken from Figure 3. The calculated activation energy of 21,000–21,700 cal/mole is in excellent agreement with the activation energy for the diffusion of carbon in iron. Similar plots for as-received and hydrogen charged Cb are shown in Figure 7. The activation energies for the strain aging process being 7,830–8,280 cal/mole, as received Cb; and 8,080–9,920 cal/mole, hydrogenated Cb. These values are in close agreement with the value of 9,370 cal/mole for hydrogen diffusion in Cb. The frequency factor, A, in the rate equation was calculated for as-received Cb and hydrogenated Cb from the Arrhenius plots for $E = 0.050 \times 10^6$ psi. More than a fourfold increase in the value of A was caused by the hydrogen charging treatment: as-received, $A = 5.9 \times 10^4$ min^{-1}; hydrogen annealed, $A = 27.5 \times 10^4$ min^{-1}.

DISCUSSION

The investigations on 1020 steel, using yield point return and dynamic modulus measurements, have shown that these techniques are satisfactory methods for studying the kinetics of the strain aging process. The close agreement between the activation energies for strain aging of steel, and that for the diffusion of carbon in iron, leave little doubt as to the applicability of the experimental approach.

146
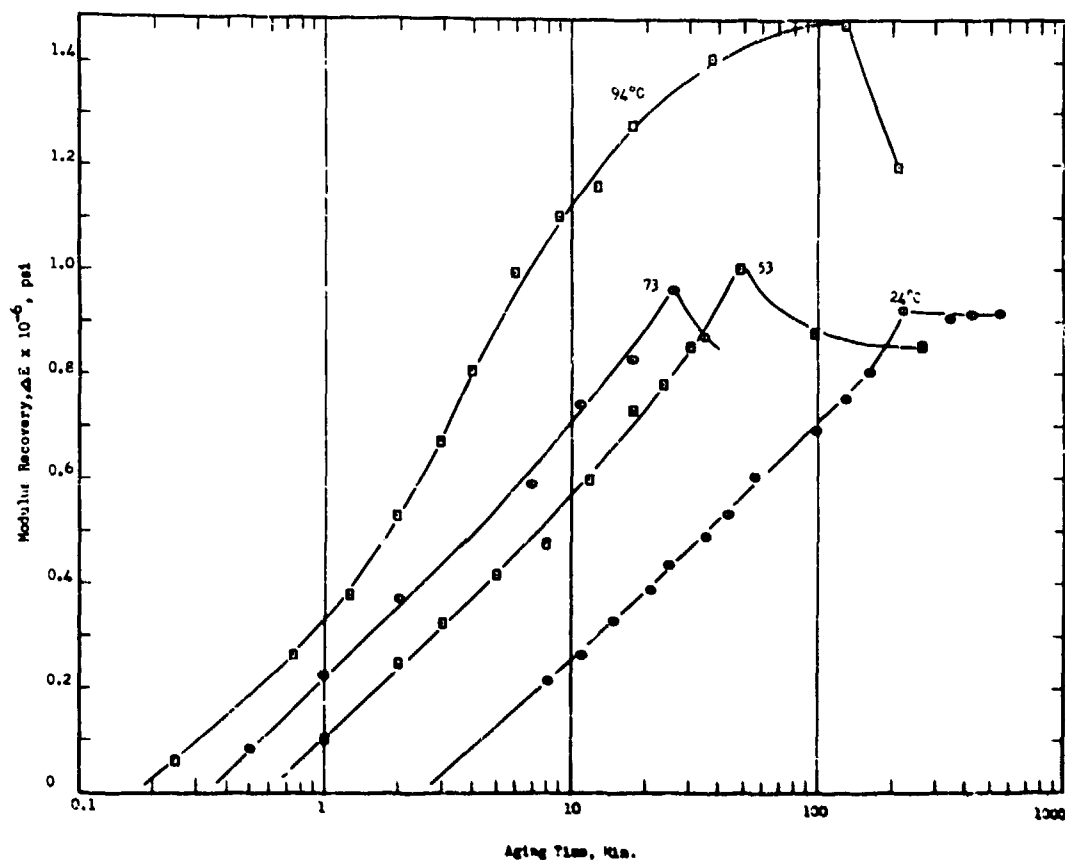
FIGURE 5. Recovery of dynamic modulus of hydrogenated Cb (650° C, 7 hr.) as a function of aging time and temperature, after 2 percent deformation by compression. All modulus measurements at room temperature.

The disagreement between the yield point strain aging work on as-received Cb and the earlier work of Begley (3), (see Fig. 2) might be related to differences in metallurgical variables such as material composition or grain size; or to test variables such as difference in strain rate. The analysis given by Begley is: 0.003–0.004 percent oxygen, 0.002–0.008 percent nitrogen, and 0.024–0.068 percent carbon. The material used in this work had a higher oxygen content and a lower carbon content (see Table 1). The grain size of Begley's material was much coarser, approximately 250 grains/mm², as compared to about 700 grains/mm² for this work; and the

strain rate considerably greater than that used in the present investigations (ε=0.06/min, Begley; ε=0.005/min, this work). It is hard to visualize, however, how any of these differences could result in a different activation energy for strain aging. The discrepancy can be rationalized, however, by eliminating one point from Begley's Arrhenius plot (see dotted curve in Fig. 2). If a straight line is drawn through the two lower points, it is seen that the slope is almost identical to that determined in this work. From examination of Begley's data it would appear that the neglected point was the one determined with the least degree of precision.

147
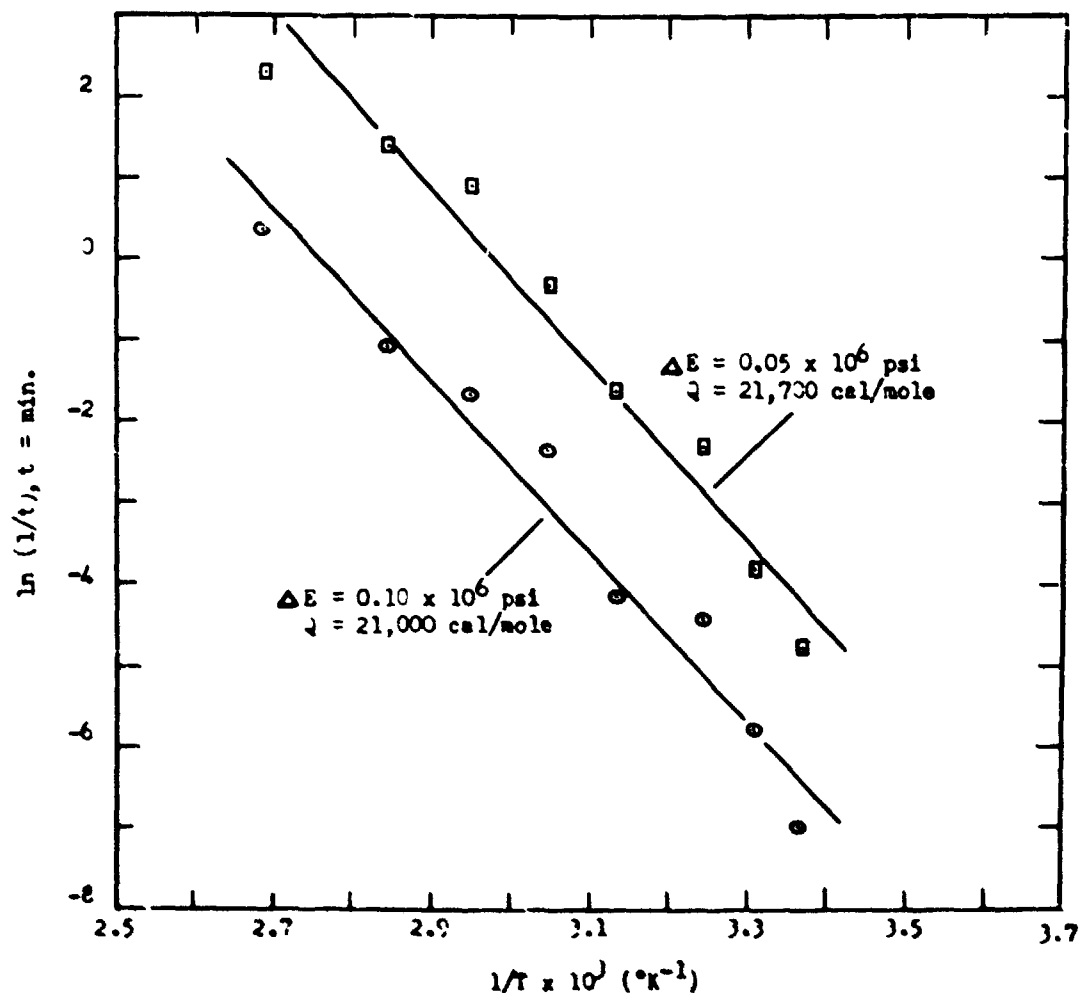
FIGURE 6. Arrhenius plot of dynamic modulus strain aging data for 1020 steel.

An interesting feature revealed in the dynamic modulus strain aging studies is that for all three materials, the strain aging curves exhibit a maximum, or aging peak. A plausible explanation for this phenomenon can be given using conclusions drawn by Thomas and Leak (23) from their internal friction strain aging investigations of alpha-iron. These workers have shown that the number of carbon or nitrogen atoms attracted to a dislocation in α-iron exceeds the solubility limit in the lattice surrounding the dislocation, thereby resulting in the formation of small coherent precipitates around the dislocation. If these precipitates contribute to the atmosphere pinning

action, then the aging peaks may possibly be due to coalescence of the precipitates as a result of "over-aging". Since the mean-free-path between particles increases, the pinning contribution of the precipitates decreases, and the modulus decreases after reaching a maximum degree of recovery.

Dislocation Densities. The dynamic modulus strain aging data has been treated to allow calculation of dislocation densities of the deformed and aged materials utilizing the Cottrell-Bilby equation (Ref. 29). The C-B analysis relates the fraction, f, of solute which has migrated to dislocations during aging after deformation to the aging time t (sec.) and temperature T (°K) by

148
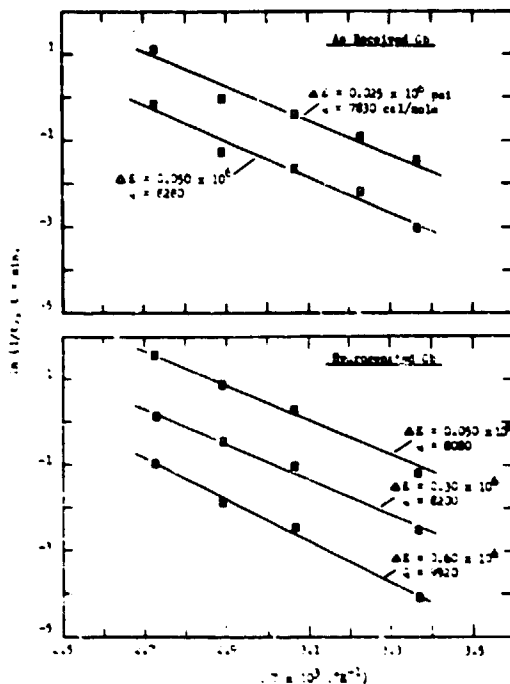
FIGURE 7. Arrhenius plots of dynamic modulus strain aging data for as-received commercial Cb and hydrogenated Cb.

the following equation:

$$f = n(t)/N_o = a\lambda(ADt/kT)^{2/3} \quad \text{(Eq. 3)}$$

where $n(t)$ is the number of solute atoms per unit volume of material that have migrated to the dislocations, N_o is the solute concentration at $t=0$, λ is the dislocation density in lines/cm², k is Boltzmann's constant $= 1.38 \times 10^{-16}$ dyne cm/°K, a is a numerical constant equal to $3(\pi/2)^{1/3}$, $D=$ the diffusity of solute in base metal in cm²/sec at temperature T, and A is a constant depending on the strain introduced into the lattice by a solute atom and has units of dyne cm².

Equation (3) is not valid for the latter stages of aging, since the first atoms to arrive at the dislocation are more effective in pinning than atoms arriving after longer aging times. However Harper (24) has proposed a simple generalization to fit the latter stages. By assuming that the rate of migration is decreased in proportion to the amount already segregated, the equation governing precipitation is then:

$$f = 1 - \exp[-a\lambda(ADt/kT)^{2/3}] \quad \text{(Eq. 4)}$$

or

$$ln(1-f) = -a\lambda(ADt/kT)^{2/3} \quad \text{(Eq. 5)}$$

Eq. (4) reduces to Eq. (3) when the exponent is small.

Determination of the constant "A" requires some consideration. Cottrell and Bilby estimated "A" to be 3.0×10^{-20} dyne cm² using lattice parameter measurements on martensite, as reported by Lepson and Parker (44). Since no experimental data is available regarding the effect of hydrogen on the lattice parameter of Cb, a special theoretical treatment (see Appendix) was necessary to determine "A" for the case of H in Cb. The value so determined is 1.4×10^{-20} dyne cm². Now by inserting the constants in Eq. (5), the following relationships are determined:

$$C \text{ in } \alpha-\text{Fe } ln(1-f) = -12.6 \times 10^{-3} \lambda(Dt/T)^{2/3}$$
(Eq. 6)

$$H \text{ in Cb } ln(1-f) = -7.5 \times 10^{-3} \lambda(Dt/T)^{2/3}$$
(Eq. 7)

Therefore if $ln(1-f)$ is plotted versus $(Dt/T)^{2/3}$, it is possible to evaluate the dislocation density, λ, from the slope.

Such plots are shown in Figure 8 for as-received Cb and hydrogen charged Cb, the measure of f being taken as $(E_t - E_s)/(E_m - E_s)$, or $\Delta E/\Delta E_{max}$. The calculated dislocation densities are: 2.5×10^7 lines/cm² for as received Cb compressed 3 percent, and 1.4×10^7 lines/cm² for hydrogen annealed Cb compressed 2 percent. A similar technique yielded a density of 8×10^{11} lines/cm² for the 1020 steel (compressed 3 percent). The dislocation densities are summarized in Table IV, together with values of λ determined by other workers from strain aging studies on steel. The density for 1020 steel is seen to be in reasonable agreement with the results of previous investigations. The values of λ for Cb might appear somewhat lower than expected. However, the low dislocation densities are not too unusual, wh it is recalled that columbium work hardens relatively slightly as compared to steel. Since the degree of work hardening is proportional, in part, to the dislocation density, a lower density for a given amount of deformation would correspond to a smaller work hardening capacity.

Hydrogen Embrittlement: As reported earlier it was noticed in the dynamic modulus strain aging studies that the hydrogen charging treatment of 650° C, 7 hr. caused severe embrittlement. In order to evaluate the degree of embrittlement, one tensile sample of Cb, which had been charged as above, was tested in tension at room tempera-

149
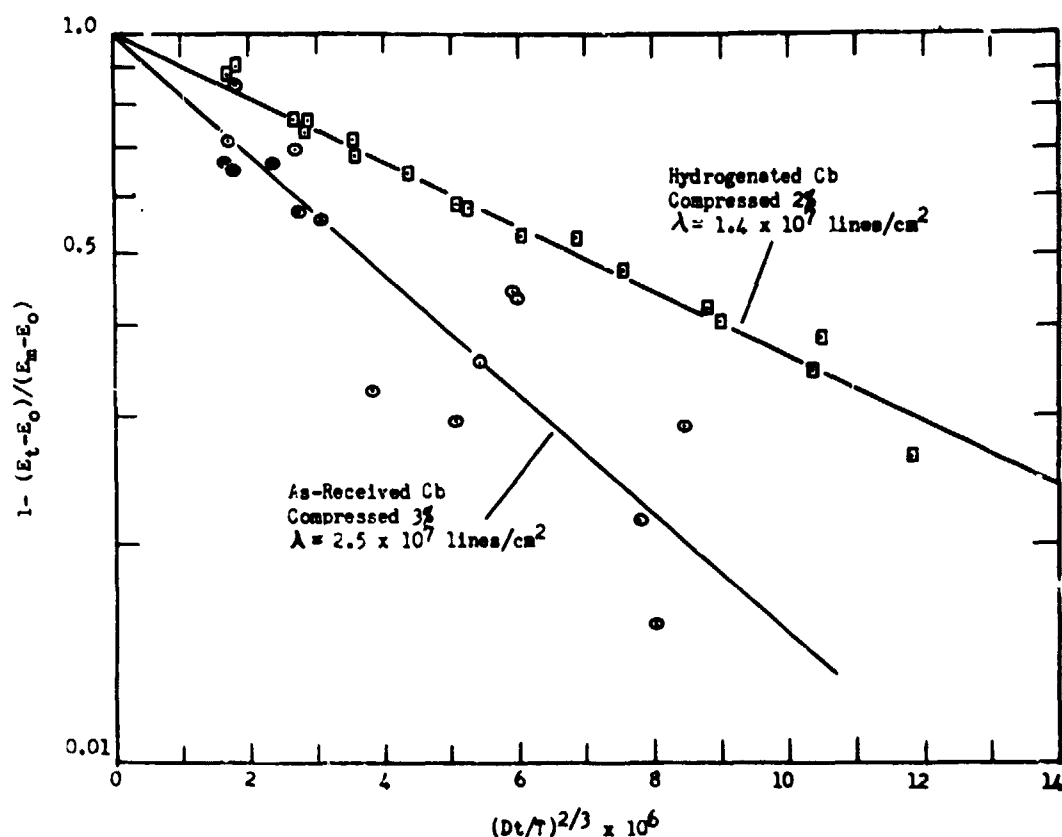
Figure 8. Dislocation densities of as-received commercial Cb and hydrogenated Cb, using Harper's modification of the Cottrell-Bilby equation.

ture and a strain rate of 0.005 min⁻¹. The sample fractured in a brittle fashion, presumably along the {100} cleavage planes, (45). A photograph of the fracture surface is shown in Figure 9 together with a ductile fracture obtained by testing a piece of as-received Cb under the same conditions of temperature and strain rate. The true fracture stress, defined as load at fracture divided by cross-sectional area at fracture, was greatly lowered by the hydrogen treatment. The ductility was also tremendously decreased, the %RA being lowered from 79 to about 2 percent

Microstructures of the as-received Cb and the hydrogenated Cb are shown in Figures 10 and 11 respectively, the latter micrograph being taken near the brittle fracture area shown in Figure 9. The hydrogen charging treatment is seen to have introduced a large amount of hydride second phase. The embrittling effect of the hydride is seen in Figure 11 by the transgranular cleavage crack. It is evident that hydrogen charging Cb

to the point of forming an internal hydride causes great embrittlement. However it still remains to be shown whether or not relatively large amounts of hydrogen in solid solution can cause a similar embrittling effect.

CONCLUSIONS

1. Yield point return and dynamic modulus measurements have been shown to be satisfactory techniques for studying the strain aging of steel and columbium.

2. The activation energies calculated for strain aging of both as-received commercial arc melted Cb and hydrogenated Cb were found to be in close agreement with the activation energy for the diffusion of hydrogen in Cb. It is therefore concluded that hydrogen is the interstitial element responsible for strain aging in columbium

3. Harper's modification of the Cottrell-Bilby "$t^{2/3}$ equation" has been satisfactorily applied to dynamic modulus strain aging data, allowing

150

TABLE IV. – *Dislocation densities in deformed Columbium and iron, determined from application of Cottrell-Bilby equation .o strain aging measurements*

Material	Means of straining	Method of meas. strain aging	Per-cent strain	Composition			Dislocation density lines/cm²	Ref.
				H	C	N		
Comm. Cb	Compression	Dynamic modulus	3	0.001	0.005	0.0049	2.5×10^7	This work.
Hydrogenated Cb	Compression	Dynamic modulus	2	0.0779		0.0546	1.4×10^7	This work.
1020 steel	Compression	Dynamic modulus	3		0.21	0.007	8×10^{11}	This work.
B.I.S.R.A. Fe	Tension	Internal friction	7			0.015	7.7×10^{10}	Thomas and Leak (25).
B.I.S.R.A. Fe	Tension	Internal friction	7		0.015		6.6×10^{10}	
B.I.S.R.A. Fe	Tension	Internal friction	7		0.0095		5.0×10^{10}	
B.I.S.R.A. Fe	Tension	Internal friction	7		0.0055		4.0×10^{10}	
Puron Fe	Tension	Internal friction	5		0.015		1.86×10^{11}	Harper (24).
Puron Fe	Tension	Internal friction	10		0.009		2.46×10^{11}	
Puron Fe	Tension	Internal friction	15		0.013		3.72×10^{11}	
Fe	Tension	Electrical resistivity	4.5		0.015		0.82×10^{10}	Dahl and Lueke (22).
Fe	Tension	Electrical resistivity	5.1		0.015		1.67×10^{10}	
Fe	Tension	Electrical resistivity	5.5		0.018		0.95×10^{10}	
Fe	Red. by drawing	Electrical resistivity	8		0.07	0.004	7×10^{10}–6×10^{11}	Cottrell and Churchman (21).
Fe	Red. by drawing	Electrical resistivity	23		0.07	0.004	8×10^{10}–7×10^{11}	
Fe	Red. by drawing	Electrical resistivity	42		0.07	0.004	9×10^{10}–8×10^{11}	
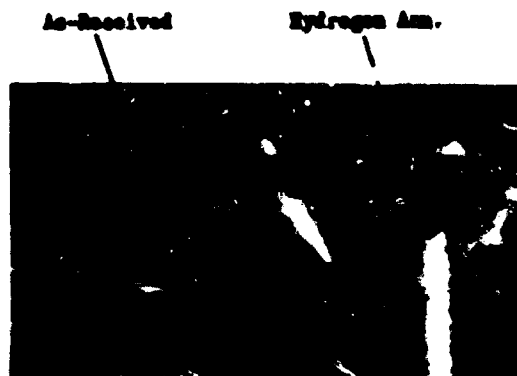
FIGURE 9. Tensile samples of as-received commercial arc melted Cb, and annealed in hydrogen (30° C, 7 hr. Tested at 24° and a strain rate of 0.005 min⁻¹. Properties listed below. 7X.

Property	As-Rec. Cb	Hyd. Ann. Cb
Hydrogen content, ppm	10	779
Proportional limit, psi	31,700	17,800
Ultimate tens. stress, psi	52,100	42,900
Engr. Fract. stress, psi	15,300	42,900
True fract. stress, psi	74,300	44,700
% El (1" l.)	44	2.5
% R.A.	79	1.7

FIGURE 10. Microstructure of as-received commercial arc melted Cb, HF-HNO₃ Etch, 100X

determination of dislocation densities. The dislocation density calculated for 1020 steel is i. reasonable agreement with data from the literature. The relatively low densities determined for columbium can be rationalized by recalling that
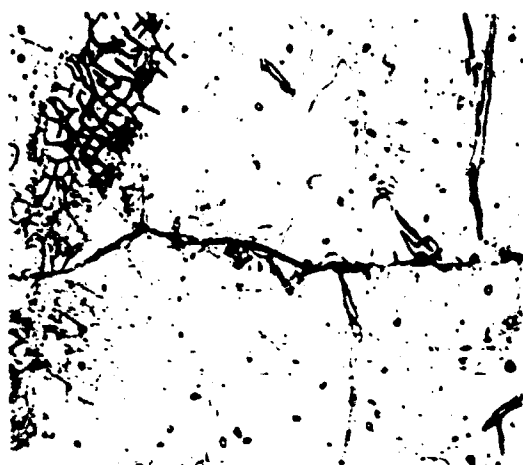
FIGURE 11. Microstructure near fracture of CB sample hydrogen annealed 650° C, 7 hr., tensile tested at 24° C and a strain rate of 0.005 min⁻¹. Note transgranular cracks and hydride second phase, HF-HNO₃ Etch, 500X.

this material displays comparatively small work hardening tendencies.

4. Hydrogen charging columbium to the point of forming an internal hydride second phase has been shown to cause severe embrittlement. It still remains to be shown whether or not appreciable amounts of hydrogen in solid solution will exert a similar effect.

ACKNOWLEDGEMENT

REFERENCES

(1) E. S. Davenport and E. C. Bain, "The Aging of Steel," ASM Trans. 1935, vol. 23, pp. 1047-1106.

(2) D. A. Loomis and O. N. Carlson, "Brittle-Ductile Transition in Vanadium," AEC Rept. No. ISC-1037, March 1958.

(3) R. T. Begley, "Development of Niobium Base Alloys," WADC TR 57-344, Part II, December 1958.

(4) J. W. Pugh, "Temperature Dependence of the Tensile Properties of Tantalum," ASM Trans., 1956, vol. 48, pp. 677-688.

(5) M. J. Marcinkowski, "The Plastic Deformation of Chromium at Low Temperatures," WADC TR 58-294, AD 216262, June 1959.

(6) A. A. Johnson, "The Effect of Grain Size on the Tensile Properties of High Purity Molybdenum at Room Temperature," Phil. Mag., 1959, Vol. 4, pp. 194-199.

(7) R. H. Atkinson et al. "Tungsten Alloy Development," Westinghouse Elec. Corp., Lamp Division, Contract No. AF 33(616)-5632, January 1960.

(8) D. J. McAdam and R. W. Mebs, Proc. ASTM, 1943, vol. 43, p. 661.

(9) T. E. Tietz, B. A. Wilcox, J. W. Wilson, "Mechanical Properties and Oxidation Resistance of Certain Refractory Metals," Stanford Res. Inst. Rept. to Navy BuAer, Contract No. AS 58-306-d, AD 214829, January 30, 1959.

(10) D. S. Wood and D. S. Clark, "The Influence of Temperature Upon the Time Delay for Yielding in Annealed Mild Steel," ASM Trans., 1951, vol. 43, pp. 571-536.

(11) J. C. Fisher, "Application of Cottrell's Theory of Yielding to Delayed Yield in Steel," ASM Trans., 1955, vol. 47, pp. 451-462.

(12) T. Yokobori, "Delayed Yield and Strain Rate and Temperature Dependence of Yield Point of Iron," J. App. Phy., 1954, vol. 23, 503-504.

(13) E. T. Wessel, "Abrupt Yielding and the Ductile-to-Brittle Transition in Body-Centered Cubic Metals," J. Met., 1957, Vol. 9, p. 930.

(14) J. A. Hendrickson, D. S. Wood, and D. S. Clark, "The Initiation of Discontinuous Yielding in Ductile Molybdenum," ASM Trans., 1958, vol. 48, pp. 540-559.

(15) R. J. H. Snead and H. N. Kurublum, 'The Pre-Yield Transient Behavior of Molybdenum," CONVAIR Pomona Tech. Memo 332-127, May 1958.

(16) N. Makrides and W. M. Baldwin Jr., "High Temperature Brittleness in Titanium Alloys," WADC TR 57-251, AD 130847, June 1957.

(17) J. C. Levy and G. M. Sinclair, "An Investigation of Strain Aging in Fatigue," U. of Ill. Tech. Rept. No. 39, Contract N6-ori-071(04), Aug. 1954.

(18) G. W. Broch and G. M. Sinclair, "Elevated Temperature Tensile and Fatigue Behavior of Unalloyed Arc-Cast Molybdenum," WADC-TN-59-89, AD 210837, Feb. 1959.

(19) F. R. Schwartzberg, H. R. Ogden, and R. I. Jaffee, "Ductile-Brittle Transition in the Refractory Metals," DMIC Rept. 114, AD 316324, OTS PB 151070, June 25, 1959.

(20) J. O. Brittain and S. E. Bronisz, "Stress Induced Strain Aging," AFOSR Rept. No. TN 59-389, AD 154273, June 6, 1958.

(21) A. H. Cottrell and A. T. Churchman, "Change of Electrical Resistance During the Strain Aging of Iron," J. Iron and Steel Inst., 1949, vol. 162, pp. 271-276.

(22) W. Dahl and K. Lücke, Arch. Eisenhuttenwesen, 1954, vol. 25, pp. 241-249.

(23) C. J. Osborn, "The Nature of Strain-Age Embrittlement," J. Iron and Steel Inst., 1956, v. 188, pp. 97-101.

(24) S. Harper, "Precipitation of Carbon and Nitrogen in Cold-Worked Alpha-Iron," Phys. Rev., 1951, vol. 83, pp. 709-712.

(25) W. R. Thomas and G. M. Leak, "The Strain Aging of Alpha-Iron," J. Iron and Steel Inst., 1955, vol. 180, pp. 155-161.

(26) R. E. Maringer and A. D. Schwape, "The Anelasticity of Molybdenum," BMI Rept. to ONR, Contract N9 ONR 82101, AD 24087, July 14, 1953.

(27) A. H. Cottrell, "Effect of Solute Atoms on the Behavior of Dislocations," Rept. of the Bristol Conf. on Strength of Solids, The Phy. Soc., London, 1948, pp. 30-38.

(28) F. R. N. Nabarro, "Mechanical Effects of Carbon In Iron," Rept. of the Bristol Conf. on Strength of Solids, The Phy. Soc., London, 1948, pp. 38-45.

(29) A. H Cottrell and B. A. Bilby, "Dislocation Theory of Yielding and Strain Aging of Iron," Phy. Soc., 1949, Vol. 62, Part A, pp. 49 62.

(30) H. C. Rogers, "A Yield Point in Steel due to Hydrogen," Acta Met., 1954, vol. 2, p. 167.

(31) H. C. Rogers, "The Influence of Hydrogen on the Yield Point in Iron," Acta Met., 1956, vol. 4, pp. 114-117.

(32) G. V. Samsonov and V. P. Latisheba, "Diffusion of Loron, Carbon, and Nitrogen Into Transition Metals of IV, V, and VI Groups of the Periodic Table," Dokiady Akad. Nauk, 1956, vol. 109, p. 582; AEC Translation 2949.

(33) A. Granoto, A. Hikata, and K. Lücke, "Recovery of Damping and Modulus Changes Following Plastic Deformation," Acta Met, 1958, vol. 6, 470 480.

(34) G. Pickett, "Equations for Computing Elastic Constants from Flexural and Torsional Resonant Frequencies of Vibration of Prisms and Cylinders," Proc. ASTM, 1945, vol. 45, pp. 846-865.

(35) W. M. Albrecht, W. D. Goode, and M. W. Mallott, "Reactions in the Niobium-Hydrogen System," J. Electrochem. Soc., 1959, vol. 106, p. 981.

(36) C. Y. Ang, "Activation Energies and Diffusion Coefficients of Oxygen and Nitrogen in Niobium and Tantalum," Acta Met., 1953, vol. 1, pp. 123-125.

(37) W. D. Klopp, C. T. Sims, and R. I. Jaffee, "High Temperature Oxidation and Contamination of Columbium," ASM Trans., 1959, vol. 51, pp. 282-298.

(38) R. W. Powers and M. V. Doyle, "Diffusion of Interstitial Solutes in the Group V Transition Metals," J. App. Phy, 1959, vol. 30, pp 514-524.

(39) J. W. Marx, G. S. Baker, and J. M. Silversten, "The Internal Friction of Tantalum and Columbium Foils at Ultrasonic Frequencies," Acta Met., 1953, vol. 1, pp. 193-201.

(40) R. W. Powers and M. V. Doyle, "Some Internal Friction Studies in Columbium," AIME Trans., 1957, vol. 209, pp. 1285-1288.

(41) W. M Albrecht and W. D. Goode, "Reaction of Nitrogen with Niobium," Battelle Mem. Inst. Rept. No. BMI-1360, July 6, 1959.

(42) C. Wert, "Measurements of the Diffusion of Interstitial Atoms in BCC Lattices," J. App. Phy, 1950. vol. 21, pp. 1196-1197.

(43) C. Wert, "Diffusion Coefficients of Carbon in Alpha Iron," Phy. Rev., 1950, vol. 79, p. 601.

(44) H. Lepson and A. M. B. Parker, J. Iron and Steel Inst., 1944, vol. 149, p. 123.

(45) M. A. Adams, A. C. Roberts, and R. E. Smallman, "Yield and Fracture in Polycrystalline Niobium," United Kingdom Atomic En. Auth. Rept. AERE M/R 2530, 1959.

APPENDIX

Calculation of Λ, a constant in the Cottrell-Bilby equation, which depends on the strain introduced into the lattice by a solute atom

The relationship defining A has been given in Ref. 29 as:

$$A = \Delta V \frac{Gd}{3\pi} \cdot \frac{1+\nu}{1-\nu} \qquad \text{Eq. (a)}$$

where ΔV is the volume change caused by introduction of an interstitial atom into the solute lattice, G is the rigidity modulus, ν is Poisson's ratio, and d is the distance of closest approach of the solvent atoms.

The determination of ΔV in the case of carbon in iron is based on lattice parameter measurements of martensite by Lepson and Parker (44), and the value given by Cottrell and Bilby is $\Delta V = 0.78 \times 10^{-n}$ cm³.

In other interstitial — BCC systems, where experimental lattice parameter data are not available, it is useful to visualize a model where the interstitial atoms occupy face-center or edge center sites in the solvent lattice, as shown in Figure a. The spherical volume around one interstitial site in the lattice, V_o (see Fig. b) is increased to V_1 by inserting the interstitial atom in the site (see Fig. c). The resulting volume change $\Delta V = V_1 - V_o$ is given by:

$$\Delta V = 4/3\pi(r_1^3 - r_o^3) \qquad \text{Eq. (b)}$$

where $r_o = a_o/2$, and $r_1 = a_1/2 = (d+s)/2$. The terms r_o and r_1 are the radii of the undistorted and the distorted spherical volumes respectively, a_o is the undistorted lattice parameter, d is the atomic diameter of the solvent, and s is the atomic diameter of the interstitial solute.
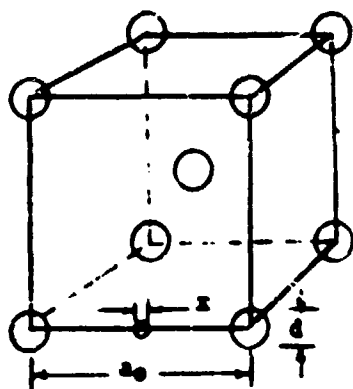
FIGURE a. Interstitial positions shown schematically in BCC lattice.

FIGURE c. (100) Plane with one interstitial atom at ½,0,0 site.

Inserting these terms in Eq. (b) gives:

$$\Delta V = \pi/6 \ [(d+x)^3 - a_o^3]$$ Eq. (c)

By inserting the appropriate values of d, x, and a_o for the Fe–C and Cb–H systems, values of ΔV are determined to be: $\Delta V = 1.87 \times 10^{-23}$ cm³ for C in Fe, and $\Delta V = 0.55 \times 10^{-23}$ cm³ for H in Cb.

It is noted that the calculated ΔV due to C in Fe is larger by a factor of two than that determined from experimental data. The error decreases considerably, however, when the distortion is less, since the decrement of distortion enters as a cubed term. It is therefore felt that the value of ΔV for H in Cb is in error by less than a factor of two.

The value of "A" for H in Cb, from Eq. (a) is determined to be 1.4×10^{-30} dyne cm², using values of $G = 3.75 \times 10^{11}$ dyne/cm², $d = 2.85 \times 10^{-8}$ cm, and $\nu = 0.38$.

FIGURE b. (100) Plane without interstitial atom.

DAVID A. KIRK

Effects of Gravity on Free Convection
Heat Transfer

1960

DAVID A. KIRK

David A. Kirk was born in Detroit, Michigan, July 19, 1931. He received both his B.S. and M.S. in chemical engineering from the University of Louisville in 1956. He was selected to attend graduate training courses sponsored by the Aeronautical Systems Division at Ohio State University during the 1960–1961 academic year and has completed both the academic and residence requirements for the doctorate degree.

Mr. Kirk was employed as a chemical engineer for Universal Oil Products Company, Riverside, Illinois, from June 1956 to April 1957 when he entered active military service. He came to the Materials Central as a lieutenant in the United States Air Force in May 1957. After completing his military tour in April 1959, he remained with the Materials Central as a civilian scientist. He is a research materials engineer in the Fluids and Lubricants Branch, Nonmetallic Materials Laboratory.

Mr. Kirk is a member of the American Chemical Society, the American Institute of Chemical Engineers, and Sigma Xi.

BIBLIOGRAPHY

Improved Flow Schemes for the Catalytic Reforming of Napthas Employing Recycle of Heavy Paraffins. Universal Oil Products Company Reports, August 1956 through January 1957.

The Regeneration of Spent Reforming Catalyst Using a Controlled Atmosphere Containing Air, Chlorine, Hydrogen Chloride, and Water. Universal Oil Products Company Report, March 1957.

Gaseous, High Temperature Halogen Addition to Isomerization Catalysts. Universal Oil Products Company Report, April 1957.

With W.L.R. Rice. The Development of Nuclear Radiation Resistant Solid Film Lubricants. Paper presented at the Third Semi-Annual Radiation Effects Symposium, Atlanta, Ga. October 28–30, 1958.

With W. L. R. Rice. The Development of Nuclear Radiation Resistant Fluids and Lubricants. Paper present at the Air Force-Navy-Industry Lubricants Conference, Dayton, Ohio, February 17–19, 1959.

Thermal and Radiation Resistant Lubricants Developed by the Air Force Industry. Paper presented at the Dayton Section, American Society of Lubrication Engineers, February 24, 1959.

With W. L. R. Rice. The Development of Nuclear Radiation Resistant Fluids and Lubricants. Paper presented at the Fifth Nuclear Engineering and Science Conference, Cleveland, Ohio, April 5–10, 1959.

The Air Force's Lubricant and Fluid Requirements for Space Applications. Paper presented at the Dayton Section, American Society of Lubrication Engineers, November 24, 1959.

With W. L. R. Rice and W. B. Cheny, Jr. Radiation Resistant Fluids and Lubricants. Nucleonics, 18(2): 67-71, February 1960. Also in Engineer's Digest, 21(4): 105-106, April 1960.

With J. Roth and H. Adams. Aerospace Working Fluids. Paper presented at the Materials Symposium, Phoenix, Ariz., September 1961.

With J. Roth. Air Force Materials Central Working Fluids Program. Paper presented at the Third Joint AEC-NASA Liquid Metal Corrosion Meeting, Brookhaven National Laboratory, Upton, Long Island, N.Y., December 1961.

The Effect of Gravity on Free Convection Heat Transfer

The Feasibility of Using an Electromagnetic Body Force

D. A. KIRK

ABSTRACT—*Theories concerning the instability and motion of a fluid heated from below predict the effect of various physical parameters. Experimental investigations have succeeded in widely varying all parameters, except gravity, in order to determine the validity of the theories. In extra-terrestrial heat transfer applications, such as in free convection, boiling, and condensation, the effect of gravity should be verified by experiment.*

This report considers the feasibility of using an impressed electromagnetic body force acting parallel to the earth's gravitational field. The resultant of this electromagnetic force and the ground level gravitational force is said to be an "equivalent gravitational" force acting on the fluid mass. Based on the analysis made, a series of experiments can be performed to ascertain the quantitative contribution of gravity, over the range from -13.6 to 15.6 times ground level gravity, on free convection heat transfer. An apparatus is presently being fabricated to conduct an experiment for the case when heat is applied from below.

Section 1.

INTRODUCTION

This report considers the feasibility of using an electromagnetic body force to act in the plane which the earth's gravitational body force acts on a liquid mass. This electromagnetic body force will be induced by passing a horizontal electric current through a conducting liquid medium in the presence of a horizontal magnetic field which is perpendicular to the impressed electric current. The net force acting can be considered as the number of "gravities" acting on a system. An apparatus has been designed and is presently being fabricated to conduct such experiments. Figure 1 shows a preliminary schematic of the test cell as designed by the University of Dayton Research Institute.

The system to be investigated is free convection heat transfer in liquids confined by two horizontal plates and heated from below. By varying the resultant body force by electromagnetic means the convective force for heat transfer can be varied without changing the temperature gradient or the liquid's properties of mass density and thermal expansion coefficient. The possible range of -13.6 to 15.6 "gravities" will enable experiments to be conducted under conditions heretofore impossible.
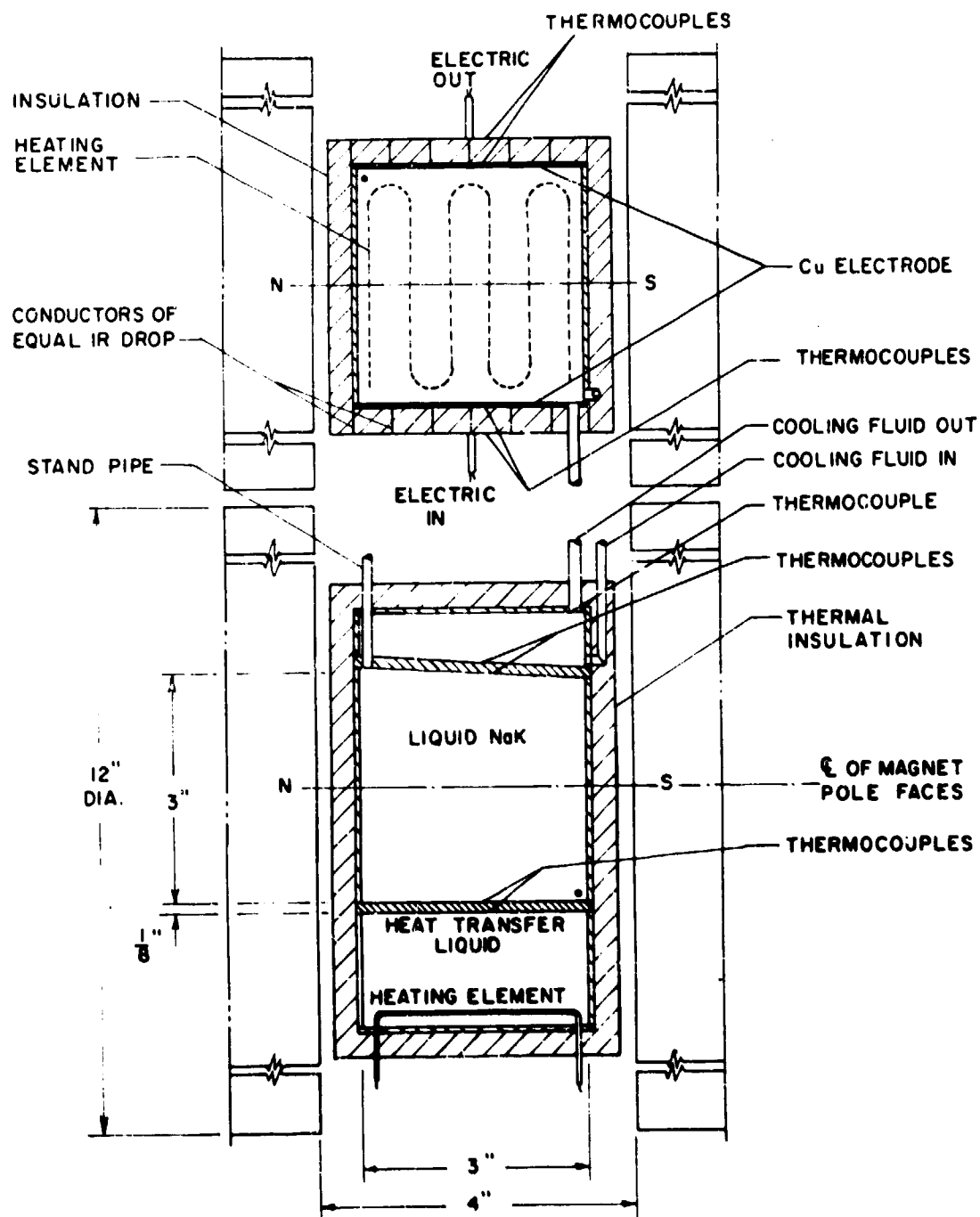
FIGURE 1. Preliminary schematic of test cell.

Sources of errors and the interfering effects of the impressed magnetic and electric fields are analyzed. Necessary introductory theory of Maxwell's field equations and free convective heat transfer are given to more easily interpret the analysis section of this report.

Except where specifically noted, the rationalized meter-kilogram-second (MKS) system will be used throughout.

Section 2.

THEORY

A. Electric and Magnetic Fields

The purpose of this section is to show briefly the source and meaning of Maxwell's equations. For a more complete development of the field equations the reader is referred to the many appropriate texts available by authors such as Bennett and Crothers (1926), Page and Adams (1940), Slater and Frank (1947), Weber (1950), and Boast (1956).

Electromagnetic theory deals with the forces acting on charges and current. An electric charge at a given point in space is acted on by two types of forces: an electric force independent of velocity, and a magnetic force proportional to its velocity. Different charges at the same point in space are acted on by different amounts of force, and the strength of the charge is defined as being proportional to the magnitude of force acting on it in a given field. Coulomb's Law states that the force on a point charge, Q, in an electrical field of intensity, E, is

$$F_e = QE \qquad (1)$$

This electric field intensity can be thought of as being caused by another point charge, Q_1, at a distance r apart from Q. Thus E can be defined as

$$\bar{E} = \frac{F_e}{Q} = \frac{Q_1 \bar{r}}{4\pi r^3} \qquad (2)$$

For a charge, Q, moving in a magnetic field of flux density, B, Ampere's force law states

$$F_m = Q(\bar{v}_e \times \bar{B}) \qquad (3)$$

The scalar potential, ϕ_e, may be defined from Coulomb's Law by considering the work required to carry the charge Q from infinity to a distance r

away from a charge Q_1. Thus

$$\phi_e = \frac{W}{Q} = \int_\infty^r \frac{-\bar{F}_e \cdot d\bar{r}}{Q} = \frac{Q_1}{4\pi\epsilon} \int_\infty^r -\frac{\bar{r} \cdot d\bar{r}}{\bar{r}^3} = \frac{Q_1}{4\pi r} \qquad (4)$$

Taking the gradient of equation (4) the following is found

$$\nabla\phi_e = \frac{Q_1\bar{r}}{4\pi\epsilon r^3} = -\bar{E} \qquad (5)$$

The force induced by motion in a static magnetic field (equation 3) does not affect the potential along the path of the charge, since

$$\phi_m = \frac{W}{Q} = \int_\infty^r (\bar{v} \times \bar{B}) \cdot d\bar{r} = \int_\infty^r \left(d\bar{r} \times \frac{d\bar{r}}{dt}\right) \cdot \bar{B} = 0 \qquad (6)$$

For conduction of charges in metals a generalized Ohm's Law may be derived from a simple force balance. In metals, the restoring force on electrons is negligible and at low electric field frequencies electron inertia can also be neglected. The total field force given by equations (2) and (3) is in equilibrium with the damping force which is assumed to be proportional to the velocity of the electron. Thus,

$$\bar{F}_t = \bar{F}_e + \bar{F}_m = Q_e(\bar{E} + \bar{v}_e \times \bar{B}) = m_e \bar{v}_e a_e \qquad (7)$$

or

$$\frac{\bar{F}_t}{Q_e} = (\bar{E} + \bar{v}_e \times \bar{B}) = \frac{m_e \bar{v}_e}{Q_e} a_e$$

where m_e is the electron's mass and a_e is the damping constant of proportionality. If N_e is the number of conducting electrons per unit volume, the current density is

$$\bar{j} = N_e Q_e \bar{v}_e = \frac{N_e Q_e^2}{m_e a_e} (\bar{E} + \bar{v}_e \times \bar{B}) = \sigma(\bar{E} + \bar{v}_e \times \bar{B}) \qquad (8)$$

where σ is the metal's conductivity or the proportionality constant of Ohm's Law.

Faraday's Law of induction is basically the same as Ampere's force law, since the former refers to magnetic field changes and fixed charges while the latter refers to a fixed magnetic field and moving charges. To see the similarity in these two laws equation (3) is written in a more general manner

$$\frac{\bar{F}_m}{Q} = \bar{E} = \frac{d(\bar{r} \times \bar{B})}{dt} = \frac{d\bar{r}}{dt} \times \bar{B} + \bar{r} \times \frac{d\bar{B}}{dt} \qquad (9)$$

161

where $\bar{r}$ is a general position vector of the charge and $\frac{d\bar{r}}{dt} = \bar{v}$ is the charge's velocity. For a stationary charge equation (9) gives one form of Faraday's law of induction.

$$\bar{E} = \bar{r} \times \left(\frac{\partial \bar{B}}{\partial t}\right) \quad (10)$$

A more common form is found by considering a positive increase in the scalar electrical potential along the line element, ds, as shown in Figure 2.

$$d\phi = \bar{E} \cdot d\bar{s} = \left(\bar{r} \times \frac{\partial \bar{B}}{\partial t}\right) \cdot d\bar{s} = (d\bar{s} \times \bar{r}) \cdot \frac{\partial \bar{B}}{\partial t} \quad (11)$$

The element of area, $-d\bar{S} = d\bar{s} \times \bar{r}$ as shown in Figure 2, is generally used to give the integral form,

$$\int_s \bar{E} \cdot d\bar{s} = -\int_s \left(\frac{\partial \bar{B}}{\partial t}\right) \cdot d\bar{S} \quad (12)$$

where S is any open surface bounded by a closed curve, s. By applying Stokes' theorem to the left side of equation (12) the differential form is found

$$\int_s \bar{E} \cdot d\bar{s} = \int_s (\nabla \times \bar{E}) \cdot d\bar{s} \quad (13)$$

$$\nabla \times \bar{E} = -\frac{\partial \bar{B}}{\partial t} \quad (14)$$

A changing magnetic flux density has been shown to produce an electric field intensity of rotational character as given by equation (14). Ampere, Rowland and Maxwell have shown by different means that the converse is true, i.e., a changing electric flux density will produce a magnetic field intensity of rotational character. This constitutes another basic experimental relation beyond those indicated by equations (2) and (3). Before this additional law is stated quanti-

162

tatively, the continuity equation of electric flux density $\overline{D}$ and electric current density $\overline{j}$ will be developed to establish their interrelationship.

From Coulomb's law (equation 2) the electric flux density is defined as

$$\overline{D}=\epsilon\overline{I}=\frac{Q_i\overline{r}}{4\pi r^3} \tag{15}$$

The net outward flux from an inclosed surface S containing n number of charges each, some distance $\overline{r}$ form the differential area $d\overline{S}$ is

$$\int_s \overline{D}\cdot d\overline{S}=\sum_{i=1}^{n}\frac{Q_i\overline{r}}{4\pi r^3}\cdot d\overline{S} \tag{16}$$

where $d\overline{S}=\overline{r}rd\Omega$ and Ω is a solid angle. Simplifying,

$$\int_s \overline{D}\cdot d\overline{S}=\sum_{i=1}^{n}\int_0^{4\pi}\frac{Q_i\overline{r}\cdot\overline{r}r}{4\pi r^3}\,d\Omega=\sum_{i=1}^{n}Q_i \tag{17}$$

Applying the divergence theorem to $\overline{D}$ and assuming a continuous distribution of charge, $q=\dfrac{d(\Sigma Q_i)}{d\tau}$, the continuity of charge equation is found

$$\int_s \overline{D}\cdot d\overline{S}=\int_\tau \nabla\cdot\overline{D}d\tau=\sum_{i=1}^{n}Q_i \tag{18}$$

$$\nabla\cdot\overline{D}=q \tag{19}$$

$d\tau$ is a differential volume contained within the closed surface S. Charge flow density $q\overline{v}$ can be thought of as electric current density $\overline{j}$ thus

$$\overline{j}=q\overline{v} \tag{20}$$

The total flux of charge flow leaving a volume τ must equal to rate of decrease of charge contained within that volume, assuming that charges are indestructible and uncreatable. In equation form this can be stated as

$$\int_s (q\overline{v})\cdot d\overline{S}=-\int \frac{\partial q}{\partial t}\,d\tau \tag{21}$$

Applying the divergence theorem to the flux term

$$\int_s (q\overline{v})\cdot d\overline{S}=\int_\tau (\nabla\cdot q\overline{v})d\tau \tag{22}$$

Combining equations (21) and (22) the continuity of charge flow density can be written

$$\nabla\cdot(q\overline{v})+\frac{\partial q}{\partial t}=0 \tag{23}$$

The rate of change of static charge density term can be evaluated from equation (19)

$$\nabla\cdot(q\overline{v})+\nabla\cdot\left(\frac{\partial\overline{D}}{\partial t}\right)_\tau=0 \tag{24}$$

or

$$q(\nabla\cdot\overline{v})+\overline{v}\cdot\nabla q+\nabla\cdot\left(\frac{\partial\overline{D}}{\partial t}\right)_\tau=0 \tag{25}$$

Each term of equation (25) can be thought of as being the divergence of a different type current density, namely, conduction, convection, and displacement, respectively. Thus equation (25) means that the total current in a specified direction across any closed surface is at any instant of time equal to zero. Total current across an open surface is then defined as sum of the conduction, convection, and displacement currents.

Maxwell generalized Ampere's and Rowland's equations into the following law which has since been experimentally verified: "Work done by a magnetic force $\overline{H}$ in moving a unit magnetic pole around any closed path s is proportional to the time rate of increase of flux of electric force $\overline{E}$ through any open surface bounded by s". Here $\overline{H}$, the magnetic force per unit pole, is defined in the same manner as $\overline{E}$, the electric force per unit charge, was defined in equation (2); however, in practice the gradient of a scalar potential is used in speaking of these vector fields as in equation (5). This law can be stated mathematically as

$$\int_s \overline{H}\cdot d\overline{s}=\epsilon\int_s \left(\frac{\partial\overline{E}}{\partial t}\right)\cdot dS=\int_s \left(\frac{\partial\overline{D}}{\partial t}\right)\cdot d\overline{S} \tag{26}$$

when the rationalized MKS system of units is used, the proportionality constant is defined as unity, and $\overline{H}$ has the units of amperes per meter. Just as the electric permittivity ϵ of an isotropic medium relates the flux density to field intensity in equation (15) the magnetic permeability of a medium is defined as

$$\overline{B}=\mu\overline{H} \tag{27}$$

The similarity between equations (12) and (26) can be seen by substituting (27) into (26). Thus,

$$\int_s \overline{B}\cdot d\overline{s}=\epsilon\mu\int_s \left(\frac{\partial\overline{E}}{\partial t}\right)\cdot d\overline{S} \tag{28}$$

163

Applying Stoke's theorem to $\overline{B}$ of equation (28) the differential form is obtained

$$\int_s \overline{B} \cdot d\overline{s} = \int_s (\nabla \times \overline{B}) \cdot d\overline{S} = \mu \int_s \left(\frac{\partial \overline{D}}{\partial t}\right) \cdot d\overline{S}$$

or

$$\frac{1}{\mu} (\nabla \times \overline{B}) = \left(\frac{\partial \overline{D}}{\partial t}\right) \tag{29}$$

The right-hand member of equation (29) refers to the total rate of change of the electric flux density through the open area $d\overline{S}$; therefore, from equation (24) and the discussion which follows equation (29) becomes

$$\frac{1}{\mu} (\nabla \times \overline{B}) = q\overline{v} + \left(\frac{\partial \overline{D}}{\partial t}\right), \tag{30}$$

By substituting equation (20) into (30) and omitting the subscript, a more common form is obtained, thus

$$\frac{1}{\mu} (\nabla \times \overline{B}) = \overline{j} + \left(\frac{\partial \overline{D}}{\partial t}\right) \tag{31}$$

Equation (21) is known as the differential form of Ampere's law with Maxwell's displacement current included.

The continuity equation for magnetic pole density is arrived at in same manner as the continuity equation for electric charge density; except, magnetic poles are assumed to occur only in pairs of north and south regardless of how small a volume considered. With no net magnetic pole density present, i.e., no excess of either north or south poles, the continuity equation is simply stated as

$$\nabla \cdot \overline{B} = 0 \tag{32}$$

Magnetic flux densities caused by steady electric currents may be calculated from the Biot-Savart law which can be derived from Ampere's law using Green's solution to Poisson's equation By defining a vector potential $\overline{A}$ such that

$$\overline{B} = \nabla \times \overline{A} \text{ and } \nabla \cdot \overline{A} = 0 \tag{33}$$

Then from equation (31) assuming no displacement currents

$$(\nabla \times \nabla \times \overline{A}) = -\nabla^2 \overline{A} = \mu \overline{j} \tag{34}$$

where the vector potential $\overline{A}$ satisfies Poisson's equation This equation has already been pre-

164

sented in the scalar form by continuity of charge equation (19) which takes the Poisson form

$$\nabla \cdot \overline{D} = -\epsilon \nabla^2 \phi_e = q \tag{35}$$

where gradient ϕ_e is defined by equation (5). From equation (4) the potential $d\phi_e$ at a point r from the point charge dQ is

$$d\phi_e = \frac{dQ}{4\pi\epsilon r} \tag{36}$$

Combining equations (35) and (36) with $q = \frac{dQ}{d\tau}$

$$4\pi\phi_e = -\int_r \frac{\nabla^2 \phi_e}{r} d\tau \tag{37}$$

where ϕ_e is the potential caused by charge density distribution q, or in general by the distribution $\nabla^2 \phi_e$, within the volume τ. Combining equations (34) and (37)

$$4\pi\overline{A} = -\int_r \frac{\nabla^2 \overline{A} d\tau}{r} = \mu \int_r \frac{\overline{j} d\tau}{r} \tag{38}$$

Taking the curl of the right-hand term

$$\nabla \times \frac{\overline{j} d\tau}{r} = d\tau \left[\left(\frac{1}{r}\right) \nabla \times \overline{j} + \nabla \left(\frac{1}{r}\right) \times \overline{j} \right] = d\tau \left[\frac{\overline{r} \times \overline{j}}{-r^3} \right]$$

Here the curl is with respect to $\left(\frac{1}{r}\right)$ only, since neither $\overline{j}$ nor $d\tau$ depend on the coordinates of the point of observation where $\overline{B}$ is evaluated. Thus

$$\nabla \times \overline{A} = \overline{B} = \frac{\mu}{4\pi} \int_r \frac{\overline{j} \times \overline{r}}{r^3} d\tau \tag{39}$$

is the generalized form of the Biot-Savart law.

B. Transport Processes

Maxwell's equations (eqs. 14, 19, 31, and 32) are relations for reversible processes while Ohm's law (eq. 8) is a relation for an irreversible process. In general, all transport processes occur irreversibly with a resultant entropy change of the system. The rate at which all irreversible processes are occurring in a given system is equal to the rate of entropy production in that system as based on the fundamental laws of macroscopic physics the law of conservation of mass and energy, the momentum law and the second law of thermodynamics. Prof. R Fieschi (1954) presents the development of the theory of irreversible processes and develops reciprocal relations employing this theory for the case of galvanomagnetic and thermomagnetic

phenomena. Before discussing specific transport processes, which are pertinent to this report, a brief introduction to the general theory of irreversible processes will be made as to the possible effect of a magnetic field.

Fieschi (1954) has presented the rate of entropy production equal to the sum of the products of quantities J_i called "fluxes" (e.g., heat flow, diffusion flow, electric current) and corresponding quantities X_i called "forces" or "affinities" (e.g., temperature gradient, gradient of chemical potential, electric field intensity). In the most general case, every flux is caused by the contribution of all the forces present, for instance, heat flow can be caused not only by a temperature gradient but also by an electric current in a magnetic field. The coefficients which establish the relationship between a given type flux J_i and another type force X_i which produces that flux is called a "phenomenological coefficient" L_{ii}. Onsager established that L_{ii} was equal to L_{ii} for scalar processes and deGroot and Mazur extended Onsager's theory to include vectorial and tensorial processes. The number of independent phenomenological coefficients for a process is greatly reduced as a result of these reciprocal relations. The end result of these relations is derived by Fieschi (1954) for simultaneous heat transfer and electric conduction in isotropic metals when a magnetic field is present. In this case only nine independent phenomenological coefficients remain out of a possible 564. Section IVC and IVD estimates errors caused by these coefficients not being zero, since in the equation of motion (83) galvanomagnetic and thermomagnetic effects are not taken into account.

When a specified type of flux J_i is caused by the same type force or affinity X_i, various well known transport laws may be arrived at assuming the following macroscopic law holds:

$$J_i = L_i X_i \qquad (40)$$

This equation holds in general for the transport of one type property or component in an isotropic medium. The flux J_i can be defined as the diffusion flow density of a component i with respect to the center of gravity motion and is given by the equation

$$J_i = \bar{\rho}_i (\bar{v}_i - \bar{v}) \qquad (41)$$

where ρ_i is its density, $\bar{v}_i$ is its velocity and $\bar{v}$ is the barycentric velocity. The affinity can be the

gradient of the density of component i or, more generally, the gradient of the potential of component i. In practice the phenomenological coefficient L_i is often called the conductivity of the medium for transporting property i. Substituting these definitions equation (40) becomes

$$\rho_i (\bar{v}_i - \bar{v}) = L_i \nabla \phi_i \qquad (42)$$

where ϕ_i is the potential of component i.

For a variable component i density and an incompressible fluid of mass density ρ the equation of continuity (23) is

$$\nabla \cdot (\rho_i \bar{v}_i) = -\frac{\partial \rho_i}{\partial t} \qquad (43)$$

$$\nabla \cdot (\rho \bar{v}) = -\frac{\partial \rho}{\partial t} = 0 \text{ or } \nabla \cdot \bar{v} = 0 \qquad (44)$$

Taking the divergence of equation (42) allows us to consider a changing ρ_i contained within a differential volume, thus

$$\nabla (\rho_i \bar{v}_i) - \nabla \cdot (\rho_i \bar{v}) = -L_i \nabla^2 \phi_i \qquad (45)$$

By equation (44)

$$\nabla \cdot (\rho_i \bar{v}) = \rho_i \nabla \cdot \bar{v} + \bar{v} \cdot \nabla \rho_i = \bar{v} \cdot \nabla \rho_i \qquad (46)$$

Combining equations (43), (45), and (46) the transport equation which is applicable to both the steady and unsteady state of ρ_i is found

$$\frac{\partial \rho_i}{\partial t} + \bar{v} \cdot \nabla \rho_i = L_i \nabla^2 \phi_i \qquad (47)$$

where the second term on the left accounts for convective transport. For transport occurring to the element of mass whose barycentric velocity is $\bar{v}$ the mobile operator is employed which is defined as

$$\frac{D}{Dt} = \frac{\partial}{\partial t} + \bar{v} \cdot \nabla \qquad (48)$$

Equation (47) then becomes

$$\frac{D \rho_i}{Dt} = L_i \nabla^2 \phi_i \qquad (49)$$

The above derivation holds true when ρ_i and ϕ_i are scalar functions; however, in special cases a similar form is arrived at for the transport of vector properties such as momentum and magnetic flux. Table 1 summarizes the result of applying equation (49) to the transport of electric charge, heat, mass, and indicates an analogous

165

TABLE 1

Transport processes applied to equation (49)			
Property or component transported, ρ.	Potential causing the transport ϕ.	Phenomenological coefficient or conductivity, L.	Name of law
Electric charge density, q	Electric potential, ϕ.	Electrical conductivity, σ	Ohm
Heat density, $\rho C_p T$	Temperature, T	Thermal conductivity, k	Biot-Fourier
Mass density of component A, ρ_A	Mass density of component A, ρ_A	Mass transfer diffusivity, D_m	Fick
Momentum density, $\rho \bar{v}$	Velocity, $\bar{v}$	Absolute viscosity, μ	Navier
Magnetic flux density, $\bar{H}$	Magnetic field intensity, $\bar{H}$	Electrical resistivity, σ^{-1}	Maxwell-Ohm, see equation (77)

form for the transport of momentum and magnetic flux.

C. Simultaneous Transport of More Than One Property

When more than one property is transported relative magnitudes may be obtained by considering the terms listed in Table 1 as they apply to equation (49). With the exception of charge transport like pairs of properties and potentials can easily be converted to the same units. The resulting coefficient is called the diffusivity which is the ratio of conductivity to capacity for that particular process. Diffusivities of various materials for transporting heat, mass, momentum, and magnetic flux density are given in Table 2 in $l^{-2}t^{-1}$(MKS). Relative ease of transport of one property compared to another may be found by simple division. Thus, dimensionless numbers, such as the Prandtl number and Lewis number, are defined in this manner.

Leaving charge transport out of these comparisons was necessary because of the manner in which the potential was originally defined. A more significant equation can be found, however, by applying equation (35) to (49), thus

$$\frac{Dq}{Dt} = -\frac{\sigma q}{\epsilon} \quad (50)$$

A comparison between liquid metals and nonpolar dielectric fluids for the same electric charge density gives drastically different discharging rates. Assuming that the electric permittivity for both materials to be approximately the same the following results are obtained

$$\frac{\left(\frac{Dq}{Dt}\right) \text{liquid metal}}{\left(\frac{Dq}{Dt}\right) \text{dielectric fluid}} = \left(\frac{\sigma/\epsilon}{\sigma/\epsilon}\right)$$

$$= \left(\frac{10^6 \text{ to } 10^7}{10^{-12} \text{ to } 10^{-18}}\right) \cong 10^{17} \quad (51)$$

Thus, unless exceedingly high voltage gradients are encountered in a liquid metal system the electric charge density can be neglected and the simpler steady state form of Ohm's law (equation 8 or 42) can be applied. For the same reason Maxwell's displacement current in equation (31) can be neglected and the total current can be considered to flow in a closed circuit just as magnetic flux lines form closed circuits.

In all but the more poorly conducting metals, the electronic contribution to the thermal conductivity completely overshadows the effect of lattice vibrations, so that the whole of the heat transported can be regarded as being carried by the electrons. In a metal, therefore, the same class of carrier transports heat and electric charge. The Wiederman-Franz law expresses the consequent state of proportionality between the thermal conductivity k and the electrical conductivity σ, thus

$$L_o = \frac{k}{\sigma T} = \frac{\pi^2}{3}\left(\frac{K'}{\epsilon}\right)^2 = 2.45 \times 10^{-8} \frac{\text{volts}^2}{°K^2} \quad (52)$$

where

$$K' = \text{Boltzman gas constant}$$
$$\epsilon = \text{charge on the electron}$$

Use of this Lorentz number L_o has been made by Miller and Epstein (Jackson, 1955, p 36, in analyzing conflicting experimental values for the

TABLE 2

Transport diffusivities of selected fluids[*]					
Fluid	Tempera-ture, °C	Diffusivity, $\frac{meters^2}{sec}$			
		Mass, D_m	Magnetic Flux,[****]	Heat, κ	Momentum, ν
Acetone	0		~1.4 (11)	1.13 (−7)	4.88 (−7)
	15		~1.4 (11)	1.09 (−7)	4.22 (−7)
	30		~1.4 (11)	1.02 (−7)[***]	3.80 (−7)
Air (at one atmosphere pressure).	0	1.32 (−7)[**]		1.83 (−5)	1.33 (−5)
	40	1.63 (−7)	>1.0 (20)	2.32 (−5)	1.69 (−5)
	100	2.12 (−7)		3.16 (−5)	2.31 (−5)
	200	3.03 (−7)		4.86 (−5)[***]	3.46 (−5)
Mercury	0	1.33 (−9)	7.48 (−1)	4.38 (−6)[***]	1.24 (−7)
	100	2.20 (−9)	8.20 (−1)	5.21 (−6)	9.15 (−8)
	200	2.91 (−9)[***]	9.07 (−1)	6.00 (−6)	8.01 (−8)
	300	3.51 (−9)[***]	1.02	6.79 (−6)	7.38 (−8)
Potassium	100		1.23 (−1)	7.15 (−5)[***]	5.31 (−7)
	200		1.73 (−1)	7.18 (−5)	3.76 (−7)
	300		2.24 (−1)	7.11 (−5)	2.95 (−7)
	400		2.75 (−1)[***]	7.00 (−5)	2.50 (−7)
Sodium	100	4.13 (−9)	7.15 (−2)[***]	7.03 (−5)[***]	7.61 (−7)
	200	8.20 (−9)	1.08 (−1)	6.73 (−5)	4.98 (−7)
	300	1.30 (−8)[***]	1.39 (−1)	6.60 (−5)	3.91 (−7)
	400	1.78 (−8)[***]	1.75 (−1)	6.48 (−5)	3.31 (−7)
NaK 77 (77.2 wt. % potassium and 22.8 wt. % sodium).	50		2.94 (−1)[***]	2.38 (−5)[***]	6.52 (−7)[***]
	100		3.12 (−1)[***]	2.85 (−5)[***]	5.65 (−7)
	150		3.31 (−1)	3.08 (−5)	4.59 (−7)
	200		3.53 (−1)	3.29 (−5)	3.89 (−7)
	250		3.79 (−1)	3.48 (−5)	3.44 (−7)
	300		4.08 (−1)	3.64 (−5)	3.08 (−7)
	350		4.37 (−1)	3.74 (−5)	2.82 (−7)
	400		4.68 (−1)	3.83 (−5)	2.65 (−7)
Water	0	1.45 (−9)	6.68 (11)	1.31 (−7)	1.79 (−6)
	10	2.02 (−9)	3.33 (11)	1.38 (−7)	1.31 (−6)
	20	2.64 (−9)	1.89 (11)	1.43 (−7)	1.01 (−6)
	30	3.39 (−9)	1.12 (11)	1.48 (−7)	8.05 (−7)
	100	1.34 (−8)[***]	1.03 (10)[***]	1.68 (−7)	2.96 (−7)

[*]See Appendix D for physical data.
[**]Notation means (n) = X (10)ⁿ, e.g., 1.32 (−7) = 1.32 × 10⁻⁷.
[***]Extrapolated.
[****]Assuming $\mu = \mu_0 = 4\pi$ (−7).

electrical conductivity of sodium-potassium alloys. According to Bosworth (1952) only the transition metals and bismuth yield Lorentz numbers significantly different than the theoretical value.

Additional dimensionless numbers may be found from the general transport equation by considering pertinent induced forces under steady state conditions. Under this condition equation (47) becomes

$$\bar{v} \cdot \nabla \rho_i = L_i \nabla' \phi_i \qquad (53)$$

For relatively small disturbances the outward transport, $\bar{v} \cdot \nabla \rho_i$, and the opposing affinity, $L_i \nabla^2 \phi_i$, may be approximated by

$$\bar{v} \cdot \nabla \rho_i \text{, proportional to } v \frac{\Delta \rho_i}{d} \qquad (54)$$

$$L_i \nabla^2 \phi_i \text{, proportional to } L_i \frac{\Delta \phi_i}{d^2} \qquad (55)$$

as far as orders of magnitudes are concerned,

where d is a characteristic dimension of the system. When momentum is transported, the outward transport is generally called an inertia force, f_I, assumed to be opposed only by a viscous force (no static pressure gradient). Where a static pressure gradient or other forces exist the ratio of inertia force to viscous force is defined as being proportional to the Reynolds number which takes the following form

$$\frac{f_I}{f_v} = \frac{r \cdot \nabla(\rho r)}{\rho \nu \nabla^2 r} \text{ prop. } \frac{V\left(\frac{\rho \Delta V}{d}\right)}{\rho \nu \left(\frac{\Delta V}{d^2}\right)} = \frac{Vd}{\nu} = Re \quad (56)$$

For the transport of heat, which is a scalar quantity. equation (53) completely describes the general steady state case, so that equations (54) and (55) are always equal, thus

$$\bar{r} \cdot \nabla(\rho C_p T) = k\nabla^2 T$$

$$V_c\left(\frac{\Delta T}{d}\right) \text{ prop. } \kappa \frac{\Delta T}{d^2}$$

or

$$V_c \text{ prop. } \frac{\kappa}{d} \quad (57)$$

This convective velocity V_c produces a frictional force f_v, given by

$$f_v = \rho \nu \nabla^2 r \text{ prop. } \rho \nu \left(\frac{V_c - V_o}{d^2}\right) \quad (58)$$

According to Archimedes' law the gravitational force or buoyancy force acting on the element of fluid volume at temperature T is

$$f_g = \bar{g}\rho - \bar{g}\rho_o = \bar{g}\rho_o \alpha(T_o - T) \quad (59)$$

where

$\alpha = \frac{-\partial \rho}{\rho_o \partial T}$ or the coefficient of volumetric expansion

T_o = mean temperature

When $T > T_o$ the fluid element will have a net buoyant force acting upward which is opposite to gravity. For free convection heat transfer between two infinite horizontal plates the only force producing the convective velocity V_c is assumed to be the buoyancy force f_g and the mean velocity V_o is zero. The measure of the instability of such a layer of fluid would be the ratio of f_g to f_v, thus applying equation (57) to (58)

$$\frac{f_g}{f_v} \text{ prop. } \frac{g\rho_o \Delta T d^3}{\rho \nu V_c} \text{ prop. } \frac{g \alpha \Delta T d^3}{\nu \kappa} = Ra \quad (60)$$

168

Rayleigh (1916) originally established this criteric of thermal instability. An exact solution to this convection problem is given by Reid and Harris (1958) which predicts that the critical value of the Rayleigh number for onset of convection is 1707.762. When the operating conditions of size and temperature difference are factored out of the Rayleigh number, the remaining terms are collectively called a convective modulus. Table 3 gives values of this convective modulus for various fluids at different temperatures assuming the gravity to have a value of 9.806 meters/second².

Another interesting thermal convection parameter may be arrived at by considering the ratio squared of inertia force to the viscous force. As

TABLE 3

Convective moduli of selected fluids[*]		
Fluid	Tempera-ture, °C	Convective Modulus = $\rho_o \alpha$, $\frac{1}{\nu k}$ meters³ °C
Acetone	0	2.34(11)[**]
	15	3.02(11)
	30	3.85(11)[***]
Air (at one atmos-phere pressure)	0	1.47(8)
	40	8.00(7)
	100	3.60(7)
	200	1.23(7)[***]
Mercury	0	5.28(9)[***]
	100	3.71(9)
	200	3.66(9)
	300	3.54(9)
Potassium	100	7.57(7)[***]
	200	1.10(8)
	300	1.44(8)
	400	1.74(8)
Sodium	100	4.12(7)[***]
	200	7.45(7)
	300	1.01(8)
	400	1.36(8)
NaK 77 (77.2 wt % potassium and 22.8 wt % sodium)	50	1.76(8)[***]
	100	1.72(8)[***]
	150	2.00(8)
	200	2.24(8)
	250	2.42(8)
	300	2.62(8)
	350	2.84(8)
	400	3.00(8)
Water	0	−2.00(9)
	10	4.44(9)
	20	1.41(10)
	30	2.48(10)
	100	1.50(11)

[*]See Appendix D for physical data.
[**]Notation means (n) = X(10)[n].
[***]Extrapolated.

before, the convective velocity V_c is assumed to be produced only by the buoyancy force f_g. For the simplest boundary conditions of $V_c=d=t=0$ under a constant acceleration, $ga\Delta T$, the following is found

$$V_c^2=2(ga\Delta T)d \qquad (61)$$

Substituting the above into the square of equation (56) the Grashof number is obtained

$$\left(\frac{f_i}{f_s}\right)^2=\left[\frac{\bar{v}_c\cdot\nabla(\rho\bar{v}_c)}{\rho\nu\nabla^2\bar{v}_c}\right]^2 \text{ prop. } \left[\frac{V_c d}{\nu}\right]^2 \text{ prop. } \frac{ga\Delta T d^3}{\nu^2}=Gr \qquad (62)$$

According to Jacok (1949, p. 478), Groeber was the first to call this quantity the Grashof number. Thus, the Grashof number may be interpreted as proportional to the square of the Reynolds number for a convective stream or cell with a characteristic dimension d.

Section 3.

DEFINITION OF THE PROBLEM

A. Electromagnetic Buoyancy Force

Charge conduction in metals is known to be carried by a continuous cloud of relatively free valence electrons. By assuming a simple damping force for electron flow, as was done in deriving equation (8), and accounting for motion of the conducting material a more general conduction equation may be derived. The total force, often called the Lorentz force, on these electrons per unit volume of space is given as a sum of a Coulomb's force (equation 1) and a Ampere's force (equation 3), thus

$$\bar{f}_e=N_eQ_e(\bar{E}+\bar{v}_e\times\bar{B}) \qquad (63)$$

where
$N_e=$ number of conducting electrons per unit volume
$Q_e=$ electric charge per electron

To account for the motion of the conducting medium, equation (41) is used to give the electron transport through this conductor material, thus

$$\bar{j}=N_eQ_e(\bar{v}_e-\bar{v})$$

or

$$\bar{v}_e=\frac{\bar{j}}{N_eQ_e}+\bar{v} \qquad (64)$$

Combining equations (63) and (64)

$$\bar{f}_e=N_eQ_e(\bar{E}+\bar{v}\times\bar{B})+\bar{j}\times\bar{B} \qquad (65)$$

This force is in equilibrium with a damping force which is assumed proportional to the conducting electron's relative velocity, thus

$$\bar{f}_e=\bar{f}_{damping}=N_em_e(\bar{v}_e-\bar{v})a_e$$

or

$$(\bar{v}_e-\bar{v})=\frac{1}{N_em_ea_e}[N_eQ_e(\bar{E}+\bar{v}\times\bar{B})+\bar{j}\times\bar{B}] \qquad (66)$$

The conduction current density is found to be

$$\bar{j}=N_eQ_e(\bar{v}_e-\bar{v})=\frac{N_eQ_e^2}{m_ea_e}(\bar{E}+\bar{v}\times\bar{B})+\frac{Q_e}{m_ea_e}(\bar{j}\times\bar{B}) \qquad (67)$$

However, by definition, the cross product $\bar{j}\times\bar{B}$ cannot have a component in the direction of $\bar{j}$; thus, equation (67) reduces to

$$\bar{j}=\sigma(\bar{E}+\bar{v}\times\bar{B}) \qquad (68)$$

where, as in equation (3),

$$\sigma=\frac{N_eQ_e^2}{m_ea_e}$$

In general, motion in a magnetic field will cause both the electric current and electric field intensity to vary as predicted by equations (14), (31), and (32).

In paragraph 2 of part IIC we saw that the net electric charge density can be neglected in metal systems where exceedingly high voltage gradients are not encountered. Then, the electromagnetic body force of equation (65) reduces to

$$\bar{f}_e=\bar{j}\times\bar{B} \qquad (69)$$

This body force acts on the mass of the conductor and does not affect the distribution of the current density within the conductor (Campbell, 1923, p. 13, and Fieschi, 1957, Chapter III) even where the Hall effect is found.

In the free convection experiment of this report, an impressed electromagnetic body force, $\bar{j}_{im}\times\bar{B}$, will be made to act in the plane of the gravitational body force, $\rho\bar{g}$. A small mass of fluid will experience a buoyancy force $\delta\bar{f}$ when its temperature T is greater than the mean value T_o by δT; thus,

$$\delta\bar{f}=\delta(\rho\bar{g})+\delta(\bar{j}_{im}\times\bar{B}) \qquad (70)$$

169

which is Archimedes' buoyancy force plus an electromagnetic buoyancy force. The only temperature dependent terms in equation (70) are the mass density ρ and the electric current density $\bar{j}$. Applying equations (59) and (68) to (70) the total buoyant force becomes

$$\partial \bar{f} = \bar{g} \partial \rho + [(\bar{E}_{\text{in pressed}}) \times \bar{B}] \partial \sigma$$
$$= -\alpha \rho_0 \bar{g} \partial T + \left(\frac{\bar{j}_{0\,\text{in}}}{\rho_0} \times \bar{B}\right) \partial \sigma$$

or

$$\frac{\partial \bar{f}}{\partial T} = -\alpha \rho_0 \bar{g} - \alpha_e (\bar{j}_{0\,\text{in}} \times \bar{B}) \qquad (71)$$

where

$\alpha = -\dfrac{\partial \rho}{\rho_0 \partial T}$, or the coefficient of thermal expansion

$\alpha_e = -\dfrac{\partial \sigma}{c_0 \partial T}$, or temperature coefficient for electric conductivity change

Both coefficients are defined so that positive values are reported for practically all metals. The equivalent gravitational field $\bar{g}^*$ created by the electromagnetic buoyancy force may be defined by the relation

$$\frac{\partial \bar{f}}{\partial T} = \alpha \rho_0 \bar{g} - \alpha \rho_0 \bar{g} \qquad (72)$$

Equating the net buoyant force in equations (71) and (72), the number of equivalent "gravities", $\bar{g}^*/g_c$, is

$$\frac{\bar{g}^*}{g_c} = \frac{\alpha e (\bar{j}_{0\,\text{in}} \times \bar{B})}{\alpha \rho_0 g_c} \qquad (73)$$

Figure 3 gives the practical range of "gravities" or g^*/g_c for various liquid metals and Appendix C, Part I, gives the sample calculations used in arriving at the various lines.

B. Magnetic Field Changes Induced by Motion of the Conduction Fluid

In Section 2.B. the solution for the case of magnetic flux diffusion in a moving liquid was indicated but not proven. A general equation for this case is derived here in the manner indicated by Cowling (1957, p. 4). The question as to whether the magnetic field lines are changed by thermal convection motion is of great importance to this report, because the constancy of the electromagnetic body force is directly affected.

Maxwell's equations are rewritten below for the case of negligible displacement currents:

$$\nabla \times \bar{E} = \frac{\partial \bar{B}}{\partial t} \qquad (14)$$

$$\Delta \times \bar{B} = \mu \bar{j}, \Delta \cdot \bar{j} = 0 \qquad (31a)$$
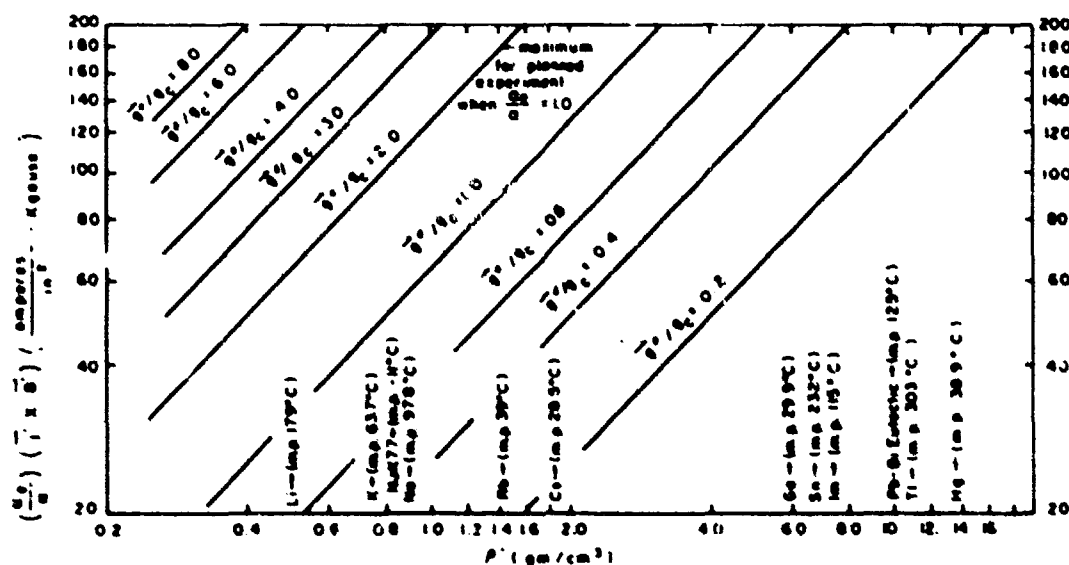
$$\nabla \cdot \bar{B} = 0 \qquad (32)$$

Figure 3. Possible "gravities" obtainable for various liquid metals.

170

Combining (14) with Ohm's general law of conduction (68)

$$\frac{\partial \overline{B}}{\partial t} = -\nabla \times \left(\frac{\overline{j}}{\sigma} - \overline{v} \times \overline{B}\right)$$

$$\frac{\partial \overline{B}}{\partial t} = \nabla \times (\overline{v} \times \overline{B}) - \frac{\nabla \times \overline{j}}{\sigma} \qquad (74)$$

From (31a) and letting $\eta = (\sigma\mu)^{-1}$

$$\frac{\partial \overline{B}}{\partial t} = \nabla \times (\overline{v} \times \overline{B}) - \frac{\nabla \times (\nabla \times B)}{\sigma\mu}$$

$$\frac{\partial \overline{B}}{\partial t} = [\nabla \cdot \overline{B}\,\overline{v} - \nabla \cdot \overline{v}\,\overline{B}] - \eta\,[\nabla\nabla \cdot \overline{B} - \nabla \cdot \nabla\overline{B}] \qquad (75)$$

From vector calculus, assuming incompressible flow, and equation (32)

$$\nabla \cdot \overline{B}\,\overline{v} = \overline{v}\nabla \cdot \overline{B} + \overline{B} \cdot \nabla\overline{v} = \overline{B} \cdot \nabla\overline{v}$$

$$\nabla \cdot \overline{v}\,\overline{B} = \overline{B}\nabla \cdot \overline{v} + \overline{v} \cdot \nabla\overline{B} = \overline{v} \cdot \nabla\overline{B}$$

Substituting this into (75)

$$\frac{\partial \overline{B}}{\partial t} = [\overline{B} \cdot \nabla\overline{v} - \overline{v} \cdot \nabla\overline{B}] + \eta\nabla^2\overline{B} \qquad (76)$$

Applying the mobile operator $\frac{D}{Dt}$, which is defined by equation (48), the following general transport equation is obtained:

$$\frac{D\overline{B}}{Dt} = \overline{B} \cdot \nabla\overline{v} + \eta\nabla^2\overline{B} \qquad (77)$$

The term $\overline{B} \cdot \nabla\overline{v}$ implies that the field changes are the same as if the magnetic lines of force are constrained to move with the material when $\sigma \to \infty$. For the ideal liquid ($\sigma = \infty$), Lundquist (1951) integrated this equation by considering any finite displacement ξ and obtained

$$\overline{B}_1 = \overline{B}_0 + (\overline{B}_0 \cdot \nabla)\overline{\xi} \qquad (78)$$

When $\overline{B}$ is initially a uniform field in the x direction the equation becomes

$$\overline{B}_1 = B_{xo}\left(1 + \frac{\partial \xi_x}{\partial x}\right)\overline{i} + B_{xo}\frac{\partial \xi_y}{\partial x}\overline{j} + B_{xo}\frac{\partial \xi_y}{\partial x}\overline{i} \qquad (79)$$

Thus only motion which is position independent will fail to change $\overline{B}$. Considering the motion of an element of mass $\sigma dldS$, a change in either its dimension or a rotational component would effect $\overline{B}$.

The last term of equation (77) gives the rate at which the magnetic field diffuses through the fluid. For a dielectric material ($\sigma \to 0$) there is negligible resistance to diffusion on a laboratory scale.

The relative importance of the constraining term to the diffusional term is brought out in the magnetic Reynolds number,

$$Re_M = \frac{dV}{\eta} \text{ prop. } \frac{\overline{B} \cdot \nabla\overline{v}}{\eta\nabla^2\overline{B}} \qquad (80)$$

Thus for the proposed thermal convection experiment

$$d = \frac{3}{2.54} \text{ cm, } r_{max} \simeq 1.0 \text{ cm/sec, } \eta_{water}$$

$$= 3.2(10^3) \text{ cm}^2/\text{sec}$$

$$Re_M = 3.7(10^{-4})$$

On this basis the constraining effect appears negligible compared to the diffusional effect, i.e., the flux lines slip or diffuse easily through the moving mass. This is sufficient indication to say that the imposed magnetic field would not be distorted by thermal convection currents.

C. Electromagnetic Body Force Changes Induced by Motion of Conducting Fluids in a Magnetic Field

Motion of a conducting liquid in a magnetic field will produce an electric field according to equation (63). Chandrasekhar (1954) has predicted that thermal convection sets in as longitudinal rolls when the magnetic field has a horizontal component and the heat transmission occurs between two infinite horizontal planes. These rolls are longitudinal with respect to the magnetic field, i.e., the axis of rotation is mutually perpendicular to both the magnetic and gravitational fields. Motion of this type induces the least reaction with the magnetic field, thereby producing less induced drag. Motion along the roll's axis of rotation is greatly inhibited, since magnetic induction occurs in this direction and the convective driving force acts only in the direction of gravity. Under the conditions of the planned experiment, motion may therefore be assumed to occur only in the gravity-magnetic field plane, and

171

no velocity component will exist in the direction of the impressed current used for the electromagnetic body force. When turbulence is encountered, small fluctuation velocities would be in all directions; however, major motions would still be constrained. In the case of water, Schmidt and Saunders (19. ') found a sharp transition from cellular to turbulent motion at a $Ra = 45,000$.

When motion is confined to the gravity-magnetic field plane, induced electric fields resulting in this motion must always lie along the axis perpendicular to this plane by equation (68). Since the electric field applied to create the electromagnetic body force is along this same axis, the resultant electric field E in equation (68) must always be parallel to this axis. Thus, for the convective motion expected, the net electromagnetic body force will always act along the gravity axis, but will not be of a constant magnitude. Variance of this body force will depend only on the vertical component of velocity at any given point.

By combining equations (68) and (69) the net electromagnetic body force is found to depend on the components of the electric field and velocity which are transverse to the impressed magnetic field, thus

$$J_e = \sigma(\bar{E} + \times \bar{v}\,\bar{B}) \times \bar{B} = \sigma(\bar{E}_t \times \bar{B}) - \sigma B^2 \bar{v}_t \quad (81)$$

Where the term containing $\bar{r}$, is the induction drag which acts as a strong "viscosity," tending to destroy motion across the magnetic flux lines, Chandrasekhar's (1952, 1954) final criterion for thermal stability in a magnetic field was the Rayleigh number and the square of the Hartman number M which is proportional to the ratio of magnetic "viscous" drag force to the ordinary viscous force of equation (58), thus

$$\frac{f_m}{f_v} = \frac{\sigma B^2 \bar{v}}{\rho \nu \nabla^2 \bar{v}} \text{ prop. } \frac{\sigma B^2 L^2}{\rho \nu} = M^2 \quad (82)$$

Actually Chandrasekhar's magnetic parameter included only the vertical component of $\bar{B}$ and considered the horizontal component separately. When no vertical component of $\bar{B}$ is present, Chandrasekhar's solution is no longer applicable. However, Cowling (1957, pp. 67-72) arrives at the same Hartman number criterion for the horizontal field case, only B in equation (92) is the horizontal component. Lehnert and Little (1957) experimentally found that the vertical component of magnetic flux would inhibit the onset of convec-

172

tion while the horizontal component had no effect on thermal stability. Since the conclusions of different investigators have not been in complete agreement, one phase of the planned experimental program will determine the effect which the horizontal magnetic field has on thermal convection.

The transverse electric field $\bar{E}_t$ in equation (81) will coincide with total electric field, since the total electric field must be transverse to the gravity-magnetic field plane. Direct evaluation of $\bar{E}_t$ is difficult, since it depends on the electric field created by motion transverse to the magnetic field and on the impressed electric field. However, in the experimental phase which determines the effect of the horizontal magnetic field, the electric field induced by motion must already be included in the final correlating equation. Thus, by impressing an electric field, a uniform electromagnetic body force will result which is in addition to that induced by the motion-magnetic field effect.

D. Equations Used in Correlating Data

Before stating the final integrated equations which are applicable to our experiment, the general differential equation of motion will be written. Actually, all parts of the equation of motion have already been discussed in the preceding text, but they have not been added to form a more general equation. The time rate of change of momentum $D(\rho\bar{v})/Dt$ is assumed to be in equilibrium with a viscous force $\rho\nu\nabla^2\bar{v}$ (Table I, Navier's law), a dynamic force or static pressure gradient ∇p, a gravity force $\rho\bar{g}$ and an electromagnetic force $\bar{j} \times \bar{B}$ (equation 69), thus

$$\frac{D(\rho\bar{v})}{Dt} = \rho\nu\nabla^2\bar{v} - \nabla p + \rho\bar{g} + \bar{j} \times \bar{B} \quad (83)$$

As discussed previously the electric current density in equation (83) is the sum of the impressed current $\bar{j}_m$ and an induced current $\bar{j}_i$, caused by motion in the magnetic field. Because of an imposed vertical temperature gradient, variations in mass density and impressed current density will occur. As Rayleigh (1916) has shown for mass density, these variations need be considered only as they modify gravity, thus applying equation (71)

$$\rho\bar{g} + \bar{j}_m \times \bar{B} = \rho\bar{g}(1 - \alpha\Delta T) + (\bar{j}_m \times \bar{B})(1 - \alpha\Delta T)$$

$$(84)$$

The induced electric current density may be eliminated by use of equation (31a), thus from vector calculus

$$\bar{j}_{in} \times \bar{B} = \frac{1}{\mu}\left[\bar{B}\cdot\nabla\bar{B} - \frac{1}{2}\nabla(B^2)\right] \qquad (85)$$

From Table I the Biot-Fourier equation for heat transfer is written

$$\frac{DT}{Dt} = k\nabla^2 T \qquad (86)$$

Equations (32), (77), '83-86) are equations of the problem which Chandrasekhar (1952, 1954) used to develop his theory, except the last term in equation (84) was not present.

Nakagawa (1960) has extended Chandrasekhar's theoretical work to yield a usable heat transfer equation. In the region of marginal stability Nakagawa found that

$$Nu = 1 + k'\left(\frac{Ra - Ra_c}{Ra}\right) \qquad (87)$$

where k' and critical Rayleigh number Ra_c are completely known functions of the vertical Hartman number squared, M^2. The horizontal magnetic field case will then be assumed to be of the same form; except that k' and Ra_c will be experimentally determined functions of the horizontal Hartman number squared.

When no electric current is impressed on the test cell, as in Chandrasekhar's and Nakagawa's work, the net electric current flowing across the entire test cell is zero, since the net mass flow rate is zero. The net result is only an increase in drag or a magnetic viscosity effect, which can be evaluated by the method in the preceding paragraph. An impressed electric current can then be used to create the uniform buoyancy force given by equations (71) and (84). The addition of $\bar{g}^*$, given by equation (73), to the ground level gravity $\bar{g}_c$ equals the net equivalent gravity $\bar{g}$ which can be applied to a dimensionless convection parameter such as the Rayleigh number.

Section 4.

ANALYSIS OF POSSIBLE ERRORS

A. Magnetic Field Induced by an Impressed Electric Current

Equation (39) gives the generalized form of the Biot-Savart law for the magnetic field induced by

a steady electric current. Since an electric current will be impressed on the test cell (Figure 1), a solenoidal magnetic field will be produced which will interact with any impressed magnetic field. Figure 4 gives the geometry used in evaluating equation (39), where the elementary volume $d\tau = dxdydz$ incloses the point $Q(x,y,z)$. At point $P(x_1,y_1,z_1)$ the magnetic field $\bar{B}$ is induced by the electric current density $\bar{j}$ located at point $Q(x,y,z)$.

The axes are chosen such that all the current flows along the positive z direction. Since the current flows in a closed path along the conductors outside the cell and in the same direction inside the cell, integration is taken along an infinite line parallel to the z axis and passing through point Q. Let

$$\left.\begin{array}{l} X = x - x_1 \\ Y = y - y_1 \\ Z = z - z_1 \\ a^2 = X^2 + Y^2 \\ r^2 = a^2 + Z^2 \\ |\bar{j}\times\bar{r}| = \bar{j}a \end{array}\right\} \qquad (88)$$

then

$$dX = dx, dY = dy, dZ = dz$$

Substituting the 5th and 6th expressions of equation (88) into the general Biot-Savart law and integrating with respect to z

$$B = \frac{\mu}{4\pi}\int_s \frac{ja}{(a^2+Z^2)^{3/2}}dzdxdy$$

$$= \frac{\mu j}{4\pi}\int_s \left[\frac{Z}{a(a^2+Z^2)^{1/2}}\right]_{-\infty}^{\infty}dxdy$$

$$B = \frac{\mu j}{2\pi}\int_s \frac{dxdy}{a} \qquad (89)$$

The factor j is not a function of position for the following reasons: (1) according to King (1945, p. 338) the current density is constant throughout the conductor when the electric field's frequency of oscillation is low, and (2) according to Campbell (1929, p. 13) and Fieschi (1954, Chapter III) the magnetic field has no effect on the electric current distribution. When a vertical temperature gradient is imposed on the test cell, a small current density variation will occur, since the electrical conductivity is temperature dependent. Based on physical property data in Jackson (1955, p. 35) for NaK 77 between 150 and 200° C a 1% varia-

173

tion in j will be caused by a $\Delta T = (0.01)\sigma$ avg.
$\left(\dfrac{\partial T}{\partial \sigma}\right) = (0.01)(43.0)\left(\dfrac{50}{2.8}\right) = 7.68°$ C. Assuming a convective modulus of 1.72×10^6 (given in Table III for NaK 77 at $100°$ C) and a depth of 3.0 inches for the test cell the critical temperature difference ΔT_c for the onset of convection is

$$Ra_c = 1708 = 1.72(10^6)d^3 \Delta T_c$$

or

$$\Delta T_c = \frac{1708}{1.72(10^6)(445.)(10^{-6})} = 0.0223°C \quad (90)$$

Thus, the variation in j will not exceed 1% until the temperature gradient exceeds 344 times the normal critical temperature for the onset of convection.

Proceeding with the integration in the x-y plane the components B_x and B_y may be found. By similar triangles

$$-dB_y = \frac{x - x_1}{a} dB \quad \text{and} \quad dB_x = \frac{y - y_1}{a} dB$$
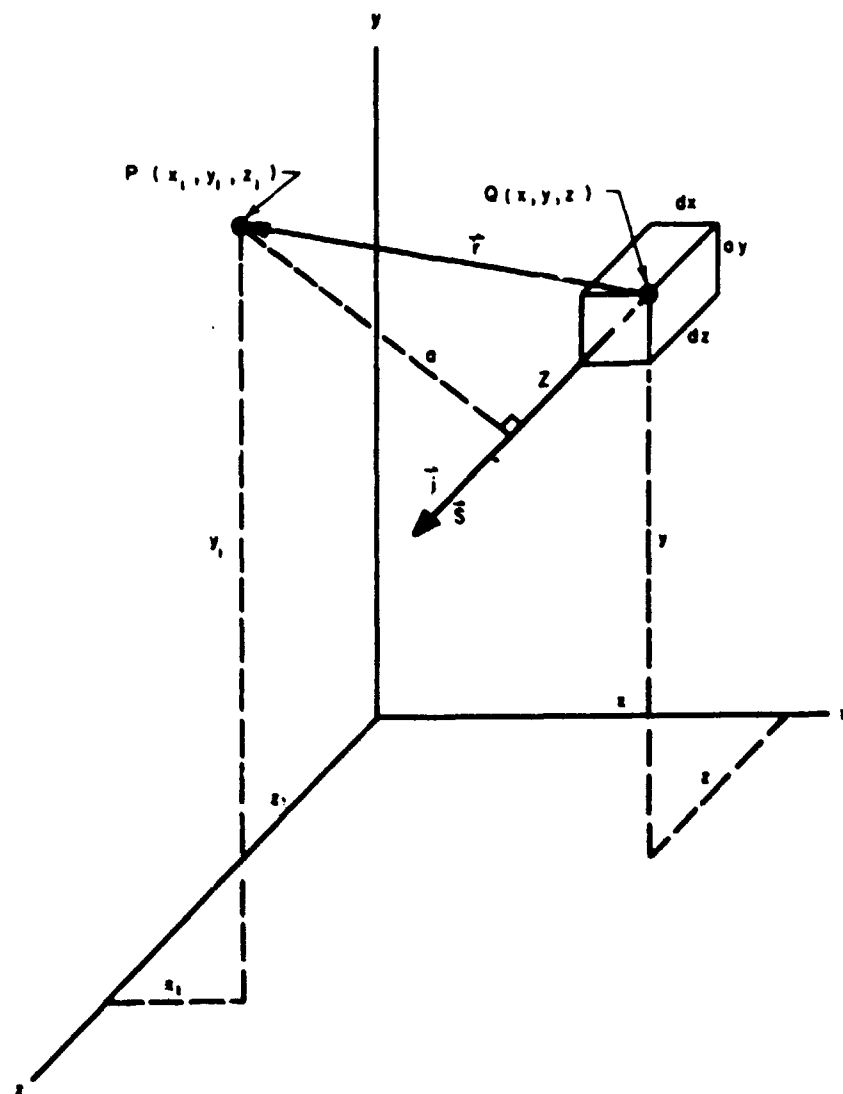

Figure 4. Geometry used in evaluating the Biot-Savart Law.

174

Combining with equation (89) and assigning the limits of z as $-\frac{w}{2}$ to $+\frac{w}{2}$ and y as $-\frac{d}{2}$ to $+\frac{d}{2}$ the following is obtained

$$-By = \frac{\mu j}{2\pi}\int_{-\frac{w}{2}}^{+\frac{w}{2}}\int_{-\frac{d}{2}}^{+\frac{d}{2}}\frac{(x-x_1)dxdz}{a^2} \qquad (91)$$

$$Bx = \frac{\mu j}{2\pi}\int_{-\frac{d}{2}}^{+\frac{d}{2}}\int_{-\frac{w}{2}}^{+\frac{w}{2}}\frac{(y-y_1)dydx}{a^2} \qquad (92)$$

Integrating

$$-By = \frac{\mu j}{2\pi}\left\{\left(\frac{w}{2}-x_1\right)\left[\cot^{-1}\left(\frac{\frac{w}{2}-x_1}{\frac{d}{2}-y_1}\right)\right.\right.$$

$$+\cot^{-1}\left(\frac{\frac{w}{2}-x_1}{\frac{d}{2}-y_1}\right)\right]-\left(\frac{w}{2}+x_1\right)\left[\cot^{-1}\left(\frac{\frac{w}{2}+x_1}{\frac{d}{2}-y_1}\right)\right.$$

$$\left.+\cot^{-1}\left(\frac{\frac{w}{2}+x_1}{\frac{d}{2}+y_1}\right)\right]+\left(\frac{d}{4}-\frac{y_1}{2}\right)$$

$$\ln\left[\frac{\left(\frac{d}{2}-y_1\right)^2+\left(\frac{w}{2}-x_1\right)^2}{\left(\frac{d}{2}-y_1\right)^2+\left(\frac{w}{2}+x_1\right)^2}\right]$$

$$+\left(\frac{d}{4}+\frac{y_1}{2}\right)\ln\left[\frac{\left(\frac{d}{2}+y_1\right)^2+\left(\frac{w}{2}-x_1\right)^2}{\left(\frac{d}{2}+y_1\right)^2+\left(\frac{w}{2}+x_1\right)^2}\right]\right\} \qquad (93)$$

$$B_x = \frac{\mu j}{2\pi}\left\{\left(\frac{d}{2}-y_1\right)\left[\cot^{-1}\left(\frac{\frac{d}{2}-y_1}{\frac{w}{2}-x_1}\right)\right.\right.$$

$$+\cot^{-1}\left(\frac{\frac{d}{2}-y_1}{\frac{w}{2}+x_1}\right)\right]-\left(\frac{d}{2}+y_1\right)\left[\cot^{-1}\left(\frac{\frac{d}{2}+y_1}{\frac{w}{2}-x_1}\right)\right.$$

$$\left.+\cot^{-1}\left(\frac{\frac{d}{2}+y_1}{\frac{w}{2}+x_1}\right)\right]+\left(\frac{w}{4}-\frac{x_1}{2}\right)$$

$$\ln\left[\frac{\left(\frac{w}{2}-x_1\right)^2+\left(\frac{d}{2}-y_1\right)^2}{\left(\frac{w}{2}-x_1\right)^2+\left(\frac{d}{2}+y_1\right)^2}\right]+\left(\frac{w}{4}-\frac{x_1}{2}\right)$$

$$\ln\left[\frac{\left(\frac{w}{2}+x_1\right)^2+\left(\frac{d}{2}-y_1\right)^2}{\left(\frac{w}{2}+x_1\right)^2+\left(\frac{d}{2}+y_1\right)^2}\right]\right\} \qquad (94)$$

Appendix C-II gives the sample calculations for evaluating equations (93) and (94) by using the test cell's planned configuration and maximum current densities. Table 4 summarizes these results when the total current is 200 amperes and $w=d=3.0$ inches. The maximum magnetic flux will occur at the outer x-y perimeter of the cell and will decrease to zero along the (o, o, z_1) cell center line. If the impressed magnetic field is varied between 900 and 8,000 gausses, the impressed electric current will affect the resultant magnetic field by no more than 1%. Much less error can be introduced by proper mutual adjustment of the impressed magnetic field and electric current.

B. Joule Heating Effect

Without an impressed electric current, thermal convective motion in the magnetic field produces an induction drag $\sigma B^2 \bar{r}$, according to equation (81). This magnetic "viscosity" effect dissipates its energy through induced current or joule type heating which can be taken into account by application of equation (87). A maximum estimate of this effect is given as follows:

$\sigma^{-1} = 41.6(10^{-8})$ ohm meter, for NaK 77 at 150° C (Jackson, 1955, p. 35).

$B_{max} = 0.8$ webers/meter^2 = 0.8 volt sec/meter^2

$(r_1)_{ave} = 1.0$ cm/sec

$$\sigma B^2 \bar{r}_1 \bar{r} = \frac{(0.64)(10^{-4})}{41.6(10^{-8})} = 154.0 \text{ watts/m}^3 \qquad (95)$$

When an electric current is impressed to produce the electromagnetic body force, joule heat is produced. If the impressed electric current density is essentially constant as discussed in paragraph 3 of section IV A, then the joule heat will be constant and will be equal to $\sigma^{-1}j^2_{impressed}$. A maximum estimate of this effect is given as follows:

$$(j_{impressed})_{max} = \frac{200}{(0.0763)^2} = 3.44(10^4) \text{ amperes/m}^2$$

$$\sigma^{-1}j^2_{max} = (41.6)(10^{-8})(11.5)(10^8) = 491.0 \text{ watts/m}^3 \qquad (96)$$

Thus, the impressed current joule heating effect is of approximately the same order of heat generation as the magnetic drag effect; however, the

former does not directly inhibit convective motion. The rate of adiabatic temperature rise in the test cell caused by the impressed electric current would be

$$\frac{\partial T}{\partial t} = \frac{\sigma^{-1}j^2}{\rho c_F} = 3.37(10^{-4})\cdot C/sec = 2.29\cdot C/hr \quad (97)$$

TABLE 4.— *Magnetic flux densities induced by the impressed electric current within the test cell*

x_1	y	$\dfrac{B_x^*}{\mu j w}$	$\dfrac{B_y^*}{\mu j w}$	$\dfrac{B^*}{\mu j w}$	B^{**} gausses
w/2	0	0	0.275	0.275	9.06
w/2	d/2	−0.181	0.181	0.255	8.40
0	d/2	−0.275	0	0.275	9.06
−w/2	d/2	−0.181	−0.181	0.255	8.40
−w/2	0	0	0.275	0.275	9.06
−w/2	−d/2	−0.181	0.181	0.255	8.40
0	−d/2	−0.275	0	0.275	9.06
w/2	−d/2	0.181	0.181	0.255	8.40
0	0	0	0	0	0
0	d/4	−0.129	0	0.129	4.25

*w = d, where w = width of test cell and d = depth of test cell.
**w 3.0 inches and $jw^2 = 200$ amperes.

where for NaK 77 at 150° C

$\rho = 0.835$ gm/cm³ (Jackson, 1955, p. 34)

$C_F = 0.2208$ cal/gm°C (Jackson, 1955, p 37)

$\rho C_F = (0.835)(10^6)(0.2208)(4.184) = 0.771(10^6)$ joule/m³°C

Since the upper and lower walls of the test cell are made to conduct heat, the rate of temperature rise will not remain very long after the impressed current is allowed to flow. The maximum temperature gradient caused by this effect will occur at the horizontal wall boundaries in the NaK77, thus

$\sigma^{-1}j^2$(volume of test cell) = 491(0.444)(10⁻³) = 0.218 watts

where

$$\left(\frac{\Delta T}{d}\right)_{max} = \frac{0.218}{Sk} = 0.790\cdot c/m \quad (98)$$

S = area over which the heat is conducted = 2(.0763)² = 1.16(10⁻²)m²

k = 0.238 watt/cm°C, for NaK 77 at 150°C (Jackson, 1955, p 35)

Sk = 0.276 watt m°C

This compares with the critical temperature gradi-

ent of 0.292°C/m required for the onset of normal convection in the test cell. The effect of the joule heating temperature gradient will be to increase the upper half of the test cell's temperature gradient and to decrease the lower half by an equal amount. The resultant redistributed temperature gradient will however, have the same average value as if no joule heating were present. Part of the planned experimental tests will be to determine the quantitative effect, if any, which the joule heating temperature gradient has on free convection heat transfer when no impressed magnetic field is present.

C. Galvanomagnetic Effects

1. A transverse galvanomagnetic potential difference—Hall effect.

The Hall effect is described on page 8 of Campbell (1923) as "The total transverse electromotive force $\Delta\phi_{EH}$ set up by the magnetic field $\overline{H}$, in a plate P, as shown (Figure 5a), carrying an electric current density $\overline{j}$ is as follows:"

$$E_H = \frac{\Delta\phi EH}{b} = R(\overline{H}\times\overline{j}) \quad (99)$$

where b = plate width

R = Hall coefficient (theoretically negative)

$\overline{j} = \overline{I}/bd$

d = plate thickness

θ = angle which the equipotential lines rotate at AB in Figure 4a

when $\overline{H} = 0$ $\quad \Delta\phi_{EH} = 0$

when $\overline{H}$ is finite

$$\Delta\phi_{EH} = Rb(\overline{H}\times\overline{j}) = \frac{R(\overline{H}\times\overline{I})}{d} \quad (100)$$

It is interesting to note on page 13 Campbell (1923) "While in the Hall effect the equipotential lines are rotated by a magnetic field, the lines of primary current are not rotated. . . ." Hall verbally tells Campbell why this should be true through the analogy of the independence of a tube flow velocity on the transverse pressure gradient caused by gravity. Therefore, if the Hall coefficient were either positive, negative, or zero for the system under study, there would be no effect on the current density distribution.

The angle of rotation θ of the equipotential lines may be obtained from Figure 5a and equation (99), thus

$$\tan\theta = \frac{E_H}{E} = \frac{(-R)Hj}{\frac{j}{c}} = (-R)H\sigma \qquad (101)$$

The Hall coefficient ν is found to be -0.0025 e.m.u. for solid sodium by Ettingshausen and Nernst (Campbell, 1923, p. 124). This compares with -0.00052 e.m.u. for mercury, the only liquid metal in Campbell, as determined by Des Coudre. The maximum angle θ for NaK 77 is estimated using the Hall coefficient and conductivity for sodium thus $(\sigma^{-1})_{min} = 5.8$ (10^{-6}) ohm cm $= 5.8$ (10^3) e.m.u. ohm cm

$$H_{max} = 8,000 \text{ gauss}$$

$$\tan\theta = \frac{(2.5)(8.0)}{5.8(10^3)} = 3.45(110^{-3}) \text{ or } \theta = 0° - 12'$$
$$(102)$$

Therefore, even if the current lines were rotated with the equipotential lines this effect could still be neglected.

2. A transverse galvanomagnetic temperature difference—Ettingshausen Effect.

The Ettingshausen effect is described on page 147 of Campbell (1923) as "The transverse change in temperature per unit width, $\Delta T/b$, was found to be proportional to the magnetic field $\overline{H}$, the current density $\overline{j}$ of the primary electric current $\overline{I}$, and the width b." Thus

$$\text{grad } T = \frac{\Delta T_s}{b} = P(\overline{j} \times \overline{H}) \qquad (103)$$

where $P =$ Ettingshausen coefficient (theoretically positive) Figure 5b shows the Ettingshausen effect when P is positive.

Zahn (Campbell, 1923, p. 152) derived a theoretical ratio of the Ettingshausen coefficient to the Hall coefficient, thus

$$\frac{(-R)}{P} = 2.5 \times 10^4 \frac{\text{emu volts}}{°K} \qquad (104)$$

Assuming that Zahn's ratio applies in this case, the Ettingshausen effect may be estimated,

$$P_{NaK} \simeq P_{Na} \simeq \frac{0.0025}{2.5 \times 10^4} = 10^{-7} \left(\frac{°K \text{ cm}}{\text{amp gauss}}\right)_{emu}$$

$$b = 3(2.54) = 7.63 \text{ cm}$$

$$H_{max} = 8000 \text{ gauss}$$

$$j_{max} = \frac{200}{9(2.54)^2} \left(\frac{1}{10}\right) = 0.345 \text{ (amp/cm}^2\text{) emu}$$

$$(\Delta T)_{max} = bPjH = (7.63)(10^{-7})(0.345)$$
$$(8.0)(10^3) = 2.10(10^{-3}) °C$$

which is quite negligible.

3. A longitudinal galvanomagnetic potential difference—Magneto-resistance effect.

This source of possible error can be neglected according to the discussion on page 194 of Campbell (1923).

"Drude and Nernst, 1891, observed that the resistance of mercury in a field of 8000 gauss increased about 0.2 percent while that of molten bismuth at 290° C increased 0.4 percent. The same year Des Coudres called attention to the fact that this increase might be attributed to heating of the metal by current.

"The work of Berndt, 1907, seemed to confirm the contention of Des Coudres. He found that the smaller the capillary tube used, the less the increase in resistance. In fields of 1000 to 3000 gauss, the increase in resistance was not more than 0.00005 percent for mercury, and 0.004 percent for molten bismuth."

4. A longitudinal galvanomagnetic temperature difference.

Insufficient data is available concerning this effect to say whether it actually exists. Thus according to page 210 of Campbell (1923),

"So littlework has been done on the longitudinal galvanomagnetic temperature difference, that no general conclusions can be drawn as to its direction of variation with field strength.

"Drude, on the basis of the dual electron theory, showed that this effect is in reality a Peltier effect."

D. Thermomagnetic Effects

1. Transverse thermomagnetic electromotive force—Nernst effect.

The Nernst effect is experienced when a transverse electromotive force $\Delta\phi_{EM}$ is set up by the magnetic field $\overline{H}$, in the plate P, carrying a heat current density $\overline{j}_H$, as shown in figure 5c. This effect follows the equation

$$E_N = \frac{\Delta\phi_{EN}}{1} = \frac{-Q}{k}(\overline{H} \times \overline{j}_H) \qquad (105)$$

where,

$1 =$ plate length
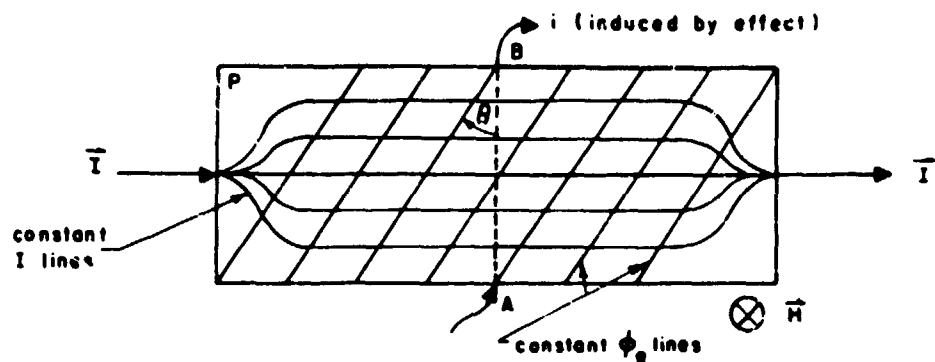
$Q =$ Nernst coefficient (theoretically positive)

$k =$ thermal conductivity

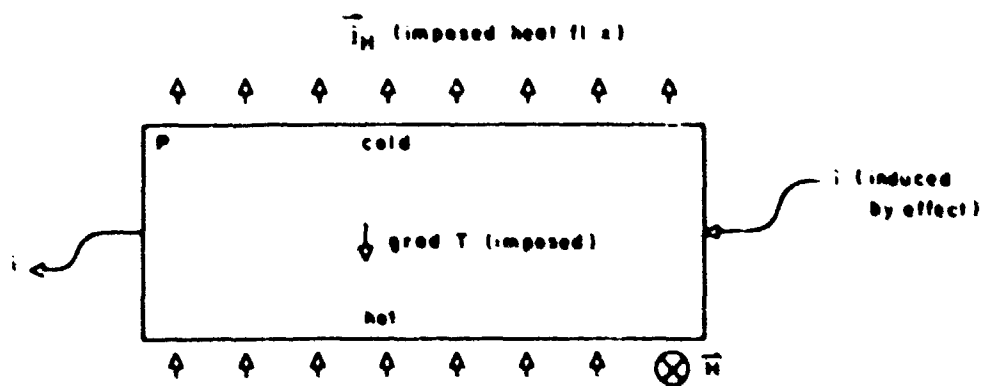$\overline{j}_H =$ conduction heat $= k\nabla T$

$\overline{i} = \sigma\overline{E}(bd)$

177

a HALL EFFECT FOR A NEGATIVE COEFFICIENT
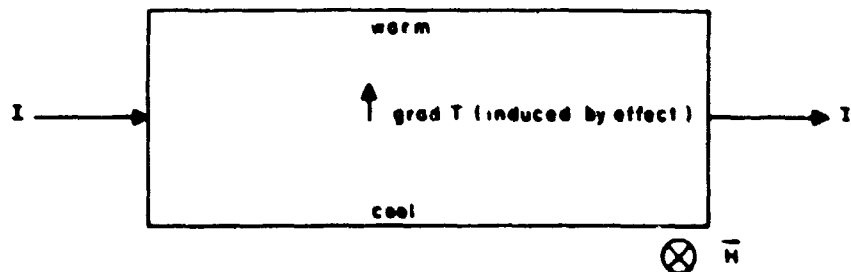
b ETTINGSHAUSEN EFFECT FOR A POSITIVE COEFFICIENT

c NERNST EFFECT FOR A POSITIVE COEFFICIENT

Figure 5 Schematic of selected galvanomagnetic and thermomagnetic effects

or in a simpler form

$$\overline{E}_N = Q\,(\overline{H} \times \nabla T) \qquad (106)$$

Campbell (1923, p. 230) has tabulated various values of the Nernst coefficient (e.m.u. units) for solid metals. Maximum values of Q, at room temperature and above are $8.6(10^{-3})$ for nickel, 0.222 for Monel and 0.26 for bismuth. Lower values were reported for Q in the following metals: $7.3(10^{-5})$ for copper, $1.66(10^{-3})$ for steel, $1.6(10^{-4})$ for lithium, and $-4.6(10^{-5})$ for silver.

In the heat transfer apparatus under analysis the impressed electric field must be opposite to E_N (for Q positive) in order to have an upward body force of $\mu \overline{j} \times \overline{H}$. The net electric field across the liquid metal, $\overline{E} - \overline{E}_N$, will produce a current density $\overline{j}$ thus,

$$\overline{j} = \sigma(\overline{E} - \overline{E}_N) = \sigma[\overline{E} - Q(\overline{H} \times \nabla T)] \qquad (107)$$

The joule heating rate per unit volume, $\dfrac{j^2}{\sigma}$, is

$$\frac{\overline{j} \cdot \overline{j}}{\sigma} = \overline{E} \cdot \overline{j} - Q(\overline{H} \times \nabla T) \cdot \overline{j} \qquad (108)$$

and is smaller than the power input per unit volume, $\overline{E} \cdot \overline{j}$. The error in a wattmeter reading, $\overline{E} \cdot \overline{j}$ is thus

$$\% \text{ error} = \frac{\overline{E} \cdot \overline{j} - \dfrac{j^2}{\sigma}}{\dfrac{j^2}{\sigma}} = \frac{Q(\overline{H} \times \nabla T) \cdot \overline{j}}{\dfrac{j^2}{\sigma}} (100) \qquad (100)$$

$$\% \text{ error} = \frac{\sigma Q H (\nabla T)}{j} (100) \qquad (109)$$

assuming that

$$Q_{max} = -1.6(10^{-3}) \frac{\text{emu volts}}{^\circ C \text{ gauss}}$$

$$Q_{max} = 1.6(10^{-10}) \frac{\text{volts}}{^\circ C \text{ gauss}}$$

$$H = 8000 \text{ gauss}$$

$$j = 3.45 \text{ amp/cm}^2$$

$$(\nabla T)_{max} = 10^2 \; ^\circ C/\text{cm}$$

$$\sigma_{max} = \frac{1}{(47)(10^{-5})} \frac{\text{amp}}{\text{volt cm}}$$

$$\% \text{ error} = \frac{1.6(10^{-3})(8.0)(10^2)(10^2)}{47(10^{-5})(3.45)} = 0.079\%$$

The Nernst effect in liquid metals is thought to be insignificant since nickel practically loses this effect at its critical temperature (700° K) and tellurium's coefficient approaches zero at its melting point, according to Campbell (1923, pp. 218 and 220).

2. Transverse thermomagnetic temperature difference—Righi-Leduc effect

Using the same geometry as in the previous figure for the Nernst effect.

$$\frac{\nabla T}{1} = (\nabla T)_{transverse} = S(\overline{H} \times \nabla T) \qquad (110)$$

where $S =$ coefficient for the Righi-Leduc effect. This transverse temperature gradient will produce an error given by

$$\% \text{ error} = \frac{(\nabla T)_{transverse}}{\nabla T} = SH(100) \qquad (111)$$

S has not been determined for liquid metals; however, Campbell (1923, p. 236) shows that the correlation between S and R of the Hall effect is excellent. The two angles of rotation are given by

$$\tan \theta_H = R \sigma H, \; \tan \theta_{R-L} = SH \qquad (112)$$

For the thirteen metals studied, equal magnetic field intensities produced the same angle of rotation for both effects. Applying this correlation, equation (111) becomes

$$\% \text{ error} = (100) \tan \theta_{R-L} = (100) \tan \theta_H \qquad (113)$$

From equation (102) the Hall effect angle is substituted thus,

$$\% \text{ error} = 0.0345\% \text{ which is negligible}$$

3. Thermomagnetic longitudinal potential difference.

This longitudinal potential difference induced by the cross effect of the temperature and magnetic field is difficult to measure. This difficulty is best summarized by Campbell (1923, p. 251). "Since the magnetic field changes the inherent thermoelectric power of the plate or the lead wire, a difference of potential will set up. There seem to be good reason to believe that both the changes in thermal conductivity and thermo-electric power are concerned in the production of a longitudinal E.M.F."

No data is presented on liquid metals and the data on solid metals is greatly dependent on the

lead wire material used. Until more information and theory is found, no definite conclusions can be reached, except to say that this effect is most likely negligible.

4. Thermomagnetic longitudinal temperature difference—a change in the thermal conductivity of the metal.

Since both the flow of electricity and heat in metals is known to occur by electron movement, then the magneto-resistance effect of Part IV.C.3. should be of the same order as this change in thermal conductivity. Theory and experimental data are in disagreement as presented by Campbell (1923, p 258), "Liven (1915) using the assumptions of a free electron theory deduced an expression for the change in thermal conductivity in a traverse magnetic field. According to his expression, the thermal conductivity should always increase, which is contrary to the data found on the few metals reported."

Section 5.

SUMMARY AND CONCLUSIONS

The basic equations were derived for the processes involved in order to elucidate the physical implications of existing theory. Motion implied by the equations of the problem and by the most pertinent previous investigations were discussed. Based on the analysis, the following statements may be made concerning the planned experiment:

A. Convective motion will not significantly distort the impressed magnetic field.

B. The impressed magnetic field will affect the convective motion, and this effect can be taken into account.

C. The impressed electric current is uniformly additive to the electric current induced by convective motion in the magnetic field.

D. Based on the above three statements the impressed electromagnetic body force will be uniform throughout the fluid mass.

E. The impressed electric current causes a negligible deviation in the impressed magnetic field.

F. Neglecting joule heating, the impressed electric current has no effect on the convective motion of the fluid.

G. Without an impressed magnetic field present the effect of joule heating will be experimentally determined. Joule heating could affect convective motion, because the usual temperature

gradient becomes distorted, even though the overall temperature difference is undisturbed.

H. Galvanomagnetic and thermomagnetic effects are considered negligible even though experimental data on NaK 77 has not been found. Additional literature searching is necessary to determine whether the data on NaK 77 is available.

On the bases of the facts presented the planned experiment is feasible and the probability of determining the effect of gravity by the electromagnetic method is very favorable.

APPENDIX A

Symbols and Their Rationalized MKS Units

English letters

$\bar{A}$ Magnetic vector potential, $\dfrac{\text{webers}}{\text{meter}}$, $lmQ^{-1}t^{-1}$

a, Electron's damping constant, $\dfrac{1}{\text{sec}}$, t^{-1}

$\bar{B}$ Magnetic flux density, $\dfrac{\text{webers}}{\text{meter}^2}$, $mQ^{-1}t^{-1}$

C, Specific heat at constant pressure,
$\dfrac{\text{joules}}{Kg\,^\circ K}$, $l^2T^{-1}t^{-2}$

$\bar{D}$ Electric flux density, $\dfrac{\text{coulombs}}{\text{meter}^2}$, $l^{-2}Q$

d A characteristic dimension of a system, meters, l

D_m Mass transport diffusivity, $\dfrac{\text{meters}^2}{\text{sec}}$, l^2t^{-1}

$\bar{E}$ Electric field intensity, $\dfrac{\text{volts}}{\text{meter}}$, $lmQ^{-1}t^{-2}$

$\bar{F}$ Force, newtons, lmt^{-2}

$\bar{f}$ Body force, $\dfrac{\text{newtons}}{\text{meter}^3}$, $l^{-2}mt^{-2}$

$\bar{g}$ Net gravitational acceleration, $\dfrac{\text{meters}}{\text{sec}^2}$, lt^{-2}

$\bar{g}^\circ$ Equivalent gravitational acceleration produced by the imposed electromagnetic body force, $\dfrac{\text{meters}}{\text{sec}^2}$, lt^{-2}

g, The earth's sea level acceleration, $\dfrac{\text{meters}}{\text{sec}^2}$, lt^{-2}

Gr Grashof number $= \dfrac{g\rho^2\Delta T d^3}{\mu^2}$, dimensionless

180

$\bar{H}$ Magnetic field intensity, $\dfrac{\text{amperes}}{\text{meter}}$, $l^{-1}Qt^{-1}$

$\bar{I}$ Electric current, amperes or $\dfrac{\text{coulombs}}{\text{sec}}$, Qt^{-1}

j Electric current density, $\dfrac{\text{amperes}}{\text{meter}^2}$, $l^{-2}Qt^{-1}$

$\bar{j}_H$ Heat flux density, $\dfrac{\text{joules}}{\text{sec. meter}^2}$, mt^{-3}

K Dielectric constant of a medium, $\dfrac{\epsilon}{\epsilon_o}$, dimensionless

k Thermal conductivity, $\dfrac{\text{joules}}{\text{sec. meter °K}}$, $lmT^{-1}t^{-3}$

k_e Equivalent thermal conductivity, $\dfrac{\text{joules}}{\text{sec. meter °K}}$, $lmT^{-1}t^{-3}$

l Length, m l

Lo Lorenze number $= \dfrac{k}{\sigma T}$, $\dfrac{\text{volts}^2}{\text{°K}^2}$, $l^4m\cdot Q^{-2}T^{-2}t^{-4}$

M Hartman number $= Bd(\sigma/\rho v)^{\frac{1}{2}}$, dimensionless

m Mass, kilograms, m

N_e Number of conducting electrons per unit volume of conductor, $\dfrac{i}{\text{meter}^3}$, l^{-3}

Nu Nusselet number $= \dfrac{k_e}{k}$, dimensionless

Pr Prandtl number $= \dfrac{v}{K}$, dimensionless

Q Electric charge, coulombs, Q

q Electric charge density, $\dfrac{\text{coulombs}}{\text{meter}^3}$, $l^{-3}Q$

$\bar{r}$ Position vector, meters, l

Ra Rayleigh number $\dfrac{g\alpha\Delta T d^3}{vk}$, dimensionless

Re Reynolds number $= \dfrac{Vd}{v}$, dimensionless

Re_M Magnetic Reynold number $= \dfrac{Vd}{\eta}$, dimensionless

S Area, meters^2, l^2

s Length of line, meter, l

T Temperature, degrees Kelvin, T

t Time, seconds, t

V Mean velocity of the mass, $\dfrac{\text{meters}}{\text{sec.}}$, lt^{-1}

$\bar{v}$ Velocity vector, $\dfrac{\text{meters}}{\text{sec.}}$, lt^{-1}

W Work, joules or newton-meters, l^2mt^{-2}

v Test cell width, meters, l

Greek letters

α Coefficient of volumetric expansion, $= \dfrac{\partial\rho}{\rho_o\partial T}$, °K^{-1}, T^{-1}

α_e Temperature coefficient for electrical conductivity change $= \dfrac{\partial\sigma}{\sigma_o\partial T}$, °K^{-1}, T^{-1}

β Mean temperature gradient $= \dfrac{T_1 - T_2}{d}$, $\dfrac{\text{°K}}{\text{meter}}$, $l^{-1}T$

ϵ Electric permittivity of a medium, $\dfrac{\text{coulombs}}{\text{meter volt}}$, $l^{-3}m^{-1}Q^2t^2$

ϵ_o Electric permittivity of space $= 8.85 \times 10^{-12}$ $\dfrac{\text{coulombs}}{\text{meter volt}}$, $l^{-3}m^{-1}Q^2t^2$

η Magnetic diffusivity $= (\mu\sigma)^{-1}$, $\dfrac{\text{meter}^2}{\text{sec}}$, l^2t^{-1}

κ Thermal diffusivity $= \dfrac{k}{C_p\rho}$, $\dfrac{\text{meter}^2}{\text{sec.}}$, l^2t^{-1}

μ Magnetic permeability of a medium, $\dfrac{\text{weber}}{\text{meter ampere}}$, lmQ^{-2}

μ_o Permeability of space $= 4\pi \times 10^{-7}$ $\dfrac{\text{Weber}}{\text{meter ampere}}$, lmQ^{-2}

μ_r Relative permeability of a medium $= \dfrac{\mu}{\mu_o}$, dimensionless

v Momentum diffusivity or kinematic viscosity, $\dfrac{\text{meter}^2}{\text{sec.}}$, l^2t^{-1}

$\bar{\xi}$ Displacement of position $= \Delta\bar{r}$, meters, l

ρ Mass density, $\dfrac{\text{kilograms}}{\text{meter}^3}$, $l^{-3}m$

σ Electrical conductivity, $\dfrac{l}{\text{ohm meter}}$, $l^{-3}m^{-1}Q^2t$

τ Volume meter^3, l^3

Φ Magnetic flux, weber or volt-seconds, $l^2mQ^{-1}t^{-1}$

ϕ_e Scalar electric potential, volts, $l^2mQ^{-1}t^{-2}$

Operators in Cartesian coordinates

Δ Difference or change in a function

$$\nabla = \bar{i}\frac{\partial}{\partial x} + \bar{j}\frac{\partial}{\partial y} + \bar{k}\frac{\partial}{\partial z}$$

$$\nabla^2 = \frac{\partial^2}{\partial x^2} + \frac{\partial^2}{\partial y^2} + \frac{\partial^2}{\partial z^2}$$

$$\nabla X \bar{F} = \begin{vmatrix} \bar{i} & \bar{j} & \bar{k} \\ \dfrac{\partial}{\partial x} & \dfrac{\partial}{\partial y} & \dfrac{\partial}{\partial z} \\ F_1 & F_2 & F_3 \end{vmatrix}$$

APPENDIX B

References

Bennett, E., and Crothers, H. M., 1926, *Introductory Electrodynamics for Engineers*, 1st ed., McGraw-Hill Book Co., New York.

Boast, W. B., 1959, *Principals of Electric and Magnetic Fields*, 2nd ed., Harper and Brothers, New York.

Bosworth, R. C. L., 1952, *Heat Transfer Phenomena*, John Wiley and Sons, Inc., New York.

Campbell, L. L., 1923, *Galvanomagnetic and Thermomagnetic Effects, The Hall and Allied Phenomena*. Longmans, Greens and Co., 55 Fifth Ave., New York.

Chandrasekhar, S., 1952, "On the Inhibition of Convection by a Magnetic Field." *Lond., Eding., Dublin Phil. Mag.*, Ser. 7, Vol. 43, pp. 501–32.

Chandrasekhar, S., 1954, "On the Inhibition of Convection by a Magnetic Field· II" *Lond., Eding., Dublin Phil. Mag.*, Ser. 7, Vol. 45, pp. 1177–91.

Cowling, T. G., 1957, *Magnetohydrodynamics*, Interscience Publishers, Inc., New York.

Ewing, C. T., et al., 1955, "Thermal Conductivity of Mercury and Two Sodium-Potassium Alloys," *J. Phys. Chem.*, Vol. 59, pp. 524–28.

Fieschi, R., 1954, *Thermodynamical Theory of Galvanomagnetic and Thermomagnetic Phenomena*, Doctor's thesis, Instituut Voor Theoretische Natuurkunde, Langebrug III, Leiden.

Gray, D. E., ed., 1957, *American Institute of Physics Handbook*, McGraw-Hill Book Company, Inc., New York.

Hodgman, C. D., ed., 1957, *Handbook of Chemistry and Physics*, Chemical Rubber Publishing Company, Cleveland, Ohio.

Jackson, Carey B., ed., 1955, *Liquid Metals Handbook—Sodium (NaK) Supplement*, 3d ed., U.S. Government Printing Office, Washington 25, D.C.

Jakob, Max, 1949, *Heat Transfer—Volume I*, John Wiley and Sons, Inc., New York.

King, R. W. P., 1945, *Electromagnetic Engineering, Volume I*, McGraw-Hill Book Co., New York.

Lehnert, B. and Little, N. C., 1957, "Experiments on the Effect of Inhomogeneity and Obliquity of a Magnetic Field in Inhibiting Convection," *Tellus*, Vol. 9, pp. 97–103.

Lundquist, S., 1951, "On the Stability of Magneto-Hydrostatic Fields," *Phys. Rev.*, Vol. 83, pp. 307–11.

Lyon, R. N., ed., 1954, *Liquid Metals Handbook*, 2nd ed. rev., U.S. Gov. Printing Office, Washington 25, D.C.

Meyer, R. E. and Nachtrieb, N. H., 1955, "Self-Diffusion of Liquid Sodium," *J. Chemical Phys.*, Vol 23, pp. 1851–54.

Nachtrieb, N. H. and Petit, J., 1956, "Self-Diffusion in Liquid Mercury," *J. Chemical Phys.*, Vol. 24, pp. 746–50.

Nakagawa, Y., 1960, "Heat Transport by Convection in the Presence of an Impressed Magnetic Field," *Phys. Fluids*, Vol. 3, pp. 87–93.

Page, L. and Adams, N.I., 1940, *Electrodynamics*, D. Van Nostrand Co., Inc., New York.

Perry, J. H., ed., 1950, *Chemical Engineer's Handbook*, 3rd ed., McGraw-Hill Book Company, Inc., New York.

Rayleigh, Lord, 1916, "Convection in a Horizontal Layer of Fluid, When the Higher Temperature is on the Underside," *Lond., Eding., Dublin, Phil. Mag.*, Ser. 6, Vol. 32, pp. 529–46.

Reid, W. H. and Harris, D. L., 1958, "Some Further Results on the Bénard Problem." *Phys. Fluids*, Vol. I, pp. 102–11.

Schmidt, R. J. and Saunders, O. A., 1937, "On the Motion of a Fluid Heated from Below," *Proc. Roy. Soc.*, Sec. A, Vol. 165, pp. 216–28.

Slater, J. C. and Frank, N. H., 1954, *Electromagnetism*, McGraw-Hill Book Co., Inc., New York.

Wang, J. H., 1951, "Self-Diffusion and Structure of Liquid Water. II. Measurement of Self-Diffusion of Liquid Water with O^{18} as Tracer," *J. Am. Chem. Soc.*, Vol. 73, pp. 4181–83.

Washburn, E. W., ed., 1929, *International Critical Tables of Numerical Data, Physics, Chemistry, and Technology*, 1st ed., McGraw-Hill Book Co., Inc., New York.

Weber, Ernst, 1950, *Electromagnetic Fields, Volume I—Mapping of Fields*, John Wiley and Sons, Inc., New York.

APPENDIX C

Sample Calculations

I. Equivalent Number of "Gravities" Induced by the Electromagnetic Body Force

Converting equation (73) into more common units than the MKS

$$\rho_o = \rho_o' \left(\frac{gm}{cm^3}\right)\left(\frac{kg}{10^3 gm}\right)\left(\frac{10^2 cm}{m}\right)^3 = \rho_o'(10^3)$$

$$g_o = 9.8065 \; m/sec^2$$

$$\bar{j}_{oim} = \bar{j}_{oim}' \left(\frac{amp}{in^2}\right)\left(\frac{10^2 in}{2.54 m}\right)^2 = \bar{j}_{oim}'(1.55)(10^3)$$

$$\bar{B} = \bar{B}'(K \; gauss)\frac{\dfrac{weber}{m^2}}{10K \; gauss} = \bar{B}'(10^{-1})$$

Substituting into equation (73)

$$\frac{\overline{q}^*}{g_c}\,\rho_o'(63.2)=\left(\frac{\alpha_s}{\alpha}\right)\,(\bar{j}_{oim}'\times\bar{B}')$$

which is plotted in Figure 3.

The motor-generator set will produce a maximum of 200 amperes and not more than 8.0 kilogauss can be obta..ed using the available electromagnet at an air gap setting of 4 inches. Using NaK 77 at 150° C the maximum number of equivalent gravities is found to be

$$\frac{g^*}{g_c}=\frac{\alpha_{c j'' B'}}{\alpha\rho_o'(63.2)}=\frac{(1.25)(200)(8.0)}{(0.288)(9.0)(0.835)(63.2)}=14.6$$

where from Table 5

$$\alpha=2.88(10^{-4})/°K$$

$$\alpha_s=\frac{-\partial\sigma}{\sigma_o\partial T}=\frac{(0.26)}{4.16(50)}=1.25(10^{-3})/°K$$

II. Magnetic Flux Density Induced by the Impressed Electric Current Flowing in the Test Cell

Before equations (93) and (94) may be evaluated two limits must first be evaluated, namely,

$$\lim_{\substack{u\to0\\c\to0}}\left[u\cot^{-1}\frac{u}{c}\right]\text{ and }\lim_{c\to0}[c\ln c^2]$$

where

$$u=w/2-x_1\text{ and }c=d/2-y_1$$

Both may be evaluated by taking ratios of their derivatives, thus

$$\lim_{\substack{u\to0\\c\to0}}\frac{\cot^{-1}\frac{u}{c}}{u^{-1}}=\frac{\left[1+\frac{u^2}{c^2}\right]^{-1}}{cu^{-2}}=\frac{cu^2}{c^2+u^2}=\frac{cu}{u}=0$$

$$\lim\frac{2\ln c}{c^{-1}}=\frac{2c^{-1}}{(-1)c^{-2}}=0$$

At $x_1=w/2$, $y_1=d/2$ and $w=d$ the magnetic flux components are found from equations (93) and (94), thus

$$-B_y=\frac{\mu j}{2\pi}\left\{0\left[\cot^{-1}\left(\frac{0}{0}\right)+\cot^{-1}\left(\frac{0}{W}\right)\right]\right.$$

$$-w\left[\cot^{-1}\left(\frac{w}{0}\right)+\cot^{-1}\left(\frac{w}{w}\right)\right]$$

$$\left.+(0)\ln\left[\frac{0+0}{0+w^2}\right]+\frac{w}{2}\ln\left[\frac{w^2+0}{w^2+w^2}\right]\right\}$$

$$-B_y=\frac{\mu j}{2\pi}\left\{w\left(-0+\frac{\pi}{4}\right)-\left(\frac{w}{2}\right)\ln(2)\right\}$$

$$B_y=\frac{\mu jw}{2\pi}[(.786)+(.3466)]\qquad B_y=\mu jw(0.1807)$$

At this point $L_z'=-B_y=-\mu jw(0.1807)$.

When $x_1=0$, $y_1=d/2$ and $w=d$ the magnetic flux is

$$-B_y=\frac{\mu j}{2\pi}\left\{\frac{w}{2}\left[\cot^{-1}\left(\frac{\frac{w}{2}}{0}\right)+\cot^{-1}\left(\frac{\frac{w}{2}}{w}\right)\right]\right.$$

$$-\left(\frac{w}{2}\right)\left[\cot^{-1}\left(\frac{\frac{w}{2}}{0}\right)+\cot^{-1}\left(\frac{\frac{w}{2}}{w}\right)\right]$$

$$\left.+(0)\ln\left[\frac{(0)+\frac{w^2}{4}}{(0)+\frac{w^2}{4}}\right]+\frac{w}{2}\ln\left[\frac{w^2+\frac{w^2}{4}}{w^2+\frac{w^2}{4}}\right]\right\}=0$$

$$B_z=\frac{\mu j}{2\pi}\left\{0\left[\cot^{-1}\left(\frac{0}{\frac{w}{2}}\right)+\cot^{-1}\left(\frac{0}{\frac{w}{2}}\right)\right]\right.$$

$$-(w)\left[\cot^{-1}\left(\frac{w}{\frac{w}{2}}\right)+\cot^{-1}\left(\frac{w}{\frac{w}{2}}\right)\right]$$

$$\left.+\left(\frac{w}{4}\right)\ln\left[\frac{\frac{w^2}{4}+0}{\frac{w^2}{4}+w^2}\right]+\frac{w}{4}\ln\left[\frac{\frac{w^2}{4}+0}{\frac{w^2}{4}+w^2}\right]\right\}$$

$$B_z=\frac{\mu j}{2\pi}\left\{0-(w)(2)(0.464)\right.$$

$$\left.-\left(\frac{w}{2}\right)(1.609)\right\}=\mu jw(0.275)$$

When $x_1=y_1=0$ in general $B_y=B_y=0$ from equations (93) and (94). When $x_1=0$, $y_1=d/4$ and $w=d$ $B_y=0$ and $B_z=-\mu jw(0.129)$. This indicates the flux decreases as x_1 and $y_1(<w/2)$ decreases, but not linearly as in a circular cross-section conductor.

Assuming a maximum current of 200 amperes and $w=d=0.0763$ meter the flux at $x_1=0$ and $y_1=d/2$ will be

$$B=B_z=\frac{\mu_z jw^2}{w}(0.275)=\frac{4\pi(10^{-7})(200)(0.275)}{(0.0763)}$$

$$=9.06(10^{-4})\frac{\text{webers}}{\text{meters}^2}$$

APPENDIX D

TABLE 5.—*Physical properties of selected fluids*

Fluid	Temperature, °C	Cp		Dm	
		joules / (Kg)(°K)	(reference)	meters² / sec	(reference)
Acetone	0	2.12(3)**	(Page 2098, Hodg-man, 1957)		
	15	2.19(3)			
	30	2.26(3)*			
Air (at one atmos-phere pressure)	0	1.00(3)	(Table 3d-3, Gray 1957)	1.32(−7)	(Eq. 50, page 538, Perry, 1950)
	40	1.00(3)		1.63(−7)	
	100	1.01(3)		2.12(−7)	
	200	1.01(3)		3.03(−7)	
Mercury	0	1.40(2)	(Table 2.2, Lyon, 1954)	1.33(−9)	(Nachtrieb and Petit, 1956)
	100	1.37(2)		2.20(−9)	
	200	1.36(2)		2.91(−9)*	
	300	1.35(2)		3.51(−9)*	
Potassium	100	8.13(2)	(Table I-20, Jack-son, 1955)		
	200	7.90(2)			
	300	7.75(2)			
	400	7.65(2)			
Sodium	100	1.38(3)	(Table I-12, Jackson, 1955)	4.13(−9)	(Meyer and Nach-trieb, 1955)
	200	1.34(3)		8.20(−9)	
	300	1.30(3)		1.30(−8)*	
	400	1.28(3)		1.78(−8)*	
NaK 77 (77 wt. % potassium and wt. % sodium	50	9.62(2)	(Table I-20, Jack-son, 1955)		
	100	9.46(2)			
	150	9.25(2)			
	200	9.12(2)			
	250	9.00(2)			
	300	8.92(2)			
	350	8.88(2)			
	400	8.83(2)			
Water	0	4.22(3)	(Pages 2079-2082, Hodgman, 1957)	1.45(−9)	(Wang, 1951)
	10	4.19(3)		2.02(−9)	
	20	4.18(3)		2.64(−9)	
	30	4.18(3)		3.39(−9)	
	100	4.22(3)		1.34(−8)*	

*Extrapolated.
**Notation means $(n) = x(10)^n$.

TABLE 5.—*Physical properties of selected fluids*—Continued

Fluid	Temperature °C	k		α	
		$\frac{watts}{(m)\,(°K)}$	(reference)	$\frac{1}{°K}$	(reference)
Acetone	0	1. 96(−1)	(page 2257, Hodgman, 1957)	1. 32(−3)	(Page 2067, Hodgman, 1957)
	15	1. 91(−1)		1. 42(−3)	
	30	1. 80(−1)		1. 52(−3)	
Air (at one atmosphere pressure)	0	2. 36(−2)	(Table 4k-6, Gray, 1957)	3. 66(−3)	(ideal gas law)
	40	2. 62(−2)		3. 20(−3)	
	100	3. 01(−2)		2. 68(−3)	
	200	3. 66(−2)*		2. 11(3)	
Mercury	0	8. 34*	(Ewing, et as., 1955)	1. 82(−4)	(cal. from page 1995, Hodgman, 1957)
	100	9. 52		1. 80(−4)	
	200	10. 69		1. 79(−4)	
	300	11. 80		1. 81(−4)	
Potassium	100	4. 76(1)*	(Table 2.2, Lyon, 1954)	2. 93(−4)	(cal. from density)
	200	4. 50(1)		3. 02(−4)	
	200	4. 24(1)		3. 12(−4)	
	400	4. 00(1)		3. 22(−4)	
Sodium	100	9. 75(1)*	(Table 1-9, Jackson, 1955)	2. 44(−4)	(cal. from page 25, Jackson, 1955)
	200	8. 15(1)		2. 55(−4)	
	300	7. 57(1)		2. 65(−4)	
	400	7. 12(1)		2. 76(−4)	
NaK 77 (77 wt. % potassium and 23 wt. sodium)	50	2. 20(1)*	(Ewing, et al., 1955)	2. 79(−4)	(cal. from density)
	100	2. 29(1)*		2. 83(−4)	
	150	2. 38(1)		2. 88(−4)	
	200	2. 47(1)		2. 92(−4)	
	250	2. 54(1)		2. 96(−4)	
	300	2. 59(1)		3. 00(−4)	
	350	2. 61(1)		3. 05(−4)	
	400	2. 62(1)		3. 10(−4)	
Water	0	5. 54(−1)	(Table 4g-4, Gray, 1957)	−6. 43(−5)	(page 2067, Hodgman, 1957)
	10	5. 76(−1)		8. 55(−5)	(cal. from density)
	20	5. 98(−1)		2. 07(−4)	
	30	6. 15(−1)		3. 02(−4)	
	100	6. 80(−1)		7. 61(−4)	

*Extrapolated.

TABLE 6.—*Physical properties of selected fluids*—Continued.

Fluid	Temperature, °C	$\nu\rho$ $\frac{Kg}{(m)(sec)}$	$\nu\rho$ (reference)	ρ $\frac{Kg}{(m)^3}$	ρ (reference)
Acetone	0 15 30	3.99(-4) 3.37(-4) 2.95(-4)	(page 2037, Hodgman, 1957)	8.18(2) 7.99(2) 7.78(2)	(page 721, Hodgman, 1957)
Air (at one atmosphere pressure)	0 40 100 200	1.72(-5) 1.91(-5) 2.18(-5) 2.58(-5)	(Table 2v-3, Gray, 1957)	1.29 1.13 9.45(-1) 7.46(-1)	(ideal gas law)
Mercury	.0 100 200 300	1.68(-3) 1.24(-3) 1.05(-3) 9.50(-4)	(page 2040, Hodgman 1957)	1.3C9(4) 1.335(4) 1.311(4) 1.288(4)	(page 1995, Hodgman 1957)
Potassium	100 200 300 400	4.35(-4) 2.99(-4) 2.27(-4) 1.94(-4)	(Table I-16, Jackson, 1955)	8.19(2) 7.95(2) 7.71(2) 7.47(2)	(Table I-14, Jackson, 1955)
Sodium	100 200 300 400	7.05(-4) 4.50(-4) ?.45(-4) 2.84(-4)	(Table I-7, Jackson, 1955)	9.?7(2) 9.04(2) 8.82(2) 8.59(2)	(Table I-6(a), Jackson, 1955)
NaK 77 (77 wt. % potassium and 23 wt. % sodium)	50 100 150 200 250 300 350 400	5.60(-4)* 4.78(-4) 3.83(-4) 3.20(-4) 2.79(-4) 2.46(-4) 2.22(-4) 2.05(-4)	(Table 2.2, Lyon, 1954)	8.59(2)* 8.47(2) 8.35(2) 8.23(2) 8.11(2) 7.99(2) 7.87(2) 7.75(2)	(Table I-14, Jackson, 1955)
Water	0 10 20 30 100	1.792(-3) 1.308(-3) 1.005(-3) 8.007(-4) 2.838(-4)	(page 2036, Hodgman, 1957)	1.00(3) 1.00(3) 9.98(2) 9.96(2) 9.58(2)	(page 1994, Hodgman, 1957)

*Extrapolated.

TABLE 5.—*Physical properties of selected fluids* Continued

Fluid	Temperature, °C	$(\sigma)^{-1}$	
		(ohm) (m)	(reference)
Acetone	0 15 30	~1.7(5)	(page 143, vol. VI, Washburn, 1929)
Air (at one atmosphere pressure)	0 40 100 200	>1.0(14)	(page 142, vol. VI, Washburn, 1929)
Mercury	0 100 200 300	9.41(−7) 1.03(−6) 1.14(−6) 1.28(−6)	(Table 2.2, Lyon, 1954)
Potassium	100 200 300 400	1.55(−7) 2.18(−7) 2.82(−7) 3.46(−7)*	(Table 2.2, Lyon, 1954)
Sodium	100 200 300 400	8.99(−8)* 1.364(−7) 1.747(−7) 2.199(−7)	(Table I-11(a), Jackson, 1955)
NaK 77 (77 wt. % potassium and 23 wt. % sodium)	50 100 150 200 250 300 350 400	3.70(−7)* 3.92(−7)* 4.16(−7) 4.44(−7) 4.76(−7) 5.14(−7) 5.50(−7) 5.88(−7)	(Table I-17, Jackson, 1955)
Water	0 10 20 30 100	8.40(5) 4.18(5) 2.38(5) 1.41(5) 1.29(4)*	(page 152, vol. VI, Washburn, 1929)

* Extrapolated.

ROBERT T. AULT

Initial Yielding and Fracture in Notched
Sheet Molybdenum

1961

190

ROBERT T. AULT

Robert T. Ault was born February 12, 1936, in Paterson, New Jersey. He was awarded a B.S. in mechanical engineering by the University of Vermont in June 1958 and an M.S. in metallurgical engineering by Ohio State University in December 1961.

Mr. Ault was employed as an assistant research engineer by the American Brake Shoe Company during the summer of 1957. After receiving his B.S. degree, he came to the Materials Central and was employed as a project engineer in the Strength and Dynamics Branch, Metals and Ceramics Laboratory. He has remained in this assignment until the present time although the period from October 1958 to October 1962 was spent in an active military status as a lieutenant in the United States Air Force.

Mr. Ault is a member of the National Engineering Honorary Society, Tau Beta Pi; the American Institute of Mining, Metallurgical, and Petroleum Engineers; the American Society for Metals; and the American Society of Mechanical Engineers.

BIBLIOGRAPHY

Rapid Loading of Aluminum Alloy Riveted Joints. WADC Technical Report No. 59-433, 1959.

Stress Corrosion of Notched and Unnotched AM-350 Alloy. WADD Technical Note No. 60-95, 1960.

With A. E. Riesen. Mechanical Properties of Beryllium. WADD Technical Report No. 60-425, 1960.

Initial Yielding and Fracture in Notched Sheet Molybdenum. ASD Technical Documentary Report No 63-223, 1963.

Initial Yielding and Fracture in Notched Sheet Molybdenum

R. T. AULT

ABSTRACT.—*The initial yielding and fracture initiation behavior of wrought stress-relieved and recrystallized molybdenum was investigated at room temperature. The effect of notch severity and grain size on the nature of plastic flow in notched sheet tensile specimens was investigated by means of photoelastic coatings. The nature of fracture initiation in notched sheet tensile specimens was studied through the use of pre-polished and etched tandem notch specimens.*

Application of the Griffith-Orowan theory for crack propagation and the Cottrell criterion for crack initiation, reveal that the effective surface energies for crack propagation and crack initiation are the same order of magnitude, which is 10^5 ergs/cm². This finding is supported by the experimental observation that no microcracks were found.

Plastic flow regions determined experimentally from the photoelastic coating studies were shown to be in good agreement, both qualitatively and quantitatively, with theoretical results predicted by elastic-plastic stress analyses.

Initial yielding at the notch root was found to occur at the same nominal stress level for a given material condition, independent of the magnitude of the stress concentration factor. This nominal stress, in the notch section was very nearly equal to the smooth tensile yield stress.

It is the objective of this program to investigate several aspects of the nature of flow and fracture in notched sheet molybdenum. The experimental approach can be conveniently divided into two phases. In Phase I the initial yielding and fracture behavior of notched tensile specimens was investigated from a mechanical state of stress point of view. Initial yielding was studied using photoelastic coating techniques. Fracture characteristics were evaluated by comparing the unnotched and notched tensile properties for various states of stress. In Phase II of the program the nature of fracture was investigated from a metallurgical structure point of view. The materials fracture characteristics were compared for the recrystallized condition in three different grain sizes and in the wrought stress-relieved condition. The fracture characteristics of the unnotched tensile specimens in the recrystallized condition were analyzed according to current effective surface energy concepts. Particular attention was paid to studying the location and mode of fracture initiation in the notched tensile specimens. Tandem notch specimens were used for this portion of the investigation. Dislocation density measurements were obtained from etch pit studies in order to determine the magnitude of plastic flow at the root of the notch.

INTRODUCTION

There has long been a need for metallic materials in the form of sheet. Recently, however, the importance of sound structural metals and alloys in sheet form has been stressed due to the requirements for such sheet materials in advanced aeronautical and space vehicle systems. There is a particularly important need for high strength to density ratio sheet materials for solid-fuel rocket motor case applications. There is also a requirement for high melting point refractory metals in sheet form for application as liners for solid-fuel rocket motor nozzles and as leading edge materials for re-entry vehicles. The refractory metals of particular importance are molybdenum, tungsten, tantalum, and columbium.

The refractory metals are known to have good elevated temperature strength, but their usefulness is limited by their relatively low resistance to oxidation. In addition, if these materials are used at low temperatures or subjected to multiaxial stress systems, they may display a pronounced tendency toward brittle behavior. This is known to be the case for high strength steels, molybdenum and tungsten. Usual design criteria cannot predict failure adequately under these conditions.

BACKGROUND

The discussions in this section are intended to provide background information which will allow a critical analysis of the experimental results presented later in the report. The complex problem of fracture in metals can be resolved into two aspects; one which deals with the microscopic or atomistic mechanisms of fracture, and the other which considers the effects of metallurgical and testing parameters. The testing variables include such things as strain rate, temperature, stress state, strain gradient and cyclic loading. This report deals primarily with the latter aspect of fracture

The mechanics of fracture might be broken into three categories as follows: ideal elastic fracture, purely plastic fracture, and elastic-plastic fracture. Ideal elastic fracture involves the breaking of atomic bonds without any plastic deformation. This type of fracture is never observed in metals; however, it is of interest since it provides the basis for the well known Griffith theory of fracture in elastic solids. Modifications of this theory have been applied to fracture in polycrystalline metals Purely plastic or ductile fracture involves the

formation of voids by the condensation of vacancies which are produced by plastic flow. The voids are then extended and joined as the result of further plastic flow. There is no real fracture stage but only a separation of the metal as a result of continued void formation and plastic flow. Separation occurs when the work hardening capacity, not the ductility, is exhausted. Ductile-fracture, although important, will not be a subject of discussion in this report. The third category, elastic-plastic fracture, is composed of a complex interaction of elastic and plastic response such as shear fracture, hetergeneous plastic flow, crack formation, plastic tearing joining adjacent cracks, and crack propagation through the release of stored elastic energy. It is elastic-plastic fracture which was studied in this work.

As the Griffith theory for purely elastic fracture and its modifications by Orowan and Irwin which apply to elastic-plastic fracture are rather well known they will not be discussed here. Similarly, the dislocation theory concepts developed by Cottrell and Petch which are pertinent to this paper are equally well known and therefore, will not be treated. In contrast there are certain mechanical, state of stress, concepts of fracture, which pertain to results presented later, which perhaps are not as well known and, therefore, will now be discussed briefly.

As one stage of an elastic-plastic fracture involves the propagation of stationary cracks, a knowledge of the stresses at the tip of the crack is essential in understanding the mechanics of fracture. Linear elasticity analyses of stresses in the vicinity of a crack have been given by Inglis (1), Westergaard (?), Irwin (3), and Williams (4). Their solutions are similar and both longitudinal and transverse stresses in the neighborhood of the crack tip are found to be inversely proportional to the square root of the distance from the crack tip. The analysis by Williams emphasizes that at the base of the crack the principal stresses are equal and thus there is a two-dimensional state of hydrostatic tension which tends to reduce the amount of yielding He finds, in agreement with the other analyses, that the maximum principal tensile stress occurs not at the horizontal axis of the crack but at an angle of ±60° from the horizontal. Williams also demonstrates that the maximum distortion strain energy occurs at an angle of ±70° from the horizontal. This observation was also determined experimentally by Post (5) using photoelastic techniques and has recently

been borne out by elastic-plastic stress analysis techniques (6).

The theory of linear elasticity, however, fails to give the true values of stresses for cracks in real metals for one of two reasons: first the elastic solutions predict infinite stress s at the crack tip, and second, the actual occurrence of large strains may invalidate the commonly-applied infinitesimal deformation theory. Thus in order to account for the real behavior of a metal either plastic or elastic-plastic solutions are necessary. The purely plastic solutions assume ideal plastic behavior of the material where elastic deformations are neglected completely. The elastic-plastic solutions, which are far more difficult, assume an elastic-plastic situation with or without strain hardening. The elastic-plastic method has been developed by Allen and Southwell (7). They have applied this method to the problem of an externally (90°) V-notched and semi-circular notched tensile bar under conditions of both plane strain and plane stress. The solution is obtained by use of the relaxation method applied to the combined field, and involves solving a linear field equation in the elastic portion and a nonlinear field equation in the plastic region by an iterative procedure.

The relaxation technique consists essentially of assuming (a) the validity of infinitesimal deformation theory, (b) a stress-strain curve, taken as elastic-plastic with no strain hardening, and (c) a yield criterion, taken as the von Mises-Hencky value. The elastic problem for the entire region is solved, and then the areas near the notch where the von Mises-Hencky stress is exceeded (the plastic enclaves) are relaxed back to the yield stress, thus overflowing the initially assumed solely elastic region. The elastic solution is recomputed and the process iterated to convergence. The important feature is that there is a linear elastic field equation outside the enclave and a nonlinear plastic field equation inside; the problem is to locate the boundary of the plastic enclave. Jacobs (8) has extended this technique to the problem of an externally cracked tensile bar subjected to plain strain, and recently Stimpson and Eaton (6) have applied this method to an externally cracked plane stress tensile specimen. The thin sheet or plane stress solution is of particular interest, and later in the report the results will be compared with the yield regions experimentally determined in this study.

As plastic flow and the state of stress and strain, both microscopic and macroscopic, are somehow intimately related to the processes of fracturing, the next logical step would be to try and incorporate the results of the ideal plastic and elastic-plastic analyses into various fracture concepts. At the present state of knowledge this appears to be a rather optimistic step; nevertheless, several investigations have made advances in this direction. Williams (9) has recently proposed a ductile fracture criterion for the tensile case with the aid of elastic-plastic stress analysis. With the aid of Stimpson and Eaton's analysis, Williams accounts for the strain energy of forming the plastic enclaves and applied this to the Griffith energy balance in developing an extended form of the Griffith criterion for a thin plate with an internal crack.

Hult and McClintock (10) have performed an elastic-plastic analysis for the case of a notch in a semi-infinite solid subject to pure shear. The material was assumed to be elastic-ideally-plastic and from the analysis the radius to the elastic-plastic interface (R) was determined for low stress levels to approach

$$R = c\left(\frac{\tau}{\tau_{0,s}}\right)^{2}, \qquad \text{Eq. (1)}$$

where c is the crack length, τ is the applied shear stress, and $\tau_{0,s}$ is the yield stress in shear. McClintock (10) later postulated a corresponding condition for fracture which stated that fracture occurs when the plastic strain throughout the distance ρ directly ahead of the crack reaches a critical value γ. The distance ρ is related to the structure of the material, being about the size within which the classical theory of plasticity no longer applies, and the strain γ is the plastic strain at fracture in the ordinary torsion test.

Cottrell (11) has recently treated the shear case for a sharp notch and has derived a very similar expression for low stress levels as follows:

$$R = \frac{\sigma^{2}}{8}\left(\frac{\tau}{\tau_{0,s}}\right)^{2} c \qquad \text{Eq. (2)}$$

where the symbols have the same meaning as in Equation (1). He proposes a modified Griffith fracture concept where the surface tension term is replaced by the work expended in plastic deformation which is equal to the yield stress in shear times the displacement at the notch tip measured in a direction normal to the tip of the notch.

Neuber (13) has presented a theoretical treatment for the stress concentration factor in the

195

Table 1.—Chemical analysis, PPM

CONDITION	C	O	N	H	Si	Al	Fe	Ca	W	Mg	Ni	Cr	Sn	Ti	Cu	Co	Zr
As-rolled prior to annealing	105	50	14	17	42	10	50	:0	200	<1	<1	<1	<10	3	2	<5	<1
Wrought, stress-relieved	265	11	1.5	0.5													
Annealed, 1,300° C -1 hr	173	17	1.2	0.4													
Annealed, 1,800° -1 hr	101	10	0.9	1.2													
Annealed, 2,100° C -1 hr	69	12	0.9	0.5													

plastic range. His model is based on a nonlinear stress-strain curve rather than the usual elastic-ideally-plastic relation. Solutions at present are available only for sharp notches having a 0° flank angle loaded in shear.

MATERIAL AND SPECIMEN PREPARATION

The wrought stress-relieved molybdenum was supplied by Climax Molybdenum Company in the form of 0.061 inch gage sheet. The recrystallized sheet molybdenum was fabricated by the authors. The composition of both the wrought stress-relieved material and the recrystallized material is given in Table I. All of the carbon analyses and the analysis of the as-rolled material prior to the annealing treatments was performed by spectrographic techniques. The gas analysis on the wrought stress-relieved material and the recrystallized material was done by vacuum fusion techniques.

The processing history and stress-relief treatment for the wrought stress-relieved material is as follows:

1. One inch thick recrystallized sheet bar was rolled in ten passes at 2,150° F (1,175° C), with six reheatings, to 0.242 inch thick.
2. Annealed for 30 minutes at 2,150° F (1,175° C).
3. Rolled in none passes at 2,050° F (1,120° C), with seven reheatings, from 0.242 inch thick to 0.120 inch thick.
4. Rolled in 16 passes at 650° F to 700° F (345° C to 370° C), with 15 reheatings, from 0.120 inch thick to 0.061 inch gage.
5. Heated for 15 minutes at 1,800° F (980° C) in a natural gas fired furnace.

The starting material for the recrystallized sheet specimens was a single ingot of arc-cast molybdenum prepared by Climax Molybdenum Company. The billet, three inches in diameter and five inches in length was extruded into sheet bar

2.5 inches by 0.5 inches. The extrusion billet was chamfered to an 88° included angle with a 1.125 inch diameter flat nose. It was then completely sprayed with a glass lubricant. The glass coating was 0.030 inch thick. The die material was a high speed tool steel, which was faced with alumina. No lubricant was used on either the die or the container. The follow up material consisted of a 2 inch graphite block plus a 1.5 inch glass coated copper block. The billet was heated in dry argon to a temperature of 2,200° F (1,205° C) and extruded in one pass, at a reduction ratio of 6:1, to sheet bar. The extrusion pressure was 452 tons and the ram speed was four inches per second. The yield in weight percent was 92.

The extruded sheet bar was then cut into eight 2.5 inch square blocks and preheated in an argon atmosphere at 1,800° F (980° C) for ½ hour prior to rolling. The blocks were cross rolled in five passes to a width of 3.5 inches and then rolled in a longitudinal direction to a thickness of 0.060 inch. The specimens were reheated in the furnace after each pass. It took three minutes to get the specimens back to temperature. The total reduction was 80 percent, with a reduction rate of 10 percent per pass.

The sheet material was then machined into tensile specimens and subsequently annealed. The recrystallization annealing treatment, provided a completely recrystallized structure with three different grain sizes. The three annealing treatments were 1,300° C (2,372° F), 1,800° C (3,272° F), and 2,100° C (3,812° F) all for one hour in a vacuum of 0.1 microns. The specimens were cooled at a relatively fast rate by shutting off the power to the furnace. The time to reach room temperature was approximately one hour and the cooling rate was approximately 200° C per minute down to 800° C. The grain size and microhardness data are given in Table II. The hardness determinations were made with a Tukon Hardness Tester using a 136° diamond penetrator and a 0.5 kilogram load.

TABLE II.—*Grain size and microhardness data*

Condition	Grain size, ASTM	Grain diameter, mm.	Hardness, DPH
Annealed, 1,300° C—1 hr	6.7	0.042	191
Annealed, 1,800° C—1 hr	3	0.152	184
Annealed, 2,100° C—1 hr	1	0.225	175
Wrought, stress-relieved			270

Material from gage section of smooth tensile specimen after fracture

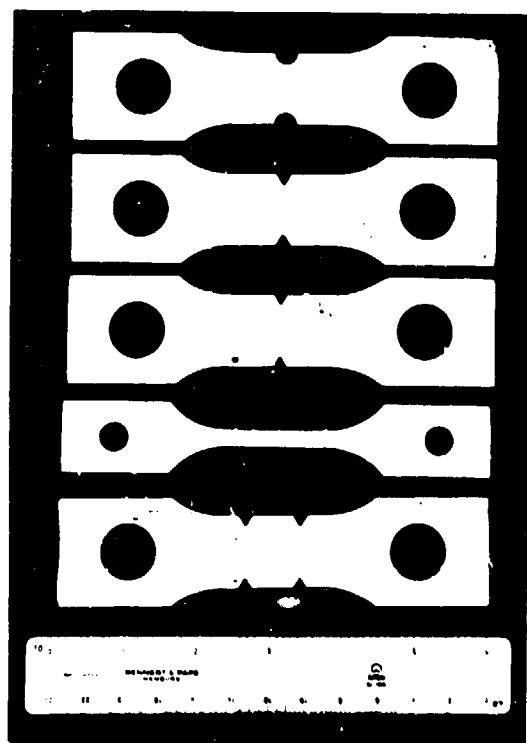|			
Annealed, 1,300° C—1 hr			230
Annealed, 1,800° C—1 hr			183
Annealed, 2,100° C—1 hr			176
Wrought, stress-relieved			270

FIGURE 1. Unnotched, notched and tandem notched sheet tensile specimens.

The sheet material was machined into smooth and notched tensile specimens as shown in Figure 1. The notches were machined by mill cutters with a 60° included angle and the following root radii: 0.030 inch and 0.005 inch. The semicircular notch had a 0.157 inch radius. A 30 percent notch depth was used in all cases. The notch specimens were lightly ground on both sides through the notch region, to provide a good flat surface to which a birefringent coating could be bonded. The tandem notch specimens for the recrystallized material contained only the 0.005 inch root radius notch. The tandem notch specimens for the wrought stress-relieved condition contained both the 0.005 inch and 0.050 inch root radii. The 0.157 inch, 0.030 inch, and 0.005 inch root radii provided the specimens with the following respective theoretical elastic stress concentration factors: $K_t=1.93$, $K_t=3.7$, and $K_t=8.3$.

EQUIPMENT AND TEST PROCEDURE

All of the tests were conducted at room temperature (78° F) (26° C). The tandem notched and unnotched tensile specimens were tested at a constant crosshead speed of 0.005 inch per minute. The notched specimens were tested using load-unload techniques. The smooth tensile tests were conducted on a "hard" Baldwin-Emery SR-4 Testing Machine, Model FGT; the load-strain curves were autographically recorded. The flow properties were obtained from strain measurements, beyond the flow stress, determined by measuring the extension of one inch gage marks with dividers. Maximum loads and fracture loads were recorded for all specimens.

The notched tensile tests were conducted on a hydraulically driven Tinius Olsen Universal Testing Machine. Initial yielding in the notched tensile specimens was studied by using photoelastic coatings. A piece of Photostress[1] plastic which had been machined to the same notch geometry was bonded to each notched tensile specimen. The Photostress plastic was 0.048 inch thick and great care was taken in machining the plastic to the exact notch depth of the metal specimen. The same mill cutters were used to machine the notch in the plastic as were used on the molybdenum sheet material. In bonding the plastic to the specimen care was taken to remove all excess adhesive from the notch root. The total shear strain and residual shear strain in the notched section was analyzed by taking a successive series of photographs through the analyzer of the polariscope as the specimen was loaded and then unloaded. This procedure was repeated until the plastic material became unbonded from the specimen or fracture occurred.

---

[1] Photostress plastic is a commercial photoelastic coating marketed by the Budd Co., Phoenixville, Pa.

197

Only in the case of the semi-circular notched specimens did the plastic material become unbonded prior to fracture.

Photoelastic coatings were not used on the tandem notch specimens. These specimens were electrolytically polished and chemically etched prior to testing. Photomicrographs at 100x were taken of all notched regions prior to and after tensile testing. The same electrolytic polishing and chemical etching procedure was used for all of the photomicrographic work and etch pit studies. The specimens were electrolytically polished for 50 seconds at 3 volts (current unknown) in an electrolyte which consisted of six parts methyl alcohol and one part concentrated sulfuric acid. The specimens were chemically etched by immersion for approximately five seconds in a solution of potassium ferricyanide, sodium hydroxide and water: 10 gm $K_3Fe(CN)_6$, 10 gm NaOH, 100 ml H_2O.

RESULTS AND DISCUSSION

The effect of notch severity and grain size on the nature of plastic flow in notched sheet tensile specimens of molybdenum was investigated by means of photoelastic coatings. The nature of fracture initiation in notched sheet tensile speci-

TABLE III. *Tensile and notch tensile properties of recrystallized molybdenum*

Unnotched specimens

Specimen	Annealing temp., °C	Upper yield stress, psi	Lower yield stress, psi	0.2% Y.S., psi	U.T.S., psi	True fracture strength, psi	Total el. (1" g.l.) %	Reduction in area, %
13-F2	1,300	53,400	42,400	48,600	66,800	137,600	45	50
13-F3	1,300	53,000	41,300	48,200	68,800	146,000	50	56
18-D1	1,800	37,100	32,700	35,900	52,500	52,500	6	0
18-C1	1,800				49,500	49,500	4	0
21-D2	2,100	41,300	40,000		53,500		7	0
21-F1	2,100	30,500	28,800	30,500	33,500	33,500	0	0

Notched specimens

Specimen	Annealing temp., °C	Type of notch specimen	a_t	Notch yield strength, psi	Notch tensile strength, psi	Notch fracture strength, psi	Reduction in area, %	Shear strain at notch root at fracture, %
13-C1	1,300	Tandem	8.3		48,100	48,100	0	
13-A4	1,300	Tandem	8.3		*35,900		0	
13-D2	1,300		8.3	32,100	36,000	36,000	0	0.37
13-B2	1,300		8.3	51,900	36,000	36,000	0	0.38
13-E1	1,300		3.7	55,000	63,400	63,400	0	
13-F1	1,300		3.7	50,300	64,400	64,400	0	1.65
13-G2	1,300		1.93	52,700	71,200	81,600	9	>2.40
13-F1	1,300		1.93	55,400	73,100	84,600	10	>2.10
18-E1	1,800	Tandem	8.3		34,400	34,400	0	
18-A1	1,800	Tandem	8.3		*29,600		0	
18-D1	1,800		8.3	31,000	31,000	31,000	0	0.23
18-B1	1,800		8.3	32,100	34,700	34,700	0	0.39
18-H1	1,800		3.7	32,500	Fracture at pin hole			
18-R1	1,800		3.7	36,000	53,300	53,300	0	
18-B1	1,800		1.93	32,500	55,300	55,000	10	
18-H2	1,800		1.93	32,000	Fracture at pin hole			
21-A1	2,100	Tandem	8.3		33,600	32,600	0	
21-A2	2,100	Tandem	8.3		32,600	32,600	0	
21-G1	2,100		8.3		35,600	35,600	0	
21-G2	2,100		8.3	34,200	36,500	36,600	0	
21-F2	2,100		3.7	35,100	Fracture at pin hole			
21-H2	2,100		3.7	34,800	Fracture at pin hole			
21-G1	2,100		1.93	33,300	48,600	48,600	0	
21-H1	2,100		1.93		Fracture at pin hole			

*Specimen was cracked prior to test

mens was studied through the use of tandem notch specimens. All tests were conducted at room temperature.

The tensile and notch tensile properties of recrystallized and wrought stress-relieved molybdenum are listed in Tables III and IV respectively.

TABLE IV. *Tensile and notch tensile properties of wrought stress-relieved molybdenum*

Unnotched specimens

Specimen	0.2% Y. S., psi	U. T. S. psi	True fracture strength, psi	Total el. (1" g. l.) %	Reduction in area, %
1	100,000	111,000	166,800	20	56
2	107,000	114,300	167,800	15	50
3	101,300	112,000	151,200	15	51

Notched specimens

Specimen	Type of notch specimen	K	Notch yield strength, psi	Notch tensile strength, psi	Notch fracture strength, psi	Reduction in area, %	Shear strain at notch root at fracture, %
III	Tandem	8.3		87,500	87,500	0	....
IV	Tandem	8.3		87,200	87,200	0	....
C		8.3		92,800	92,800	0	....
F		8.3		67,600	67,300	0	....
I	Tandem	3.7		113,800	113,800	0	....
II	Tandem	3.7		113,100	113,100	0	....
B		3.7	100,000	116,200	116,200	0	1.10
E		3.7	101,500	117,200	117,000	0	1.50
D		1.93	105,000	115,800	115,800	0	1.80
A		1.93	106,600	117,400	128,000	8	....

TABLE V. *Average Mechanical Property Data*

Unnotched specimens

Annealing temp., °C	0.2% Y. S., psi	U. T. S., psi	True fracture strength psi	Total el. (1" g.l.) %
1,300	48,400	67,800	141,800	47
1,500	35,900	51,000	51,000	5
2,100	30,500	33,500	33,500	0
Wrought-S R	103,700	112,400	160,700	17

Notched specimens

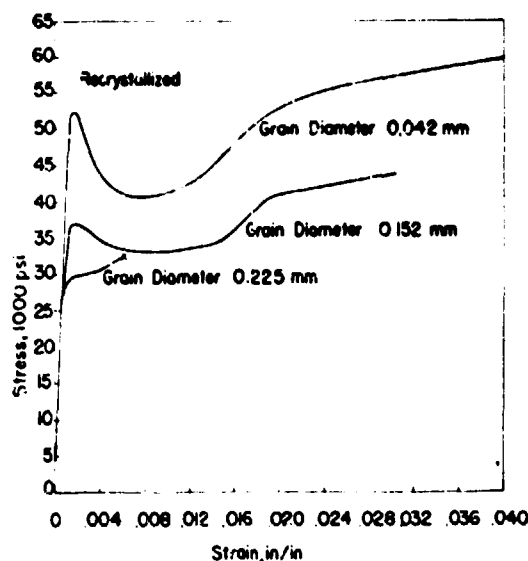| Annealing temp., °C	K	Notch yield strength, psi	Notch tensile strength, psi	Notch fracture strength, psi	Shear strain at notch root at fracture, %
1,300	8.3	52,100	56,000	56,000	0.47
1,300	3.7	51,100	84,400	84,400	1.65
1,300	1.93	54,000	72,100	83,100	2.25
1,500	8.3	31,500	34,600	34,600	0.31
1,500	3.7	34,200	53,300	53,300	
1,500	1.93	32,300	58,300	65,000	
2,100	8.3	34,200	34,300	34,300	
2,100	3.7	34,500			
2,100	1.93	33,200	48,600	48,600	
Wrought-S R	8.3		83,300	83,800	
Wrought-S R	3.7	100,700	115,000	115,000	1.30
Wrought-S R	1.93	105,800	116,600	121,800	1.80

194

Figure 2. Effect of grain size on stress-strain curves of recrystallized molybdenum.
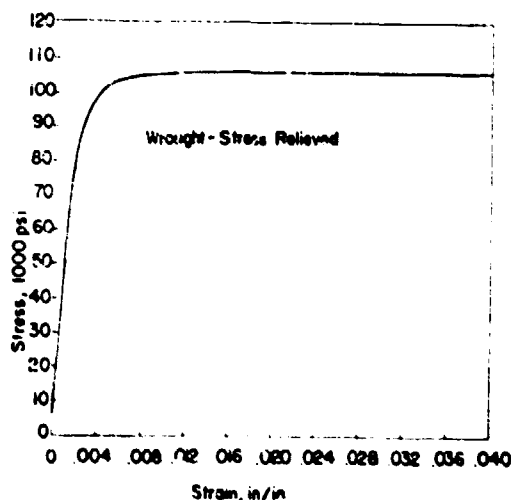

Figure 3. Stress-strain curve for wrought stress-relieved molybdenum.

The average mechanical property data are presented in Table V. The shear strain data, presented in the tables was determined from the photoelastic coating studies. The stress-strain curves for the recrystallized and wrought stress-relieved material are shown in Figure 2 and 3 respectively. Figure 2 illustrates the dramatic effect of grain size on the flow properties of recrystallized

molybdenum. This behavior is in good agreement with the findings of Johnson (14). The fine grain size material exhibited over 50 percent reduction in area (R. A.). Prior to fracture while the two larger grain size materials fractured at the maximum load point with 0 percent R. A.

The data on the smooth tensile specimens in Table III show that one of the large grain size specimens (spec. 21-D2) had exceptionally high yield and tensile strength values. Both of the 2,100° C annealed specimens were found to have the same grain size and a chemical analysis check revealed that the O, N, H and C levels were the same for both specimens. The specimen which showed the anomalous behavior was observed to have a much more pronounced yield point and a rippled irregular surface in the gage length. No sound explanation for this behavior was found; however, it may possibly be an effect of orientation. Recent studies by Rose, Ferriss and Wulff (15) on the yield and plastic flow behavior of tungsten single crystals found the proportional limit to be a function of orientation. They found that crystals whose tensile axes were near the [110] direction were about three times as strong as [100] crystals. It was also found that [110] crystals displayed yield phenomena and strain harden little, whereas the [111] and [100] orientations yield smoothly and showed considerable strain hardening. Whatever the reason may be for the observed anomalous behavior it was felt that these data should not be included in the average base line data.

Before discussing the results in detail some general observations should be made. In all of the specimens tested, fracture was observed to occur by transgranular cleavage. This was true even for the smooth tensile specimens of the fine grain recrystallized material and the wrought stress-relieved material which exhibited gross plastic flow prior to fracture. All of the notched and unnotched specimens of the wrought stress-relieved material were transverse to the rolling direction of the sheet. It was observed that for all of the material conditions there was never sufficient plastic deformation to cause an increase in the notch root radius for the sharply notched specimens ($K_t=8.3$). Only for the fine grain recrystallized material was there sufficient plastic strain to cause a slight increase in root radius and slight dimpling at the notch root for ($K_t=3.7$).

INFLUENCE OF NOTCH SEVERITY ON STRENGTH PROPERTIES

The effect of stress concentration on the notch strength ratio—notch tensile strength divided by ultimate tensile strength—is illustrated in Figure 4. The notch strength ratio (N.S.R.) is observed to increase to a maximum value at approximately $K_t = 2$ and then decrease with increasing stress concentration factor for all material conditions. There are several interesting features about this diagram. It is first noticed that the degree of notch weakening at the highest stress concentration factor is not very severe. For a truly brittle material elastic theory predicts that the N.S.R. = $1/K_t$. This behavior has in fact been experimentally observed for at least two structural alloys (16). It is readily seen that none of the material conditions investigated approach truly brittle behavior as defined above. This must be explained by one of two reasons: (1) the material does not obey the maximum principal stress theory (the fracture strength is a material constant); or (2) plastic deformation, either macroscopic of microscopic, precedes fracture. In light of much experimental evidence it seems very likely that plastic deformation prior to fracture is the governing factor. As macroscopic plastic flow was not observed in the two larger grain size materials, local microscopic plastic deformation must occur.

The observation that the N.S.R. decreases with increasing values of K_t is readily understood from the observation (17) that the biaxiality of stresses at the notch root increases with increasing K_t. The increased biaxiality of stresses causes a lowering of the shear stress (which is equal to half the difference of the principal stresses) and, therefore, plastic flow is inhibited thus the maximum tensile stress is not relieved and increased hydrostatic stress conditions promote fracture at lower applied stress levels. Stroh (15) has offered an alternative reason for notch weakening. In explaining the observed increase in transition temperature with notched specimens, Stroh reasons that the increased plastic strain rate in the flow region at the root of the notch is responsible for increasing the transition temperature. Although the effects of strain rate and biaxiality or triaxiality of stresses may be equivalent, the quantitative relationship between the two and their effect on notch weakening has not yet been able to be demonstrated. In the present work the method used of loading and unloading to observe the flow pattern would

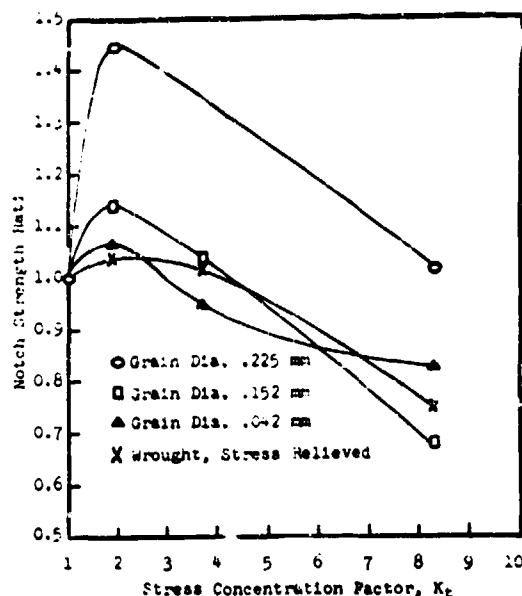seem to minimize the effect of strain rate and favor the biaxiality of stresses reasoning.

FIGURE 4. The effect of stress concentration on the notch strength ratio of sheet molybdenum.

Another curious effect which is observed in Figure 4 is that almost without exception the material which showed the least ductility in the smooth tensile tests demonstrated a higher value of N.S.R. for each respective value of K_t. This is in contrast to usual observed effect that the more ductile material will have a higher N.S.R. for a given value of K_t. It should be pointed out that the extremely high value of N.S.R. for the large grained material, $K_t = 193$, is not thought to be valid. This point is based on only one specimen and this specimen was observed to have a roughened rippled surface after fracture, similar to that observed in the smooth tensile specimen of the same grain size described earlier. Following the same reasoning it is felt that the notch strength value is too high and not representative. However, the trend of higher N.S.R. values for the less ductile materials may still be valid. This seems difficult to believe in light of the amount of evidence to the contrary. Ingram et al. (13) have shown for molybdenum and other refractory metals that the N.S.R. for a given notch geometry decreases as the material ductility is decreased with decreasing test temperature. Weiss (17) has found the same behavior on several high strength

sheet alloys. Because of the observation that N.S.R. decreases with decreasing ductility whether due to decreasing test temperature or increasing stress biaxiality (increasing K_t) Weiss concludes that notch sensitivity, as indicated by N.S.R. VS K_t curves, is an indicator of all ductility changes regardless of their nature. Because of the limited data available in this study it is felt that many more tests must be performed before this behavior can be confirmed. It also must be remembered that the material ductility in this study was varied by changing the grain size and, therefore, the behavior demonstrated here may well not be a reflection of tensile ductility, as the brittle grain boundary film in the larger grain size material is surely playing an important role in governing the fracture behavior. Thus when the material is sufficiently embrittled, the effect of increasing the notch sharpness on the materials strength properties may become of negligible importance.

The notch strengthening effect in the mild notch region (K_t 2) although widely observed is not well understood. Because it is observed on such a wide range of metals and alloys it must be connected with the particular state of stress of this notch geometry. Voorhees and Freeman (20) have also observed the same behavior in creep-rupture studies of notched specimens on high temperature alloys. It is also observed (19) that round bar specimens with the same notch geometry demonstrate a greater notch strengthening effect than sheet specimens. Therefore, the mechanism of notch strengthening is more responsive to triaxial states of stress than biaxial states of stress.

EFFECT OF GRAIN SIZE ON STRENGTH PROPERTIES

The effect of grain size on the yield stress, fracture stress and notch fracture stress is illustrated in Figure 5. The fracture stress and yield stress curves are seen to follow the generally observed linear dependence with (grain size)$^{1/2}$. The notched fracture stress (fracture load divided by cross sectional area at fracture) curves do not show this same dependence. In all the tests conducted on both notched and unnotched tensile specimens, for all of the material conditions, no microcracks were found which were not a result of the fracture process itself. In the tandem notch specimens which were polished and etched prior to testing no surface microcracks could be found in
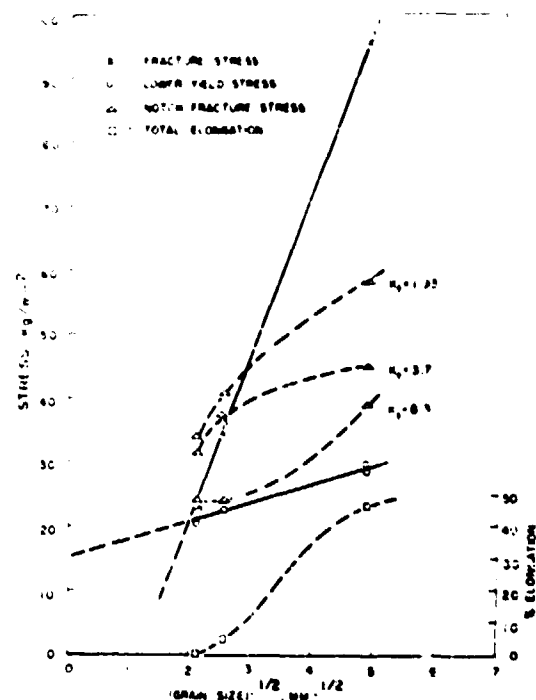
202

Figure 5. The effect of grain size on the lower yield stress, fracture stress, and notch fracture stress of molybdenum.

the unfailed notch section. These sections were subsequently mounted and metallographically examined through the sheet thickness and again no microcracks were observed. The smooth tensile specimens were metallographically examined through the sheet thickness after testing and only a very few microcracks were observed and these were immediately adjacent to the fracture surface and quite apparently occurred as the result of fracture. These few cracks adjacent to the fracture surface were found only in the 1,300° C and 1,800° C annealed material and none were observed for the 2,100° C annealed material nor for the wrought stress-relieved material. The cracks found in the notched tensile specimens for all root radii, were large secondary cracks resulting from the fracture process.

The ductile-brittle transition temperature (or temperature range) for molybdenum has been shown (21) to be about room temperature. The ductile-brittle transition temperature as determined in a smooth tensile test is usually defined as the temperature at which the reduction in area curve versus test temperature drops rapidly

The transition temperature can be raised by increasing grain size, strain rate, interstitial content and by introducing biaxial or triaxial states of stress. Ingram et al. [?] have shown that the transition temperature of fine grain recrystallized molybdenum sheet is raised from about 50° C to 125° C with a notch, with K_t 3. For wrought stress-relieved molybdenum sheet they observed an increase in transition temperature from about −15° C to 0° C for the same notched condition. The two larger grain size materials in this study demonstrated 0% reduction in area. Therefore, it can be considered that for these tests which were conducted at room temperature, the wrought stress-relieved material was tested slightly above the transition temperature and the recrystallized material was tested slightly below the transition temperature.

More important than the precise transition temperature under which each test was conducted is the knowledge of the amount of plastic flow which preceded fracture. From the stress-strain curves it is seen that all of the smooth tensile specimens fractured beyond the yield stress with varying amounts of strain hardening and total strain to fracture. Therefore, none of the material conditions was sufficiently brittle such that microcracks are formed simultaneously with plastic flow at the upper yield point, as predicted by Wessel [22] in a yield model for BCC metals exhibiting brittle behavior. Likewise neither are the fine grained or wrought stress-relieved conditions sufficiently ductile as to fail in a ductile fibrous manner. Thus, the type of fracture mechanism described by Petch [23] in which nonpropagating microcracks are joined by plastic tearing, producing a fracture of fibrous character which contains some cleavage facets, is not applicable for these tests. The fractures occurring in these samples are thus probably best described as ductile cleavage or quasi ductile cleavage fractures. Thus, it is of interest to analyze the present results in light of Cottrell's [24] theory of cleavage fracture.

In analyzing the smooth tensile test data it can be seen from Figure 3 that the lower yield stress follows the predicted relationship of Petch [25] that $\sigma_y = \sigma_i + k_y d^{-1/2}$ (Equation (3)). In this equation σ_i and σ_y are shear stresses (½ of the tensile stress) and d is equal to the half grain diameter. If the data in Figure 3 are plotted using shear stress and the half grain diameter the following results are obtained $\sigma_i = 7.8$ kg/mm², $k_y = 3.0 \times 10^?$

dynes/cm². These values are in relatively good agreement with the values obtained by Johnson [1] on molybdenum of approximately the same purity. Johnson obtained values of $\sigma_i = 5.5$ kg/mm² and k_y 6.01 × 10⁵ dynes/cm².

In Cottrell's [24] theory of brittle fracture a ductile-brittle transition criterion is derived on a grain size basis rather than temperature. According to this theory the limiting condition for crack formation is given by the relation in Equation (4), $\sigma_y k_y d^{1/2} = \beta \mu \lambda$ where β is a constant = 1 for simple tension, 2 for torsion and approximately ⅓ for the plastically constrained zone of a notch, μ is the shear modulus and λ is the effective surface energy for fracture. When the left hand side of Equation (4) exceeds the right hand side brittle behavior is expected as the yield stress is more than sufficient to cause the crack to grow into a complete fracture. When the left hand side is smaller than the right hand side, ductile behavior is expected. The fracture stresses are also observed to fit the inverse square-root law. From the intersection of the fracture stress curve with the lower yield stress curve the transition grain diameter is found to be 0.250 mm which is just slightly larger than the largest grain size used in this study. Thus, according to this grain size transition criterion all of the specimens tested are on the ductile side of the transition point. Equation (4) therefore, provides a means for estimating the effective surface energy (λ) for cleavage crack initiation. Using $\beta = 1$, $\mu = 12.2 \times 10^{11}$ kg/mm², $\sigma_y = 10.5$ kg/mm², $k_y = 3.0 \times 10^?$ dynes/cm², and $2d = 0.250$ mm, we obtain $\lambda = 2900$ ergs/cm². This compares with values of 8,000 ergs/cm² estimated by Cottrell [24] and 12,000 ergs/cm² estimated by Johnson [1]. The theoretical surface tension of molybdenum has been calculated by Taylor [26] to be 2,240 ergs/cm²; therefore, apparently the effective surface energy for crack initiation in molybdenum, according to the above criterion, is very close to the true surface tension. It should be cautioned that the Cottrell grain size transition criterion is derived from a model which states that a cleavage crack is formed within a grain by the junction of two intersecting slip planes. All of the fractures in this study were observed to initiate at grain boundaries; therefore, this criterion may not be applicable for these tests. It should also be mentioned that Cottrell predicts that on the ductile side of the transition point the fracture stress should increase linearly with

d^{-1} along a line which extrapolates back to $\sigma_f = 0$ at $d^{-1} = 0$. This is predicted from the ductile cleavage fracture expression

$$\sigma_f = \frac{3\mu\lambda}{k_y} d^{-1}$$ Eq (5)

where σ_f is the ductile cleavage fracture stress. It can be seen in Figure 5 that although the fracture stress plot is linear it does not extrapolate back to the origin. Another point of interest here is that the Cottrell theory predicts that on the ductile side of the transition point, where the left hand side of Equation (4) is smaller than the right hand side, it is expected that microcracks will form but not propagate. Such non propagating microcracks have been observed in steel; however, it was seen in this study that no such microcracks were found. It is suggested therefore, that although Equation (4) may adequately describe the limiting condition for crack initiation from slip bands in steel, it may not have general applicability to all BCC metals. As many other studies have shown, the precise relationship between heterogeneous plastic flow and crack nucleation is an extremely complex and unclear one. It also seems reasonable to expect that the relationship between dislocation movement and crack formation at grain boundaries is even more complex than in the interior of the grain. It is also noted that only in the case of steel, and these data are limited, has there been adequate experimental verification of the ductile cleavage fracture relationship, expressed in Equation (5), which predicts that the fracture stress curve should extrapolate to the origin.

It is of interest now to treat the same data by the Griffith-Orowan (27) theory of fracture. The Griffith-Orowan treatment of brittle fracture describes the conditions for the propagation of cleavage fracture from pre-existing cracks. The energy term P in the Griffith-Orowan equation

$$\sigma = \left[\frac{2EP}{\pi c}\right]^{\frac{1}{2}}$$ Eq (6)

is the effective surface energy for spontaneous crack propagation to ultimate fracture. In a study of the effects of microstructure on brittle fracture Low (28) has shown that the crack length c in Equation (6) for a polycrystalline material might be expected to be equal or proportional to the grain size and therefore, from Equation (6) the fracture stress should vary as the

grain size.[19] He demonstrated that this was experimentally the case for a low carbon steel tested at −195° C. Thus, if the crack length c is assumed equal to the grain size d the Griffith-Orowan relation for spontaneous crack propagation is $\sigma_f d^{\frac{1}{2}}$ = constant, and thus P is a material constant for a given set of test conditions. This relationship also predicts that the fracture stress curve should extrapolate to zero at $d^{-\frac{1}{2}} = 0$. From Figure 5 it appears that the relation $\sigma_f d^{\frac{1}{2}}$ = constant is satisfied; however, if we assume $c = d$ and from Equation (6) calculate the value P for each grain size we find that the values of P are 1.88×10^5, 9.15×10^4, and 5.98×10^4 ergs cm² for grain diameters equal to 0.092, 0.152, and 0.225 mm respectively. The largest variation being a factor of 3. However, from the metallographic evidence we cannot make the assumption that $c = d$, as no microcracks were observed. A better assumption would be that the critical crack size for this material must at least be smaller than the smallest grain diameter. Let us arbitrarily assume then that the critical crack size is equal to ½ the smallest grain diameter or $c = 0.02$ mm. When c is assumed constant equal to 0.02 mm, the values of P from Equation (6) for the smallest to largest grain diameter respectively are 9.0×10^3, 1.2×10^4, and 5.3×10^4 ergs cm². Thus, the effective surface energy for crack propagation appears to be about 10^4 ergs cm² which is one order of magnitude higher than the effective surface energy for crack initiation.

This indicates that the resistance to crack propagation is greater than the resistance to crack initiation. This was shown by Hahn et al. (29) to be the case for cleavage microcrack initiation and propagation in steel tested at low temperatures. However, no nonpropagating microcracks were observed in molybdenum, but were observed by Hahn in the studies on steel. Thus, the above statement that crack propagation in molybdenum is more difficult than crack initiation may well be erroneous. We can, with equal validity, assume that the critical crack size is smaller than ¼ the smallest grain diameter. If we choose $c =$ ¼ the smallest grain diameter ($c = 0.01$ mm) we find that the respective values of P are 4.5×10^3, 6×10^3, and 2.65×10^4 ergs cm². The effective surface energy for crack propagation is now the same order of magnitude as the effective surface energy for crack initiation. Therefore, in agreement with the experimental finding that no nonpropagating microcracks were observed, it

more correctly appears that the resistance to crack propagation is about the same as the resistance to crack initiation for recrystallized molybdenum at room temperature. The observation that the effective surface energies for fracture are so nearly equal to the true surface tension, indicates that under the proper test conditions recrystallized molybdenum would exhibit very low energy fractures.

It must be pointed out that P in the Griffith-Orowan equation is a material constant for spontaneous crack propagation only for a given set of test conditions and does not have any general significance. As was pointed out by Low [28] P is composed of two components, the energy of deformation for the formation of cleavage steps within the grain, and the energy for shear deformation required to join adjacent cleavages. The energy for shear deformation is much the larger component in the value of P. The value of P will, therefore, reflect the ratio of number of sheared crystallites to cleaved crystallites. Thus, as the yield strength is raised or lowered by decreasing or increasing the test temperature this ratio and thus the value of P would be expected to change. The ratio of sheared to cleaved crystallites would also be expected to be strongly dependent on grain size as the grain boundaries act as strong barriers to the propagation of cleavage cracks. The observation that grain boundaries act as barriers to the propagation of cleavage cracks is well illustrated in Figure 6. This figure shows a secondary crack, which emanated from the fracture surface, propagating from left to right. The shift in orientation of the crack from grain to grain is also readily observed. Owen, Averbach, and Cohen [30] in studying the brittle fracture of mild steel also pointed out that P should be a function of grain size. The results showing that P increased with decreasing grain size, although only slightly, supports this argument.

FRACTURE INITIATION

The tandem notch specimens were used in order to study the location and mode of fracture initiation. The tandem notch specimens were carefully machined such that the largest variation in notch depth was 0.003 inch. Thus, when fracture occurs the state of stress and strain or degree of plastic flow that exists in the unfractured notch section, is that which exists just prior to fracture. All of the tandem notch specimens were electrolytically polished and chemically etched prior to testing. Photomicrographs at 100 x were taken of all notched regions prior to and after tensile testing. The results of this portion of the investigation revealed that no visible plastic deformation took place prior to fracture for any of the material conditions with the sharpest notch (K_t 8.3). As both the fine grained recrystallized material and the wrought stress-relieved material were observed to undergo over 50 percent reduction in area in the unnotched tensile test, this illustrates the extreme effectiveness of a notch in restricting plastic flow prior to fracture. Tandem notch specimens with a 0.030 inch root radius (K_t 3.7) were tested only for the wrought stress-relieved material condition. In these tests a slight amount of plastic deformation in the vicinity of the notch root was observed, however, this amount of deformation was insufficient to cause an increase in the notch root radius. It was noted that the greatest amount of plastic deformation occurred in regions away from the bottom center of the notch root. The reasons for this behavior will be discussed in a later section. It was also observed that the fracture originated at the bottom of the notch root in the region of least plastic flow. All of the fractures in the recrystallized specimens except one were observed to initiate at grain boundaries. The fracture which did not originate at a grain boundary was found to initiate at an irregularity in the root of the notch. All of the fractures were found to occur predominately by transgranular cleavage crack propagation. Even when the crack appeared occasionally to be intergranular upon closer examination it could be found that the crack merely ran adjacent to the grain boundary but not through it. This is illustrated in Figure 6. These observations are in good agreement with those of Bechtold [5] who observed that fractures in polycrystalline, molybdenum, niobium and tungsten almost always start at grain boundaries, although the fracture may propagate almost entirely transgranularly. Two of the specimens were studied with the aid of high speed motion pictures in order to determine the mode of fracture initiation. Specimens 21 H2 and 21 E2 (K_t 3.7) which had previously failed at the pin hole were tested again at a very high loading rate and motion pictures of the notch section were taken at 5000 frames per second. The film of specimen 21 H2 revealed that apparently the specimen broke

a) Fracture surface and secondary crack, 100X.

b) Secondary crack, 500X.

FIGURE 6 View of fracture surface (a) and secondary cracks (a) and (b) in 1,800° C annealed material.

simultaneously across the entire notch section and no initiation phase could be detected. Fracture in specimen 21 E2 was observed to initiate at the surface of one of the notch roots and propagate across the notch section. From the film speed in these tests the approximate time for fracture to occur was found to be 10⁻⁴ seconds.

Cleavage facets for all of the material conditions were examined and typical cleavage step "river patterns" were observed.

In attempting to locate the precise origin of fracture at the notch root, it was found that several regions through the thickness adjacent to the notch root, appeared to be the initiation site. These sites were found by following the "river patterns" back to their common genesis. In all cases this genesis was found to be a grain boundary Crussard, et al., (32) in an extensive study of the nature of brittle fracture in notch impact tests found this same behavior. Investigating the fracture surface in the region of the notch, by electron microscopy, they found that there was no unique point of origin for all portions of the fracture and that cracking was associated with a series of successive initiations. They observed that the directions of rivers and microtears were quite random but could be grouped around a number of "burst centers" from which the fracture markings radiate in all directions. It appears then that fracture initiates at the notch root through the joining of a number of separate microcracks which form almost simultaneously.

These results emphasize the importance of the intergranular carbide precipitates in controlling the fracture behavior in recrystallized molybdenum. That the grain boundary film is assumed to be carbide precipitates is readily understood from the chemical analysis of the recrystallized specimens. The chemical analysis also shows that the vacuum annealing atmosphere effectively lowers the gas content and may also remove part of the carbon. From the molybdenum carbon phase diagram of Spacil and Wulff (33), it is apparent that all of the specimens were annealed in the single phase terminal solid solution region and thus the power off cooling rate used in this study was not sufficiently fast to hold the carbon in solution. That the carbide precipitates are responsible for the observed low ductility was demonstrated by Spacil and Wulff when they found that molybdenum wire, with 100 PPM carbon, when quenched from a 30-minute anneal at 2,100° C, and subsequently tensile tested, had a ductility of 85 percent reduction in area.

INITIAL YIELDING STUDIES

The studies of initial yielding in the notched specimens provided both qualitative and quantitative information concerning the nature of plastic flow prior to fracture. The yielding was studied by means of photoelastic coatings and load-unload techniques as described in the section on experimental procedure. A few additional brief details may be of value to those unfamiliar with this technique. When the specimen under load is viewed through a reflection polariscope the total

shear strains on the surface of the sheet can be determined directly from the isochromatic fringe patterns. An isochromatic is a line of constant color or line of constant magnitude of shear strain (γ), where $\gamma = \epsilon_1 - \epsilon_2$. The fringe patterns observed when the specimen is unloaded are thus the residual or plastic shear strains occurring in the metal. The linear strain optical response of the plastic used in this study was approximately 3 percent strain. Thus, for deformations larger than 3 percent this technique is no longer valid. In several cases it was found that the plastic bonded to the specimen came off just prior to fracture without cracking and it was observed in all cases that the plastic exhibited 0 percent residual strain; therefore, in all of these studies the plastic strains observed were due only to plastic response in the metal. The magnitude of shear strain for each fringe can be determined by knowing the strain-optical coefficient of the plastic and the plastic thickness. For these studies the shear strain per fringe was 2,960 microinch per inch, or very nearly 0.3 percent strain. The strain correction factor for the reinforcing effect of the coating was calculated to be 1.008 and was therefore, neglected. The isoclinics were also determined. An isoclinic is the locus of points along which the principal stresses have parallel directions. Zandman (34) has presented in detail the principles of photoelastic coatings. A comparison of techniques such as photoelastic coatings, etching, and brittle coatings, used to detect Lueders' lines in mild steel has been made by Durelli, et al. (35).

The nature of yielding in the various notch tensile specimens is shown by the isochromatic fringe patterns in Figures 7 and 8. With the exception of the strain pattern in Figure 7(a) all of the fringe patterns illustrate plastic strain regions (zero load). These plastic flow regions have been termed enclaves by Allen and Southwell (7). In Figure 7(a) and Figure 7(b) the difference between the total (elastic and plastic) shear strain and the plastic shear strain is shown, for the wrought stress-relieved material, and $K_t = 3.7$. This photograph was taken when the nominal stress in the notch section (σ_n) was equal to 95.7 percent of the notch tensile strength ($\sigma_{N.T.S.}$). Figure 7(b) illustrates that yielding proceeds away from the notch at an angle of 45° from the horizontal and does not proceed across the minimum notch axis. The black region in the center of the specimen indicates that this section has

about 0 percent shear strain. The observation that the greatest amount of yielding emanates and proceeds away from the minimum notch section explains the plastic flow behavior in the tandem notch specimen ($K_t = 3.7$), where the greatest amount of plastic flow occurred away from the notch root bottom. The flow pattern just prior to fracture for two of the wrought stress-relieved specimens is shown in Figures 7 (c) and (d). Figure 7(c) shows the yield region for $K_t = 3.7$, when $\sigma_n/\sigma_{N.T.S.} = 0.995$. We see that yielding has now proceeded across the entire section except in the center along the notch waist where the strain is approximately 0.15 percent. The plastic shear strain at the notch root is now 1.5 percent. The yield region for $K_t = 1.93$, when $\sigma_n/\sigma_{N.T.S.} = 0.994$ is shown in (d). Here we see that plastic flow has extended across the entire notch waist, although the greatest amount of yielding still occurs away from the notch waist. We also notice that the enclave area nearest the notch is now more circular in shape and not as pinched as it was for the sharper notch. That yielding proceeded across the entire notch waist for the mild notch but not for the sharper notch is indicative of the lower degree of stress biaxiality for the mild notch.

The extent of deformation just prior to and after fracture for the sharpest notch ($K_t = 8.3$) is shown in Figure 8. Photographs (a) and (b) were taken for specimen 18-B1 (recrystallized at 1800° C) at $\sigma_n/\sigma_{N.T.S.} = 0.965$, and after fracture. Here we see that the high biaxiality of stresses has extremely limited the degree of plastic flow prior to fracture. Yielding occurs now only in the immediate vicinity of the notch. The photograph in (b) shows that slightly more yielding occurred prior to fracture but that the center portion of the specimen is essentially still elastic, after the crack has passed. This illustrates rather vividly that by far the largest amount of energy expended in a ductile cleavage fracture is associated with plastic flow prior to fracture initiation and that little deformation occurs during the propagation of the crack. The same behavior is observed in (c) and (d) for specimen 13-B2 (recrystallized at 1,300° C). The yielding shown in (c) was at $\sigma_n/\sigma_{N.T.S.} = 0.905$. Again we see that plastic flow is very localized but more yielding did occur before fracture as seen in (d). We also notice that the specimen was under a small degree of eccentric loading; however, the fracture is seen to initiate at the notch which underwent the least amount of plastic flow. This
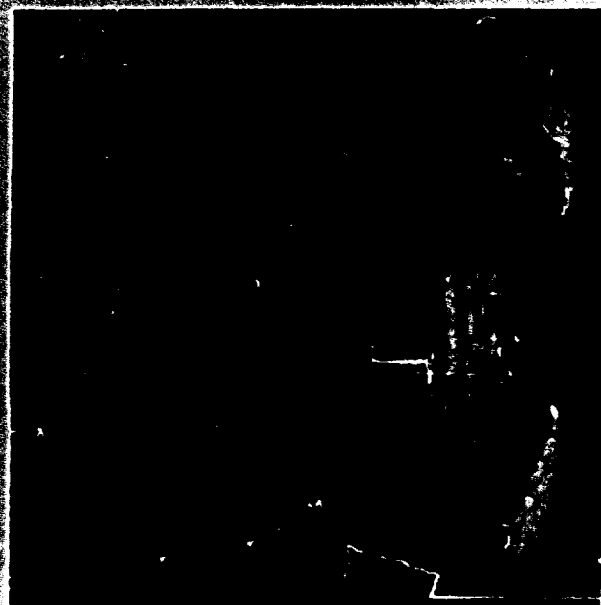
207
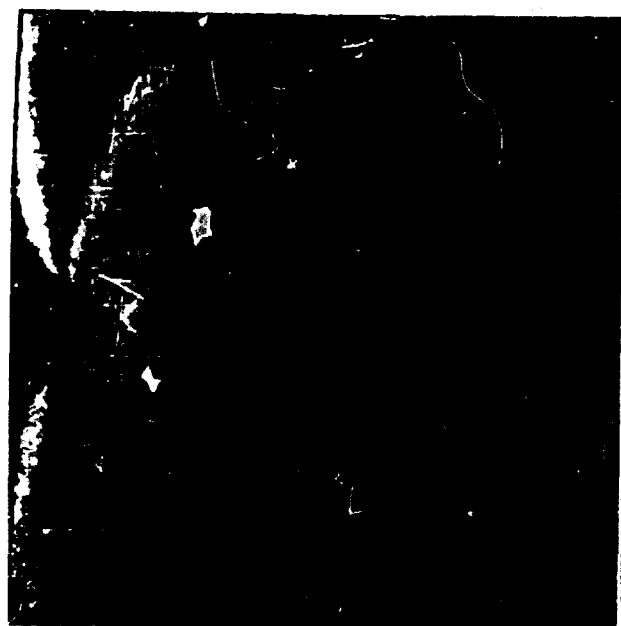
(a) Total shear strain, $K_t = 3.7$.
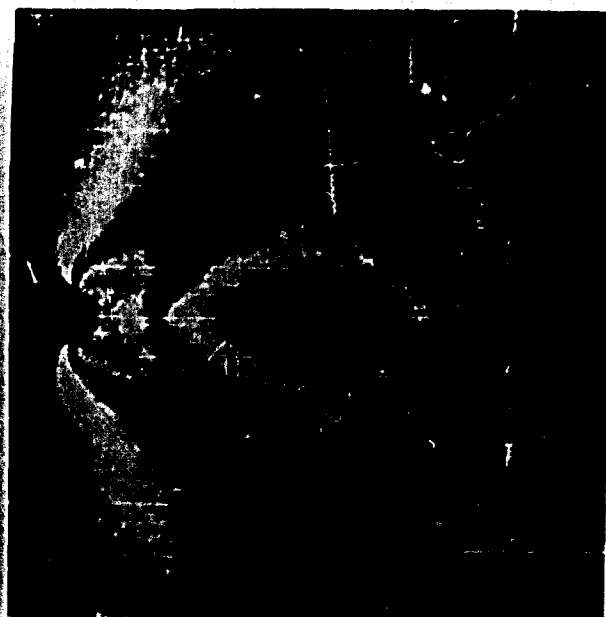
(b) Plastic shear strain, $K_t = 3.7$.

(c) Plastic shear strain, $K_t = 3.7$.

(d) Plastic shear strain, $K_t = 1.93$.

FIGURE 7. Isochromatic fringes for wrought stress-relieved material, 2X.
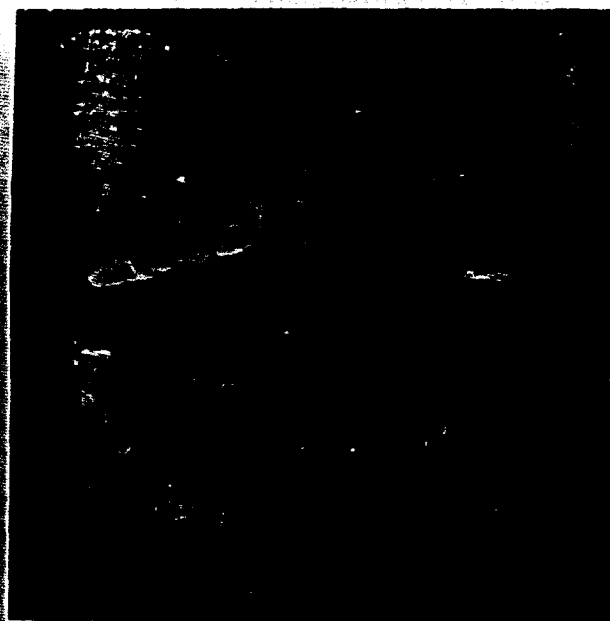
specimen was the only one observed to fracture out of the minimum section. The crack seen emanating from the left hand notch occurred in the coating only and not in the metal. Comparing (c) and (d) with (a) and (b) we see that there is very little difference in the amount of plastic flow prior to fracture. If we recall that the 1,300° C annealed material exhibited 47 percent elongation in the smooth tensile test and that the 1,800° C

annealed material had 5 percent elongation, we can see that ductility measured under a uniaxial state of stress has little or no bearing on the ductility observed prior to fracture under a biaxial state of stress.

The strain-hardening exponent (n) was determined for the 1,300° C annealed material and the wrought stress-relieved material. There was insufficient strain prior to fracture to determine n

208

(a) Annealed—1,800° C, just prior to fracture.   (b) Annealed—1,800° C, fracture.

(c) Annealed—1,300° C, just prior to fracture.   (d) Annealed—1,300° C, fracture.

FIGURE 8.—Isochromatic fringes showing yielding in the recrystallized materials, $K_t = 8.3$, 2X.

for the two larger grain sized materials. The strain-hardening exponent (n) was determined from the empirical relationship $\sigma = K\delta^n$, which has been found to adequately describe the plastic stress-strain behavior of many metals. A plot of true stress (σ) versus true strain (δ) on logarithmic coordinates is a straight line with slope n. The coefficient K is equal to the true stress at unit true

658180 -- 62 --- 15

strain. The results obtained from these plots are shown below.

	1,300° C anneal	Wrought stress-relieved
n	$= 0.160$	$n = 0.057$
K	$= 103,000$ psi	$K = 138,000$ psi
δ max load	$= 0.149$	δ max load $= 0.066$

It can be shown that the true strain at the maximum load point is equal to n. Therefore, a test of the adequacy of the actual stress-strain response for the particular material is to compare the values of n with δ at the maximum load. It can be seen from the data above that the values are in reasonably good agreement. The values of n are thus in agreement with the qualitative information from the stress-strain curves which indicated that the recrystallized material strain-hardened much more readily than the wrought stress-relieved material. The microhardness data in Table II also indicates that little or no strain-hardening occurs in the wrought stress-relieved material.

The shear strain at the notch root at fracture was calculated from the isochromatic data and is presented in Tables III, IV and V. These are values of plastic shear strain observed just prior to fracture. In cases where the plastic strain pattern was not observed near the fracture load no data are presented. Although the data are limited it is apparent that the plastic strain at the root of the notch just prior to fracture decreases sharply with increasing stress concentration factor. This is indicative of increasing biaxiality at the notch root with increasing stress concentration factor.

The notch yield strength values presented in Tables III, IV and V require some explanation and analysis. These values were obtained by determining the nominal stress in the notch section, when yielding was first observed at the root of the notch. Yielding at the root of the notch is defined here as occurring when the plastic shear strain at the notch root is equal to 0.3 percent (the first fringe). This is, of course, not the yield stress or yield point load as defined by Hill (36) and others as the load when the plastic enclaves have just proceeded across the entire notch section. This yield stress will be discussed in more detail later. Defining initial yielding as occurring when 0.3 percent strain is reached at the notch root has several advantages. First of all the first fringe which is equal to 0.3 percent shear strain is very accurately and readily determined. Secondly, 0.3 percent shear strain at the

notch root corresponds closely with the 0.2 percent offset yield stress in the smooth tensile test. It can be shown from elasticity theory that ϵ_1 at a free surface is as follows:

$$\epsilon_1 = \frac{\epsilon_1 - \epsilon_2}{1 + v} = \frac{\gamma}{1 + v} \qquad \text{Eq. (7)}$$

where v is Poisson's ratio. If v is assumed equal to 0.5 in the plastic range we see that $\epsilon_1 = 0.003/1.5 = 0.002$ or 0.2 percent strain at the free surface of the notch root. Thus as defined yielding at the notch root surface is similiar to the common 0.2 percent offset technique used for uniaxial tension. The estimated accuracy of the notch yield stress values presented in the tables is $\pm 1,500$ psi. Two interesting observations are made. The data indicate that for a given material condition, yielding at the notch root occurs at the same nominal stress level irrespective of K_t. Secondly, this stress level corresponds reasonably well with the yield stress in the unnotched specimens. Thus it appears that the material at the notch root is ignoring the effect of the stress concentration factor. From elastic considerations it is expected and usually assumed that plastic deformation begins at the root of the notch when the nominal stress level is equal to the yield stress of the unnotched material divided by the theoretical stress concentration factor ($\sigma_n = \sigma_{y,s}/K_t$). This we see was not found to be true experimentally. Thus it appears that the material surrounding the notch root region is very effectively constraining this region and not allowing it to behave in a uniaxial manner. It may be argued that if a very small strain gage were placed in the notch root to measure ϵ_1 directly on the notch surface rather than on the surface of the sheet, results closer to those predicted by the theory may be obtained. This may be the case; however, the yielding of an infinitely thin surface layer of material would have very little effect on the flow behavior of a structure of the size used in this investigation.

It was mentioned previously that the yield point load in notched specimens is usually defined as the load at which yielding just extends across the entire notch section. Allen and Southwell (7) have performed an elastic-plastic stress analysis, using a relaxation technique, and have predicted the yield point load for a non-strain-hardening material for a semi-circular and a V-notch of 50 percent notch depth for both the case of plane

210

strain and plane stress. It is of interest to compare the yield point loads predicted by Allen and Southwell for the plane stress case with those experimentally determined in this study. This comparison is shown below.

Notch	Material	$\sigma_n/\sigma_{u.s.}$
Semi-circular	Allen and Southwell.	1.12
K_t 1.93.	Wrought—S. R.	1.09
K_t 1.93	Annealed—1,300° C	1.13
V-notch	Allen and Southwell	1.24
K_t 3.7.	Wrought—S. R.	1.09
K_t 3.7.	Annealed—1,300° C	1.12

Comparisons cannot be made for the sharp notch (K_t 8.3) as the yield point load was never reached. The elastic-plastic stress analysis is seen to predict an increase in the applied nominal stress (σ_n) at the yield point as the notch sharpness is increased. The data for both the wrought stress-relieved material and the annealed material, however, show that the notched to unnotched yield stress ratio is apparently constant, regardless of the notch sharpness. It is also noticed that although the annealed material strain hardened quite readily it does not seem to invalidate the comparison even though the theory was predicted for a non-strain-hardening material. The observation that the yield point stress in the notched specimens was higher than the yield stress in the unnotched specimens is explained by the fact that the contraction in sheet thickness which ordinarily accompanies a uniform axial extension is restricted by the larger adjoining bulk of essentially elastic material in the notch region. This produces a transverse tensile stress which in turn reduces the necessary shear stress for yielding and thus the nominal axial stress must be increased. In this connection, Orowan (37) has defined a notch or "plastic constraint factor." He defines the mean constraint factor as being equal to the ratio of the nominal stress in the notch section at the yield point to the uniaxial yield stress. He defines the maximum constraint factor as the ratio of the highest value of σ_n in the notch section to the uniaxial yield stress. Orowan has calculated that the maximum constraint factor of an ideally plastic material is about 3.3, and the mean constraint factor about 2.9. The maximum, as well as the mean, constraint factor for the two-dimensional ideal notch in an ideally plastic solid was calculated to be 2.57. Thus, no notch or crack can, from plastic constraint, raise the tensile stress above 2.57 or 3.3 (approximately 3) times the uniaxial yield stress. From the data presented

above, it was seen that for both the wrought stress-relieved material and the recrystallized material that the mean constraint factor was about 1.1. This low plastic constraint factor is indicative of the observed behavior that very little plastic flow occurred prior to cleavage fracture. We saw that the sharp notch specimens fractured before the yield point load was reached, and that in the most ductile notch fractures only about 2.5 percent strain was observed at the notch root. It will be shown later that the plastic constraint factor in the yield region at the root of the notch can be about twice as large as this mean constraint factor in the notch section.

While several investigators have applied an elastic analysis to the state of stress and strain at the root of a notch or the tip of a crack in tension, very little has been done in the way of an elastic-plastic stress analysis. The principal exception to this is the extensive analysis of Allen and Southwell (7) who have applied an elastic-plastic analysis to the problems of v-notched and semicircular notched tensile bars under conditions of both plane strain and plane stress. The relaxation procedures used by Allen and Southwell have been extended to the case of an externally cracked tensile bar subjected to plane strain by Jacobs (8). Recently, Stimpson and Eaton (6) have applied an elastic-plastic stress analysis to the case of an externally cracked tensile specimen under plane stress conditions. The plastic enclaves determined experimentally in this study allow a comparison to be made with the theoretical results from the elastic-plastic analysis by Allen and Southwell and Stimpson and Eaton. The results are compared for the wrought stress-relieved material with $K_t = 3.7$. It was shown before that the wrought stressed-relieved material is a very good approximation to a non-strain-hardening material which is an assumption used in the elastic-plastic analysis. The experimental enclaves determined in this study are shown in Figure 9.

The yielding is shown to progress away from the notch root as the nominal stress in the notch section (σ_n) is increased. The enclaves are shown quantitatively as a function of the octahedral shear stress (τ_{oct}), as in the elastic-plastic analysis, the octahedral shear limitation of the von Mises-Hencky theory is chosen as the yield criterion. This criterion states that yielding first occurs when any combination of the principal stresses reaches a critical (constant) value.
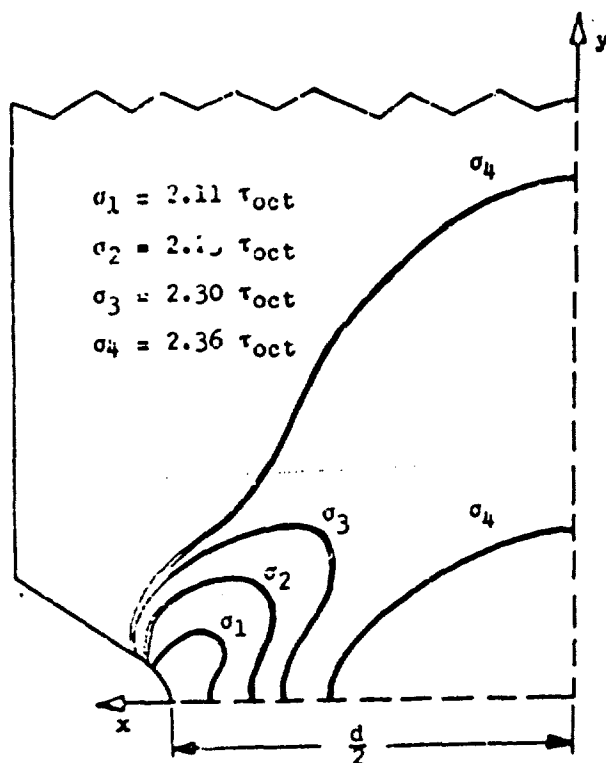
211

$\sigma_1 = 2.11\ \tau_{oct}$

$\sigma_2 = 2.1\smile\ \tau_{oct}$

$\sigma_3 = 2.30\ \tau_{oct}$

$\sigma_4 = 2.36\ \tau_{oct}$

FIGURE 9. Sequence of plastic enclaves for wrought stress-relieved material 30% notch depth, K_t -3.7.

$\sigma_1 = 2.50\ \tau_{oct}$

$\sigma_2 = 2.58\ \tau_{oct}$
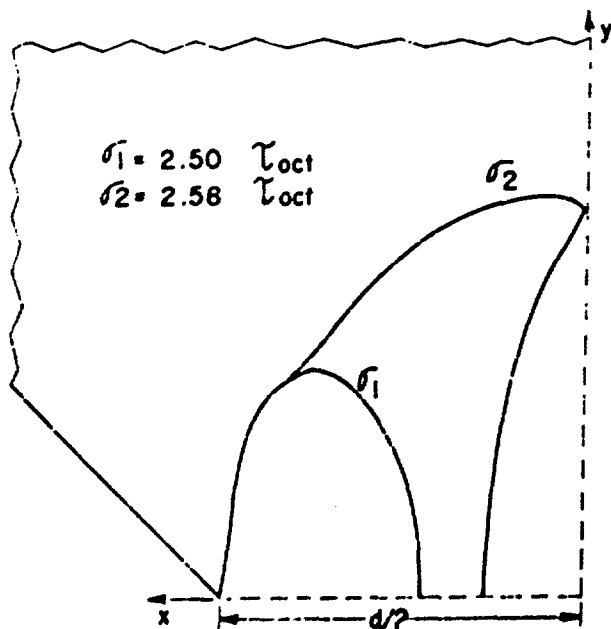
FIGURE 10. Sequence of plastic enclaves (plane stress), 50% notch depth (Ref. 7).

212

$\sigma_1 = 1.66\ \tau_{oct}$

$\sigma_2 = 2.04\ \tau_{oct}$

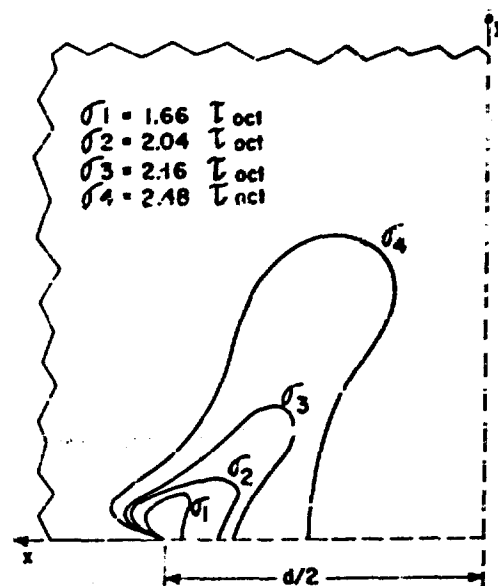$\sigma_3 = 2.16\ \tau_{oct}$

$\sigma_4 = 2.48\ \tau_{oct}$

FIGURE 11 Sequence of plastic enclaves (plane stress), crack is 50% through width (Ref. 6).

$$(3\tau_{oct})^2 = (\sigma_1 - \sigma_2)^2 + (\sigma_2 - \sigma_3)^2 + (\sigma_3 - \sigma_1)^2 \quad \text{Eq. (8)}$$

In simple tension $\tau_{oct} = \sqrt{2/3}\,\sigma_1$, or $\tau_{oct} = 0.471\sigma_1$, where σ_1 is the yield stress. The theoretical plastic enclaves are shown in Figures 10 and 11. The enclaves are shown for one quadrant of the notched section and the Y axis is the tensile direction. Figure 10 shows the sequence of plastic yielding for the 90° v-notch of Allen and Southwell and the crack notch specimen of Stimpson and Eaton is shown in Figure 11. Both qualitatively and quantitatively there appears to be good agreement. The experimentally determined enclaves, however, appear to be more pinched along the notch waist than those predicted for the v-notch. It is also observed that they climb back along the notch side which was not predicted for the v-notch. A quantitative comparison of the enclave areas as a function of applied stress of Allen and Southwell and Stimpson and Eaton has recently been made by Williams (9). This comparison along with the experimental results of this study are shown in Figure 12. The enclave area per quadrant, where d is the notch width, is shown as a function of the ratio σ_n/τ_{oct}. The agreement between the experimental and the theoretical elastic-plastic results is seen to be very good. It was stated previously that $\tau_{oct} = \sqrt{2/3}\,\sigma_{y.s.}$ in simple tension, or $\sigma_{y.s.} = 2.12\sigma_{oct}$, thus we see in Figure 12 that when the nominal stress in the notch section becomes equal to the
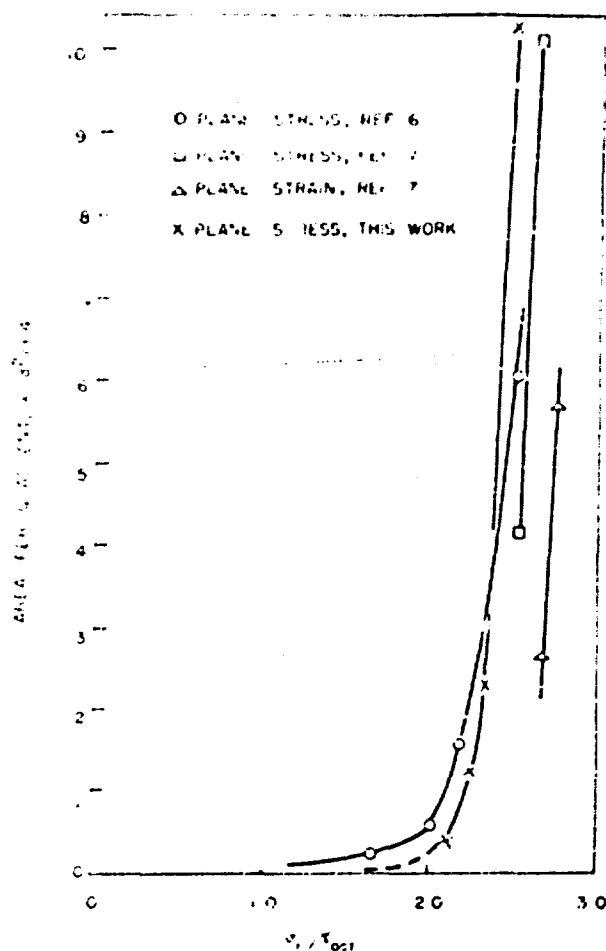
Fig. 12. Comparison of theoretical and experimental enclave areas versus nominal stress in notch section.

smooth tensile stress, there is a rapid increase in the amount of yielding.

The work of Stimpson and Eaton has also shown that the axial stress in the notch section increased from the root of the notch to a maximum value, at the elastic-plastic interface, equal to about 2.3 times the uniaxial yield stress. Thus, the maximum plastic constraint factor in the yield region at the crack tip is 2.3. This calculation was made for a value of the nominal stress equal to 2.16 τ_{oct} or $\sigma_n = 1.02 \sigma_y$. The extent of the yield region for this value is shown in Figure 11 as σ_3. This yield region is quite similar to the yield region in Figure 8(a) for $K_t = 8.3$. For the yield region shown in Figure 8(a) the value of the nominal stress in the notch section is 2.1 τ_{oct} or $\sigma_n = 0.93 \sigma_y$. These figures indicate that it is reasonable to compare the results of the elastic-plastic stress analysis for the cracked specimen to those for the sharply notched specimen. Thus, the axial stress at the

elastic-plastic interface shown for the 1.800° C annealed material in Figure 8(a) should be about $2\sigma_y$, or somewhat less than the 2.3 value for the cracked specimen. The value of the shear strain to cause this plastic constraint is about 0.3 percent. The enclave shown in Figure 7(b) for the wrought stress-relieved material, which is σ_3 in Figure 9, is perhaps a better comparison with the σ_2 enclave in the cracked specimen in Figure 11. Therefore, the ratio of the axial stress to the uniaxial yield stress should be about 2.3 at this elastic-plastic interface. We demonstrated earlier that the mean plastic constraint factor for $K_t = 3.7$ was about 1.1. Thus, we see that while the mean plastic constraint factor can be quite low, that in the flow region at the root of the notch the plastic constraint factor can be considerably higher, and as was shown for the sharp notch the magnitude of the strain necessary to raise the axial stress to about $2\sigma_y$ is quite small. This observation is quite important as it illustrates that only a small amount of strain is necessary to cause a considerable increase in the axial stress at the tip of a notch or crack, which will obviously play an important role in the fracture initiation process, when cracks initiate by cleavage. This maximum plastic constraint factor would be expected to be larger and closer to Orowan's value of 3 for a triaxial stress condition. It is interesting to note here that these experimental observations were realized earlier by Cottrell. It was Orowan's maximum plastic constraint factor which provided the basis for Cottrell's value of β equal approximately to ⅓ in his ductile-brittle transition criterion expressed in Equation (4). Cottrell stated that the localized plastic strain needed to raise the tensile stress by a factor of 3 is small and of the same order as the elastic strain. He thus applied the plastic constraint argument on a microscopic scale and in the derivation of Equation (4) stated that the microscopic tensile stress acting on the two intersecting slip planes will be increased by the factor 3 or equivalently change β to ⅓.

At least two investigators have applied elastic-plastic stress analysis solutions to the problem of fracture initiation in cylindrical notched tensile bars. Hendrickson, Wood, and Clark (88) have applied Allen and Southwell's plane strain analysis in studying fracture initiation in round notched tensile specimens of an annealed low-carbon steel at low temperatures. Their results showed that the maximum tensile stress within the specimen occurred at the elastic-plastic interface

213

below the root of the notch. Their results also indicated that brittle fracture initiated at the elastic-plastic interface when the stress there reached a maximum critical value, and that this critical stress was independent of temperature and rate of loading. The location of the elastic-plastic interface was verified by microhardness studies; however, no metallographic evidence was presented to show that the fracture did indeed initiate at the elastic-plastic interface. This premise is supported indirectly, however, by the work of Troiano (39), who in studying the effect of hydrogen on the delayed failure behavior of steel and other alloys, found in sustained load tests on hydrogenerated notched specimens that cracks initiated below the notch root in the region of highest triaxiality of stresses. In studying fracture initiation in creep-rupture studies of notched specimens, Mirkin and Trunin (40) also found that the maximum tensile stress occurred at the elastic-plastic interface. In their study, metallographic evidence showed that microcracks did indeed initiate at the elastic-plastic boundary.

Elastic-plastic stress analysis results have shown that the maximum transverse or radial stress also occurs at the elastic-plastic interface. This result is experimentally verified in this work by the isoclinic data which was obtained from the photoelastic coating studies. From principles of photo-elasticity, Frocht (41) has shown that where the zero isoclinic (locus of points along which the principal stress σ_1 is parallel to the tensile axis) intersects the axis of symmetry, the transverse (σ_2) stresses must have maximum or minimum values. By comparing the zero degree isoclinics for elastic loads and after yielding had occurred, it was observed that the zero isoclinic intersected the horizontal axis at the elastic-plastic interface indicated by the first fringe. Thus, σ_2 as well as σ_1 reaches a maximum value at the elastic-plastic interface and, therefore, a hydrostatic state of tension would tend to favor fracture initiation at this location. It is interesting to note that the two studies mentioned above that have shown metallographically that microcracks initiate below the root of the notch have both utilized sustained loading techniques. That microcracks are easier to detect with this type of loading in contrast to monotonic loading is readily apparent. In this respect, it is also felt that the tandem notch specimens used in this study should be a valuable tool in locating the site of crack initiation with the added advantage

of being able to vary the loading rate when this variable is of importance. In this study, it has been shown that cracking initiated at the notch root surface at grain boundary sites. That crack initiation was not observed to be associated with the elastic-plastic interface is not surprising when one considers molybdenum's low resistance to cleavage crack initiation and the small amount of plastic flow that was observed in these specimens. For the two sharper notches it is recalled that the maximum amount of strain that was observed was about 1.5 percent and in no case was any reduction in sheet thickness observed nor was there any indication of a shear lip. Another important factor is that the biaxial state of stress in a sheet specimen would not be expected to be nearly as effective in promoting crack initiation as the triaxial state of stress in notched cylindrical specimens which were used by both Troiano and Mirkin and Trunin.

ENERGY OF DEFORMATION DURING FRACTURE

Let us now look at another aspect of this complex fracture problem and consider the energy of deformation during fracture. It was stated earlier that the energy expended in the total fracture process can be broken into two parts: that which occurs in plastic flow prior to crack initiation and that which occurs during the propagation of the crack. It was concluded previously from the initial yielding studies that for these specimens, all of the detectable yielding occurred prior to crack initiation. Let us now treat the matter in a somewhat more quantitative manner. The effective surface energies for crack propagation which were calculated earlier may be misleading for two reasons. First, the precise critical crack size was not able to be obtained and secondly the effective surface energy expressed as energy per unit area of cracked surface does not allow us to determine the energy expended in plastic flow either prior to or during crack propagation which occurs in a unit volume of the material and not on a unit surface. Moser (42) in 1924, in a study of the interpretation of notched bar impact tests results, demonstrated that the quantity of energy absorbed by the unit of volume of material undergoing deformation is a constant for a given material and is thus a material characteristic. The value of the "work-constant" of the unit volume was independent of the size of the specimen and the shape of the notch and could

214

only be changed by changing the nature of the material, such as different heat treatments. This principle must certainly be general and, therefore, applicable to the tensile case. Hahn (43) has pointed out that the effective surface energies determined either from the Griffith-Orowan or the Griffith-Irwin treatments are not a basic material property but a function of yield strength, delayed yield effects, work hardening, plastic constraint and effective surface energy. It has also been pointed out by Wessel (43), that fracture energy measurements should be related to the volume of affected metal and not the unit area of the fractured surface.

In light of the above discussion, it is tempting to try to estimate the energy per unit volume involved in plastic flow prior to fracture in the notched tensile specimens. The energy expended in yielding of the notched specimens can be estimated from knowing the volume of deformed metal, the mean stress (σ_m) acting on the deformed volume and the mean strain (ϵ_m) in the deformed volume. Thus, the work function or the energy per unit volume (W_s) can be estimated from

$$W_s = \sigma_m \cdot \epsilon_m \qquad \text{Eq. (9)}$$

In Equation (9) an ideally plastic stress-strain curve is assumed. Calculations of these quantities are made for the sharp notch $(Kt=8.3)$ specimen of the 1,800° C recrystallized material where the deformation is confined to the immediate vicinity of the notch root. The isochromatic data reveal that the mean shear strain (γ_m) in the yielded region is approximately 0.003 inch per inch. It has been shown theoretically and recently experimentally (44) that a plane strain region exists beneath the root of a sharp notch; therefore, it can safely be assumed that $\epsilon_m = \gamma_m$. An estimate of σ_m is a little more difficult; however, we know that the stress at the root of the notch cannot be less than the yield stress of the material (35,900 psi), and from elastic-plastic stress analysis results we know that the tensile stress increases across the yield region to a maximum value at the elastic-plastic interface. It is worth noting here that this fact has not been recognized by many investigators who usually assume that the tensile stress is a constant value equal to the yield stress in the plastic flow region at the tip of a crack or a notch. This is not the case, however, and the elastic stress gradient is reversed after yielding occurs and the stress increases as you proceed away from the notch across the yielded region.

The tensile stress in the plastic range can be expressed by

$$\sigma_1 = \frac{D}{1-v^2} (\epsilon_1 + v\epsilon_2) \qquad \text{Eq. (10)}$$

where v is Poisson's ratio equal to 1/2, and D is the plastic modulus determined from the slope of the stress-strain curve at a strain value of 0.003 inch per inch. The use of engineering stresses and engineering strains is a valid assumption as we are dealing with small values of plastic strain. For large plastic strains, true stresses and true strains must be used. From Equation (10) σ_t is calculated to be 48,500 psi. From the elastic-plastic stress analysis of an externally cracked specimen, Stimpson and Eaton show that σ_m in the plastic flow region should be about twice the applied stress. If this result is applied to the sharp notched specimen in this case, σ_m is determined to be 67,000 psi. Thus, the value of σ_m calculated to be 48,500 psi seems reasonable. If we now put the values of $\sigma_m=48,500$ psi and $\epsilon_m=0.003$ inch per inch into Equation (10) and multiply by 2 to account for both notches, we calculate W_s to be 2.0×10^7 ergs/cm³. This work function can be compared with the area under the smooth tensile stress-strain curve which is the energy absorbed per unit volume in fracturing. This area was measured and the work function was calculated to be 1.2×10^5 ergs/cm³. By comparison, the area under the stress-strain curve for the 2,100° C annealed material was found to be 1.3×10^7 ergs/cm³. Admittedly, these calculations are quite approximate; however, there is at least sufficient agreement to suggest that this is a fruitful avenue of approach and warrants more highly refined experiments, so that a precise knowledge of the stored energy in the system is known at the onset of rapid fracture. Knowledge of a true material characteristic such as the work function which is independent of test conditions and specimen shape would be invaluable to the materials engineer.

ETCH PIT STUDIES

The final portion of this investigation deals with dislocation density measurements determined by etch pit techniques. It was hoped that the strain distribution at the roots of the notched specimens

could be studied by dislocation density measurements. A comprehensive investigation of etch pit techniques for revealing dislocations and subgrains in molybdenum has been conducted by Adams et al., (45). The etch pit studies were carried out on both the tandem notch specimens and the smooth tensile specimens for the 1,300° C and 1,800° C annealed materials. The specimens were heated in hydrogen at 950° C for 30 minutes prior to the electrolytic polishing and chemical etching technique described in the experimental procedure. The calculated dislocation densities are listed below. All of the etch pit observations were made at a magnification of 1800x.

Material condition	% strain	Dislocation density lines/cm²
Annealed—1,300° C.. ...	0	5.4 × 10⁷
Annealed—1,300° C	16	......
Annealed 1,800° C..	0	3.1 × 10⁷
Annealed 1,800° C	3.4	9.4 × 10⁷

The data listed above was obtained from the smooth tensile specimens. The etch pits for the 1,300° C annealed material strained 16 percent and for the wrought stress-relieved material both strained and unstrained were too dense to count. Substructure formation was observed in these specimens. The increase in dislocation density with percent strain is illustrated in figure 13.

The etch pit investigations at the root of the sharply notched specimens in the section which did not fail, revealed that there was no increase in density over the annealed condition for both the 1,300° C and 1,800° C material conditions. This result is expected when we recall that the maximum strain at the root of the sharply notched specimens was about 0.5 percent and for the 1,800° C condition it was observed that the dislocation density increased only by a factor of 3 for a strain of 3.4 percent. It appears from this very limited etch pit study that a quantitative measurement of strain at the root of a sharp notch in recrystallized molybdenum would be difficult to obtain from dislocation density measurements. A more complete investigation should be conducted, however, so that the precise dislocation multiplication rate can be determined.

SUMMARY

This is not intended to be a comprehensive summary of all the test results but merely an attempt to assemble together the results concerning the nature of fracture in the notched specimens

216
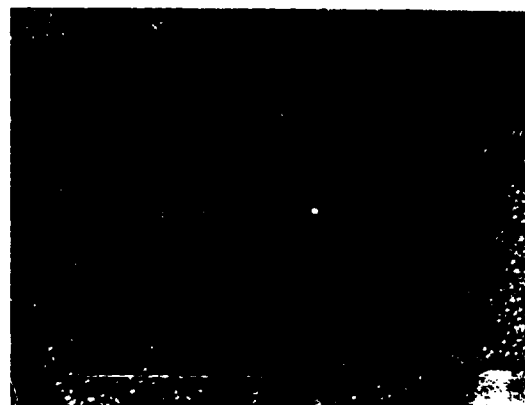
(a) 0% strain.

(b) 3.4% strain.

FIGURE 13. Etch pits in 1,800° C—Annealed material with varying amounts of strain, 1800×.

of polycrystalline molybdenum sheets. From the initial yielding studies and also from the fracture and yield stress data in Figure 5 it is seen that fracture is always preceded by yielding and that the yielding is quite local for the sharp notch. Thus, plastic flow is an essential condition for fracture under these conditions. It was also seen, however, that fracture occurred at the notch root bottom but the region of greatest strain energy and largest amount of plastic flow was located away from the notch bottom at some acute angle from the horizontal notch axis.

It was shown in Figure 8(d) that fracture initiated at the notch with the least amount of plastic flow. It seems therefore, that yielding or plastic strain is an essential condition for fracture but not

the governing factor in initiation in this case. It was also demonstrated that initial yielding at the notch root occurred at the same nominal stress level independent of K_t, yet the notched samples were considerably more brittle than the smooth samples, as both the magnitude of strain and stress at fracture were decreased in the presence of a notch.

In Figure 5 it is clear that the decrease in fracture strength due to the presence of a notch is greatest for the most ductile material condition and that this effect diminishes with increasing material brittleness. This evidence seems to lead to the conclusion that plastic constraint must be the important factor in governing fracture behavior in these notched specimens. It has been shown that for the sharp notch specimens, plastic constraint can increase the local axial stress beneath the notch root to a value of about two times the yield stress at the notch root surface and that this occurs at small values of strain. That fracture was not observed to initiate at the elastic-plastic interface may well be due to the overriding importance of the low cohesive strength of the grain boundary. Also because of the very low effective surface energy for fracture the importance of internal stress concentration factors at grain boundary intersections may well be playing an important role in determining the fracture initiation site in these specimens.

In terms of understanding notch behavior the results obtained lead to some logical extensions of this work. To understand further the importance of plastic constraint, it would be desirable to duplicate these tests using sheet thickness as a variable and going to very thin sheets. The role of the elastic-plastic interface might be clarified by conducting similar tests over a range of temperatures. It would also be highly desirable to conduct bi-crystal experiments to determine the role of the grain boundary and the grain boundary precipitate in governing fracture initiation behavior.

CONCLUSIONS

1. Fracture in notched recrystallized molybdenum initiates at grain boundary sites at the notch root surface and propagates almost entirely by transgranular cleavage.

2. For relatively ductile fine grained molybde-

num the general effect of increasing notch severity is to decrease the fracture strength by inhibiting plastic flow; however, for the larger grain size recrystallized material in which the ability to flow plastically is reduced, the detrimental effects of increasing notch severity are lessened.

3. Tandem notch specimens have been shown to be a helpful tool in studying fracture initiation.

4. Analysis of the smooth tensile properties for the recrystallized material, according to the Griffith-Orowan theory for crack propagation and the Cottrell criterion for crack initiation, show that the effective surface energies for crack propagation and crack initiation are the same order of magnitude, which is 10^5 ergs/cm². This finding is supported by the experimental observation that no microcracks were found.

5. Photoelastic coatings have been shown to be a useful tool in studying initial yielding in notched sheet tensile specimens.

6. Plastic flow regions determined experimentally from the photoelastic coating studies have been shown to be in good agreement, both qualitatively and quantitatively, with theoretical results predicted by elastic-plastic stress analysis.

7. The initial yielding studies have shown that the volume of plastically deformed metal decreases as the stress concentration factor increases, and that all of the detectable yielding occurs prior to crack initiation.

8. Initial yielding at the notch root was found to occur at the same nominal stress level for a given material condition, independent of the magnitude of the stress concentration factor. This nominal stress in the notch section was very nearly equal to the smooth tensile yield stress.

9. Limited dislocation density measurements determined by etch-pit techniques reveal that a quantitative measurement of strain at the root of a sharp notch in recrystallized molybdenum is difficult to obtain by such a technique. It is felt, however, that a more complete investigation is necessary in order that a precise dislocation multiplication rate can be determined.

LIST OF REFERENCES

1. Inglis, C. E., "Stress in a Plate Due to the Presence of Cracks and Sharp Corners," Transactions of the Institution of Naval Architects, London, England, Vol. 60, (1913), p. 219.

2. Westergaard, H. M., "Bearing Pressures and Cracks," Trans. ASME, Vol. 61 (1934), p. 49–53–A.

3. Irwin, G. R., "Analysis of Stresses and Strains Near the End of a Crack Traversing a Plate," J. Appl. Mech., Vol. 24, 1957, p. 361.

4. Williams, M. L., "On the Stress Distribution at the Base of a Stationary Crack," J. Appl. Mech., March 1957.

5. Post, D., "Photoelastic Stress Analysis for an Edge Crack in a Tensile Field," Proc. Society of Experimental Stress Analysis, Vol. 12, n. 1, 1954, p. 99.

6. Stimpson, L. D., Eaton, D., "The Extent of Elasto-Plastic Yielding at the Crack Point of an Externally Notched Plane Stress Tensile Specimen," ARL 24, Office of Aerospace Research, July 1961.

7. Allen, D. N. DeG., Southwell, R. V., "Plastic Straining in Two-Dimensional Stress Systems," Royal Society (London), Phil. Trans. Series A, Vol. 242, 1944–50.

8. Jacobs, J. A., "Relaxation Methods Applied to Problems of Plastic Flow. I. Notched Bar Under Tension," Phil. Mag., Vol. 41, 1950, p. 349.

9. Williams, M. L., "A Review of Recent Research at GALCIT Concerning Fracture Initiation," ARL–1, Office of Aerospace Research, April 1961.

10. Hult, J. A., and McClintock, F. A., "Elastic-Plastic Stress and Strain Distributions Around Sharp Notches Under Repeated Shear," Ninth Int. Congr. Appl. Mech., Brussels, Vol. 8, 1956, p. 51.

11. McClintock, F. A., "Ductile Fracture Instability in Shear," J. Appl. Mech., Vol. 25, p. 581, 1958.

12. Cottrell, A. H., "Fracture of Metals," a lecture presented at the Charles M. White Dedication Lectures, Case Institute of Technology, October 1961.

13. Neuber, H., "Research on the Distribution of Tension in Notched Construction Parts," WADD TR–60–906, Jan. 1961.

14. Johnson, A. A., "The Effect of Grain Size on the Tensile Properties of High-Purity Molybdenum at Room Temperature," Phil. Mag., 4, p. 194, 1959.

15. Rose, R. M., Ferriss, D. P., Wulff, J. "Yielding and Plastic Flow in Single Crystals of Tungsten," to be published.

16. Weiss, V., Sessler, J. Sachs, G., "Analysis of Brittle Fracture in Sheet Materials," Symposium on Design with Brittle Materials, Materials Advisory Board, 1960.

17. Weiss, V., Sessler, J., "Analysis of the Effects of Test Temperature on the Notch Strength of High Strength Sheet Alloys," Symposium on Low-Temperature Properties of High Strength Aircraft and Missile Materials, Am. Soc. Test. Mat. (1960).

18. Stroh, A N., "A Theory of the Fracture of Metals," Adv. in Phy., 6, p. 418 (1957).

19. Imgram, A. G., Holden, F. C., Ogden, H. R., Jaffee, R. I., "Notch Sensitivity of Refractory Metals," WADD TR–60–278, September 1960.

20. Voorhees, H. R., Freeman, J. W., "Notch Sensitivity of High-Temperature Alloys," WADC TR–59–470, July 1959.

21. Bechtold, J. H., and Wessel, E. T., "Ductile-to-Brittle Transition in Molybdenum," The Metal Molybdenum, ASM, Chapter 12 (1958).

22. Wessel, E. T., "Abrupt Yielding and the Ductile-to-Brittle Transition in Body-Centered, Cubic Metals," J. Met., 9, p. 930, 1957.

23. Petch, N. J., Phil. Mag., 1956, Vol. 1, 1. 186.

24. Cottrell, A. H., "Theory of Brittle Fracture in Steel and Similar Metals," Trans. Amer. Inst. Min. Met. Engrs., 212, p. 192 (1958).

25. Petch, N. J., "The Cleavage Strength of Polycrystals," J. Iron and Steel Inst., 174, p. 25 (1953).

26. Taylor, J. W., Metallurgia 50, 1954, 1. 161.

27. Orowan, E., "Fundamentals of Brittle Behavior in Metals," p. 139, Fatigue and Fracture of Metals, John Wiley and Sons, Inc., New York (1952).

28. Low, J. R., "The Relation of Microstructure to Brittle Fracture," Relation of Properties to Microstructure, (1954), p. 163, American Society for Metals.

29. Hahn, G. T., Averbach, B. L., Owen, W. S., Cohen, M., "Initiation of Cleavage Microcracks in Polycrystalline Iron and Steel."

30. Owen, W. S., Averbach, B. L., Cohen, M., "Brittle Fracture of Mild Steel in Tension at −196° C," Trans. Amer. Soc. Metals, 50 (1958), p. 634.

31. Bechtold, J. H., "Cleavage in the Refractory Metals," Reference 29.

32. Crussard, C., Barione, R., Plateau, J., Morillon, Y., and Marotroy, F., "A Study of Impact Tests and the Mechanism of Brittle Fracture," J. Iron and Steel Inst., 1, 146, June 1956.

33. Spacil, H. S., Wulff, J., "Effects of Oxygen, Nitrogen, and Carbon on the Ductility of Wrought Molybdenum," The Metal Molybdenum, ASM, Chapter 13 (1958).

34. Zandman, F., "Photostress Principles and Applications," Society of Non-Destructive Testing Handbook, 1959 Edition.

35. Durelli, H. J., Kobayashi, A., Hofer, K., "Lueders' Lines Detecting by Means of Brittle Coatings," Soc. Exp. Stress Analysis, Paper No. 563, October 1959.

36. Hill, R., Plasticity, Oxford at the Clarendon Press, 1950, p. 245.

37. Orowan, E., "Fracture and Strength of Solids," Reports on Progress in Physics, 12, p. 185, 1948–49.

38. Hendrickson, J. A., Wood, D. S., and Clark, D. S., "The Initiation of Brittle Fracture in Mild Steel," Trans. Am. Soc. Met., 50, p. 656, 1958.

39. Troiano, A. R., "The Role of Hydrogen and Other Interstitials in the Mechanical Behavior of Metals," Trans. Am. Soc. Met., 52, p. 54, 1960.

40. Mirkin, I. L., and Trunin, I. I., "An Investigation of Creep and Failure of Steel in the Zone of Stress Concentration," Trudy Tsentral'nyy Navchno-Issledovatel'skiy Institut Tekhnologii i Mashionstroenii, 79, p. 24, 1957.

41. Frocht, M. M., *Photoelasticity*, John Wiley and Sons Inc., New York, 1941, p. 215.
42. Moser, M., "A New Method of Interpreting Notch-Bar Impact Test Results," Trans. Am. Soc. Metals, 1, p. 297, 1925.
43. Wessel, E. T., "The Influence of Pre-Existing Sharp Cracks on Brittle Fracture of a Nickel-Molybdenum-Vanadium Forging Steel," Trans. Am. Soc. Metals, 52, p. 277 (1960).
44. Grewal, K. S., Weiss, V., Sachs, G., Sessler, J., "A Study of Plastic Deformation in Flat Notch Tension Specimens as Function of Strength Level and Initial Stress Concentration Factor," Syracuse University Research Institute Final Report II, December 1960.
45. Adams, M. A., Iannucci, A., "The Investigation of the Mechanism of Substructural Formation in Refractory Metals and the Relation to the Observed Mechanical Properties," WADC TR 59-441, Part II, December 1960.